Temperature Scales and the "Lithium Problem"

Adam Hosford

November 2009

University of Hertfordshire

Submitted to the University of Hertfordshire in partial fulfilment of the requirements of the degree of Ph.D.

Abstract

The discovery of the Spite plateau in the abundances of ^{7}Li for metal-poor stars led to the determination of an observationally deduced primordial lithium abundance. However, with the determination of the baryon density, $\Omega_{\mathrm{B}} h^2$, from the Wilkinson Microwave Anisotropy Probe (WMAP) data, a discrepancy arose between observationally determined and theoretically determined abundances of ^{7}Li. This is what has become known as the "lithium problem". Of all the uncertain factors in determining a stellar Li abundance, the effective temperature is the most important. This thesis is concerned with determining an accurate effective temperature scale for metal-poor halo dwarfs, paying specific attention to eliminating any possible systematic errors. This is done by utilising the exponential term, χ/T, of the Boltzmann equation. Two assumptions are adopted; firstly the simplifying assumptions of local thermodynamic equilibrium (LTE), and secondly the more sophisticated techniques of non-local thermodynamic equilibrium (NLTE). The temperature scales are compared to others derived using different techniques; a photometric scale, where I find comparable T_{eff} in LTE and hotter temperatures by an average of ~ 150 K in NLTE; a scale derived using Balmer lines, for which I have comparable values in LTE and hotter T_{eff} values, by typically 110 K – 160 K, in NLTE; and finally a scale derived using an infrared flux method (IRFM). Here I find their T_{eff} values are hotter by ~ 250 K for LTE and ~ 190 K in NLTE. Lithium abundances are then calculated for the program stars and a mean Li abundance is derived. I find values ranging from A(Li) = 2.10 dex – 2.16 dex with the LTE scales and A(Li) = 2.19 dex – 2.21 dex for the NLTE scales. These mean Li abundances are compared to other observationally deduced abundances, for which I find comparable results in LTE and higher values in NLTE, and to the WMAP + big bang nucleosynthesis calculated

Li abundance. I find that my new values are still considerably lower than the WMAP value and are therefore unable to reconcile the lithium problem.

Second to this primary investigation, I use Ti as an independent test of the derived T_{eff} values and log g's. I find that Ti is not a useful constraint on the temperatures or, therefore, on the lithium problem. I also assess the impact of the new T_{eff} scales on the different models of Galactic chemical evolution (GCE), comparing newly calculated abundances with GCE determined abundances. It was found that trends exist in several of the elements; however, these were not statistically relevant. Also a larger degree of scatter was found in the abundances compared to the Arnone et al. (2005). This scatter was not to the degree found in the Argast et al. (2000). Reasons for the differences have been discussed.

Contents

List of Figures

Chapter 5

Chapter 7

Chapter 8

Chapter 9

List of Tables

Chapter 7

Chapter 8

Chapter 9

Acknowledgments

I would like to thank my supervisors for their hard work. Sean G. Ryan, who always had time to sit and discuss my work, even with his busy schedule, and guide me through a very interesting project, and Ana E. García Pérez, who had the hard task of guiding me through the intricacies of NLTE. Thank you both. I gratefully acknowledge the help from my collaborators on the papers that appear in this thesis, their guidance and suggestions have lead to two very good papers. I also thank my family for their support and putting up with me prolonging my student life for another three years, and their financial support through the years that has allowed me to follow the path I wanted to take. Finally I thank all my very good friends that have seen me through many highs and a few lows, and have helped me come out the other side relatively unscathed, thank you all.

1. Introduction

It was as far back as 1802 when the first spectral lines in sunlight were observed by Wollaston. Following this, in 1814 the first systematic study of these features was performed by Fraunhofer, the set of lines that he discovered now known as Fraunhofer lines. These discoveries began a vast field in astronomy, and opened up a whole new method of studying the Universe. Following these initial discoveries many steps have taken place that furthered our knowledge of spectra. Kirchhoff & Bunsen (1860) discerned that the dark absorption lines in stellar spectra represent the absorption from particular elements, and the strength of absorption was a measure of the abundance of the element. Classification of spectra was possible, based on which lines were present and their strengths. Large scale classification took place in the early 20th century, by the likes of Annie Cannon at Harvard leading to the O – B – A – F – G – K – M sequence. This scale was later found to be representative of the temperatures of the stars through the work of Cecilia Payne (1925) using the Saha ionisation law.

The use of stellar spectra as a tool to determine the abundances of elements within stars was first developed by Minnaert and co-workers in Utrecht in the middle of the 20th century, the introduction of terms such as "equivalent width" and "curve of growth" coming from their work. It was my time spent undertaking research in Utrecht in 2004/05 that first sparked my interest in the subjects of spectroscopy and radiative transfer. Throughout the 20th century modelling techniques and more general line-formation theory was developed, allowing for precise abundance determinations. Important papers on this subject are included in Menzel & Milne (1966). It is with these tools that we can delve into the processes that occur within stellar atmospheres and better understand the evolution of the stars we see overhead.

These spectroscopic tools where utilised by Spite & Spite (1982) to examine Li abundances of unevolved halo stars. In this work they discovered a plateau in Li abundances when plotted against metallicity. This plateau was hypothesised to be representative of the primordial abundance of Li from the Big Bang. However, the mean abundance that is now calculated is at odds with the primordial abundance calculated by theorists using theoretical big bang nucleosynthesis (BBN) models: observational values are a factor of 3 lower than theoretical values (Cyburt et al. 2008). This discrepancy is better known as the "lithium problem". In this project I use the tools of spectroscopy to try and solve this cosmological question: is the discrepancy between the abundance from the theory of BBN and observationally determined abundances for the primordial abundance of lithium due to the calculated temperature of the stars under study?

For this to be better understood some knowledge of both the theory and observation is needed. The main theory is that of BBN (e.g. Coc et al. 2002, Cyburt, Fields & Olive 2003) which concerns the production of the light elements H, He, and trace amounts of ^{7}Li and ^{7}Be in the few minutes after the formation of the universe, ^{7}Be later decaying back into ^{7}Li via electron capture: $^7\text{Be} + e^- \rightarrow \, ^7\text{Li} + \nu_e$. The whole period of BBN only lasted ≈ 17 minutes at which point the temperature and density of the universe was too low for further nucleosynthesis to occur. It is the production of ^{7}Li during this period that I am concerned with. ^{7}Li has two modes of creation. Firstly at a low baryon to photon ratio, η, or equivalently low baryonic density $\Omega_b h^2$, it is formed through the reaction $^3\text{H}(\alpha, \gamma) \, ^7\text{Li}$. Secondly at higher η or $\Omega_b h^2$ it is formed indirectly via $^3\text{He}(\alpha, \gamma) \, ^7\text{Be}$ with the ^{7}Be later decaying to ^{7}Li. The one free parameter in standard BBN is the baryon density; precisely determining this leads to a precise value for the primordial abundance of ^{7}Li.

Through the observation of the cosmic microwave background (CMB) radiation, and the derivation of its power spectrum, a precise value of the baryon density was obtained recently (Cyburt et al. 2008). At the value inferred, the primordial abundance of ^{7}Li, as deduced from BBN, is a factor of 3 higher than the value determined from observations of metal-poor stars, which I describe below. We see now the formation of the "lithium problem". One possible explanation for this discrepancy is that the atmospheric parameters derived from observation suffer from systematic errors, and cause a lower abundance to be calculated.

Observationally the primordial ^{7}Li abundance is calculated from metal-poor halo stars. These are the oldest stars surrounding our Milky Way and their metal abundances represent the abundances of the early Galaxy. It was Spite & Spite (1982) who first discovered the plateau in the abundance of lithium, now known as the Spite plateau, which was thought to represent this primordial abundance. Following on from this many further studies have confirmed its existence, e.g. Spite et al. (1996), Ryan et al. (2000), Meléndez & Ramírez (2004) and Bonifacio et al. (2007). However, it was realised that all of these studies fall short of finding a lithium value that is reconciled with the BBN+WMAP calculated abundance. One major source of possible error in these works is the calculation of stellar effective temperature. It is the temperature that is the most important parameter in determining the lithium abundance observationally. The temperature scales used by different authors can vary vastly, the difference between Ryan et al (2001) and Meléndez & Ramírez (2004) having typical differences of ~ 200 K reaching a maximum difference of ~ 500 K at the lowest metallicities.

It is therefore the temperature scales of metal-poor halo stars that this thesis is principally concerned with. Other possible reasons for the discrepancy are briefly discussed in Chapter 4 [Paper I]. The tools of spectroscopy are utilised to derive new temperatures for a

group of metal-poor halo stars, the main goal being to identify systematic errors that may lead to a temperature scale zero point being too low. This is done using two different assumptions. Firstly in Chapters 2, 3, 4 (Paper I) and 5 the temperatures are calculated under the assumption of local thermodynamic equilibrium (LTE). This is a simplifying assumption which is very powerful and quick, allowing for abundances to be determined with relative ease. However, this simplifying assumption breaks down under certain conditions. Calculations now suggest that this is the case for metal-poor stars; the combination of their lower atmospheric free electron densities (leading to less dominance of collisions to drive the kinetic equilibrium), more scattering, and a lack of UV blanketing due to metal deficiency lead to greater levels of non-local phenomena. The second part of this thesis, Chapters 6, 7 (Paper II) and 8, therefore concerns the vastly more complicated methods of non-local thermodynamic equilibrium, the aim being to discern whether this new method, and the corrections to abundances that it implies, has a dramatic effect on the calculated temperatures. With doing this it was hoped that either the lithium problem would be reconciled or that the temperature scale would be eliminated as a possible explanation of the discrepancy. The outcome, as it turned out, was the latter.

With the large spectral range of the program data, lines of several other elements other than Fe, which is primarily used in this thesis, are also available. It is therefore possible to use these other elements to offer further constraints on the effective temperature scales of the stars in this study. Ti II has the most lines available after Fe, and with Ti I also measureable it is possible to constrain log g through ionisation balance as well. In the final part of this thesis I present the results of this Ti analysis and the effect it has on the lithium problem. The lithium problem is part of the greater issue of galactic chemical evolution (GCE). Therefore, along with the Ti analysis I also present a chemical abundance analysis of

heavier elements (e.g. Mg I, Si I, Ca I, Al I, Ba II) using the my newly derived stellar parameters and discuss the implications of the results in regard to GCE (Chapter 10).

The study of halo stars allows for a direct look at the oldest component of the Milky Way, which is the stars themselves. Due to their low mass and therefore long lifetimes, the elemental abundances within these stars reflect the composition and inhomogeneity of the ISM during the formation of the halo. Abundance ratios can be used as a diagnostic to the initial mass function (IMF), star formation rate (SFR) of the Galaxy and to the number and yield of different types of supernovae (SNe). Complementing the observation of these elements and their abundances are theoretical models that attempt to describe the trends and scatter seen observationally. Two contrasting models are the simple one-zone model (e.g. Schmidt 1963 and Pagel & Patchett 1975) and inhomogenous galactic chemical evolution (iGCE) models (e.g. Argast et al. 2000). In the one-zone model the evolution is within a closed system, subsequent generations of stars being formed out of the available ISM gas. With each generation of stars the ISM is instantaneously replenished with newly formed metals, while gas locked within the low-mass stars no longer plays a role on further star formation. In this model the metallicity always increases with time and is perfectly homogenous. In the iGCE model the desired spatial volume is divided up into several thousand separate cells, a volume of 2.5 Kpc divided into 50^3 cells in the case of Argast et al. (2000), each containing detailed information about the ISM. Star formation can occur in a set of randomly chosen cells, up to 20000, at each time step, depending on a probability that is proportional to the square of the local ISM density. The mass of the stars that are produced is chosen randomly from a Salpeter IMF. These stars are left to evolve enriching the local ISM with varying amounts of material depending on the mass, e.g. stars with masses $10 - 50 \, M_{\odot}$ will explode as type II SNe. This more sophisticated modelling seems to reproduce the

observed abundance trends and inhomogeneties far better than the one-zone model (Argast et al. 2000, 2002).

In this thesis I perform a preliminary investigation into GCE, calculating the abundances of available elements within the spectrum of the program stars. In doing this I am able to compare results with other works, e.g. the observational work of Arnone et al. (2005) and the theoretical work of Argast et al. (2000). In particular I am interested in the implications of any trends with [Fe/H] and any scatter about this trend. Through this study some initial statements can be made about what kind of situation, i.e. inhomogeneous or homogeneous, may be supported, or rejected by the abundance ratios, and any trends or scatter in them.

2. Data Reduction

This thesis concerns the study of a group of 18 metal-poor stars near the main sequence turn-off. It is this class of star that is thought to hold the Li remnants of the Big Bang within their chemical composition. The first part of this thesis (Chapters 2 – 5) concerns a program to calculate new temperatures for metal-poor stars which have previously been used to study the primordial Li abundance. In these chapters I use LTE methods to calculate spectroscopic effective temperatures (T_{eff}) of the program stars. Chapter 4 - Paper I (Hosford et al. 2009) - presents all the major relevant aspects of the analysis that are important to a reader who is concerned with the temperature scales and the lithium problem; sample selection, methodology, results, discussions and conclusions. Within this preceding chapter, Chapter 2, I include additional work that was not reported on in Paper I, i.e. a more in depth discussion of the data reduction and further quality checks of my data. The Data Reduction discussion outlines the processes that go into making the data suitable for use in this work. Following Paper I, further quality checks are discussed.

For the purposes of high-precision abundance analysis, high resolution, high signal/noise spectra with wide wavelength coverage are required of each of the program stars. With modern échelle spectrographs this is possible. For this work data were obtained using the Anglo-Australian 4m telescope with the UCLES instrument. UCLES is an échelle spectrograph, which allows higher orders of the diffraction pattern to be viewed. This is achieved by moving the Fourier component which represents the diffraction envelope, i.e. the envelope that determines the intensity of an interference peak at different values of n, where n is the spectral order integer, to higher orders, allowing these higher orders to have a greater maximum intensity. Higher resolution is then obtained, as the dispersion is greater at higher orders, whilst still collecting a large number of photons giving a high signal/noise ratio. The

high dispersion of the échelle grating means that a CCD length covers only a short wavelength range; therefore in order to cover a larger wavelength range many spectral orders must be produced. Due to the nature of the grating equation, i.e. $\frac{n\lambda}{d} = \sin\alpha + \sin\beta$ where λ is the wavelength, d is the slit spacing, α is the angle of incidence and β is the angle of diffraction, the different orders overlap, especially when working at high order numbers as with an échelle spectrograph. Thus a cross-dispersion is performed, by passing the light through cross-dispersion prisms, to produce order separation. The orders are then imaged onto a CCD. The observations are described in Paper I, what follows here is a description of the process of reducing these data.

The data were reduced using several packages within the IRAF program. This process proceeds in several steps which will be explained here. The first step was to remove the electronic bias that is applied to the CCD to stop the occurrence of negative values due to noise, and to remove the variation in the bias that arises from the fact that the read-out of the CCD takes time. The bias is additive and therefore needs to be subtracted from all data frames. This is done by taking several BIAS frames when observing. These BIAS frames are zero second exposures of the CCD. In our observations 10 such frames were taken at the start of each of the three nights. These frames are then cleaned, i.e. cosmic rays and spurious positive spikes are removed, and combined using the *zerocombine* routine. The cleaning is done in the routine prior to the combining by setting reject in the parameters of *zerocombine* to *sigclip*. The *sigclip* algorithm computes the average at each output pixel and the sigma about this average. Points that fall outside a specified sigma range are rejected. This routine combines the BIAS images using the average.

Second to the BIAS subtraction there is the subtraction of the thermal dark current that is present in the CCD. This arises from either a general background level from thermally

26

generated electrons or locally hot pixels. 10 × 100 s DARK frames were taken at the end of each observing run. Like the BIAS frames these are also cleaned and combined, this time using the *darkcombine* routine. This works in the same way as *zerocombine*. For modern CCDs the dark count is very low and in some cases subtraction of the dark frame is not needed, as was the case for my data. Nevertheless, the data frames had to be reduced in order to reach this conclusion. These combined and cleaned frames can then be used to subtract the BIAS (which I did) and DARK (which I ignored) levels from the data frames using the *ccdproc* routine.

Another set of calibration images that is taken are the flat fields (FLAT). This is done so that a frame can be created that can be used to divide out the pixel to pixel variations. These variations are caused by differences in pixel sizes, wavelength dependent quantum efficiencies in different pixels, fringing problems which create global interference patterns and effects due to obstructions in the optical path, such as dust. The idea is that any non-uniform gain, the ratio: input signal/output signal, can be removed and any features left over should be that of the spectra. This is done with 10 × 100 s FLAT images taken of a quartz lamp, which acts as a smoothly varying light source, at the start of each observing run. At this point the FLAT frames are also combined, using *flatcombine*. This works in the same way as *zerocombine* and *darkcombine*.

A fourth step is the mapping of where the échelle spectral orders, as discussed above, are located on the CCD frames. This is done using the *apall* routine. Within this process, the location and width of each échelle order, called apertures, are defined. Initially a reference template for the apertures is constructed using the spectrum of a rapidly rotating star. This type of star is used to obtain high-signal-to-noise with few features in the spectrum, whilst still going through the same optical path as the program data. In defining the apertures, several routines are called by the *apall* routine, all of which need several parameters to be set.

Once all initial parameters are set then *apall* can be run. This will find, size and trace the apertures. To find the apertures *apall* calls a separate routine, *apfind*, this takes a cross-cut through the spectra, finds the local maxima, and rejects weaker peaks that are not separated by a given number of pixels. It keeps the number of peaks as specified by the number of apertures given. In sizing the apertures the routine is supplied with the approximate width, in pixels, and a searching radius and threshold value. These values allow the algorithm to search, by linear interpolation, within given upper and lower limits, for a specified value that defines the aperture edge. Figure 1 is an example of the defining of the aperture centres and widths. If, after the routine has attempted to find the apertures, they are not centred properly or are of incorrect width then they can be interactively set in the *apall* editor. I checked apertures in several lines across the CCD; some at either edge of the CCD frame and some at the centre, to confirm the fitting had gone correctly, i.e. the whole aperture is covered and that its centre is correctly defined. Well defined apertures sizes are needed so that the tracing along the dispersion axis can be done accurately. The tracing is done by *aptrace*. This takes the positions of the centroids of each aperture along the dispersion axis and fits a smooth function, a polynomial of order three, to their positions. I do this as the orders are not parallel to the edge of the CCD chip, but can be at angles across the chip. This function is then used to determine the shift of the aperture centre, at each wavelength, across the CCD chip. A plot of line versus column is produced, Figure 2; this shows the fit to the aperture centres. The *aptrace* routine was set to reject bad points that lie outside a given range of sigma values, in this case a lower value of 4, i.e. -4σ, and upper value of 3, i.e. $+3\sigma$.

During the modelling of the apertures, the aperture background level is interactively set as the inter-order minima. The background contains several pieces of information necessary for the reduction of échelle spectra. These include the general scattered/diffuse

NOAO/IRAF V2.12.2a-EXPORT ahosford@uhppc54.herts.ac.uk Fri 16:06:43 07-Nov-
Image=09mar10045, Sum of lines 1019-1028
Define and Edit Apertures
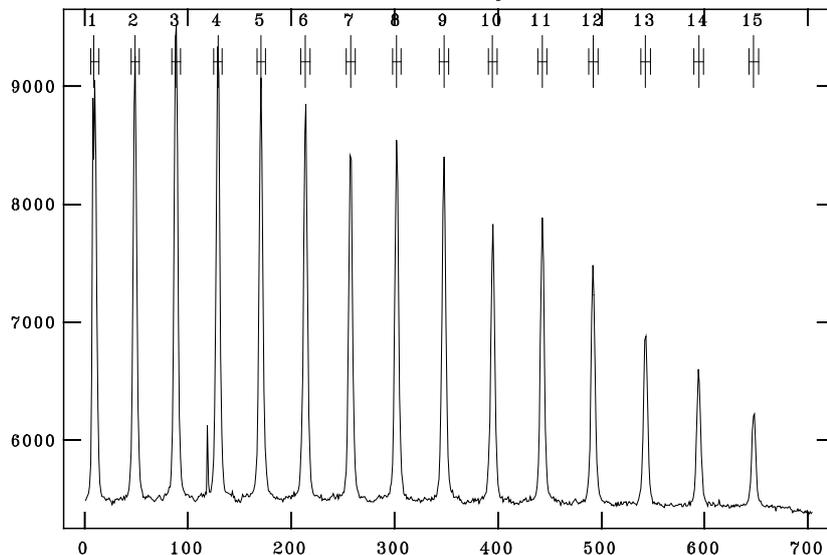
Figure 1 An example of the defining of the centres of the apertures (the peaks) for a selected column using the markers across the top of the plot.

NOAO/IRAF V2.12.2a-EXPORT ahosford@uhppc54.herts.ac.uk Wed 14:02:59 14-Oct-
func=legendre, order=3, low_rej=4, high_rej=3, niterate=10, grow=0
total=204, sample=204, rejected=3, deleted=0, RMS=0.05503
Aperture 2 of BD+262621_02.o
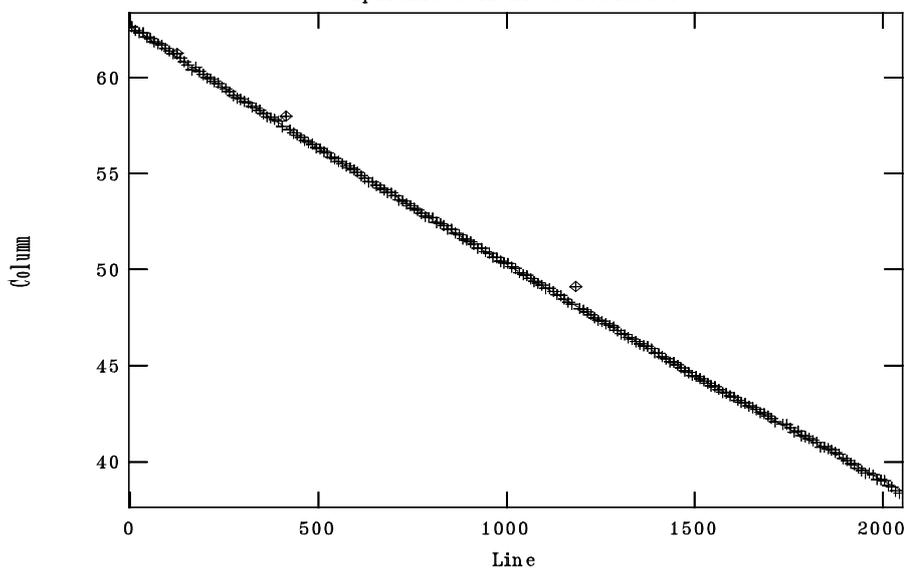
Figure 2 An example of the tracing of one aperture centre across all lines and a range of columns of the CCD. The diamonds are points that have been rejected in the fit.

light from adjacent orders and the sky background. In order for the object spectra to be accurately computed, all these contributions have to be removed. This is done by modelling a background surface through the inter-order minima and subtracting this from the data. The actual subtraction is done during extraction, i.e. the creation of 1D intensity versus pixel plots, and within the *apflatten* routine when normalizing the flat field, and after the scattered light has been defined. These processes are discussed below.

Once the aperture reference frame has been completed it is then possible to normalise the combined FLAT field frames. This is done so that a frame can be created that can be used to divide out the pixel to pixel variations. This process was done using the *apflatten* routine. This models the flat field data within the apertures, along the dispersion direction, with a polynomial. The model is then divided into the flat field data to produce the normalised flat field. The routine also subtracts the background using the previously defined inter-order minima. The normalised flat field was then visually inspected to check that the process had worked properly. When the normalised flat field had been created it was then used to flatten the stellar spectral data, i.e. to remove the features that aren't part of the star's spectrum. It was accomplished using *ccdproc*, which divides the spectral data by the flat field. Any signal left over should be that of the stellar spectra without any artifacts. The final step before the data can be extracted is to remove the scattered light. For this the *apscatter* routine is implemented to model the scattered light. This is done by first creating a fit to the inter-order troughs, which is the background, along all columns, then smoothing this along all lines. This creates a smooth 2D surface that can be subtracted off the data. For this step we again interactively set the fit for several lines and columns to confirm the job has been done adequately, before letting the routine automatically fit the rest.

With all of this done it is then possible to extract the spectra with the *apall* routine using the apertures that where defined previously. This means that 1D intensity versus pixel

plots of each aperture are extracted from the 2D images of the spectra. This is done by summing the pixels across the spatial axis at each wavelength within each defined aperture.

The next tasks are then to wavelength calibrate, clean cosmic rays from, and continuum normalise the data. To wavelength calibrate the spectra several ThAr lamp frames are taken through the course of the observing night. It is possible to manually identify known ThAr spectral lines within the first ThAr frame, which in IRAF is done with the *ecidentify* routine. By doing this a dispersion relation, e.g. a relation between the pixel number and the wavelength, can be built up by, progressively constraining the parameters "match" and "threshold" whilst increasing the number of features identified with "maxfeat". "Match" defines the latitude the algorithm has in matching its library of wavelengths to your features, while "threshold" gives the minimum intensity the pixel must have for it to be identified as an emission line. This is done until the majority of the lines have been identified and trends in the residuals of the dispersion relation have been removed. This dispersion relation can be solved for the other ThAr frames using *ecreidentify*. Having found the dispersion relations these can then be applied to the stellar spectra by first using *refspectra* to identify which ThAr frame corresponds to which star, i.e. which ThAr spectrum was taken closest in time to each stellar spectrum. The routine *dispcor* is then used to apply the solution to the spectra.

The next step is to clean the spectra so that cosmic rays and other artefacts are removed. To do this I went through four steps. Firstly a smoothed version of the spectrum is created with the routine *median*. This routine filters the image with a box of specified dimensions, in our case $\Delta x = 5$ and $\Delta y = 1$, which moves along the spectrum replacing the center point of the box with the median of all the points in the box. This smoothed spectrum is then divided into the real spectra to remove the blaze shape, giving a flat spectrum. This was done as we use the routine *lineclean*, which needs a flat spectrum to work properly, to remove cosmic rays. *Lineclean* fits a 1D fit to each spectrum, I used a cubic spline and

31

rejected points above and/or below certain sigma values; I used a *high_reject* = 5 and a *low_reject* = 0. The 0 low_reject is needed so that no absorption lines are removed in this process. In doing this, cosmic ray spikes are removed. After this the cleaned spectra are multiplied by the smoothed version to regain the original spectra minus the cosmic rays.

To normalise the continuum and remove the blaze profile, the routine *continuum* is applied. Within this routine the continuum is manually fitted to the line free regions of the spectra by adjusting the order and hi/low rejects of the fit, Figure 3 shows a part of a spectrum with the fit for the continuum. Once normalised the spectra should have a continuum set to one as given by the fit, however, in practice it is hard to get a perfect fit, thus the continuum tends to vary around one which can give a wave-like look to the spectra.

The final step in the reduction was to make corrections for the Doppler shift of the spectra. This is calculated by comparing the wavelength of known spectral lines, e.g. Hγ, to the wavelengths of those spectral features in the stellar spectrum. The difference between these wavelengths can then be used to determine the velocity of the star, using the formula: $\Delta v = c\, \Delta\lambda/\lambda$, where Δv is the Doppler velocity, $\Delta\lambda$ is the shift in wavelength and λ is the rest wavelength of the line in question. The value Δv is used with the routine *dopcor* to apply the velocity shift to the spectra so that the final result is that all wavelengths are in the rest frame of the star. At this point the spectrum is ready to have line strengths measured for lines of interest, as I go on to describe in Chapter 4.
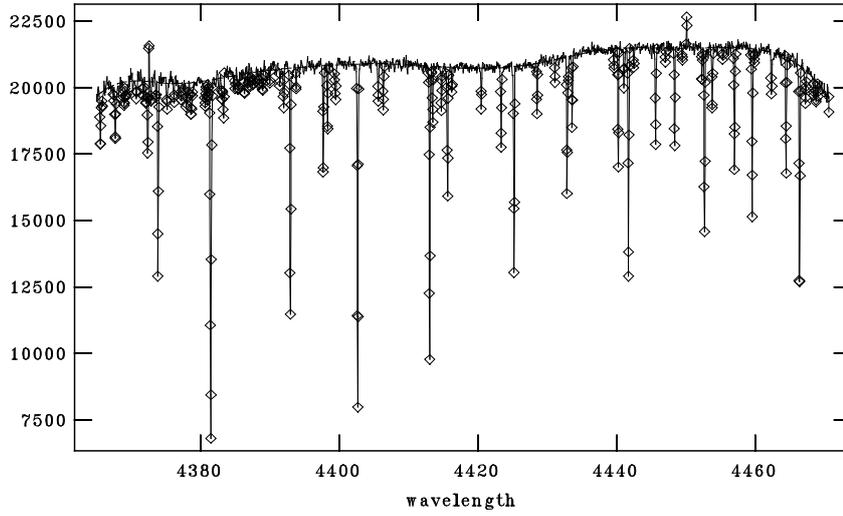
Figure 3 Example of fitting the continuum to the spectra.

3. Broadening of spectral lines

The reason we see a spectral line as a wide feature in the spectrum of a star as opposed to a thin sharp line is due to broadening. There a several mechanisms that affect the shape of a spectral line, and depending on the type of analysis undertaken, these may need to be taken account of to create an accurate interpretation of the line. There are two possible methods of spectral line analysis: one that uses equivalent widths to represent the flux absorbed by a line, and thus allows chemical abundances to be calculated; and one that synthesises the shape of spectral lines, taking into account the relevant science, and compares these synthesised profiles to observed profiles. The equivalent width analysis has the advantage that it is only affected by micro-scale broadening, i.e. on length scales less than the mean-free path of the photon. This includes microturbulence, temperature and surface gravity. The line profile synthesis method suffers from these mechanisms and also macro-scale broadening, i.e. on scales greater than the mean-free path of the photon. Such mechanisms include macroturbulence and stellar rotation. Throughout this thesis I adopt an equivalent width analysis. This means that macro-scale broadening and similarly instrumental broadening can be assumed not to affect the process. However, along with a discussion of all the broadening mechanism, this chapter will also show that the rotation of the program stars is small and confirms that rotational broadening can be discounted.

3.1 Broadening mechanisms and damping constants

The shape of a spectral line is dictated by several sources of line broadening. It is the convolution of these broadening mechanisms that gives rise to the shape of the line seen. Below I will outline the main sources of broadening and the implications from them that impact on this work. These sources of broadening are classified as natural/radiation broadening, pressure broadening, thermal broadening, microturbulence and rotational

broadening. This theory can be found in many texts, e.g. Gray (2005). Below I outline the main factors in spectral line broadening; all equations are taken from Gray (2005).

Natural broadening arises from the fact that the two energy levels that form a transition, and hence a spectral line, have an intrinsic energy width ΔW. Therefore an electron making the transition between levels can start from anywhere within this energy range in the lower level and end up within the energy range of the upper level. Through many electron transitions there is a broadening of the line around this energy width. This width is set by the important damping constant, γ. This shapes the line through the natural absorption coefficient per atom, α, given by the equation:

$$\alpha = \frac{e^2}{mc} \frac{\lambda^2}{c} \frac{\gamma\lambda^2/4\pi c}{\Delta\lambda^2 + (\gamma\lambda^2/4\pi c)^2} \qquad (3.1)$$

where e is the electron charge, m the electron mass, c the speed of light and λ the wavelength. The term in $\Delta\lambda$ in this equation has the form $\frac{a\gamma}{\Delta\lambda^2 + (a\gamma)^2}$ (where a is a constant for a spectral line) which is the Lorentzian form, symmetric about $\Delta\lambda = 0$, reaching a maximum at $\Delta\lambda = 0$, and asymptotically to 0 as $|\Delta\lambda|$ increases. This form of the equation is for wavelength units. The full coefficient will be the convolution of α for the lower and upper level. The damping constant is obviously an important parameter; an inaccurate value could translate through the whole of the analysis and lead to incorrect abundance calculations. The treatment of the damping values in this work will be discussed later in this chapter.

Several other mechanisms in the stellar atmosphere also lead to the broadening of a spectral line. Thermal broadening arises from the different velocities of the particles along our line of sight due to thermal motion. These motions cause Doppler shifts to the emitted photons. The combined effect of these wavelength shifts causes a broadening of the line. The absorption coefficient for thermal broadening is given by:

$$\alpha \mathrm{d}\lambda = \frac{\pi^{1/2}e^2}{mc} f \frac{\lambda_0^2}{c} \frac{1}{\Delta\lambda_D} \mathrm{e}^{-(\Delta\lambda/\Delta\lambda_D)^2} \mathrm{d}\lambda \qquad (3.2)$$

where λ_0 is the central wavelength of the line and $\Delta\lambda_D$ is the dispersion due to the Doppler shift, given by:

$$\Delta\lambda_D = \frac{\lambda_0}{c}\left(\frac{2kT}{m}\right)^{1/2} \qquad (3.3)$$

The term in $\Delta\lambda$ in Eq. (3.2) has the form $\exp - \left(\frac{\Delta\lambda^2}{aT}\right)$ (where a is a constant for a spectral line) which is a Gaussian form, symmetric about $\Delta\lambda = 0$, reaching a maximum at $\Delta\lambda = 0$, tending exponentially to zero as $|\Delta\lambda| = 0$ increases.

Microturbulence is directly analogous to thermal broadening, with small scale mass motions causing velocity fields that cause the Doppler shift. Here $\Delta\lambda_D$ in Eq. (3.2) is replaced by ξ, which is the microturbulence.

Pressure broadening of a line is the result of collisional interactions between the atoms absorbing the light and other particles. These other particles can be ions, electrons or atoms and in the case of cool stars may be molecules. This interaction causes the upper and lower levels of a transition to be perturbed, with the upper level suffering the larger effect, and is a function of the separation, R, between the two particles. Through many interactions this causes a given spectral line to become broadened. The change of energy due to these collisions can be approximated by a power law:

$$\Delta W = \mathrm{constant}/R^n \qquad (3.4)$$

Here n is dependent on the type of collision:

- $n = 2$ is known as the linear Stark effect, this interaction is due to the effect of protons and electrons on hydrogen lines.

- $n = 4$ is the quadratic Stark effect, this concerns most lines, especially in hot stars, and is the result of collisions with ions and electrons.

- $n = 6$ is the van der Waals effect, this concerns most lines, especially in cool stars, and is the result of collisions with neutral hydrogen.

The above interactions are the most important in stars. If Eq. (3.4) for the lower level is subtracted from that from the upper then a frequency shift can be calculated:

$$\Delta v = C_n / R^n \qquad (3.5)$$

C_n is the interaction constant. This must be calculated or measured for each transition and type of interaction. This equation becomes useful in deriving the collisional damping constant, γ_n, which arises from the derivation of the atomic line absorption coefficient for collisional broadening:

$$\alpha = \frac{\gamma_n/4\pi}{(v - v_0)^2 + (\gamma_n/4\pi)^2} \qquad (3.6)$$

To judge whether collisions have an effect they are placed into one of two groups depending on the strength of the encounter. The strength is measured by the size of the phase shift of the photon caused by the interaction. If the phase is shifted by a certain amount then it is counted. The effect of many phase shifts will then give rise to a frequency shift and is what is desired to calculated the broadening. The cumulative phase shift is given by:

$$\phi = 2\pi \int_0^\infty \Delta v \, dt = 2\pi \int_0^\infty C_n R^{-n} \, dt \qquad (3.7)$$

Using the criteria that any phase shift greater than 1 rad is counted, and that $\rho = R\cos\theta$, where ρ is the impact parameter and θ is the angle between the atom and perturber, allows for a limiting impact parameter to be defined such that:

$$\rho_0 = \left[\frac{2\pi C_n}{v} \int_{-\pi/2}^{\pi/2} \cos^{n-2}\theta \, \mathrm{d}\theta \right]^{1/(n-1)} \tag{3.8}$$

where v is the average velocity of the perturbers. This parameter gives the minimum value for which collisions are said to broaden the line. The integral in Eq. (3.8) has the value of π for $n = 2$, $\pi/2$ for $n = 4$ and $3\pi/8$ for $n = 6$. This equation is then used in the damping constant. The number of relevant collisions is given by $\pi\rho_0^2 vN\Delta t_1$, where N is number of perturbers per unit volume and Δt_1 is the time interval over which the collisions are counted. If we set $\Delta t_1 = \Delta t_0$, with Δt_0 the average collisional time for the gas, on average the number of collisions in this time is one and therefore $\pi\rho_0^2 vN\Delta t_0 = 1$. It follows on that:

$$\gamma_n = \frac{2}{\Delta t_0} = 2\pi\rho_0^2 vN \tag{3.9}$$

where v is the average relative velocity of the atom and perturber. The damping constant can be evaluated numerically for different values of n. In particular I look at the quadratic Stark effect and the van der Waals effect; however it is the van der Waals effect that is most important for Fe lines in metal-poor stars.

The Stark effect is due to perturbations from charged particles. Using Eq. (3.8) and Eq. (3.9) the damping constant is:

$$\gamma_4 = 2\pi vN \left(\frac{\pi^2 C_4}{v} \right)^{2/3} \approx 39 v^{1/3} C_4^{2/3} N \tag{3.10}$$

Evaluated numerically this becomes:

$$\log \gamma_4 \approx 19 + \frac{2}{3}\log C_4 + \log P_e - \frac{5}{6}\log T \tag{3.11}$$

The interaction constant C_4 is found from laboratory measurements.

For van der Waals, perturbations from interactions with neutral particles, the values for the damping constant are:

$$\gamma_6 \approx 17 v^{3/5} C_6^{2/5} N \tag{3.12}$$

which reduces to:

$$\log \gamma_6 \approx 20 + 0.4 \log C_6 + \log P_g - 0.7 \log T \tag{3.13}$$

Unsöld (1955) showed using simple approximations that the difference between the energies of the two levels leads to an evaluation of the interaction constant C_6. His methods have been widely adopted for many years, however, they have been shown to underestimate the values of γ_6. This led to the introduction of an empirical enhancement factor for γ_6 ranging from 1.0 – 1.5 depending on the excitation energy (Simmons & Blackwell 1982).

The theory of van der Waals along with the Unsöld treatment of C_6 has now been superseded by newer theory. Anstee & O'Mara (1995) and Barklem et al. (1998a) have developed collisional line broadening theory that uses the principal quantum number n and the angular momentum component l of the levels under consideration to calculate γ_6. Application of these newer results led Anstee, O'Mara & Ross (1997) to derive values of the solar iron abundance that matched the meteoritic abundance values. Anstee & O'Mara (1995) and Barklem et al. (1998a) have created tables of broadening cross sections for many transitions. These can then be used to calculate the damping constant for pressure broadening, and hence the amount of broadening of the line in question.

This kind of broadening most affects strong lines, i.e. lines with equivalent widths greater than $\approx$ 50 mÅ, through their wings. It can be seen from Eq. (3.11) and Eq. (3.13) how the wings are dependent on both the temperature and the pressure. These effects vary with the type of line considered.

Absorption coefficients for each type of broadening can be combined through multiple convolutions ($*$) such that:

$$\alpha(\text{total}) = \alpha(\text{natural}) * \alpha(\text{Stark}) * \alpha(\text{van der Waals}) * \alpha(\text{thermal}) * \alpha(\text{micro})$$

The first three coefficients each have dispersion (Lorentzian) profiles whose shape is dictated by the relevant damping constant, γ, as discussed above. The last two produce Gaussian profiles. The final line is therefore in essence the convolution of a composite Gaussian with a composite dispersion profile. The Gaussian describes the core of the line whilst the dispersion profile sets the shape of the wings in a spectral line.

In many studies, weak lines are adopted as it was assumed that these lines are not affected by collisional broadening to the same extent as stronger lines. However, Ryan (1998) demonstrated that even with weak lines careful consideration of the collisional damping constant is needed. He showed, his Fig 2, that the different methods for calculations of the damping constant leads to different abundances for both the weak and strong lines. The abundances can differ by up to 0.1 dex for a factor of 2.5 change in the damping constant for lines with equivalent widths $<$ 65 mÅ. This highlights that our understanding of line formation is incomplete and reaching abundances accurate to a few $\times$ 0.01dex will not be possible until the gaps in our knowledge and bridged. Because of these uncertainties, I adopt the Anstee & O'Mara (1995) damping values, as this is the most up to date formulation of the calculation of damping constants. Their tables are used to calculate the relevant values needed for the single line radiative transfer program WIDTH6 adopted for this work. These

are tabulated in a line list for all the lines within our spectra. WIDTH6 calculates the broadening using the relevant equations as described above. Microturbulence, however, is derived after the implementation of WIDTH6 by ensuring that there is no trend in plots of abundance vs. equivalent width. This nulling procedure may also reduce the error induced by inaccurate collisional damping constants (Ryan 1998).

3.2. Rotational broadening and $v \sin i$

A further means of broadening a spectral line comes from the rotation of the star itself, quantified by $v \sin i$. With increased rotation, a spectral line's wings are broadened whilst the core is flattened. Figure 4 gives an example of the effect rotation has on the broadening of the line. The equivalent width of a spectral line should not change, since rotation shifts the wavelength at which flux from the star is observed, but does not affect the passage of that flux through the atmosphere (Gray 2005, Chapter 18). In this thesis I use equivalent widths, so my results are not affected by rotation. Furthermore, stars in this study are expected to have a very low rotational velocity (see below). This effectively allows me to ignore the rotation of the star as a source of uncertainty in this investigation. However, I estimate the $v \sin i$ values of the program stars to confirm that this is the case.

To check approximately that the program stars have a small $v \sin i$, I first calculate the mean value of the Gaussian full width at half maximum (GFWHM) from Fe lines with an equivalent width between 30 mÅ and 70 mÅ. For this I obtain values ranging from roughly 9.7 km s^{-1} to 10.8 km s^{-1}.

From Ryan et al. (2002) Figure 3, it is seen that metal-poor dwarf stars with lines whose values of GFWHM lie within this range have $v \sin i$ values less than 5 km s^{-1}. It is possible to calibrate the Ryan et al. (2002) Figure 3, to give the equation:
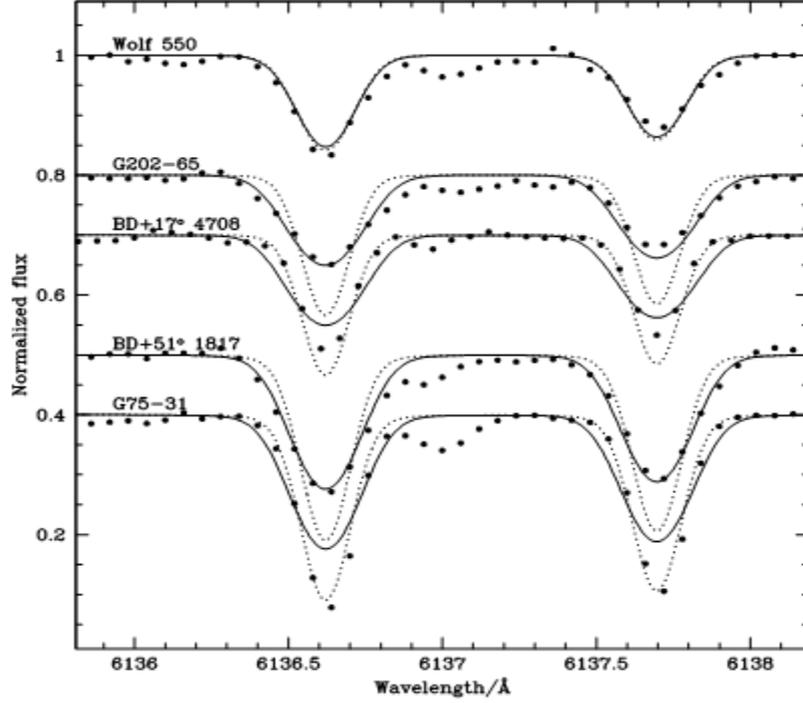
Figure 4. Example of the effects of line broadening on spectral lines, taken from Ryan et al. (2002). The rotation increases from the dotted line to the solid line. Wolf 550 has $v \sin i$ of 5.0 and 5.5 km/s for the solid and dotted lines respectively. G202-65 and BD+17 4708 have $v \sin i = 0$ and 8.5 km/s for the solid and dotted lines respectively. BD+51 1817 and G75-31 have $v \sin i = 0$ and 7.5 km/s for the solid and dotted lines respectively

$$v \sin i = 3.96 \sqrt{(\text{FWHM}_{50} - 9.22)} \qquad (3.14)$$

where FWHM_{50} is the Gaussian full width at half maximum in km s^{-1} at 50 mÅ. This allows for a more precise estimate of the $v \sin i$ values of the program stars; these are listed in Table 1. It is clear that the rotation velocity of the program stars is small. The Ryan et al. (2002) study consists of metal-poor turnoff stars that are very similar to those in this study, obtained with the aim of deriving Li abundances and very similar spectra were obtained. In that work, the realistic limit for measuring rotation was ~ 2.2 km s^{-1} (their Table 1). From this evidence, combined with my adoption of an equivalent width analysis as opposed to a synthetic profile fitting analysis, it is safe to assume that the effects of rotation on the spectral lines in this

study are negligible. I therefore proceed with the calculation of new effective temperatures

from the Fe I lines in the spectrum of my stars. This is carried out in the next chapter.

Table 1. A list of $v \sin i$ values estimated from the calibration (Eq. 3.14) of the Ryan et al (2002) Figure 3.

Star	$v \sin i$ (km/s)
BD+20 2030	4.2
BD+24 1676	4.8
BD+26 2621	4.0
BD+26 3578	3.9
BD+3 740	4.9
BD+9 2190	5.0
BD-13 3442	4.9
CD-24 17504	4.1
CD-33 1173	5.1
CD-35 14849	3.1
CD-71 1234	2.9
G64-12	4.5
G64-37	4.4
HD140283	2.0
HD74000	4.2
HD84937	3.6
LP635-14	3.9
LP815-43	5.0

4. Paper I – Lithium abundances of halo dwarfs based on excitation temperature. I. LTE

This Chapter is a paper which appeared as Hosford, A., Ryan, S. G., García Pérez, A. E. Norris, J. E., and Olive, K. A. 2009, A&A, 493, 601 - 612. The roles of the co-authors were as follows:

- S. G. Ryan played a major part in devising this project and as my principal supervisor was the main guide through the work. His background in spectroscopy, LTE line formation, chemical abundances and studies of metal-poor stars meant that he was heavily involved in discussions and suggestions on the direction of the work, and guidance in writing the paper. He also undertook the first of the two observing run to collect the initial data for the project.

- A. E. García Pérez and I undertook the second observing run to collect the final data for the project. She helped extensively in the reduction of this data, as described in Chapter 2. As my second supervisor she was part of discussions on the direction of the work. Having a background in NLTE line formation she contributed to the discussion on NLTE within the paper.

- J. E. Norris played a part in devising the project and contributed suggestions on the improvement of the paper

- K. A. Olive has a background in cosmology and BBN. He was also part of devising the project; he also offered suggestions on improvements to the paper and contributed parts of the introduction that discuss the aspects of BBN.

Figures and tables are renumbered to continue the sequence of the thesis, rather than the published version of the paper. The font and spacing has been changed from the published

Astronomy & Astrophysics styles to the only that most closely, but not perfectly, matches the remaining parts of the thesis. The pages have been renumbered to continue the sequence of the thesis.

Lithium abundances of halo dwarfs based on excitation temperature. I. LTE

A. Hosford[1], S.G. Ryan[1], A.E. García Pérez[1], J.E. Norris[2], and K.A. Olive[3]

[1] Centre for Astrophysics Research, University of Hertfordshire, College Lane, Hatfield, AL10 9AB, UK

e-mail: a.hosford@herts.ac.uk, s.g.ryan@herts.ac.uk, a.e.garcia-perez@herts.ac.uk

[2] Research School of Astronomy and Astrophysics, The Australian National University, Mount Stromlo Observatory, Cotter Road, Weston, ACT 2611, Australia

e-mail: jen@mso.anu.edu.au

[3] William I. Fine Theoretical Physics Institute, School of Physics and Astronomy, University of Minnesota, Minneapolis, MN 55455

e-mail: OLIVE@mnhep.hep.umn.edu

ABSTRACT

Context.

Aims. The discovery of the Spite plateau in the abundances of ^{7}Li for metal-poor stars led to the determination of an observationally deduced primordial lithium abundance. However, after the success of the Wilkinson Microwave Anisotropy Probe (WMAP) in determining the baryon density, $\Omega_B h^2$, there was a discrepancy between observationally determined and theoretically determined abundances in the case of ^{7}Li. One of the most important uncertain factors in the calculation of the stellar ^{7}Li abundance is the effective temperature, $T_{\rm eff}$.

Methods. We use sixteen metal-poor halo dwarfs to calculate new $T_{\rm eff}$ values using the excitation energy method. With this temperature scale we then calculate new Li abundances for this group of stars in an attempt to resolve the ^{7}Li discrepancy.

Results. Using high signal-to-noise (S/N $\approx$ 100) spectra of 16 metal-poor halo dwarfs, obtained with the UCLES spectrograph on the AAT, measurements of equivalent widths from a set of unblended Fe I lines are made. These equivalent widths are then used to calculate new $T_{\rm eff}$ values with the use of the single line radiative transfer program WIDTH6, where we have constrained the gravity using either theoretical isochrones or the Hipparcos parallax, rather than the ionization balance. The lithium abundances of the stars are calculated with these temperatures.

Conclusions. The physical parameters are derived for the 16 programme stars, and two standards. These include $T_{\rm eff}$, log g, [Fe/H], microturbulence and ^{7}Li abundances. A comparison between the temperature scale of this work and those adopted by others has been undertaken. We find good consistency with the temperatures derived from the Hα line by Asplund et al. (2006), but not with the hotter scale of Meléndez & Ramírez (2004). We also present results of the investigation into whether any trends between ^{7}Li and metallicity or temperature are present in these metal-poor stars.

Key words. Galaxy: halo – Cosmology: early Universe – nuclear reactions – nucleosynthesis – abundances – stars: abundances

1. Introduction

1.1. The Lithium Problem

The development of the Big Bang theory brought about predictions for the primordial abundances of the nuclides, ^{2}H, ^{3}He, ^{4}He, and ^{7}Li (Olive et al. 2000, Fields & Sarkar 2006). These values, determined from calculations of Big Bang Nucleosynthesis (BBN) for an assumed baryon to photon ratio η, are in at least partial agreement with those primordial abundances determined from observations of ^{2}H, ^{3}He, ^{4}He, and ^{7}Li relative to ^{1}H. Historically this has given constraints on η, or equivalently the baryon density fraction, $\Omega_{\rm B}h^2$, which is standard BBN's one free parameter, where h is the Hubble constant in units of 100 km^{-1} Mpc^{-1}. Precisely determining $\Omega_{\rm B}h^2$ by other means can narrow down the range for the calculated primordial abundances, and thus confirm whether the observationally inferred primordial abundances are consistent.

The Wilkinson Microwave Anisotropy Probe (WMAP) achieved high precision in measuring $\Omega_{\rm B}h^2$. Using measurements of the cosmic microwave background (CMB) radiation, the value $\Omega_{\rm B}h^2 = 0.0227 \pm 0.0006$ was inferred (Dunkley et al. 2008). This value is in excellent agreement with that derived from BBN via the measured ^{2}H/^{1}H and ^{4}He/^{1}H ratios, although the systematic uncertainties in the latter make ^{4}He a poor discriminant. However, for other primordial isotopes the results are not in such good agreement (Coc & Vangioni 2005, their Fig. 4). The baryon densities inferred from ^{3}He and ^{7}Li abundances differ significantly. ^{7}Li has the greatest deviation. The deviation of the observationally inferred primordial ^{7}Li abundance from that deduced from WMAP and from ^{2}H via BBN has become known as the "lithium problem".

The ^{3}He discrepancy can be accommodated within large uncertainties concerning the mechanisms in its production and destruction in stars (Vangioni-Flam et al. 2003). It is not clear that the ^{7}Li discrepancy can be explained as easily.

The primordial Li abundance was first deduced from observations of halo stars by Spite & Spite (1982) when they discovered the ^{7}Li plateau, now known as the Spite plateau, with a mean abundance of $n(^7{\rm Li})/n({\rm H}) =$

$1.12(\pm 0.38) \times 10^{-10}$. Many new obsevationally determined abundances have been published, the values of which can differ significantly, for example from the low value of $n(^{7}\text{Li})/n(\text{H}) = (1.23^{+0.68}_{-0.32} \times 10^{-10})(95\%$ confidence limits) (Ryan et al. 2000), to a decidedly larger value of $n(^{7}\text{Li})/n(\text{H}) = 2.34 \times 10^{-10}$ (Meléndez & Ramírez 2004). In comparison the abundance calculated from WMAP and from ^{2}H via BBN is $n(^{7}\text{Li})/n(\text{H}) = (4.15^{+0.49}_{-0.45} \times 10^{-10})$ (Coc et al. (2004)) or $(^{7}\text{Li})/n(\text{H}) = (4.26^{+0.73}_{-0.60} \times 10^{-10})$ (Cyburt et al. 2001, Cyburt 2004) . It is obvious that the theoretical and observational values are not in accord with each other. The observed ^{7}Li abundance is a factor of 2 to 3 times lower than that given by BBN/WMAP, far beyond the stated range of systematic uncertainties from observational analysis or BBN calculations.

Several possibilities have emerged in an attempt to explain this ^{7}Li discrepancy, but none of these, as yet, fully explains the problem. Broadly speaking these lie in the categories:

1. The discrepancy is due to unrecognised or underestimated systematic errors in the calculations of the observationally inferred present-day Li abundance.
2. The stars studied have destroyed some of the Li with which they were formed.
3. Some Galactic Li was destroyed before these stars formed.
4. The discrepancy is due to systematic uncertainties in the nuclear cross sections used in BBN calculation.
5. Standard BBN has failed to accurately predict the primordial abundances.

A possible solution in the second category is diffusion. Several studies have been conducted on this subject recently, e.g. Richard, Michaud & Richer (2005) and Korn et al. (2006). There it is suggested that the primordial Li is depleted in the star by diffusion, through gravitational settling, to layers in which the Li can not be detected. The models used in this process are manipulated to minimize destruction of Li due to nuclear burning. However, they do not completely manage to eliminate this destruction. Although these predictions do lead to a possible solution to the Li problem, they are still subject to questions and uncertainties. Using atomic diffusion alone does not recreate the plateau, but causes a drop in Li abundance in stars with $T_{\text{eff}} > 6000$ K. It is also often hard to explain the smallness of the star to star scatter in ^{7}Li using these processes. To solve these problems some form of turbulence at the bottom of the convective zone has to be invoked. The source of this turbulence is still uncertain, as is the amount needed, which can vary from star to star. The turbulence is also dependent on the temperature scale used. If a cooler T_{eff} scale is used then more turbulence is needed. However, observations of ^{6}Li in the atmospheres of metal-poor turn off stars (Asplund et al. 2006, García Peréz et al. 2008) rule out the use of a more turbulent scheme, as it would destroy the ^{6}Li. It would therefore seem that the success of this solution to the lithium problem rests on an accurate T_{eff} scale, and confirmation of whether ^{6}Li is present on the surface of metal-poor stars. However, it should be noted that the presence of ^{6}Li is still in question. It has been shown (Cayrel et al. 2007 and García Peréz et al. 2008)

that a reappraisal of previously derived ^{6}Li abundance should be undertaken. The presence of ^{6}Li also causes problems if ^{7}Li undergoes nuclear burning. Although the models of diffusion and turbulence are tuned so as to reduce this burning it is not clearly stated whether they eliminate it completely. As ^{6}Li is destroyed at a lower temperature than ^{7}Li, the presence of ^{6}Li would rule out the possibility of any models in which ^{7}Li is destroyed.

Possible explanations in the third category are relatively new. One such mechanism involving stellar processing is that of Piau et al. (2006). However, the amount of material which this requires to be cycled through stars creates other problems; the implications of such models require further investigation.

It is of course possible that certain nuclear cross sections used in BBN calculations have been poorly determined. The effect of changing the yields of certain BBN reactions was recently considered by Coc et al. (2004). They found for example, that an increase of the ^{7}Be(d,p)2^{4}He reaction by a factor of 100 would reduce the ^{7}Li abundance by a factor of about 3 in the WMAP η range. This reaction has since been remeasured and precludes this solution (Angulo et al. 2005). There is also the possibility that systematic errors in the ^{3}He$(\alpha, \gamma)^7$Be reaction are the cause of the ^{7}Li discrepancy. This channel was considered in detail in Cyburt et al. (2004). Although the absolute value of the cross section for this key reaction is known relatively poorly both experimentally and theoretically, the agreement between the standard solar model and solar neutrino data provides additional constraints on variations in this cross section. Using the standard solar model of Bahcall et al. (2001), and recent solar neutrino data (Ahmed et al. 2004), one can exclude systematic variations of the magnitude needed to resolve the BBN ^{7}Li problem at the $\gtrsim 95\%$ confidence level (Cyburt et al. 2004).

The fifth category represents an interesting challenge, with several cosmological and particle physics possibilities arising which could affect BBN (Coc & Vangioni 2005). For example, the variation of the fine structure constant can induce a variation in the deuterium binding energy and could yield a decrease in the predicted abundance of ^{7}Li (Dmitriev et al. 2004, Coc et al. 2007). The modification of the expansion rate during BBN (Salati 2003) will also affect the light element abundances. Another possibility is that gravity is not described by general relativity but is instead attracted toward general relativity during the evolution of the Universe (Damour & Nordtvedt 1993a, Damour & Nordtvedt 1993b). BBN has been extensively studied in that scenario (Damour & Pichon 1999, Coc et al. 2006). Finally, it may be that physics beyond the standard model is responsible for the post BBN processing of the light elements. One possibility recently discussed is that particle decay after BBN could lower the ^{7}Li abundance and produce some ^{6}Li as well (Jedamzik 2004). This has been investigated in the framework of the constrained minimal supersymmetric standard model if the lightest supersymmetric particle is assumed to be the gravitino (Feng et al. 2004, Ellis et al.2005, Hamaguchi et al. 2007). Some models have been found which accomplish these goals (Jedamzik et al.2006, Cyburt et al.2006). However,

all of these possibilities lack confirmation at present. Also the other four categories of explanation listed above need to be ruled out in order for the last to gain significant favour.

It is the first category of explanation that we address in this work. The largest of the uncertainties arises from the uncertain effective temperature scales for metal-poor stars, which we now examine in greater detail, before going on to calculate new effective temperatures and lithium abundances for a sample of metal-poor main-sequence stars, which is the ultimate aim of this work.

1.2. Effective Temperature (T_{eff}) Scale Problems

In calculating the abundances of Li, $A(\mathrm{Li})$[1], from spectral measurements, the effective temperature is the most important atmospheric parameter, as $A(\mathrm{Li})$ has a high sensitivity to temperature: $\partial A/\partial T_{\mathrm{eff}} \sim 0.065$ dex per 100 K for halo main-sequence turnoff stars. The temperature scale adopted by different authors varies considerably. A comparison of effective temperatures adopted by Ryan et al. (2001) and Ramírez & Meléndez (2005) shows differences for very low metallicities ([Fe/H] < -3) by as much as 500 K, with typical differences of ~ 200 K. Concerning the very metal-poor star G64-37 which features in the present paper, the difference in temperature between Ryan et al. (1999), at 6240 K, and Meléndez & Ramírez (2004), at 6775 K, is 535 K. In these cases Ramírez & Meléndez (2005) and Meléndez & Ramírez (2004) have the hotter temperature scale, and hence they infer higher primordial abundances as noted above.

Several methods are routinely adopted in calculating the effective temperature. These include using the strong Balmer line wings (e.g. Asplund et al. 2006), photometric methods including the Infrared Flux Method (IRFM) (e.g. Ramírez & Meléndez 2005) and a spectroscopic method that utilizes the temperature dependence of the atomic-level populations, as given in local thermodynamic equilibrium (LTE) by the Boltzmann equation.

In the first method, the Balmer line wings are used as a temperature indicator as they have strong temperature sensitivities, whilst maintaining a low sensitivity to other physical parameters, i.e. log g (Fuhrmann et al. 1992). $H\alpha$ in particular has a high sensitivity to T_{eff}, ~ 0.5 Å in the width of the wings per 100 K, and is the least sensitive to other parameters. This technique is widely used, e.g. Fuhrmann et al. (1994), Barklem et al. (2002), and Asplund et al. (2006). It assumes that the wings are formed in LTE. This assumption makes it simpler to model, thus leading to more sturdy temperature scales.

The preferred temperature scale in many studies is that derived by the IRFM. This method uses IR photometry and model fluxes to constrain the temperature. The basic idea is to compare a theoretically calculated infrared flux with an observed infrared flux to derive an angular diameter, given by the equation:

$$\theta = 2\sqrt{\frac{f_{\mathrm{obs,IR}}}{f_{\mathrm{theo,IR}}}}, \tag{1}$$

---

[1] $A(\mathrm{Li}) \equiv log_{10}\left(\frac{n(\mathrm{Li})}{n(\mathrm{H})}\right) + 12.00$

where $f_{\rm obs,IR}$ and $f_{\rm theo,IR}$ are the observed and theoretical infrared fluxes respectively. This θ can then be used, along with the integrated observed flux, to calculate an effective temperature, using the equation:

$$T_{\rm eff} = \left(\frac{4F_{\rm obs}}{\sigma\theta^2}\right)^{\frac{1}{4}},$$
(2)

where $F_{\rm obs}$ is the observed integrated flux at the Earth and σ is the Stefan-Boltzmann constant. This is an iterative process where the $T_{\rm eff}$ is used to refine the theoretical fluxes, thus refining the angular diameter and the effective temperature. In essence the method comes down to simultaneously solving equations 1 and 2 to derive values of θ and $T_{\rm eff}$. Due to the lower sensitivity of the infrared flux to temperature compared to shorter wavelengths, when equation 1 and equation 2 are solved simultaneously the calculated temperature for the star is better defined, and hence more accurate (see Blackwell et al. (1979) Fig.1). Mean random errors for recent work using this method are $\sim$ 60 - 75 K, depending on the type of star analysed, from Ramírez & Meléndez (2005), and $\sim$ 70 K from Alonso et al. (1999). Temperatures from this method have been used to calibrate other photometric indices (e.g. Magain (1987) and Alonso et al. (1996))

The third method usually relies on the assumption of LTE. This implies that the Boltzmann equation can be utilized in the derivation of the effective temperatures. Boltzmann's equation contains an exponential term in χ_i/T, where χ_i is the excitation energy of the given energy level i, and T is the temperature of the gas. Each measured equivalent width (EW) of an element, in most cases Fe I, is used to determine an abundance for that element. If the temperature used in the calculation is too high, then an over-population of the more excited levels will be calculated with the Boltzmann equation. This will lead to the inference that there are already more absorbers in higher levels, and hence it would then be calculated that fewer absorbers were needed to reproduce the measured EW. A dependence of abundance on excitation energy would then be seen due to these miscalculated populations. The correct temperature will therefore be the one that nulls any trend in the plot of abundance against excitation energy (e.g. Peterson & Carney 1979).

However, all methods have, along with their strengths, significant deficiencies. Barklem (2007) has questioned whether the assumption that the wings of the Balmer lines form under conditions of LTE is reliable. This therefore casts doubt on the accuracy of the derived temperatures, with a possible temperature rise of 100 K compared to those derived in LTE. Along with this there are also uncertainties in the way hydrogen-hydrogen collisions, so-called self-broadening, are treated. Barklem et al. (2000) found differences in $T_{\rm eff}$ of up to 150 K between the their theory and the Ali-Griem treatment of self-broadening. This difference was also found by Bonifacio et al (2007) using a Ali-Griem theory which has modified broadening coefficients, which allow for a good match to solar Balmer lines. The IRFM relies heavily on photometry and modelled fluxes to derive the temperatures. It can therefore suffer from photometric errors. This method also has a dependency on model atmosphere. Finally, temperatures derived using the excitation energy technique currently depend

on the accuracy of assumptions about LTE, about the structures of 1D model atmospheres and the errors in gf values, damping values and equivalent width measurements. It has been shown (Thévenin et al. 1999 and Asplund et al. 1999) that the assumptions of 1D, LTE atmospheres are not always suitable for modelling radiative transfer of Fe lines in metal–poor stars, although Gratton et al. (1999) infer there is little sensitivity to non-LTE. It is thus unclear how strong these effects are.

In previous work by some of the present authors (Ryan et al. 1999), temperatures were derived using a calibration of BVRI colours and medium resolution ($\Delta\lambda \approx 1\text{Å}$) spectroscopy, tied principally to the Magain (1987) b-y calibration of IRFM temperatures. In Ryan et al. (2000), an adjustment of +120 K was made to the temperature scale to make it similar to the IRFM scale of Alonso et al. (1996). Alonso et al. (1996) report similarly a mean difference of 112 K between their IRFM values and Magain's. The aim of the present work was to explore the use of the excitation energy technique to further constrain the effective temperature scale. In other studies where excitation-energy temperatures have been derived, only limited attention has been paid to quantifying the random and systematic uncertainties on those values. Given the importance of the temperature scale to the lithium problem, we endeavor here to track the uncertainties more closely.

1.3. 1D-LTE vs. 3D/1D-Non-LTE

Because the calculation of an effective temperature from the excitation-energy technique requires that the populations of the different energy levels be known, it is necessary to investigate non-LTE effects in metal-poor stars and their effect on the temperature scale calculation.

As discussed by Asplund et al. (1999) the level populations for the Fe lines are affected by departures from LTE, as radiation fields higher than the local Planck function lead to over-ionisation of the atom compared to the LTE case. That is, applying Saha's equation with the local value of the temperature at some depth in the atmosphere will underestimate the degree of ionisation. Moreover, different energy levels will be affected differently by non-LTE, so it is not possible to apply a single ionisation correction to all levels of a given ionisation state. A second factor that could affect excitation equilibrium is that of the use of 3D atmospheres. It can be seen in Asplund (2005) (his Figure 8) that there can be a significant χ-dependent effect on the abundances produced. However, in the same paper it is stated that non-LTE corrections appear to have the opposite effect to the 3D corrections and these corrections also become larger when 3D atmospheres are used. This could lead to 3D non-LTE becoming very similar to 1D non-LTE. It is not known, however, that this is always the case. Non-LTE effects, 3D effects, and their combination relative to 1D-LTE will therefore have to be studied to assess the exact impact on the temperatures derived by this technique.

However, it is well known that non-LTE calculations for Fe I in metal-poor stars are quite uncertain, principally because of uncertainty in the role of collisions with hydrogen. Thévenin & Idiart (1999) and

Gratton et al. (1999) reached opposite conclusions about the importance, or otherwise, of non-LTE in such stars. 3D calculations are also relatively rare to date. Because of these uncertainties, we proceed in two stages. For the present paper we shall concentrate on a 1D LTE analysis, and this will be the focus for the remainder of this paper. In a second paper we will examine the complexities introduced by attempting a non-LTE analysis.

2. Observations

2.1. Sample Selection

The sample of stars was taken from one constructed by Ryan et al. (1999) which contains 24 metal-poor stars spread around the sky. It is a carefully selected sample at the Population II main-sequence turnoff, with as few star-to-star variations as possible. This included limiting the effective temperature to a range of 6100 K $\lesssim T_{\mathrm{eff}} \lesssim 6300$ K and the metallicity to -3.5 $\lesssim$ [Fe/H] $\lesssim$ -2.5. These restrictions allow the sample to have roughly the same evolutionary state, in this case around the MS turn-off, which also has the effect of limiting log g. The low metallicity restrictions mean that we are sampling stars that contain material that has undergone a limited amount of processing since the Big Bang. The sample was previously studied to determine not only Li abundances, but also those of magnesium (Arnone et al. 2005), based on red spectra.

The intention in the present work was to obtain blue high–resolution spectra for a subset of these stars. This was to enable us to use the excitation-energy technique to determine the T_{eff}, and determine what, if any, correction is required to the photometric T_{eff} scale used previously. This also allows for a comparison between the excitation-energy T_{eff} and those scales used by Asplund et al. (2005) and Meléndez & Ramírez (2004).

2.2. Data Acquisition and Reduction

Spectra of 16 of the program stars plus two standards, out of the 22 program stars and two standards, HD140283 and HD74000, in the Ryan et al. (1999) study, were obtained using the UCLES instrument on the 3.9m Anglo-Australian Telescope (AAT) during two separate observing runs. The first run, July 31-August 3 2006, was undertaken by S.G. Ryan and J.D. Tanner. The second run, March 9-11 2007, was undertaken by A. Hosford and A.E. García Peréz. The setup was the same for both observing runs: the 79 lines/mm grating was used, centred at 4174 Å with a slit width of $1.0''$, which achieves a resolving power of $R \equiv \lambda/\Delta\lambda = 43000$. The wavelength range is from 3700 Å - 4900 Å. In Table 2 we present the basic information including the photometric (and partially spectroscopic) temperature, T_{phot} (Ryan et al. 1999) for each of the stars, along with the S/N per 0.025 Å pixel near 4300 Å from the present work.

The data reduction was done using standard routines within the IRAF package.

Table 2. Background infomation for the stars analysed in this work.

Star name	RA (1950)	DEC (1950)	V	B-V	S/N @ 4300	T_{phot} (K)	Initial [Fe/H]
BD-13°3442	11h 44m 18s	−13°49′54″	10.37	0.33	80	6210	−2.73
BD+20°2030	08h 13m 13s	19°51′24″	11.20	0.40	95	6200	−2.64
BD+24°1676	07h 27m 39s	24°11′42″	10.80	0.40	100	6170	−2.38
BD+26°2621	14h 52m 00s	25°46′12″	11.01	0.50	95	6150	−2.54
BD+26°3578	19h 30m 29s	26°17′06″	9.37	0.43	110	6150	−2.24
BD+3°740	04h 58m 38s	04°02′24″	9.82	0.38	100	6240	−2.70
BD+9°2190	09h 26m 35s	08°51′24″	11.14	0.36	95	6250	−2.83
CD-24°17504	23h 04m 39s	−24°08′42″	12.18	0.32	100	6070	−3.24
CD-33°1173	03h 17m 34s	−33°01′21″	10.91	0.39	100	6250	−2.91
CD-35°14849	21h 30m 48s	−35°39′12″	10.63	0.37	105	6060	−2.38
CD-71°1234	16h 02m 18s	−71°14′00″	10.44	0.46	95	6190	−2.60
G64-12	13h 37m 30s	00°12′54″	11.49	0.41	110	6220	−3.24
G64-37	13h 59m 53s	−05°24′18″	11.14	0.36	100	6240	−3.15
LP635-14	20h 24m 13s	−00°47′00″	11.33	0.47	115	6270	−2.66
LP815-43	20h 35m 21s	−20°36′30″	10.91	0.39	95	6340	−3.00
HD 84937	09h 46m 17s	13°59′18″	8.28	0.42	110	6160	−2.12
HD 140283	15h 40m 22s	−10°46′18″	7.24	0.46	170	5750	−2.54
HD 74000	03h 38m 31s	−16°09′36″	9.671	0.43	150	6040	−2.02

3. Data Analysis

Analysis of the data proceeded in, broadly, two stages. Firstly, the equivalent widths of spectral lines of Fe were measured. For the second stage we use WIDTH6 (Kurucz & Furenlid 1978) to calculate the abundances for each line, from which the physical parameters can be deduced. The remainder of this section discusses these stages.

3.1. Equivalent Width Measurement and Data Quality Checks

Equivalent widths (EW) of apparently unblended Fe I and Fe II lines in the spectrum of each star were measured by fitting Gaussian profiles using the IRAF 'splot' program. Graphs of the Gaussian FWHM in velocity space (v_{FWHM}) were plotted against the measured equivalent width of the line, see Figure (5). Due to the nature of echelle spectra, in which $\Delta\lambda/\lambda$ is constant throughout the spectrum (where $\Delta\lambda$ is the width of a pixel in wavelength units), it is possible to use these plots as checks of the quality of the measurements. The weak lines, EW $\lesssim$ 90 mÅ, form a plateau due to the constancy of the FWHM of the Doppler core of lines on the linear part of the curve of growth. The Doppler core is of course broadened by the instrumental profile, which likewise has a constant width in velocity units. For intermediate strength and stronger lines, the plot curves upward due to the increase in their line wing strength, leading to larger FWHM. Lines whose equivalent widths fell significantly outside of these trends were re-measured or discarded as blends or noise-dominated measurements, and were rejected from further calculations. The equivalent widths measured in each star are listed in Table A1, A2 and A3 in the appendix to this paper. (The appendix is available online only.)

A comparison between equivalent widths of the Fe lines in the star CD-24°17504 measured by Norris et al. (2001) and remeasured by A. Hosford showed good precision. The standard deviation of the
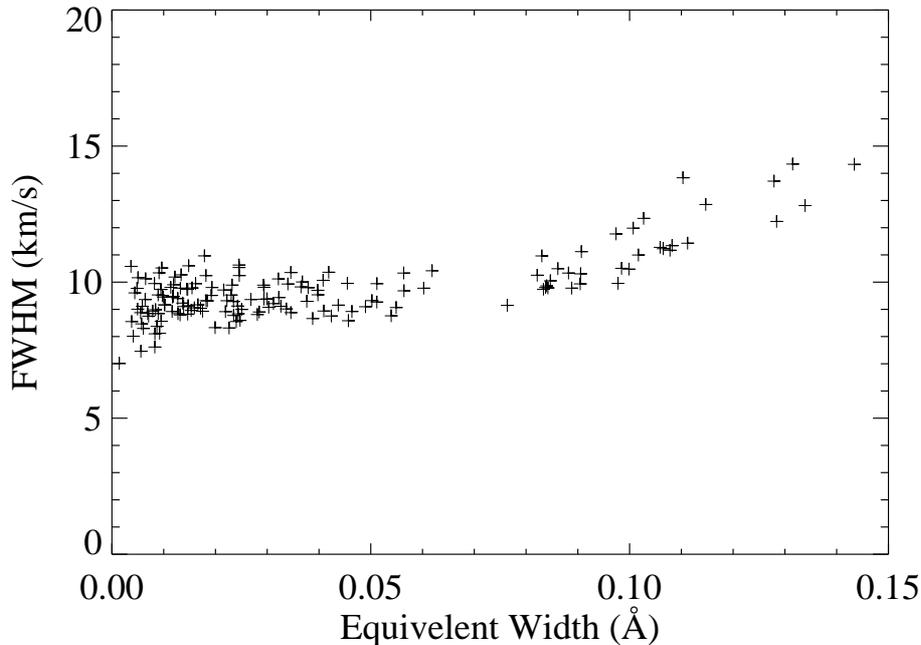
Fig. 5. Plot of v_{FWHM} versus equivalent width for the retained lines in the star HD140283

difference between the two sets of equivalent widths was 1.3 mÅ with a mean of -0.58 mÅ for lines measured from the same spectra. Lines which were measured in two spectra, one obtained from Norris et al. (2001) at $\mathrm{S/N} \approx 100$, and one obtained by A. Hosford at $\mathrm{S/N} \approx 50$, were also compared. This comparison gave a standard deviation of 5.8 mÅ and a mean of -0.39 mÅ. To increase the accuracy of the EW measurements for the star CD-24°17504 we used a combination of EW measurements from both the Norris et al. (2001) spectra and the A. Hosford spectrum, weighting each measurement by the inverse of the uncertainty in the EW (σ_{EW}). This σ_{EW} is calculated using the equation:

$$\sigma_{\mathrm{EW}} = \frac{\Delta\lambda_{pix}\sqrt{M}}{S/N}, \tag{3}$$

where $\Delta\lambda_{pix}$ is the width of a pixel in wavelength units, M is the number of pixels comprising the full width of the spectral line and S/N is the signal-to-noise of the spectra.

3.2. Abundance Calculations

To calculate the abundances from the measured lines we use the single line radiative transfer program WIDTH6. This program calculates the EW of an unblended absorption line for a 1D model atmosphere. It varies the starting abundance, iteratively calculating an EW until that equals the measured EW for the line.

The KURUCZ06 (http://kurucz.harvard.edu/grids.html, downloaded in Nov 2006) model atmospheres have been adopted for this work as it has been stated (Castelli et al. 1997) that these no-overshooting models are preferable in deriving accurate temperatures to earlier Kurucz overshooting models (Kurucz 1993). This is due to the effect the different methods of treating convection have on the temperature structure of the atmosphere,

and therefore on the spectral features. The no-overshooting models lead to a better fit to observable spectral features at different temperatures. These models are interpolated in T_{eff}, log g and [Fe/H] over the ranges $3500 \leq T_{\mathrm{eff}} \leq 50000$, $0.0 \leq \log g \leq 5.0$ and $-0.5 \geq [Fe/H] \geq -4.0$. A comparison between temperatures derived using the different overshooting models can be seen in Sect. 3.3.

The log gf values of the Fe I lines were compiled from several sources: Blackwell et al. (1979), Blackwell et al. (1979), Blackwell et al. (1980), Blackwell et al. (1982), Blackwell et al. (1982), collectively the 'Oxford Fe I consortium', Fuhr et al. (1988), Bard et al. (1991), O'Brian et al. (1991), Bard & Kock (1994) and Thévenin et al. (1989); in some cases the mean of several log gf values is adopted, see Table A1 for details. The Fe II log gf values are compiled from: Hannaford et al. (1992), Heise & Kock (1990), Kroll & Kock (1987), Moity (1983) and Schnabel, Kock & Holweger (1999). Values given by Moity (1983) are corrected by -0.06 dex, for those lines with upper-level energy < 48000 cm^{-1}, and -0.24 dex for lines with upper-level energy greater than the above value; this follows the suggestion by Fuhr et al. (1988). Damping values have been calculated using the tabulations of Anstee & O'Mara (1995), Barklem & O'Mara (1997), and Barklem et al. (1998). Ryan (1998) noted that the damping treatment has a significant effect on the excitation energy temperatures because of the χ-dependence of damping treatments.

3.3. Adopted Approach to Constraining Parameters

Several other physical parameters of a star, in addition to temperature, could in principle be constrained using WIDTH6, given appropriate data. These are log g, metallicity and microturbulence. Metallicity is determined from the calculated Fe abundance. Log g could be constrained by ensuring that the abundances derived for Fe I and Fe II lines are equal, and microturbulence is found by making sure there is no trend between the measured equivalent widths of the lines and the abundance.

It would, in principle, seem possible to simultaneously constrain both log g and T_{eff}. However, as previously mentioned, there are concerns about the non-validity of the assumption of LTE for Fe I lines in metal-poor turnoff stars. This would therefore make it dangerous to try to constrain T_{eff} at the same time as log g. This concern became evident when T_{eff} and log g where simultaneously constrained via a WIDTH6 analysis for the star HD140283, using Fe I and Fe II lines. For this star results converged at $T_{\mathrm{eff}}/\log g/[\mathrm{Fe/H}]/\xi = 5573/3.1/-2.67/1.5$ using the KURUCZ06 models[2]. However, we know that the Hipparcos parallax gives a reliable value for log g for HD140283: log $g = 3.73 \pm 0.11$ for a mass of 0.8360 $M_{\odot}$ as taken from the Yonsei-Yale isochrones (http://csaweb.yonsei.ac.kr/~kim/yyiso.html). The uncertainty is dominated by the parallax error. Clearly the log g value we have derived is too low. This star has also appeared in many other studies leading to temperatures around 5750 K (Table 2), approximately 200 K hotter than we derived. It can

---

[2] We also tried this with the KURUCZ93 models and found 5439/2.8/-2.79/1.5.

then be seen that for this star, attempting to constrain $T_{\rm eff}$ and log g simultaneously from Fe I and Fe II lines drives the gravity and possibly the temperature values down to unusually low levels. Non-LTE effects may be responsible. It is, however, still viable to use WIDTH6 to constrain the $T_{\rm eff}$. This is because the main non-LTE correction involved in Fe is expected to be overionisation, which may significantly affect the abundance of Fe I and therefore have a substantial effect on log g when calculated through ionisation balance. The correction on χ is very roughly the same for all levels within a particular star. This can be seen from Figures 2 and 3 from Collet et al. 2005, while Asplund (2005) also states this view. Shchukina et al. (2005) do find that the effect can be different for different excitation potentials, however, this seems far more pronounced when using 3D atmospheres, compared to using 1D atmospheres. Therefore overionisation will have less affect on the trend between [Fe/H] and χ, and it is still acceptable to use this to constrain $T_{\rm eff}$, subject to the caveats in Sect. 1.3.

Table 3. List of results for log g and $T_{\rm eff}$ of the star HD140283 derived using different techniques.

Study	Temperature	$T_{\rm eff}/\log g$
This work	Simultaneous fit	5573/3.1 [a]
Asplund et al. (2006)	Balmer line wing	5753/3.7 [b]
Ryan et al. (1996)	Photometry	5750/3.4
Alonso et al. (1996)	IRFM	5691/4.0 [c]

[a] The uncertainties are 75 K and 0.15 dex respectively
[b] The uncertainties are 30 K and 0.04 dex respectively
[c] The uncertainties are 69 K and 0.5 dex respectively

It is therefore preferable to constrain log g independently of deducing $T_{\rm eff}$, rather than using Fe lines to constrain both. There are several options for doing this. In rare cases the Hipparcos parallax could be used. However a large proportion of the program stars do not have these data available, and for the stars where it is available the parallax errors are large. Alternatively, WIDTH6 could be used with a fixed temperature, such as an assumed photometric temperature, $T_{\rm phot}$ from previous work, to constrain log g through ionisation balance. This method still leads to concerns with the non-validity of LTE and the sensitivity of the method to the assumed temperature. As a third option, theoretical isochrones for old, metal-poor stars near the main sequence turnoff can be used. This method, however, leads to a range of possible values for log g, mainly due to the uncertainty in age and evolutionary state, i.e. whether a given star is pre- or post-turnoff.

Because of the various concerns raised above, we adopted the following two stage procedure to analyse the stars. The first step is to use the Hipparcos parallax of the star if available. Table 4 contains gravities calculated from the Hipparcos parallax, log $g_{\rm Hipp}$, for each star, where possible, with masses taken from the Yonsei-Yale isochrones with an assumed age of 12 Gyr and a metallicity suitable for the star. We obtain two Hipparcos gravities due to the different stellar masses the star could have depending on whether it is on the main sequence

(MS) or subgiant branch (SGB). In practice, the difference between these two values is small compared to the uncertainty arising in the parallax, and so we quote at most one value of $\log g_{\text{Hipp}}$ for each star. Many of the stars' parallaxes have extremely large errors, to the point where they would have been unsatisfactory to use, and are excluded. In the case of the HD stars, we have taken the $\log g_{\text{Hipp}}$ as the final gravity as they have small errors. However, for the other five stars with $\log g_{\text{Hipp}}$ in Table 4, we have taken $\log g_{\text{Hipp}}$ to be only an interim value. A theoretical gravity, $\log g_{\text{iso}}$, is then used to determine a temperature as described below. We have used T_{phot} to calculate the Hipparcos gravity, $\log g_{\text{Hipp}}$, but note that it has only a low sensitivity to T_{phot} of +0.04 dex per 100 K.

We also run WIDTH6 with a fixed T_{phot} (see Table 1) to find an interim (ionization-balance) $\log g$, which we call $\log g_{\text{Tphot}}$. The results of this analysis are found in Table 4. The sensitivity of $\log g_{\text{Tphot}}$ to T_{phot} is +0.15 dex per 100 K. The difference between the gravities, $\log g_{\text{Tphot}}$ - $\log g_{\text{Hipp}}$, ranges from -0.18 to -0.52, with a mean of -0.37. This suggests that this method, using the T_{phot} and the Fe ionisation balance, underestimates the gravity by $\sim$0.4 dex. This could be due to T_{phot} being too cool by $\sim$270 K, or may be evidence of non-LTE effects (overionisation) affecting Fe I. We make no further use of the $\log g_{\text{Tphot}}$.

Because of the lack of reliable Hipparcos parallaxes, the unreliability of $\log g_{\text{Tphot}}$, and concerns about trying to constrain T_{eff} and $\log g$ simultaneously with WIDTH6, we then switched to using the $\log g_{\text{iso}}$ implied by the Yonsei-Yale theoretical isochrones. These isochrones can be seen in Figure 6. Three different metallicities are plotted; the other available metallicities are [Fe/H] = -2.3 and -2.76. We use T_{phot} to obtain $\log g_{\text{iso}}$, and then null the trends of abundance with excitation energy to obtain the excitation energy temperature, T_{χ}. In most cases this leads to two scales for temperature: a MS value and a SGB value. Only if the Hipparcos gravity is sufficiently accurate can we be sure of the evolutionary state

An initial comparison between results calculated using the KURUCZ93 models, with overshoot, and those for the new KURUCZ06 models, with no-overshooting, was carried out for the star HD140283. This was done using the calculated Hipparcos gravity for the star, $\log g = 3.73$. It was found that the KURUCZ06 models gave T_{χ} hotter by 41 K than the KURUCZ93 models. We decided that for the remainder of the analysis the KURUCZ06 models would be used; see Sect. 3.2 for a discussion on the reasons for this.

4. Results

The physical parameters for the sixteen programme stars and the two standards are given in Table 4.

The effective temperatures for all but the HD stars in Table 4 were found using isochronal gravities, $\log g_{\text{iso}}$, based in turn on photometric temperatures. In order to understand how reliable our T_{χ} determinations are, it is essential that we quantify the various sources of possible error that contribute. As stated above, we defer discussions of non-LTE effects to Paper II. One source of error is the adopted gravity, $\log g_{\text{Hipp}}$, for the
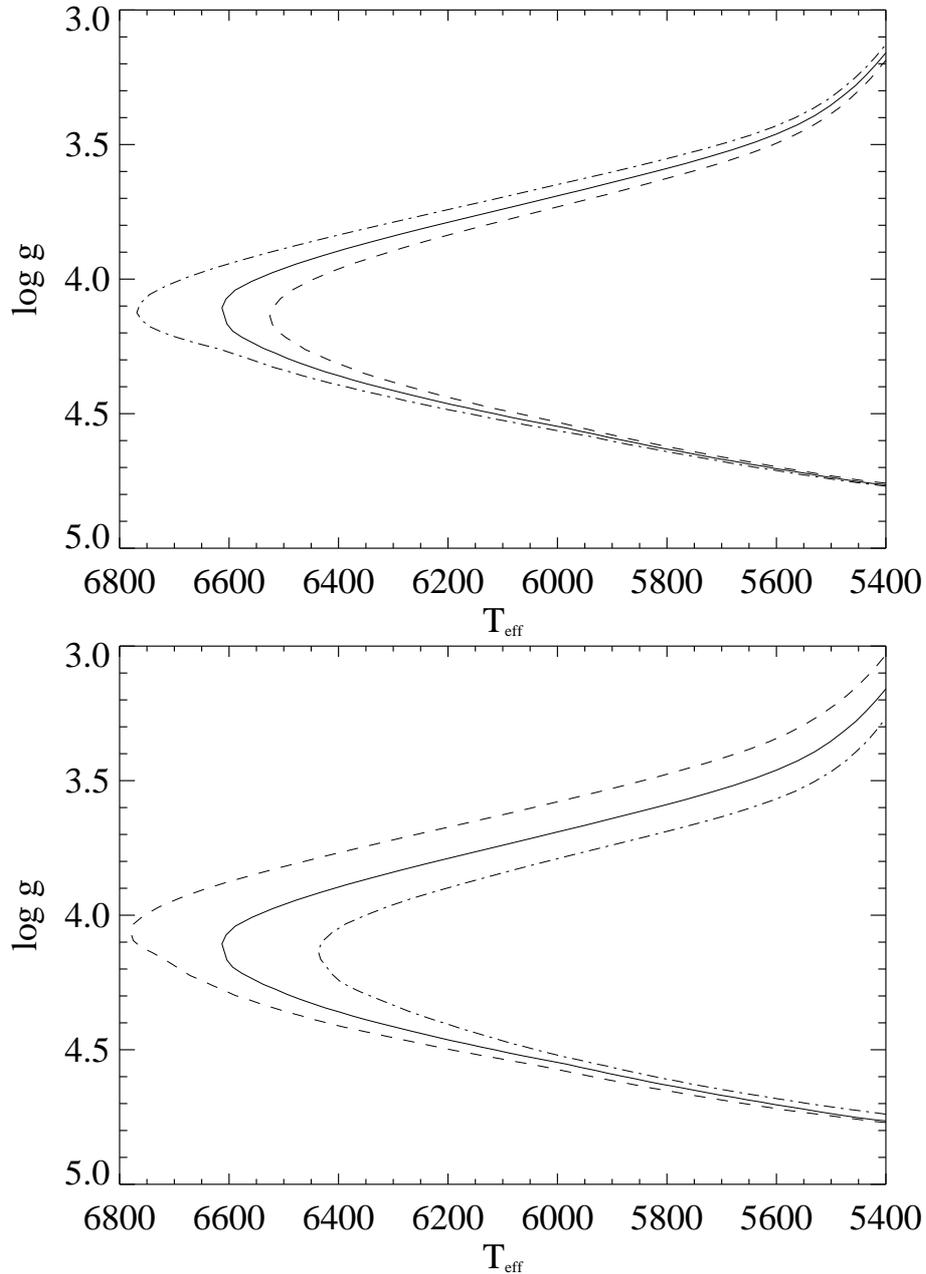
Fig. 6. Theoretical isochrones used in the determination of log g. Different ages are represented in the top panel, with the dashed line 13 Gyr, the solid line 12 Gyr, and the dot dashed line 11 Gyr. The bottom panel gives examples for different [Fe/H]. The dashed line is -3.3, the solid line -2.5 and the dot dashed line -2.15

HD stars and log g_{iso} for the remainder. Choice of isochrones older/younger by 1 Gyr would change log g_{iso} by $\sim$0.03 dex for MS and $\sim$0.06 dex for SGB stars, corresponding to changes in T_χ by 12 K and 24 K respectively. The isochronal gravity is also sensitive to the choice of T_{eff}, for which we use T_{phot}. An error of +100 K in T_{phot} would produce an error of typically +0.06 dex in log g_{iso} in the SGB gravity, and -0.06 dex in the MS gravity, though more at the turnoff. This in turn produces an error of typically +24 K in the SGB T_χ, and -24 K in the MS T_χ. Hence, and importantly, the inferred T_χ is only weakly dependent on an imperfect value of T_{phot}. Concerning microturbulence, we see that an error of 0.1 kms^{-1} leads to, on average, an error of $\approx$60 K in T_χ. Typical errors in microturbulence for this work range from $\sim$0.05 - 0.15 km s^{-1}

Table 4. Parameters deduced using the photometric temperatures and the gravities calculated using the Hipparcos parallax. Errors in $\log g_{\mathrm{Tphot}}$ are from the ionisation balance using WIDTH6, whilst those in $\log g_{\mathrm{Hipp}}$ are from the errors in the Hipparcos parallax. The error in $\log g_{\mathrm{Tphot}}$ comes about from the statistical error in making sure the abundance from different ionisation states is the same, ionisation balance.

Star name	No. of Fe I lines measured	T_{phot} (K)	$\log g_{\mathrm{Tphot}}$	[Fe/H]	ξ(Km/s)	$\log g_{\mathrm{Hipp}}$
BD-13°3442	86	6210	3.77 ± 0.04	-2.72	1.30	...
BD+20°2030	98	6200	3.985 ± 0.04	-2.62	1.20	...
BD+24°1676	96	6170	3.68 ± 0.04	-2.60	1.40	...
BD+26°2621	107	6150	3.88 ± 0.10	-2.69	1.20	4.28 ± 0.31
BD+26°3578	126	6150	3.72 ± 0.08	-2.39	1.35	3.94 ± 0.30
BD+3°740	94	6240	3.68 ± 0.12	-2.77	1.50	4.18 ± 0.21
BD+9°2190	146	6250	3.68 ± 0.10	-2.84	1.50	...
CD-24°17504	69	6070	3.57 ± 0.30	-3.35	1.30	...
CD-33°1173	126	6250	3.87 ± 0.10	-3.04	1.50	4.33 ± 0.27
CD-35°14849	69	6060	3.92 ± 0.07	-2.44	1.20	4.44 ± 0.25
CD-71°1234	127	6190	3.90 ± 0.07	-2.54	1.50	
G64-12	59	6220	4.05 ± 0.08	-3.40	1.40	...
G64-37	71	6240	4.29 ± 0.04	-3.24	1.30	...
LP635-14	163	6270	3.90 ± 0.10	-2.49	1.50	...
LP815-43	157	6340	3.78 ± 0.12	-2.74	1.40	...
HD 84937	164	6160	3.66 ± 0.10	-2.32	1.30	3.98 ± 0.12
HD 140283	124	5750	3.40 ± 0.04	-2.53	1.50	3.73 ± 0.12
HD 74000	84	6040	3.77 ± 0.03	-2.19	1.20	4.03 ± 0.18
Sensitivity to +100 K in T_{phot}			$+0.15$			±0.04

Table 5. The final physical parameters deduced in this work for the main sequence (MS) scale and the sub giant (SGB) scale. The three HD stars had gravities determined by their Hipparcos parallaxes and as such their evolutionary state can be deduced.

Star name	$\log g_{\mathrm{iso}}$ (MS)	T_χ (K) (MS)	[Fe/H] (MS)	ξ (Km/s) (MS)	$\log g_{\mathrm{iso}}$ (SGB)	T_χ (K) (SGB)	[Fe/H] (SGB)	ξ (Km/s) (SGB)
BD-13° 3442	4.46 ± 0.14	6321 ± 87	-2.66	1.20	3.79 ± 0.14	6186 ± 87	-2.74	1.30
BD+20° 2030	4.46 ± 0.14	6208 ± 104	-2.63	1.00	3.79 ± 0.14	6099 ± 104	-2.69	1.20
BD+24° 1676	4.47 ± 0.14	6296 ± 55	-2.53	1.20	3.78 ± 0.14	6220 ± 55	-2.57	1.40
BD+26° 2621	4.49 ± 0.14	6233 ± 107	-2.67	1.20	...	...	...	...
BD+26° 3578	...	...	...	...	3.76 ± 0.14	6148 ± 81	-2.42	1.35
BD+3° 740	4.44 ± 0.14	6344 ± 113	-2.72	1.50	3.81 ± 0.14	6188 ± 113	-2.82	1.50
BD+9° 2190	4.44 ± 0.14	6486 ± 129	-2.68	1.50	3.81 ± 0.14	6352 ± 129	-2.75	1.50
CD-24° 17504	4.55 ± 0.14	6102 ± 232	-3.33	1.00	3.61 ± 0.14	6110 ± 232	-3.31	1.30
CD-33° 1173	4.44 ± 0.14	6386 ± 55	-2.94	1.50	...	...	...	...
CD-35° 14849	4.52 ± 0.14	6168 ± 38	-2.36	1.00	...	...	...	...
CD-71° 1234	4.46 ± 0.14	6194 ± 53	-2.52	1.20	3.78 ± 0.14	6172 ± 53	-2.54	1.50
G64-12	4.49 ± 0.14	6333 ± 90	-3.32	1.30	3.67 ± 0.14	6304 ± 90	-3.31	1.40
G64-37	4.48 ± 0.14	6175 ± 106	-3.29	1.20	3.69 ± 0.14	6181 ± 106	-3.30	1.40
LP635-14	4.43 ± 0.14	6319 ± 114	-2.48	1.50	3.83 ± 0.14	6135 ± 114	-2.61	1.50
LP815-43	4.40 ± 0.14	6529 ± 107	-2.61	1.40	3.87 ± 0.14	6400 ± 107	-2.68	1.40
HD84937	...	...	...	...	3.98 ± 0.12	6168 ± 102	-2.34	1.30
HD140283	...	...	...	...	3.73 ± 0.12	5769 ± 39	-2.54	1.50
HD74000	4.03 ± 0.18	6070 ± 127	-2.20	1.20	...	...	...	...

The major contributions to the uncertainty in T_χ comes from the procedure of nulling the dependence of [Fe/H] on χ. This involves making a linear least squares fit to the n pairs of χ, [Fe/H] values for a star, using n Fe lines, as may be seen in Figure 7. As there is a spread of [Fe/H] values for a given star, the slope can only be determined to a certain statistical accuracy, which turns out to be of order $\sigma \approx 0.01$ - 0.015 dex per eV, which corresponds to a temperature uncertainty of order $\sim$60 - 80 K. The range in [Fe/H] values encapsulates

Table 6. The final lithium abundances calculated with the excitation energy temperatures (T_χ)

Star name	EW (Li)	$T_{\rm eff}$ (K) (MS)	A(Li) (MS)	$T_{\rm eff}$ (K) (SGB)	A(Li) (SGB)
BD-13° 3442	21.0	6321 $\pm$ 87	2.20 $\pm$ 0.057	6186 $\pm$ 87	2.10 $\pm$ 0.057
BD+20° 2030	20.5	6208 $\pm$104	2.11 $\pm$ 0.068	6099 $\pm$104	2.03 $\pm$ 0.068
BD+24° 1676	21.1	6296 $\pm$ 55	2.18 $\pm$ 0.009	6220 $\pm$ 55	2.13 $\pm$ 0.009
BD+26° 2621	22.5	6233 $\pm$ 107	2.17 $\pm$ 0.070	...	...
BD+26° 3578	24.6	...	...	6148 $\pm$ 81	2.15 $\pm$ 0.053
BD+3° 740	19.5	6344 $\pm$ 113	2.18 $\pm$ 0.074	6188 $\pm$ 113	2.07 $\pm$ 0.074
BD+9° 2190	14.6	6486 $\pm$ 129	2.14 $\pm$ 0.084	6352 $\pm$ 129	2.05 $\pm$ 0.084
CD-24° 17504	18.1	6102 $\pm$ 232	1.98 $\pm$ 0.151	6110 $\pm$ 232	1.98 $\pm$ 0.151
CD-33° 1173	17.2	6386 $\pm$ 55	2.15 $\pm$ 0.036	...	...
CD-35° 14849	28.8	6168 $\pm$ 38	2.24 $\pm$ 0.025	...	...
CD-71° 1234	25.9	6194 $\pm$ 53	2.21 $\pm$ 0.035	6172 $\pm$ 53	2.19 $\pm$ 0.035
G64-12	21.2	6333 $\pm$ 90	2.21 $\pm$ 0.059	6304 $\pm$ 90	2.19 $\pm$ 0.059
G64-37	18.2	6175 $\pm$ 106	2.03 $\pm$ 0.070	6181 $\pm$ 106	2.03 $\pm$ 0.070
LP635-14	20.2	6319 $\pm$ 114	2.18 $\pm$ 0.074	6135 $\pm$ 114	2.05 $\pm$ 0.074
LP815-43	16.1	6529 $\pm$ 107	2.21 $\pm$ 0.069	6400 $\pm$ 107	2.13 $\pm$ 0.069
HD84937	24.9	...	...	6168 $\pm$ 102	2.17 $\pm$ 0.066
HD140283	47.9	...	...	5769 $\pm$ 39	2.21 $\pm$ 0.025
HD74000	22.1	6070 $\pm$ 127	2.05 $\pm$ 0.083	...	...

the impact of random (not χ-correlated) line-to-line errors in equivalent widths, *gf*, and damping values. We determine this value for each star, finding a particularly large value for CD-24°17504 on account of the small number of Fe I lines in this very metal-poor star. The final 1σ uncertainty in T_χ, given in Table 5, includes the quadrature sum of the (dominant) statistical error arising from nulling the [Fe/H],χ trend, and contributions for Δage $= 1$ Gyr, $\Delta\xi = 0.1$ kms^{-1}, Δ[Fe/H] $= 0.05$, and an allowance of $\Delta T_{\rm phot} = 100$ K.

We comment briefly on the larger scale of the uncertainties quoted here, compared to the relatively small values (30 - 40 K) quoted for $T_{\rm phot}$ by Ryan et al. (1999). The aim of the previous work was to derive temperatures that minimised the impact of possible systematic errors. The purpose was to investigate the spread of Li abundances by ensuring random errors were kept to a minimum, while at the same time acknowledging that large zero-point errors might persist but be of approximatly the same size in all stars. In the current work, however, the emphasis has been to constrain the zero-point, albeit at the expense of larger random errors for individual stars.

These temperatures have been used in combination with the Li equivalent widths measured by Ryan et al. (1999), and a grid of equivalent width versus abundance for different $T_{\rm eff}$'s taken from Ryan et al. (1996), to calculate new Li abundances. The grid was constructed by determining different ^{7}Li equivalent widths for a number of different $T_{\rm eff}$ and [Fe/H] values. This was done by producing synthetic spectra of the ^{7}Li region with an LTE code originating from Cottrell & Norris (1978). The log *gf* values and wavelengths of the four components of ^{7}Li were taken from Andersen, Gustafsson, & Lambert (1984) and the model atmospheres were interpolated from the Bell (1981) grid. The details of the process can be found in Norris et al. (1994). Table 6 presents these values.
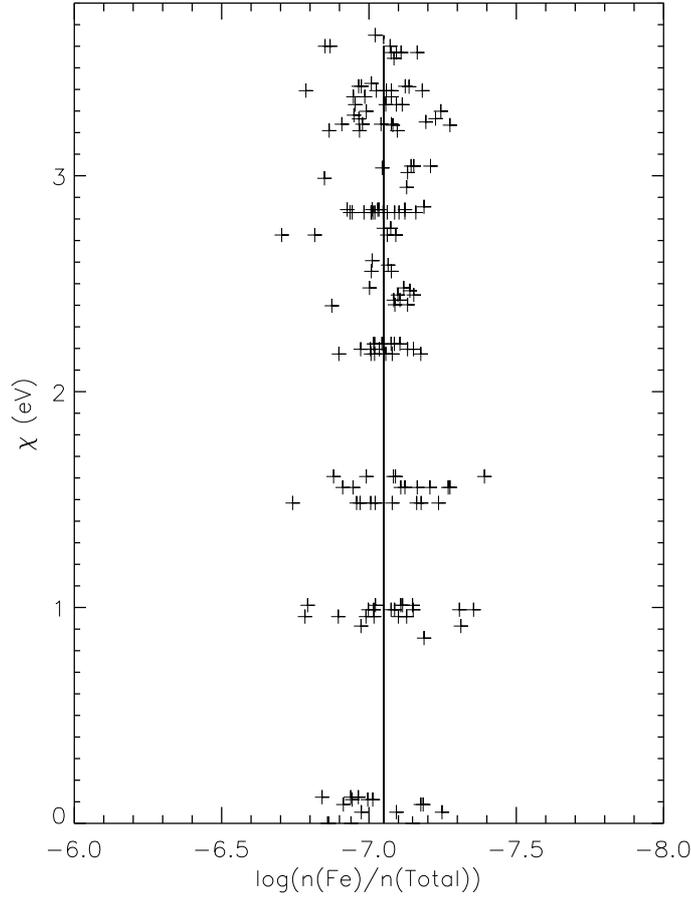
Fig. 7. Plot of χ versus $\log\left(\frac{n(Fe)}{n(Total)}\right)$ showing the trend nulling involved in constraining the T_{eff}.

5. Discussion

5.1. Comparison with other temperature scales

With the determination of the effective temperatures using the excitation method we can now compare our temperature scale to that of others, in particular to the IRFM of Meléndez & Ramírez (2004), the Balmer line wing method of Asplund et al. (2006), and the principally photometric temperatures of Ryan et al. (1999).

In Figure 8 the comparison with the IRFM T_{eff} of Meléndez & Ramírez (2004) is plotted. That scale is clearly hotter than ours, by an average of ~ 250 K. This is not to say that either scale is right, but it does lead us to the conclusion that our temperature scale will not reconcile the Li problem; the Meléndez & Ramírez (2004) IRFM scale was on the borderline of doing so. Our scale will give a lower mean Li abundance than will the IRFM. The difference in temperatures could have several possible explanations. It could be due to problems with our use of LTE in the excitation method, causing it to calculate lower temperatures. An incorrect bolometric flux, F_{bol}, calibration used in the IRFM could lead to that method having higher temperatures. It has also been noted (Alonso et al. 1996) that the errors in determining the absolute IR flux calibration have different effects on the derived IRFM temperatures, depending on what photometric band is used. The effect
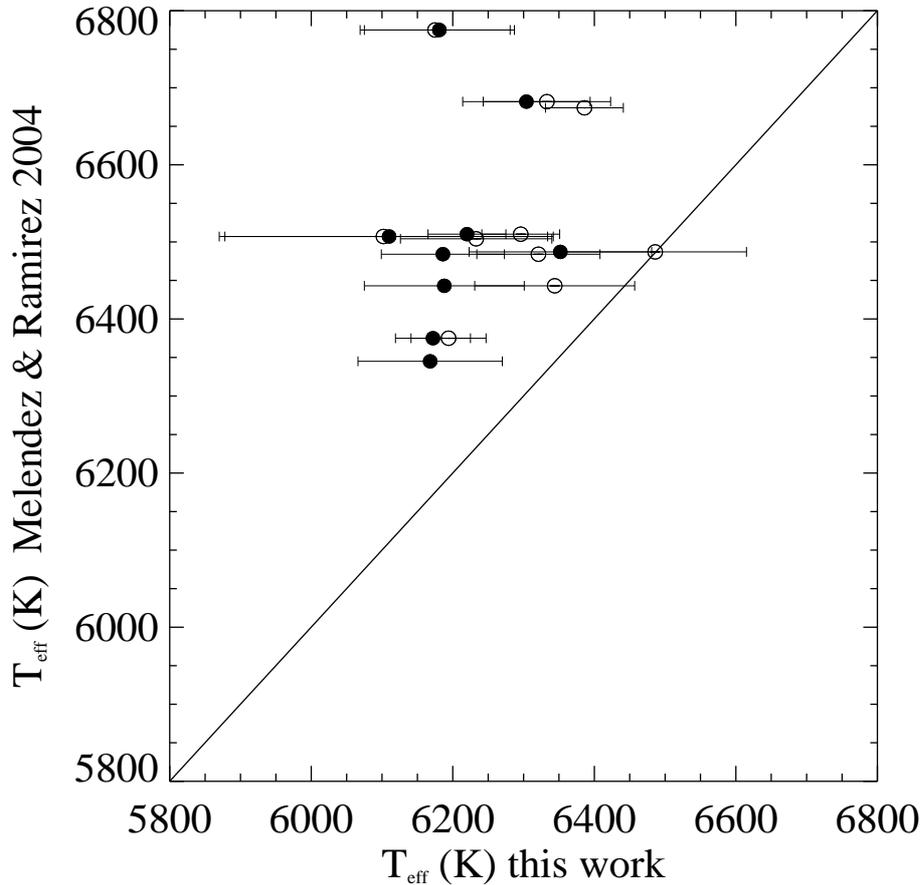
Fig. 8. Comparison of the Meléndez & Ramírez (2004) temperatures and the temperatures from this work. Filled circles represent SGB temperatures and open circles represent MS temperatures. Those stars of unknown evolutionary state have two points on the plot.

of these different errors on the derived temperatures is to move the zero point of the temperature scale. This could be another reason that the Meléndez & Ramírez (2004) temperatures are hotter.

The comparison between the temperatures of Asplund et al. (2006) and this work is plotted in Figure 9. Here we see that the two scales are comparable. As discussed in Sect. 1.2 both of these methods may suffer from LTE effects. A departure from LTE of only a few percent would increase Balmer wing temperatures by of order 100 K (Barklem 2007). It is speculated that the use of LTE in the treatment of the Fe atom may be inaccurate, e.g. overionisation of the element relative to LTE may occur (Thévenin et al. 1999). If true this would also lead to the excitation temperatures changing, as they are based on an LTE treatment. As yet the value of the temperature change is not determined and the sensitivity of each method to non-LTE may be very different. This is an aspect that we intend to look into in future work. It is clearly of interest to know whether non-LTE corrections to these scales could increase both to be akin to that of the IRFM scale, and push the mean Li abundances toward that of the WMAP inferred abundances. This agreement between the two scales also gives an indirect comparison with the Balmer wing temperature scale of Bonifacio et al (2007).
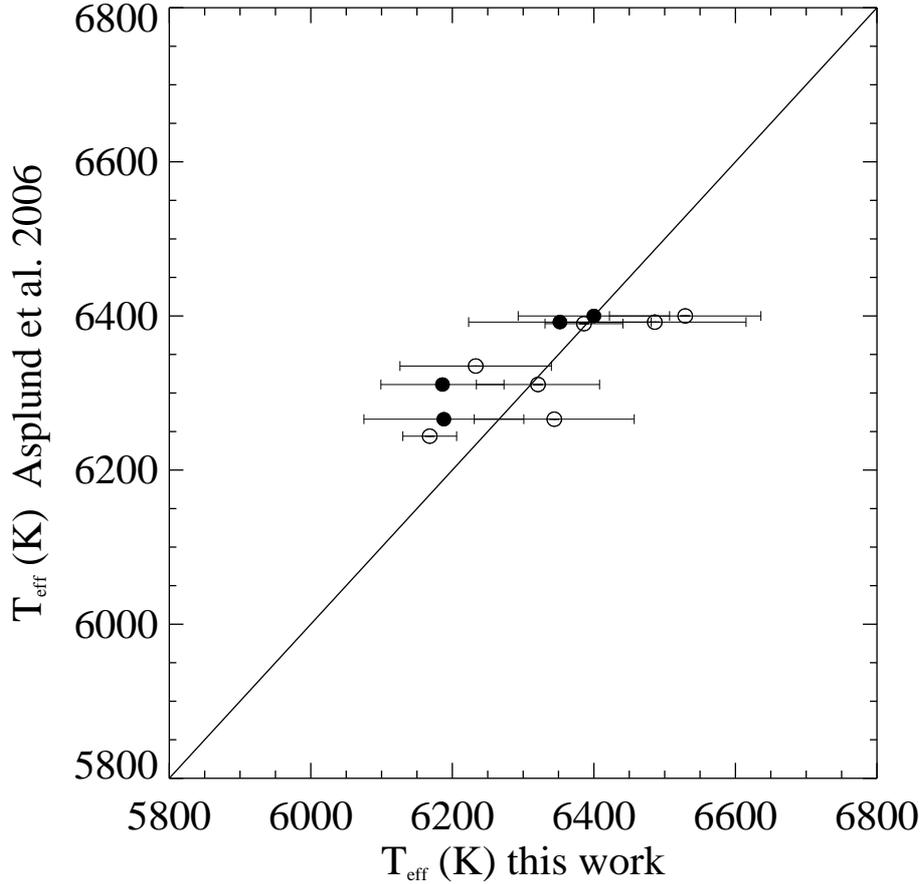
Fig. 9. Comparison of the Asplund et al. (2006) temperatures and those from this work. Filled circles represent SGB temperatures and open circles represent MS temperatures. Those stars of unknown evolutionary state have two points on the plot.

They found that their temperature scale was essentially the same as Asplund et al. (2006), which is in turn similar to ours.

Finally, Figure 10 presents the comparison between the photometric temperatures of Ryan et al. (1999) and T_χ of this work. At lower temperatures, $T_\chi < 6250$ K, the two scales are in excellent agreement. For the MS scale we have seven stars cooler than 6250 K. The difference, $T_\chi - T_{\mathrm{phot}}$, ranges from -126 K to 56 K, with a mean of -19 K. For the SGB scales we have eleven stars cooler than 6250 K, with the difference ranging from -99 K to 47 K and a mean of -18 K. However, at higher values, $T_\chi \geq 6250$ K, we see that the excitation scale becomes hotter. In this case, for eight MS scale stars we have a range of 87 K to 262 K and a mean of 143 K, and for three SGB scale stars a range of 57 K to 117 K with a mean of 73K. This suggests that the T_{phot} values are reliable for $T_\chi \lesssim 6250$ K, but may be ~70 - 140 K too cool for $T_\chi \gtrsim 6250$ K. Photometric temperature errors can be induced through inaccurate dereddening, inaccurate calibration to standards, or a flawed colour-temperature calibration. The last of these is perhaps the most readily encountered; earlier in this work we cited differences of ~100 K between the IRFM scales of Magain (1987) and Alonso et al. (1996). Of

course, the difference could also be due to inaccuracies in the model atmospheres used in this work to derive T_χ.

5.2. Lithium Abundances

Concerning the lithium problem, with our temperature scales we achieve a mean Li abundance of $A(\mathrm{Li})=$ 2.16 dex for the MS scale and $A(\mathrm{Li})=$ 2.10 dex for the SGB scale, with a scatter of 0.074 dex and 0.068 dex respectively. The mean Li abundance determined from the five stars whose evolutionary state is defined is $A(\mathrm{Li})=$ 2.18 dex with a scatter of 0.038 dex. It is pleasing to note the similarity between our mean ^{7}Li abundances and that derived by Spite et al. (1996), $A(\mathrm{Li})=$ 2.08 ($\pm$0.08) dex, who also use a temperature scale based on iron excitation. Bonifacio et al (2007) also found a similar result, $A(\mathrm{Li})=$ 2.10 ($\pm$0.09) dex, with their Balmer line wing temperature scale.

These values are obviously still too low to reconcile with the WMAP value of $A(\mathrm{Li})\approx$2.62 dex. Even if we later find that non-LTE corrections give temperature rises of roughly 150 K, we would get mean lithium abundances of $A(\mathrm{Li})\approx$2.26 dex and $A(\mathrm{Li})\approx$2.20 dex for the MS and SGB scales respectively. This value is
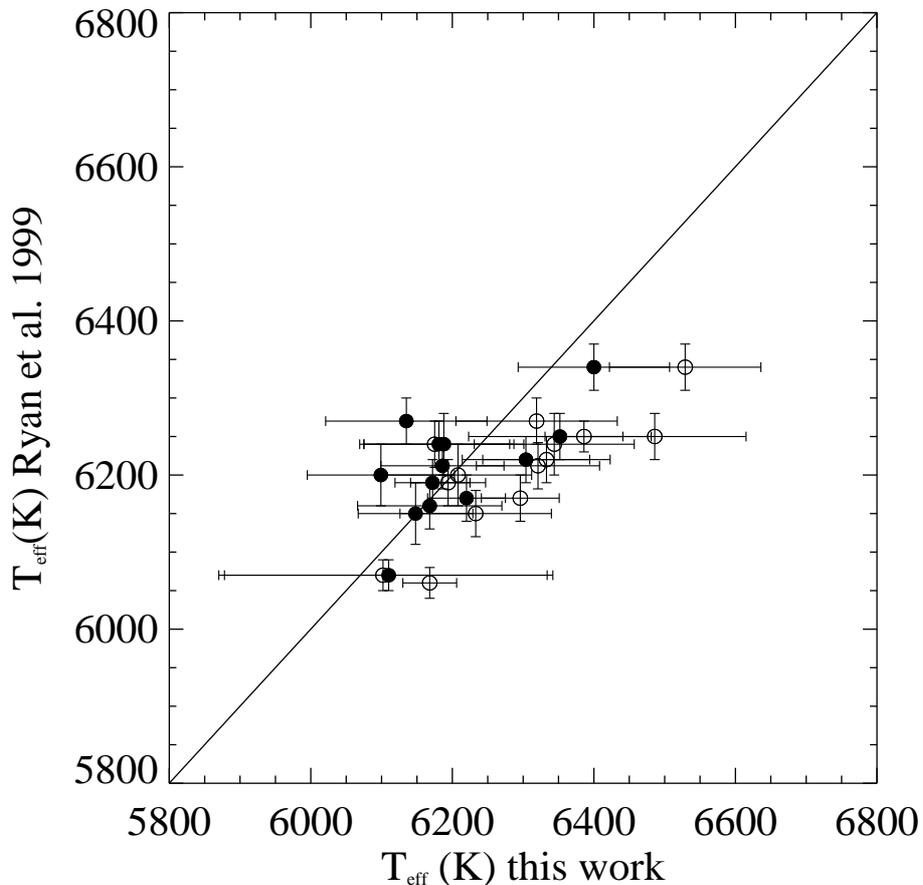
Fig. 10. Comparison of the Ryan et al. (1999) temperatures and those of this work. Filled circles represent SGB temperatures and open circles MS temperatures. Those stars of unknown evolutionary state have two points on the plot.

still too low. However, it is not yet known what is the true effect of non-LTE and/or 3D corrections on our temperature scale.

Although the primary purpose of this analysis was to investigate possibly large systematic errors in temperature, we can also investigate whether there is evidence for dependencies of $A(\mathrm{Li})$ on T_{eff} and [Fe/H] within the sample. With the $A(\mathrm{Li})$ values from Table 5 and the physical parameters calculated for each star we are able to perform a multiple regression fit, linear in T_{eff} and [Fe/H]. In these fits we include the stars with known evolutionary state, three on the MS and two on the SGB, combined with the eleven remaining stars of unknown evolutionary state for which we assess two cases: all MS and all SGB. This produces the equation

$$A(\mathrm{Li})=1.36(\pm0.84)+0.00019(\pm0.00013)\,T_{\mathrm{eff}}\,+0.138(\pm0.048)[\mathrm{Fe/H}]$$

for the MS case and

$$A(\mathrm{Li})=0.79(\pm1.22)+0.00025(\pm0.00019)\,T_{\mathrm{eff}}\,+0.095(\pm0.055)[\mathrm{Fe/H}]$$

for the SGB case. Here the bracketed values are 1 σ errors in the coefficients. The large errors seen in the intercept coefficient comes from the large extrapolation to $T = 0$ and [Fe/H] $= 0$. We see no statistically significant trend in either T_{eff} or in [Fe/H] for the SGB as each coefficient has errors of similar size to the coefficient itself. Although there is the possibility of a trend existing in [Fe/H] for the MS case (the coefficient is $\sim 3\sigma$) there is no certainty in this as it is not known whether all the stars belong in the MS evolutionary state.

The lack of significant trends here, in contrast to the significant [Fe/H] dependence in the study by Ryan et al. (1996) (and by Asplund et al. (2006)), comes about because the random uncertainties on the T_{χ} values are much larger than achieved by Ryan et al. (1999) using photometry. We recall that the primary purpose of the present work was to search for potentially large *systematic* errors in the temperatures, and for that purpose the larger random errors here are tolerable. However, the larger random errors greatly undermine the second use of the dataset.

We have also performed single parameter regression fits in T_{eff} and [Fe/H]. Figure 11 presents the results of the fits to temperatures. The values of the temperature coefficients imply

$$A(\mathrm{Li})=0.51(\pm1.00)+0.00026(\pm0.00016)\,T_{\mathrm{eff}}$$

for the MS case, and

$$A(\mathrm{Li})=0.71(\pm1.33)+0.00022(\pm0.00021)\,T_{\mathrm{eff}}$$

for the SGB case. There is clearly no statistically significant trend with temperature in either the MS or the SGB result, again since the temperature coefficient errors are of similar size to the coefficients themselves. For the fit to [Fe/H] we obtained the equation

$$A(\mathrm{Li})=2.58(\pm0.14)+0.152(\pm0.049)[\mathrm{Fe/H}]$$

for the MS case, and

$$A(\mathrm{Li})=2.35(\pm0.16)+0.089(\pm0.056)[\mathrm{Fe/H}]$$

for the SGB case. Figure 12 shows a plot of these fits. Here we confirm the similarity in values of the metallicity coefficient with Ryan et al. (1999) and Asplund et al. (2006), but again the large errors for the SGB case do not usefully constrain a metallicity trend. The metallicity coefficient for the MS case is $> 3\sigma$, but we caution again that we cannot be sure that all stars are on the MS.

We have also used the fitting form as described by Ryan et al. (2000) to deduce the primordial Li abundance. This fit is of the form:

$$Li/H = a^{'} + b^{'} Fe/Fe_{\odot} \tag{4}$$

where $a^{'}$ is the intercept and measures the primordial abundance directly. From this we obtain a value of $^{7}\mathrm{Li/H} = (1.18\pm0.10)\times10^{-10}$ for the MS case and $^{7}\mathrm{Li/H} = (1.10\pm0.1)\times10^{-10}$ for the SGB case. Comparing this to the value deduced from WMAP via BBN, $^{7}\mathrm{Li/H} = 4.15^{+0.49}_{-0.45}\times10^{-10}$, we once again see we have not reconciled the lithium problem.

We can see from this work that it has not been possible to find a solution to the lithium problem through the use of temperatures derived using the excitation technique. The T_{χ} values are lower than the Meléndez & Ramírez (2004) values, and more similar to the Hα and photometric temperature estimates. It would seem that one of the biggest outstanding problems is the assumption of LTE in the calculations. As has been stated in previous sections, we have begun our own investigation into the effects of non-LTE on abundance analysis, and therefore the effective temperatures, of this group of stars.

6. Conclusions

The physical parameters of 16 program stars, and two standard stars, have been calculated using WIDTH6. In particular, we have derived excitation energy temperatures by nulling the dependence of abundance on excitation potential for Fe I lines. We have compared our temperatures with those calculated in other works using different techniques, the IRFM of Meléndez & Ramírez (2004), the Balmer line wing method of Asplund et al. (2006), which is similar to that of Bonifacio et al (2007), and the photometric method of Ryan et al. (1999).

We have shown that the IRFM scale of Meléndez & Ramírez (2004) is hotter than ours by an average of $\sim$250 K. This difference may be the effect of the F_{bol} calibration used in IRFM or it could be a shift of the zero-point as an effect of the errors induced by using different photometric bands in the IRFM calculations. On the other hand it may be the effects of assuming LTE on our temperature scale.
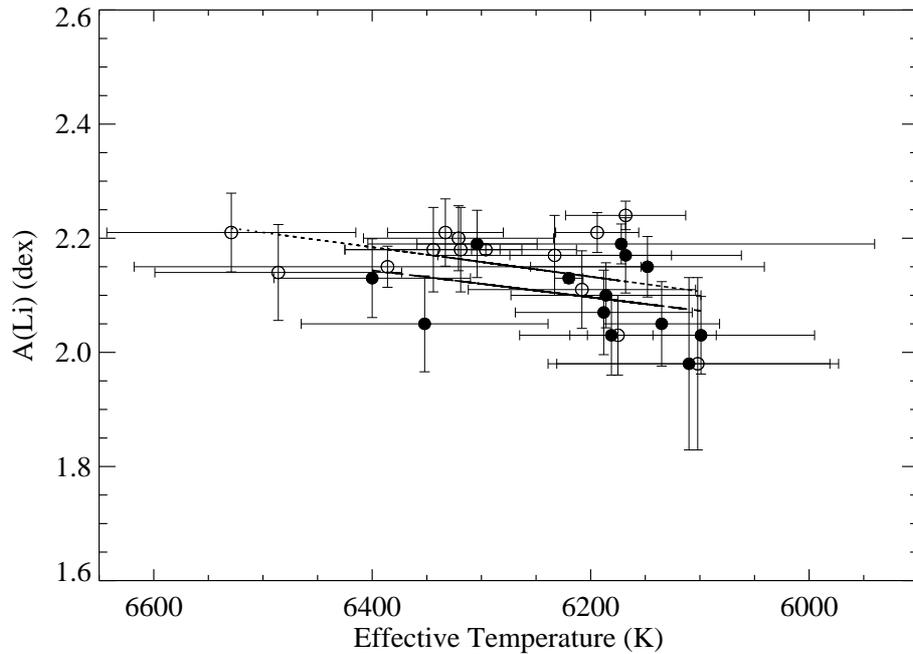
Fig. 11. Li abundances as a function of temperature. The dotted line is the fit to the MS temperatures (open circles) and the dashed line is the fit to the SGB temperatures (filled circles). Those stars of unknown evolutionary state have two points on the plot.
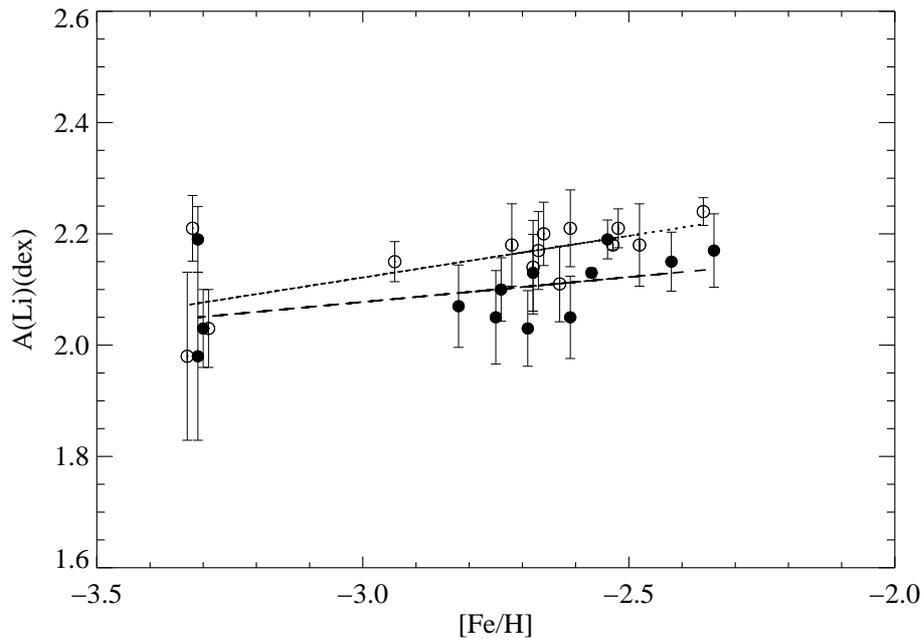
Fig. 12. Li abundances as a function of metallicity. The dotted line is the fit to the MS metallicities (open circles) and the dashed line is the fit to the SGB metallicities (filled circles). Those stars of unknown evolutionary state have two points on the plot.

It has been found that our methods have produced temperatures comparable with those derived using the Balmer line wing method. Both of these scales are too low to reconcile the lithium problem. It has been noted that the LTE assumptions of the Balmer line wing method may be leading to temperatures that are on order of 100 K too low. The method used in this work may also suffer from problems with LTE, but the full effect of non-LTE on the excitation method used here is unknown. This is something we will research in future work.

Finally we also see comparable results with the photometric temperature scale, although at higher temperatures, $T_\chi \geq 6250$ K, there is a shift towards our scale becoming hotter. This suggests that the photometric temperatures are reliable up until ~ 6250 K. The most readily detected error in photometric calculations comes from the colour-temperature calibration and differences in values derived from different calibrations can be as much as ~ 100 K.

With our derived temperatures we have calculated the Li abundances of the program stars. Due to large uncertainties, we do not see statistically compelling trends in $A(\text{Li})$ with either T_{eff} or [Fe/H]. Due to the uncertainty in evolutionary state for the majority of the stars we have two mean lithium abundances, $A(\text{Li}) = 2.16$ dex for the main sequence case and $A(\text{Li}) = 2.10$ dex for the SGB case. Five of the stars do have defined evolutionary states. The mean Li abundance from these five stars is $A(\text{Li}) = 2.12$ dex. These values are lower than the WMAP determined value of $A(\text{Li}) \approx 2.62$ dex. For the observationally deduced value to be comparable with the WMAP value our temperatures would need to increase by approximately 700 K.

References

Ahmed, S. N., et al. 2004, Physical Review Letters, 92, 181301

Alonso, A., Arribas, S., & Martínez-Roger, C., 1996, A&AS, 117, 227

Alonso, A., Arribas, S., & Martínez-Roger, C., 1999, A&A, 139, 335

Andersen, J., Gustafsson, B., & Lambert, D. L. 1984, A&A, 136, 65

Angulo, C., et al. 2005, ApJ, 630, L105

Anstee, S. D., & O'Mara, B. J. 1995, MNRAS, 276, 859

Arnone, E., Ryan, S. G., Argast, D., Norris, J. E., & Beers, T. C. 2005, A&A, 430, 507

Asplund, M., Nordlund, E., Trampedach, R., & Stein, R. F. 1999, A&A, 346, L17

Asplund, M., 2005, ARA&A, 43, 481

Asplund, M., Nissen, P. E., Lambert, D. L., Primas, F. & Smith, V. V. 2005, IAU Symp. 228, 53

Asplund, M., Lambert, D. L., Nissen, P. E., Primas, F., & Smith, V. V. 2006, ApJ, 644, 229

Bahcall, J. N., Pinsonneault, M. H., & Basu, S. 2001, ApJ, 555, 990

Bard, A., Kock, A., & Kock, M. 1991, A&A, 248, 315

Bard, A. & Kock, M. 1994, A&A, 282, 1014

Barklem, P. S., & O'Mara, B. J. 1997, MNRAS, 290, 102

Barklem, P. S., O'Mara, B. J., & Ross, J. E. 1998. MNRAS, 296, 1057

Barklem, P. S., Piskunov, N., & O'Mara, B. J. 2000, A&A, 363, 1091

Barklem, P. S., Stempels, H. C., Allende Prieto, C., Kochukhov, O. P., Piskunov, N., & O'Mara, B, J. 2002, A&A, 385, 951

Barklem, P. S. 2007, astro-ph/0702222B

Bell, R. A. 1981 private communication

Blackwell, D. E., Ibbetson, P. A., Petford, A. D., & Shallis, M. J. 1979, MNRAS, 186, 633

Blackwell, D. E., Petford, A. D., & Shallis, M. J., 1979, MNRAS, 186, 657

Blackwell, D. E., Shallis, M. J., & Selby, M. J. 1979, MNRAS. 188, 847

Blackwell, D. E., Petford, A. D., Shallis, M. J., & Simmons, G. J. 1980, MNRAS, 191, 445

Blackwell, D. E., Petford, A. D., Shallis, M. J., & Simmons, G. J. 1982, MNRAS, 199, 43

Blackwell, D. E., Petford, A. D., & Simmons, G. J., 1982, MNRAS, 210, 595

Bonifacio, P., Molaro, P., Sivarani, T., Cayrel, R., Spite, M., Spite, F., Plez, B., Andersen, J., Barbuy, B., Beers, T. C., Depagne, E., Hill, V., François, P., Nordström, & Primas, F. 2007, A&A, 462, 851

Castelli, F., Gratton, R. G., & Kurucz, R L. 1997, A&A, 318, 841

Cayrel, R., Steffen, M., Chand, H., Bonifacio, P., Spite, M., Spite, F., Petitjean, P., Ludwig, H. G., & Caffau, E., 2007, A&A, 473, 37

Coc, A., Nunes, N. J., Olive, K. A., Uzan, J.-P., & Vangioni, E. 2007, Phys. Rev. D, 76, 023511

Coc, A., Olive, K. A., Uzan, J.-P., & Vangioni, E. 2006, Phys. Rev. D, 73, 083525

Coc, A., Vangioni-Flam, E., Descouvemont, P., Adahchour, A. & Angulo, C., 2004, ApJ, 600, 544

Coc, A., & Vangioni, E. 2005, IAU Symp, 228, 13

Collet, R., Asplund, M., & Thévenin, F. 2005, A&A, 442, 643

Cottrell, P. L., & Norris, J. E. 1978, ApJ, 221, 893

Cyburt, R. H. 2004, Phys. Rev. D, 70, 023505

Cyburt, R. H., Ellis, J., Fields, B. D., Olive, K. A., & Spanos, V. C. 2006, Journal of Cosmology and Astro-Particle Physics, 11, 14

Cyburt, R. H., Fields, B. D., & Olive, K. A. 2001, New Astronomy, 6, 215

Cyburt, R. H., Fields, B. D., & Olive, K. A. 2004, Phys. Rev. D, 69, 123519

Damour, T., & Nordtvedt, K. 1993, Physical Review Letters, 70, 2217

Damour, T., & Nordtvedt, K. 1993, Phys. Rev. D, 48, 3436

Damour, T., & Pichon, B. 1999, Phys. Rev. D, 59, 123502

Dmitriev, V. F., Flambaum, V. V., & Webb, J. K. 2004, Phys. Rev. D, 69, 063506

Dunkley, J., et al. 2008, ArXiv e-prints, 803, arXiv:0803.0586

Ellis, J., Olive, K. A., & Vangioni, E. 2005, Physics Letters B, 619, 30

Feng, J. L., Su, S., & Takayama, F. 2004, Phys. Rev. D, 70, 075019

Fields, B.F., & Sarkar, S., 2006 in Yao, W.-M., & et al. 2006, Journal of Physics G Nuclear Physics, 33, 1

Fuhr, J. R., Martin, G. A., & Wiese, W. L. 1988, Journal of Physical and Chemical Reference Data, 17, 4

Fuhrmann, K., Axer, M., & Gehren, T. 1992, A&A, 271, 451

Fuhrmann, K., Axer, M., & Gehren, T. 1994, A&A, 285, 585

García Peréz, A. E., Inoue, S., Aoki, W., & Ryan, S. G. 2008, Precision Spectroscopy in Astrophysics, Proceedings of the ESO/Lisbon/Aveiro Conference, 9

Gratton, R. G., Carretta, E., Eriksson, K., & Gustafsson, B. 1999, A&A, 350, 955

Hamaguchi, K., Hatsuda, T., Kamimura, M., Kino, Y., & Yanagida, T. T. 2007, Phys. Lett. B, 650, 268

Hannaford, P., Lowe, R. M., Grevesse, N. & Noels, A. 1992, A&A, 259, 301

Heise, C. & Kock, M. 1990, A&A, 230, 244

Jedamzik, K. 2004, Phys. Rev. D, 70, 063524

Jedamzik, K., Choi, K.-Y., Roszkowski, L., & Ruiz de Austri, R. 2006, Journal of Cosmology and Astro-Particle Physics, 7, 7

Korn, A. J., Grundahl, F., Richard, O., Barklem, P. S., Mashonkina, L., Collet, R., Piskunov, N., & Gustafsson B. 2006, Nature, 442, 657

Kroll, S. & Kock, M, 1987, A&AS, 67, 225

Kurucz, R. L. 1993, IAU Colloq. 138: Peculiar versus Normal Phenomena in A-type and Related Stars, Astronomical Society of the Pacific Conference Series, 44, 87

Magain, P. 1987, A&A, 181, 323

Meléndez, J., & Ramírez, I. 2004, ApJ, 615, L33

Moity, J. 1983, A&AS, 52, 37

Norris, J. E., Ryan, S. G., & Stringfellow, G. S. 1994, ApJ, 423, 386

Norris, J. E., Ryan, S. G., & Beers, T. C. 2001, ApJ, 561, 1034

O'Brian, T. R., Wickliffe, M. E., Lawler, J. E., Whaling, W., & Brault, J. W. 1991, JOptSocAmB, 8, 1185

Olive, K. A., Steigman, G., & Walker, T. P. 2000, Phys. Rep., 333, 389

Peterson, R., Carney, B. W. 1979, ApJ, 231, 762

Piau, L., Beers, T. C., Balsara, D. S., Sivarani, T., Truran, J. W., & Ferguson, J. W. 2006, ApJ, 653, 300

Richard, O., Michaud, G., & Richer, J. 2005, ApJ, 619, 538

Ramírez, I., & Meléndez, J. 2005, ApJ, 626, 446

Ryan, S. G. Beers, T. C., Deliyannis, C. P., Thorburn, J. A. 1996, ApJ, 458, 543

Ryan, S. G., Norris, J. E., & Beers, T. C. 1996, ApJ, 471, 254

Ryan, S. G. 1998, A&A, 331, 1051

Ryan, S. G., Norris, J. E., & Beers, T. C. 1999, ApJ, 523, 654

Ryan, S. G., Beers, T. C., Olive, K. A., Fields, B. D. & Norris, J. E. 2000, ApJ, 530, L57

Ryan, S. G., Kajino, T., Beers, T. C., Suzuki, T. K., Romano, D., Matteucci, F., & Rosolankova, K. 2001, ApJ, 549, 55

Salati, P. 2003, Phys. Lett. B,571. 121

Schnabel, R., Kock, M. & Holweger, H. 1999, A&A, 342, 610

Spite, F. & Spite, M. 1982, A&A, 115, 357

Spite, M., François, P., Nissen, P. E., & Spite, F. 1996, A&A, 307, 172

Shchukina, N. G., Trujillo Bueno, J., & Asplund, M. 2005, ApJ, 618, 939

Thévenin, F. 1989, A&AS, 77, 137

Thévenin, F. & Idiart, T. P. 1999, ApJ, 521, 753

Vidal, C. R., Cooper, J., & Smith, E. W. 1973, ApJS, 25, 37

Vangioni-Flam, E., Olive, K A., Fields, B. D. & Cassé, M. 2003 ApJ. 585, 611

Appendix A: Measured equivalent widths for all the lines present in the program stars

Measured equivalent widths in mÅ for the program stars

Wavelength (Å)	log *gf*	*Ref.*	χ (eV)	BD-13°3442	BD+3°740	BD+9°2190	BD+20°2030
FeI							
3718.41	-1.13	4	2.76	...	...	...	...
3719.93	-0.43	4	0.00	110.9	101.8	110.0	...
3724.38	-0.82	4	2.28	...	...	...	...
3727.62	-0.62	4,5	0.96	62.3	73.4	66.2	...
3731.37	-1.42	5	2.61	...	...	...	...
3733.32	-1.39	4	0.11	...	...	77.1	...
3735.32	-0.29	4	2.94	...	...	...	...
3743.36	-0.78	4,5	0.99	64.2	72.3	71.9	74.3
3744.10	-0.70	4	3.04	...	...	...	...
3745.56	-0.77	4	0.09	103.8	102.7	89.2	98.5
3745.90	-1.34	4,5	0.12	74.2	77.7	71.5	80.2
3748.26	-1.01	4,5	0.11	94.0	81.6	87.5	85.8
3756.07	-2.12	4	2.18	...	...	...	...
3756.94	-0.25	3	3.57	...	...	...	...
3758.23	-0.02	4,5	0.96	100.1	92.4	91.8	95.6
3760.05	-0.81	4,5	2.40	...	...	13.9	14.2
3760.53	-1.23	4	2.22	...	...	...	9.8
3763.79	-0.23	5	0.99	89.0	86.3	79.6	87.1
3765.54	0.48	4	3.24	34.5	28.5	24.2	36.0
3767.19	-0.39	4,5	1.01	73.3	73.1	69.1	74.4
3774.82	-1.45	4	2.22	...	...	...	...
3776.46	-1.49	4	2.18	...	...	...	...
3781.19	-1.94	4	2.20	...	...	...	...
3786.68	-2.19	2,4,5	1.01	...	...	...	14.8
3787.88	-0.85	4,5	1.01	66.2	58.5	59.7	62.8
3789.18	-1.29	4	2.73	...	...	...	...
3790.09	-1.74	2,4,5	0.99	23.2	22.1	...	36.4
3795.00	-0.75	4,5	0.99	...	72.6	59.6	70.4
3799.55	-0.82	4,5	0.96	61.6	59.6	...	...
3804.01	-1.04	3	3.33	...	...	...	...
3805.34	0.31	4	3.30	29.0	...	13.6	22.8
3806.22	-0.82	3	3.41	...	...	...	5.1
3807.54	-0.99	4	2.22	...	9.5	9.2	...
3808.73	-1.14	4,5	2.56	...	...	6.5	...
3812.97	-1.03	2,4	0.96	56.7	56.7	52.2	64.0
3814.52	-2.36	2,4	1.01	...	...	...	...
3815.84	0.23	1,4	1.48	90.2	87.5	83.4	91.3
3816.34	-1.20	4	2.20	8.0	7.0	...	8.0
3820.43	0.14	4,5	0.86	98.5	...	100.2	112.7
3821.18	0.20	4	3.27	20.7	...	16.4	24.2
3821.84	-1.10	4	2.61	...	...	4.4	...
3824.44	-1.35	4,5	0.00	85.4	88.4	81.5	94.4
3825.88	-0.03	4,5	0.91	93.3	94.0	89.7	100.1
3827.82	0.08	1,4,5	1.56	75.8	75.9	72.1	84.4
3833.31	-1.03	4	2.56	...	...	...	...
3834.22	-0.28	4,5	0.96	...	...	...	...
3839.26	-0.33	4	3.05	...	...	...	...
3840.44	-0.50	4,5	0.99	74.7	71.6	65.7	75.0
3841.05	-0.05	2,4	1.61	68.9	67.9	63.3	71.8
3843.26	-0.24	4	3.05	...	12.7	...	20.8

continued.

Wavelength (Å)	log *gf*	*Ref.*	χ (eV)	BD-13°3442	BD+3°740	BD+9°2190	BD+20°2030
3846.41	-0.47	4	3.57	...	...	...	...
3846.80	-0.02	4	3.25	21.7	...	11.0	17.3
3849.97	-0.87	4,5	1.01	56.2	61.6	60.3	70.7
3850.82	-1.74	2,4,5	0.99	36.3	25.5	24.3	35.5
3852.57	-1.19	4	2.18	11.4	...	...	13.8
3856.37	-1.28	4,5	0.05	82.9	85.7	83.1	83.7
3859.21	-0.75	4	2.40	15.3	14.3	...	25.7
3859.91	-0.70	4,5	0.00	111.9	108.0	97.0	108.6
3865.52	-0.97	4,5	1.01	70.1	60.6	55.6	63.6
3867.22	-0.45	4	3.02	...	11.8	7.1	11.2
3872.50	-0.91	1,4,5	0.99	66.2	66.7	56.8	68.8
3876.04	-2.86	2,4	1.01	...	...	...	...
3878.02	-0.91	4,5	0.96	66.3	71.9	61.1	70.9
3878.57	-1.36	2,4	0.09	...	93.8	86.8	...
3884.36	-1.09	4	2.69	...	...	5.9	...
3885.51	-1.09	4	2.42	...	...	...	7.9
3886.28	-1.07	4,5	0.05	84.4	85.4	82.1	83.5
3887.05	-1.12	4,5	0.91	59.0	...	50.5	...
3895.66	-1.66	2,4,5	0.11	61.3	66.6	59.1	69.9
3897.45	-1.28	4	2.95	...	...	...	...
3899.71	-1.52	4,5	0.09	77.3	75.3	66.8	73.7
3902.95	-0.43	2,4,5	1.56	59.6	61.2	55.3	60.2
3906.48	-2.20	2,4,5	0.11	44.3	38.5	36.9	52.8
3910.84	-1.55	1,4	2.76	...	...	...	...
3916.73	-0.58	1	3.24	...	...	...	...
3917.18	-2.15	4,5	0.99	14.8	16.3	...	18.7
3920.26	-1.74	2,4,5	0.12	64.6	65.4	63.0	69.4
3922.91	-1.64	4,5	0.05	...	73.2	67.7	75.4
3925.64	-1.03	4	2.83	...	...	...	...
3925.94	-0.94	4	2.86	...	...	...	...
3927.92	-1.52	4	0.11	78.3	76.0	71.2	76.9
3930.30	-1.49	4	0.09	74.8	75.8	...	80.2
3937.33	-1.46	4	2.69	...	...	...	...
3940.88	-2.55	4,5	0.96	...	...	...	...
3942.44	-0.95	4	2.84	...	...	...	...
3946.99	-1.00	4	3.21	...	...	...	...
3948.10	-0.56	4	3.24	9.1	...	...	7.6
3949.95	-1.25	4	2.18	11.5	...	9.1	...
3955.34	-1.01	3	3.28	...	...	...	...
3966.06	-1.55	2	1.61	...	...	...	12.7
3981.77	-1.12	4	2.73	...	...	8.9	12.8
3983.96	-1.02	4	2.73	...	...	5.1	...
3995.98	-1.57	4	2.73	...	...	...	...
3997.39	-0.48	4	2.73	...	13.0	14.5	19.6
4001.66	-1.90	4	2.18	...	...	...	...
4005.24	-0.60	4,5	1.56	51.8	53.7	50.3	...
4009.71	-1.25	4	2.22	...	10.5	7.3	...
4021.87	-0.73	4	2.76	...	9.3	7.7	...
4031.96	-1.06	3	3.27	...	...	...	...
4032.63	-2.38	4	1.48	...	...	...	5.3
4040.64	-1.12	4	3.30	...	...	...	...

continued.

Wavelength (Å)	log *gf*	*Ref.*	χ (eV)	BD-13°3442	BD+3°740	BD+9°2190	BD+20°2030
4044.61	-1.22	4	2.83	...	...	...	...
4045.81	0.28	4,5	1.48	96.1	116.1	90.9	94.6
4062.44	-0.86	4	2.84	...	7.4	7.5	...
4063.28	0.81	4	3.37	...	...	...	...
4063.59	0.06	4	1.56	81.5	77.0	79.9	87.9
4066.98	-1.02	6	2.83	...	...	...	...
4067.27	-1.40	4,5	2.56	...	...	...	11.2
4067.98	-0.47	4	3.21	...	7.3	...	...
4070.77	-0.79	3	3.24	...	...	...	...
4071.74	-0.02	4,5	1.61	69.4	76.5	80.4	71.9
4073.76	-0.90	4	3.27	...	...	...	...
4074.79	-1.11	4	3.05	...	...	...	...
4076.63	-0.53	4	3.21	...	...	...	...
4079.84	-1.36	4	2.86	...	...	3.8	...
4080.21	-1.22	3	3.28	...	...	...	...
4084.49	-0.71	4	3.33	...	...	...	7.2
4085.00	-1.28	3	2.84	...	...	...	...
4095.97	-1.48	4	2.59	...	...	...	...
4107.49	-0.88	4	2.83	...	...	...	8.1
4114.44	-1.30	4	2.83	...	...	...	5.6
4118.54	0.22	4	3.57	12.2	13.2	...	...
4120.21	-1.27	4	2.99	...	...	...	...
4121.80	-1.45	4	2.83	...	...	3.3	...
4126.18	-0.96	3	3.33	...	...	...	...
4132.06	-0.68	4	1.61	48.9	52.6	42.4	57.0
4132.90	-1.01	4	2.84	...	...	...	8.2
4134.68	-0.65	4	2.83	15.8	10.5	11.2	...
4137.00	-0.45	4	3.41	...	...	...	5.9
4143.41	-0.20	4	3.05	...	14.5	11.2	16.7
4143.87	-0.51	4	1.56	57.7	57.4	55.8	...
4147.67	-2.09	4,5	1.48	...	10.0	...	9.1
4152.17	-3.20	4,5	0.96	...	...	...	...
4153.90	-0.32	4	3.40	...	...	...	10.6
4154.50	-0.69	4	2.83	...	6.5	8.6	9.4
4154.81	-0.40	4	3.37	...	6.1	5.4	...
4156.80	-0.81	4	2.83	...	...	...	...
4157.78	-0.40	4	3.42	4.9	6.5	...	...
4158.79	-0.67	3	3.43	...	...	...	...
4174.91	-2.95	4,5	0.91	...	...	...	...
4175.64	-0.83	4	2.84	10.6	7.1	...	...
4176.57	-0.68	6	3.37	6.4	...	...	6.6
4177.59	-3.02	4,5	0.91	...	...	...	...
4181.76	-0.37	4	2.83	17.0	...	...	24.4
4182.38	-1.18	4	3.02	...	...	...	...
4184.89	-0.87	4	2.83	...	5.4	...	...
4187.04	-0.53	4,5	2.45	21.5	18.7	20.3	25.8
4187.80	-0.53	4,5	2.43	23.1	21.3	19.9	26.2
4191.43	-0.67	4	2.47	15.5	16.8	15.4	20.9
4195.33	-0.49	4	3.33	...	5.4	6.0	5.9
4196.21	-0.70	4	3.40	...	...	...	5.0
4198.31	-0.67	4,5	2.40	19.9	18.5	18.6	27.9

continued.

Wavelength (Å)	log *gf*	*Ref.*	χ (eV)	BD-13°3442	BD+3°740	BD+9°2190	BD+20°2030
4199.09	0.16	4	3.05	25.0	28.0	22.1	31.5
4200.92	-0.83	4	3.40	...	...	...	...
4202.03	-0.70	4,5	1.48	56.0	56.3	49.9	59.7
4207.13	-1.46	3	2.83	...	...	...	...
4210.34	-0.93	4	2.48	...	...	7.8	14.2
4216.18	-3.36	4,5	0.00	...	...	...	13.3
4217.54	-0.48	4	3.43	...	...	...	6.3
4219.36	0.00	4	3.57	12.4	11.6	...	12.7
4222.21	-0.94	4,5	2.45	12.3	...	...	12.1
4224.17	-0.51	4	3.37	...	7.6	...	...
4225.45	-0.51	4	3.42	7.3	3.4	...	6.5
4227.43	0.27	4	3.33	...	21.2	19.3	28.5
4233.60	-0.59	4,5	2.48	15.1	18.1	14.6	23.9
4235.94	-0.33	4,5	2.43	29.0	33.1	26.9	35.4
4238.02	-0.62	4	3.42	...	4.7	...	...
4238.81	-0.23	4	3.40	7.5	...	8.3	9.2
4282.40	-0.78	4	2.18	22.0	22.6	16.3	24.2
4294.13	-1.04	2,4	1.48	51.9	51.1	45.1	60.4
4299.23	-0.38	1,4	2.43	27.1	26.7	22.0	26.1
4307.90	-0.07	4	1.56	91.6	92.7	87.4	...
4325.76	0.01	4	1.61	78.1	76.0	73.3	...
4337.05	-1.70	4,5	1.56	...	8.2	...	...
4352.73	-1.29	4	2.22	...	...	7.5	10.1
4369.77	-0.80	4	3.05	...	4.2	...	...
4375.93	-3.02	4,5	0.00	12.9	16.3	13.2	18.7
4383.54	0.20	4,5	1.48	94.0	86.1	91.9	95.1
4388.41	-0.68	4	3.60	...	...	...	4.8
4404.75	-0.13	2,4,5	1.56	75.4	77.2	75.2	80.1
4408.41	-1.78	4	2.20	...	...	...	5.6
4415.12	-0.62	4,5	1.61	54.5	54.7	51.5	60.0
4427.31	-2.92	4	0.05	14.2	16.9	12.5	18.9
4430.61	-1.69	4,5	2.22	...	...	...	...
4433.22	-0.70	3	3.65	...	...	...	...
4442.34	-1.24	4,5	2.20	...	6.6	9.2	11.2
4443.19	-1.04	4	2.86	6.3	...	...	...
4447.72	-1.34	4,5	2.22	...	8.1	6.0	...
4454.38	-1.30	4	2.83	...	...	...	...
4459.12	-1.31	4,5	2.18	13.8	9.6	...	13.5
4461.65	-3.20	4,5	0.09	12.4	11.1	9.3	...
4466.55	-0.60	4	2.83	11.0	8.9	10.3	10.0
4482.17	-3.48	4,5	0.11	...	...	...	13.8
4484.22	-0.86	4	3.60	...	...	...	...
4485.68	-1.02	3	3.69	...	...	...	...
4489.74	-3.93	4,5	0.12	...	...	...	...
4494.56	-1.14	4,5	2.20	10.1	13.1	9.5	16.5
4528.61	-0.85	4,5	2.18	21.7	19.3	18.0	24.0
4531.15	-2.13	4,5	1.48	...	...	6.2	...
4592.65	-2.46	4	1.56	...	...	...	...
4602.94	-2.21	4	1.48	...	4.9	...	7.8
4618.76	-2.41	4	2.95	...	...	...	...
4619.29	-1.12	3	3.60	...	...	...	...

continued.

Wavelength (Å)	log *gf*	*Ref.*	χ (eV)	BD-13°3442	BD+3°740	BD+9°2190	BD+20°2030
4625.05	-1.34	3	3.24	...	...	...	...
4637.51	-1.39	3	3.28	...	...	...	...
4638.01	-1.12	4	3.60	...	...	...	...
4647.43	-1.35	4	2.95	...	...	...	...
4678.85	-0.83	4	3.60	...	...	...	3.0
4707.28	-1.08	3	3.24	...	...	...	...
4736.77	-0.75	4	3.21	...	...	...	...
4789.65	-0.96	4	3.55	...	...	...	...
4843.15	-1.84	3	3.40	...	...	...	...
FeII							
3824.91	-3.41	10	2.58	...	...	...	...
3974.16	-3.51	10	2.70	...	...	...	...
4122.66	-3.38	10	2.58	...	...	...	...
4178.86	-2.54	9	2.58	12.0	7.0	7.5	9.4
4233.17	-1.87	11	2.58	25.5	24.7	21.2	28.6
4296.57	-3.01	10	2.70	...	...	...	...
4303.17	-2.56	8,9	2.70	6.3	7.0	5.3	6.2
4385.38	-2.57	10	2.78	5.2	6.7	...	...
4416.82	-2.60	10	2.78	...	3.7	...	6.5
4489.19	-2.97	10	2.83	...	...	...	...
4491.40	-2.74	10	2.86	4.5	...	...	...
4508.28	-2.39	3	2.86	5.6	5.9	...	10.8
4515.33	-2.48	3	2.84	...	...	...	...
4520.22	-2.61	3	2.81	...	5.1	5.3	5.9
4522.63	-2.14	9	2.84	13.4	12.2	10.8	12.8
4541.52	-3.05	10	2.86	...	4.1	...	...
4555.89	-2.37	10	2.83	6.0	...	...	7.8
4576.33	-2.96	7,10,11	2.84	3.7	...	...	...
4583.83	-1.91	3	2.81	19.8	18.6	19.3	21.9
4620.51	-3.24	7,10,11	2.83	...	...	...	...
4731.45	-3.36	10	2.89	...	...	...	...
4923.92	-1.36	3,9,10	2.89	...	...	...	40.2

Ref. 1-Bard & Kock (1994), 2-Bard et al. (1991), 3-Fuhr et al. (1988), 4-O'Brian et al. (1991), 5-Oxford Fe I consortium
6-Thévenin et al. (1989), 7-Hannaford et al. (1992), 8-Heise & Kock (1990), 9-Kroll & Kock (1987), 10-Moity (1983)
11-Schnabel, Kock & Holweger (1999)

Table A.7. Measured equivalent widths in mÅ for the program stars

Wavelength (Å)	BD+24°1676	BD+26°2621	BD+26°3578	CD-33°1173	CD-71°1234	CD-24°17504
FeI						
3718.41	...	...	...	...	...	...
3719.93	...	119.5	127.8	99.7	...	...
3724.38	21.2	...	...	...	26.0	...
3727.62	75.9	76.6	89.8	67.9	82.5	51.2
3731.37	...	...	...	...	...	...
3733.32	...	72.2	80.7	...	88.0	52.9
3735.32	...	...	...	...	...	...
3743.36	84.5	76.7	...	56.2	78.5	46.0
3744.10	...	...	...	...	...	...
3745.56	109.0	110.5	113.8	93.0	106.9	84.6
3745.90	75.3	91.2	94.1	73.9	78.8	59.1
3748.26	...	94.1	93.1	74.8	98.0	72.3
3756.07	...	...	...	...	...	...
3756.94	...	...	10.8	...	...	...
3758.23	98.1	95.4	112.3	85.2	109.0	70.4
3760.05	18.0	18.7	25.8	...	17.3	4.6
3760.53	9.8	...	13.4	...	...	...
3763.79	89.7	80.6	95.3	...	96.5	63.9
3765.54	34.1	29.7	39.6	18.4	40.5	...
3767.19	80.2	81.3	87.6	61.5	82.9	52.3
3774.82	...	...	...	...	...	...
3776.46	...	...	15.8	...	...	...
3781.19	...	...	...	...	...	...
3786.68	14.7	21.2	23.5	...	19.9	...
3787.88	70.0	63.3	80.6	47.9	78.1	46.6
3789.18	6.5	...	...	...	...	...
3790.09	33.8	35.4	47.1	13.2	40.5	12.6
3795.00	68.8	...	83.4	...	85.9	45.9
3799.55	63.6	...	...	57.2	...	43.5
3804.01	...	...	...	...	...	...
3805.34	28.1	23.3	32.9	15.3	30.5	13.7
3806.22	...	...	...	...	...	...
3807.54	16.0	11.5	21.5	...	...	...
3808.73	...	...	...	...	...	...
3812.97	74.0	63.7	81.9	48.1	78.0	37.6
3814.52	...	20.3	...	...	...	...
3815.84	94.6	88.4	106.5	77.2	98.3	69.6
3816.34	10.0	...	17.9	...	10.1	...
3820.43	115.2	109.6	122.7	98.4	122.1	85.1
3821.18	23.7	25.0	34.0	...	29.7	11.3
3821.84	...	...	11.8	...	13.2	...
3824.44	103.3	88.5	113.5	75.0	101.5	69.7
3825.88	102.4	103.4	114.5	84.4	106.9	77.1
3827.82	85.0	78.6	92.1	64.8	91.9	59.0
3833.31	...	...	...	...	...	...
3834.22	...	...	...	...	...	...
3839.26	...	...	...	...	...	4.7
3840.44	79.9	76.6	86.9	61.6	85.3	53.3
3841.05	73.4	70.9	80.9	60.5	73.5	50.5
3843.26	18.0	...	27.6	...	20.5	...

Table A.7. continued.

Wavelength (Å)	BD+24°1676	BD+26°2621	BD+26°3578	CD-33°1173	CD-71°1234	CD-24°17504
3846.41	5.1	...	...	...	...	...
3846.80	...	...	28.9	11.9	22.3	...
3849.97	69.3	67.4	79.6	52.4	73.5	40.1
3850.82	35.9	26.3	49.8	...	39.7	...
3852.57	11.8	...	17.2	...	16.1	...
3856.37	90.8	83.4	95.2	74.2	99.9	66.5
3859.21	19.9	...	29.0	...	29.6	...
3859.91	111.7	108.9	116.5	99.2	...	96.1
3865.52	79.3	61.1	73.2	46.3	75.4	38.6
3867.22	12.5	...	19.3	...	14.5	...
3872.50	71.2	68.6	75.8	51.2	70.5	39.8
3876.04	...	...	...	...	7.2	...
3878.02	...	65.3	78.7	48.8	75.1	42.4
3878.57	...	96.2	...	68.2	...	60.8
3884.36	...	...	11.8	...	...	...
3885.51	...	14.5	14.6	...	...	...
3886.28	89.6	96.6	102.3	86.9	97.1	75.1
3887.05	55.0	58.7	68.7	...	62.5	...
3895.66	76.1	63.2	80.0	58.5	77.1	47.5
3897.45	...	...	...	...	...	...
3899.71	81.2	74.1	83.5	61.9	82.8	56.7
3902.95	68.5	62.5	74.0	46.5	70.9	36.3
3906.48	54.2	49.6	62.5	25.0	61.0	22.6
3910.84	...	...	...	...	...	...
3916.73	...	...	13.6	...	11.2	...
3917.18	19.2	18.4	26.7	...	20.6	11.1
3920.26	73.3	67.2	79.3	49.5	77.8	44.5
3922.91	79.4	79.2	89.6	58.4	82.9	55.3
3925.64	...	...	...	...	...	...
3925.94	10.4	...	...	...	...	...
3927.92	83.5	86.8	89.1	69.4	89.0	55.2
3930.30	79.4	70.5	89.1	71.5	91.2	60.9
3937.33	...	...	5.3	...	...	...
3940.88	8.2	8.8	14.2	...	13.1	...
3942.44	7.4	...	8.1	...	...	...
3946.99	...	...	6.5	...	...	...
3948.10	7.4	7.3	13.0	...	8.9	...
3949.95	...	...	22.1	...	16.1	...
3955.34	...	...	...	...	...	...
3966.06	11.6	11.9	...	...	15.7	...
3981.77	...	...	22.1	...	...	...
3983.96	10.5	...	20.3	...	13.5	...
3995.98	...	...	...	...	...	...
3997.39	21.5	18.7	32.6	11.4	23.2	...
4001.66	...	...	6.8	...	...	...
4005.24	66.2	58.3	68.7	40.5	68.7	32.7
4009.71	11.3	13.1	18.4	...	14.1	...
4021.87	...	...	17.5	7.4	16.0	...
4031.96	...	...	4.3	...	...	...
4032.63	...	...	6.4	...	...	...
4040.64	...	...	...	...	...	...

Table A.7. continued.

Wavelength (Å)	BD+24°1676	BD+26°2621	BD+26°3578	CD-33°1173	CD-71°1234	CD-24°17504
4044.61	4.6	...	7.4	...	6.2	...
4045.81	92.8	93.8	136.0	81.2	107.3	71.1
4062.44	8.5	...	13.2	...	13.8	...
4063.28	...	8.7	...	...	...	...
4063.59	91.2	...	98.0	72.2	94.9	60.8
4066.98	5.6	...	10.0	...	...	...
4067.27	...	...	8.7	...	6.4	...
4067.98	11.0	11.4	18.1	...	12.4	...
4070.77	...	6.2	...	...	...	...
4071.74	83.5	75.8	97.3	65.0	87.5	54.0
4073.76	...	...	7.9	...	...	...
4074.79	...	...	7.5	...	...	...
4076.63	11.4	...	14.0	...	...	...
4079.84	...	...	...	...	...	...
4080.21	...	...	...	...	...	...
4084.49	6.1	...	8.7	...	...	...
4085.00	...	...	...	...	...	...
4095.97	...	...	...	...	...	...
4107.49	8.7	12.3	...	6.7	9.5	...
4114.44	...	...	...	...	...	...
4118.54	...	15.4	30.1	...	21.3	...
4120.21	...	...	...	...	...	...
4121.80	...	...	5.3	...	...	...
4126.18	...	...	...	...	...	...
4132.06	61.1	52.9	68.8	36.9	62.2	26.6
4132.90	7.4	...	14.6	...	9.8	...
4134.68	15.6	...	21.6	10.2	18.0	...
4137.00	6.7	...	9.6	...	...	...
4143.41	22.1	16.9	27.8	12.8	23.5	...
4143.87	68.0	61.7	73.6	52.5	68.9	41.7
4147.67	9.3	...	13.4	...	9.1	...
4152.17	...	...	...	...	...	...
4153.90	10.9	...	15.0	...	...	...
4154.50	13.1	...	17.9	...	14.3	...
4154.81	7.4	...	...	...	11.5	...
4156.80	14.5	14.6	...	...	14.4	...
4157.78	...	...	12.4	...	...	...
4158.79	...	...	6.8	...	...	...
4174.91	4.7	...	12.0	...	...	...
4175.64	9.6	...	15.8	...	14.6	3.3
4176.57	6.5	...	9.1	...	...	...
4177.59	...	...	...	...	...	...
4181.76	24.3	22.6	30.8	11.0	26.6	7.2
4182.38	...	...	6.1	...	...	...
4184.89	...	...	14.0	...	11.2	...
4187.04	30.6	21.0	40.1	...	33.7	9.1
4187.80	...	24.5	49.7	...	33.7	9.6
4191.43	22.6	17.3	33.4	8.0	25.8	6.8
4195.33	7.0	...	11.9	...	10.3	...
4196.21	...	...	...	...	...	...
4198.31	33.9	...	42.2	11.5	38.5	...

Table A.7. continued.

Wavelength (Å)	BD+24°1676	BD+26°2621	BD+26°3578	CD-33°1173	CD-71°1234	CD-24°17504
4199.09	34.5	26.9	49.3	17.8	37.7	...
4200.92	...	...	...	...	...	...
4202.03	65.7	53.9	71.0	41.2	67.5	32.2
4207.13	...	...	...	...	...	...
4210.34	18.5	12.9	22.9	...	15.5	4.8
4216.18	13.5	...	18.3	5.3	16.6	...
4217.54	...	...	10.8	...	7.3	...
4219.36	15.5	...	23.2	...	16.4	...
4222.21	15.8	13.8	21.5	...	16.3	...
4224.17	9.9	...	13.9	...	...	...
4225.45	...	...	10.8	...	9.8	...
4227.43	31.5	24.2	40.0	...	33.8	12.9
4233.60	29.5	20.1	34.4	10.4	25.0	6.9
4235.94	41.0	32.7	50.0	20.0	41.5	14.2
4238.02	...	...	3.9	...	4.6	...
4238.81	10.5	12.5	19.4	...	15.1	4.0
4282.40	29.0	23.0	37.6	8.9	32.9	...
4294.13	64.3	58.0	76.7	37.0	67.8	24.5
4299.23	39.9	29.0	...	13.9	38.1	12.2
4307.90	108.2	93.4	...	74.6	104.7	58.8
4325.76	86.1	71.3	91.4	63.8	85.4	54.0
4337.05	14.9	...	...	...	16.7	...
4352.73	...	...	13.9	...	14.4	...
4369.77	6.2	...	7.4	...	9.0	...
4375.93	24.2	18.1	29.8	7.9	26.5	6.1
4383.54	101.7	92.9	109.5	81.4	112.2	72.4
4388.41	...	4.5	...	...	...	...
4404.75	85.0	78.2	91.2	62.8	88.4	55.8
4408.41	5.5	...	...	...	6.2	...
4415.12	66.4	58.3	70.7	40.8	67.7	32.3
4427.31	24.0	18.5	33.5	...	26.3	...
4430.61	...	...	...	...	...	...
4433.22	...	...	...	...	3.4	...
4442.34	14.8	9.7	20.8	...	14.0	...
4443.19	9.1	...	...	...	7.6	...
4447.72	10.2	12.8	17.0	...	14.2	...
4454.38	...	...	5.7	...	...	...
4459.12	20.2	...	22.7	...	15.8	...
4461.65	10.9	12.3	18.8	...	18.3	...
4466.55	17.8	15.9	20.5	7.9	15.9	4.5
4482.17	...	...	21.7	...	...	...
4484.22	...	...	...	...	...	...
4485.68	...	...	...	...	...	...
4489.74	...	...	...	...	...	...
4494.56	17.8	13.5	24.6	7.1	19.0	...
4528.61	32.4	29.1	40.3	12.3	34.3	9.0
4531.15	9.2	...	15.0	...	8.8	...
4592.65	3.4	...	...	...	...	...
4602.94	7.7	5.1	12.7	...	...	...
4618.76	...	...	5.1	...	...	...
4619.29	...	...	...	...	...	...

Table A.7. continued.

Wavelength (Å)	BD+24°1676	BD+26°2621	BD+26°3578	CD-33°1173	CD-71°1234	CD-24°17504
4625.05	...	...	...	...	...	...
4637.51	...	...	...	...	...	...
4638.01	...	...	...	...	...	...
4647.43	...	...	...	...	...	...
4678.85	...	...	8.2	...	...	...
4707.28	6.0	...	5.8	...	5.3	...
4736.77	7.0	...	...	...	8.9	...
4789.65	...	...	...	...	...	...
4843.15	...	...	...	...	...	...
FeII						
3824.91	...	...	...	...	...	...
3974.16	...	...	...	...	...	...
4122.66	...	...	...	...	...	...
4178.86	11.9	9.5	16.4	4.3	12.5	...
4233.17	35.1	23.3	40.7	14.2	31.6	7.7
4296.57	...	...	8.4	...	...	...
4303.17	9.2	5.5	12.0	...	...	...
4385.38	7.3	8.1	13.3	...	...	...
4416.82	7.2	6.8	10.8	...	...	...
4489.19	...	...	6.1	...	...	...
4491.40	...	...	5.3	...	4.5	...
4508.28	11.3	...	17.4	...	9.8	...
4515.33	9.0	...	10.4	...	7.1	...
4520.22	9.1	6.1	8.9	...	8.9	...
4522.63	...	...	...	6.2	17.6	6.3
4541.52	...	...	3.7	...	...	...
4555.89	11.3	8.9	...	...	8.0	...
4576.33	...	...	5.5	...	4.9	...
4583.83	29.7	17.0	36.5	12.5	28.9	6.5
4620.51	...	...	4.6	...	...	...
4731.45	...	...	...	...	...	...
4923.92	50.3	...	...	...	...	...

Table A.8. Measured equivalent widths in mÅ for the program stars

Wavelength (Å)	CD-35°14849	G64-12	G64-37	HD74000	HD84937	HD140283	LP635-14	LP815-43
FeI								
3718.41	...	...	...	13.9	...	11.7	...	...
3719.93	140.3	83.9	85.0	...	...	...	126.6	99.9
3724.38	31.3	...	...	33.4	22.4	...	21.5	...
3727.62	97.0	42.4	52.0	...	94.1	110.3	86.0	67.2
3731.37	...	...	...	...	8.2	...	...	...
3733.32	92.9	...	...	...	...	...	...	...
3735.32	20.8	...	...	...	...	...	...	...
3743.36	102.4	38.0	45.8	...	...	...	82.3	56.3
3744.10	...	...	...	19.5	...	16.2	7.4	...
3745.56	121.0	71.0	77.3	146.4	122.6	143.4	111.9	95.9
3745.90	98.4	47.3	56.4	108.2	95.9	114.7	93.2	67.6
3748.26	99.4	63.3	67.5	113.2	...	...	...	78.3
3756.07	...	...	...	5.7	...	...	...	...
3756.94	...	...	...	13.0	12.1	11.4	...	...
3758.23	114.5	68.3	73.4	130.6	114.6	151.5	100.7	86.6
3760.05	...	...	...	34.8	...	32.6	19.1	...
3760.53	...	...	...	...	17.0	23.0	8.9	...
3763.79	106.8	59.0	57.3	110.8	100.9	111.2	95.5	79.3
3765.54	42.9	...	15.2	53.5	44.9	51.2	...	21.5
3767.19	91.9	48.4	52.4	116.0	89.2	139.2	...	64.9
3774.82	...	...	...	...	11.0	...	...	...
3776.46	...	...	...	20.6	13.1	16.6	...	...
3781.19	...	...	...	...	...	5.5	...	...
3786.68	25.6	...	...	38.0	27.4	36.8	16.9	...
3787.88	84.2	41.7	42.7	90.2	...	90.7	69.9	53.9
3789.18	...	...	...	...	7.8	8.9	...	...
3790.09	50.2	...	12.7	53.7	47.0	56.4	28.1	22.3
3795.00	76.7	32.7	40.4	81.4	78.7	97.4	72.6	...
3799.55	75.7	...	...	79.1	81.7	...	...	57.4
3804.01	...	...	...	...	...	4.1	...	...
3805.34	38.1	...	9.3	52.6	39.7	40.8	31.8	...
3806.22	...	...	...	7.7	...	...	...	...
3807.54	24.5	6.1	...	33.8	24.9	34.6	14.1	...
3808.73	...	...	...	22.1	12.4	18.2	...	...
3812.97	89.0	28.2	36.9	...	...	100.7	71.3	57.7
3814.52	...	...	...	...	...	...	...	...
3815.84	112.9	65.3	67.7	125.4	108.8	127.9	97.8	81.1
3816.34	...	...	...	24.7	16.1	24.6	...	...
3820.43	136.6	84.5	85.3	198.2	131.1	172.3	118.4	103.7
3821.18	36.7	...	...	44.3	39.3	37.7	26.4	...
3821.84	...	...	...	...	...	17.9	...	7.9
3824.44	107.8	65.0	65.4	133.7	116.6	131.5	102.3	82.4
3825.88	116.1	70.8	...	143.8	115.4	133.9	102.8	95.7
3827.82	94.0	53.1	54.0	107.9	95.1	105.9	85.6	77.8
3833.31	...	...	...	19.3	...	...	...	...
3834.22	91.5	...	...	...	...	...	...	...
3839.26	23.8	...	...	27.9	18.7	...	...	...
3840.44	89.7	47.0	51.5	96.0	87.3	99.9	87.6	70.2
3841.05	84.0	40.4	47.2	92.2	82.1	90.5	78.2	66.7
3843.26	32.0	...	...	36.4	28.6	30.0	16.3	20.4

8. continued.

Wavelength (Å)	CD-35°14849	G64-12	G64-37	HD74000	HD84937	HD140283	LP635-14	LP815-43
3846.41	9.1	...	...	...	7.1	8.3	...	...
3846.80	24.3	...	...	34.0	29.3	29.4	24.1	17.3
3849.97	76.7	37.3	42.2	90.3	82.8	88.8	72.0	56.7
3850.82	47.7	...	10.2	59.8	49.7	60.2	37.6	20.7
3852.57	23.1	...	...	30.2	22.6	29.3	11.4	...
3856.37	89.7	61.2	71.8	123.9	99.0	107.8	98.8	81.7
3859.21	30.4	...	...	34.3	31.0	37.9	22.5	14.6
3859.91	118.1	83.6	95.3	139.0	125.8	167.1	114.6	100.9
3865.52	75.7	31.9	38.4	83.7	78.4	86.2	69.9	57.3
3867.22	19.4	...	...	25.3	20.6	23.2	14.0	...
3872.50	81.2	35.1	43.1	...	82.9	88.2	67.2	58.6
3876.04	9.8	...	...	11.4	...	...	...	...
3878.02	77.2	35.8	43.3	89.9	83.3	90.5	77.6	58.7
3878.57	...	58.5	60.7	...	...	...	109.6	83.6
3884.36	...	...	...	...	8.2	...	...	6.3
3885.51	...	...	...	20.6	16.1	...	...	...
3886.28	98.4	70.9	71.4	...	100.0	...	114.7	84.1
3887.05	70.9	...	...	...	...	...	...	...
3895.66	85.3	38.6	41.2	102.2	84.3	101.7	79.8	58.3
3897.45	...	...	...	8.6	6.5	...	...	...
3899.71	87.7	49.6	54.8	91.7	89.3	97.8	80.5	...
3902.95	80.6	30.3	35.8	86.6	78.7	84.0	68.1	49.7
3906.48	62.3	22.2	21.4	76.8	62.4	76.4	50.8	32.4
3910.84	...	...	...	7.8	...	...	...	...
3916.73	...	...	...	17.8	11.4	13.7	...	...
3917.18	30.2	...	5.3	37.7	29.5	40.9	20.1	...
3920.26	79.4	40.3	46.5	86.0	83.6	102.7	72.9	60.9
3922.91	85.8	44.8	53.8	95.9	89.1	98.4	81.7	69.3
3925.64	...	...	...	15.7	9.8	14.8	6.7	...
3925.94	...	...	...	21.3	20.4	...	...	...
3927.92	98.9	49.3	59.7	99.7	92.5	106.5	88.0	70.0
3930.30	90.4	51.3	55.6	97.1	92.6	...	87.1	81.6
3937.33	...	...	...	...	...	...	...	...
3940.88	16.2	...	...	21.9	13.6	24.3	10.4	...
3942.44	...	...	...	18.6	10.3	12.8	9.0	...
3946.99	...	...	...	...	7.2	9.6	...	...
3948.10	14.2	...	...	20.1	15.2	15.3	8.9	...
3949.95	19.6	...	4.4	30.0	20.6	29.4	...	...
3955.34	...	...	...	...	4.9	...	...	...
3966.06	22.3	...	...	...	...	...	...	...
3981.77	17.1	...	...	...	...	25.1	14.8	...
3983.96	18.4	...	...	26.3	19.1	24.6	...	...
3995.98	...	...	...	...	6.8	...	...	...
3997.39	31.2	...	...	41.1	31.9	36.5	22.3	16.8
4001.66	...	...	...	8.9	5.1	8.2	...	...
4005.24	71.7	26.9	32.3	84.5	75.3	82.1	63.9	54.9
4009.71	18.5	...	...	30.5	21.6	26.9	13.3	...
4021.87	19.4	...	...	29.6	20.7	24.8	15.7	...
4031.96	...	...	...	...	...	...	...	...
4032.63	...	...	...	...	...	9.5	4.2	...
4040.64	...	...	...	...	...	4.8	...	...

8. continued.

Wavelength (Å)	CD-35°14849	G64-12	G64-37	HD74000	HD84937	HD140283	LP635-14	LP815-43
4044.61	...	...	...	11.1	7.8	9.7	5.3	...
4045.81	114.8	69.9	73.6	177.9	117.4	157.7	102.1	91.4
4062.44	15.8	...	...	20.7	16.0	18.4	9.2	8.4
4063.28	...	...	...	...	...	...	...	...
4063.59	100.6	56.5	61.6	137.1	102.8	108.2	...	75.9
4066.98	13.0	...	...	14.2	11.6	12.2	...	...
4067.27	...	...	...	13.5	7.2	10.2	...	...
4067.98	...	...	2.7	26.1	19.1	17.5	...	...
4070.77	...	...	...	14.1	12.2	9.2	...	...
4071.74	92.9	52.0	59.1	...	95.0	127.0	87.1	73.1
4073.76	...	...	...	11.5	6.7	8.7	...	...
4074.79	...	...	...	11.4	...	...	...	...
4076.63	...	...	...	...	...	...	...	...
4079.84	...	...	...	7.9	4.7	...	...	...
4080.21	...	...	...	...	...	4.4	...	...
4084.49	...	...	...	17.4	11.0	...	5.4	...
4085.00	...	...	...	...	...	10.1	...	5.9
4095.97	...	...	...	11.0	...	8.4	...	...
4107.49	12.4	...	...	22.6	14.8	19.3	...	...
4114.44	...	...	...	11.8	6.7	6.1	...	5.2
4118.54	24.4	...	...	...	41.4	32.2	...	13.2
4120.21	...	...	...	...	4.6	9.1	...	...
4121.80	7.3	...	...	10.2	6.3	7.1	...	...
4126.18	...	...	...	6.0	5.2	5.6	...	...
4132.06	67.7	25.1	27.5	81.1	72.4	83.0	61.6	46.0
4132.90	...	...	...	19.2	...	14.6	8.8	4.6
4134.68	18.5	...	...	30.9	24.1	28.1	17.2	...
4137.00	...	...	...	13.2	8.5	11.7	5.1	...
4143.41	28.5	8.3	5.6	39.0	32.6	33.7	21.9	12.3
4143.87	79.2	34.0	38.0	82.3	77.6	84.7	66.9	53.0
4147.67	14.5	...	...	23.5	17.1	23.5	10.7	...
4152.17	...	...	...	...	...	9.5	...	...
4153.90	...	...	...	25.8	19.9	19.2	...	...
4154.50	17.2	...	...	26.6	22.3	22.2	11.7	...
4154.81	...	...	...	21.5	15.9	15.9	13.8	6.5
4156.80	17.8	...	...	29.5	21.0	24.6	11.7	...
4157.78	...	...	...	20.7	15.3	13.2	8.3	...
4158.79	...	...	...	10.3	...	...	4.2	...
4174.91	9.6	...	...	14.3	8.9	14.7	6.1	4.0
4175.64	14.1	...	...	26.9	18.0	19.9	...	...
4176.57	11.6	...	...	15.0	10.9	11.9	...	...
4177.59	10.6	...	...	...	...	...	...	...
4181.76	32.1	...	5.9	45.5	38.0	39.7	33.4	14.3
4182.38	6.0	...	...	8.4	5.5	...	4.6	...
4184.89	...	...	...	20.6	14.7	17.1	12.6	3.2
4187.04	38.6	6.2	...	52.5	42.8	46.4	31.1	14.2
4187.80	39.7	9.5	8.9	56.1	43.4	50.2	32.5	16.6
4191.43	27.2	5.6	6.8	46.9	33.7	38.8	26.4	12.8
4195.33	...	...	...	21.7	15.3	18.2	...	...
4196.21	...	...	...	10.5	8.1	8.3	5.7	...
4198.31	42.9	...	10.6	64.8	48.3	56.4	38.6	20.5

8. continued.

Wavelength (Å)	CD-35°14849	G64-12	G64-37	HD74000	HD84937	HD140283	LP635-14	LP815-43
4199.09	43.3	9.5	14.3	51.9	48.1	49.0	40.1	22.7
4200.92	...	...	...	6.5	...	5.0	...	...
4202.03	74.7	26.4	31.4	82.4	75.6	83.8	64.3	45.0
4207.13	...	...	...	9.0	...	...	...	...
4210.34	22.9	...	...	38.6	27.7	32.2	20.3	...
4216.18	21.1	...	...	29.1	19.5	39.8	15.2	...
4217.54	...	...	...	14.8	10.8	13.9	8.6	6.6
4219.36	18.9	...	4.2	30.3	20.9	23.5	16.9	...
4222.21	20.5	...	...	32.9	23.7	28.5	21.5	8.7
4224.17	11.2	...	...	16.6	13.3	15.5	8.9	...
4225.45	14.5	...	...	...	12.0	14.5	8.0	...
4227.43	39.5	7.6	9.1	51.2	44.5	45.5	31.1	23.2
4233.60	32.7	...	7.5	49.0	39.5	43.7	28.3	13.5
4235.94	50.2	10.1	14.3	66.1	56.4	61.8	41.8	24.5
4238.02	...	...	...	10.3	7.8	11.9	4.8	...
4238.81	16.5	...	...	26.3	20.4	21.6	12.0	8.5
4282.40	39.3	...	7.5	46.9	38.8	45.7	34.0	20.2
4294.13	72.0	22.0	25.0	...	...	84.2	67.6	43.0
4299.23	...	10.9	13.0	...	...	...	39.6	26.0
4307.90	121.9	57.1	64.7	...	...	...	...	84.4
4325.76	92.5	52.6	56.3	107.0	107.2	116.5	90.7	69.4
4337.05	20.6	...	8.5	33.3	21.3	41.9	...	...
4352.73	16.6	...	...	29.2	...	24.4	11.2	...
4369.77	...	...	...	18.6	13.0	...	8.5	...
4375.93	36.0	...	6.7	47.3	36.4	53.9	25.9	...
4383.54	111.9	72.5	74.5	128.8	109.2	128.4	104.0	84.1
4388.41	5.6	...	...	9.1	6.7	5.9	...	...
4404.75	88.8	50.0	55.4	107.9	96.3	108.8	85.8	64.5
4408.41	...	...	...	16.5	11.2	12.7	...	...
4415.12	71.2	27.6	33.2	87.7	78.3	83.4	65.0	48.5
4427.31	33.8	...	...	47.5	43.7	54.9	26.7	...
4430.61	...	...	...	15.3	10.5	13.2	4.5	...
4433.22	...	...	...	...	4.6	5.7	...	...
4442.34	22.2	...	3.6	33.2	23.2	31.2	18.3	...
4443.19	8.6	...	...	15.7	11.4	9.9	7.1	...
4447.72	18.6	...	...	26.8	19.8	24.0	13.0	7.1
4454.38	7.5	...	...	11.8	...	8.9	...	...
4459.12	26.6	...	...	39.0	26.9	34.0	...	9.8
4461.65	25.8	...	...	34.9	25.5	42.4	16.3	11.0
4466.55	22.4	...	...	32.1	26.7	30.3	16.4	...
4482.17	...	...	...	...	27.8	...	...	...
4484.22	...	...	...	9.5	5.9	6.5	3.8	...
4485.68	...	...	...	3.2	...	...	...	...
4489.74	...	...	...	8.9	4.9	11.6	...	...
4494.56	24.9	4.1	...	38.3	28.5	34.6	17.5	12.0
4528.61	38.2	6.5	9.3	55.7	45.4	51.2	35.0	17.2
4531.15	13.3	...	...	24.8	15.2	22.6	8.6	...
4592.65	...	...	...	14.2	7.7	13.4	5.2	...
4602.94	...	...	3.0	22.5	12.9	21.9	8.6	...
4618.76	...	...	...	...	...	...	...	...
4619.29	...	...	...	5.7	...	...	...	...

8. continued.

Wavelength (Å)	CD-35°14849	G64-12	G64-37	HD74000	HD84937	HD140283	LP635-14	LP815-43
4625.05	...	...	...	2.8	...	3.8	...	...
4637.51	...	...	...	4.5	...	...	...	...
4638.01	...	...	...	6.9	...	...	...	...
4647.43	...	...	...	9.4	4.3	5.0	6.1	...
4678.85	...	...	...	10.1	...	6.9	4.6	...
4707.28	...	...	...	...	...	7.9	...	...
4736.77	11.4	...	...	19.0	13.6	14.6	...	...
4789.65	3.6	...	...	...	...	3.7	...	...
4843.15	...	...	...	...	...	1.4	...	...
FeII								
3824.91	...	...	...	...	4.1	...	...	...
3974.16	...	...	...	3.3	...	...	...	...
4122.66	...	...	...	...	5.8	...	...	...
4178.86	...	...	...	23.5	19.4	17.6	12.1	9.4
4233.17	35.4	6.6	8.6	52.1	50.6	43.2	34.6	21.9
4296.57	...	...	...	11.8	9.1	...	...	...
4303.17	10.0	...	...	14.9	13.3	15.4	8.5	...
4385.38	...	...	...	...	10.4	11.4	8.5	...
4416.82	...	...	...	15.4	13.4	11.8	5.8	3.3
4489.19	...	...	...	...	...	5.7	5.9	...
4491.40	...	...	...	...	8.2	7.2	5.3	2.6
4508.28	11.4	...	...	19.0	17.8	17.2	13.2	5.5
4515.33	...	...	...	16.8	12.8	13.5	7.7	...
4520.22	7.1	...	...	16.7	12.5	12.8	...	6.6
4522.63	...	...	...	32.3	25.9	24.7	16.0	9.9
4541.52	...	...	...	5.4	...	5.1	4.7	...
4555.89	13.4	...	...	21.2	18.1	18.3	8.6	...
4576.33	...	...	...	8.4	6.7	...	...	4.7
4583.83	30.3	4.3	...	45.4	42.5	38.6	27.1	20.8
4620.51	4.3	...	...	...	...	2.9	...	...
4731.45	...	...	...	...	...	5.0	...	...
4923.92	...	13.9	13.7	66.0	...	...	...	...

5. Quality checks and model atmospheres

The following information was not included in the published paper (Chapter 4), but provides more detail on quality checks employed in the study to ensure that the data we used were reliable and checks on the adopted model atmospheres

5.1. Quality checks.

As an extra check on the quality of the input data for WIDTH6, residuals of the individual Fe line abundances were calculated. Lines for which the calculated abundance residual was systematically large for all stars were treated as lines for which the WIDTH6 calculations are possibly inaccurate. This may be due to the input data being imperfect, i.e. the use of poor quality log *gf* values, or lines whose equivalent widths are affected by artefacts such as blends with other large absorption lines and which were measured in only a
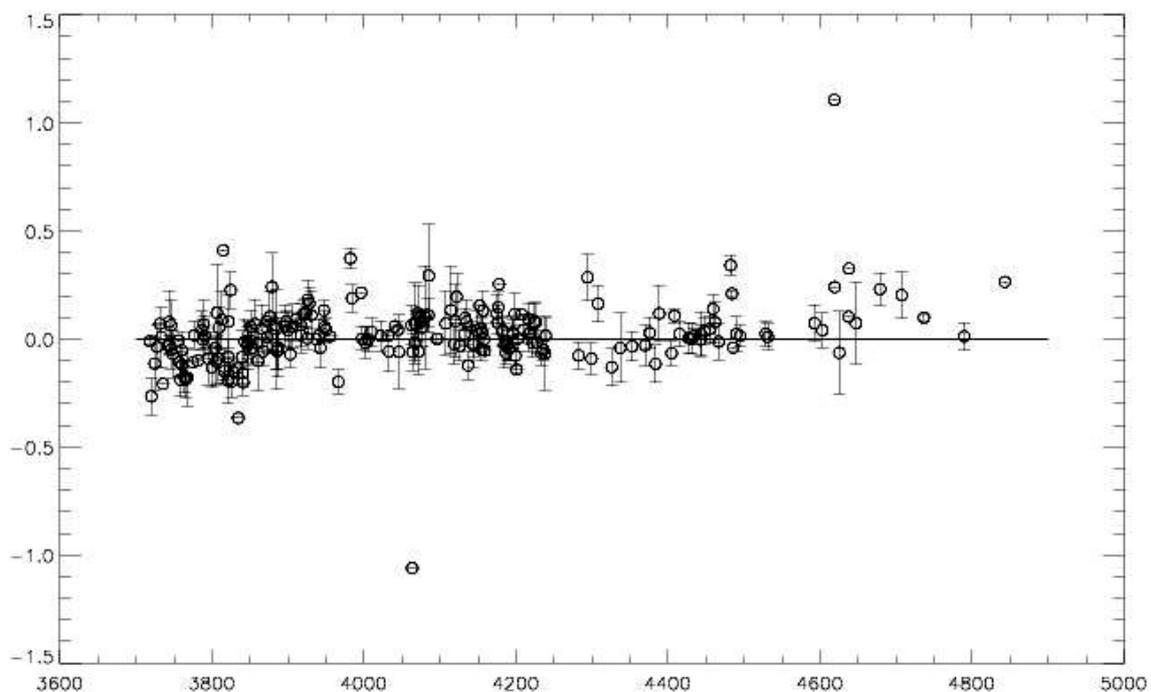
Figure 13 Mean residuals of the abundances calculated for each line in the star over the whole spectral range.

91

few stars.

Figure 13 is an initial plot of the mean value of the residuals for all stars for each line. The error bars are the standard deviations of the residuals for each line for the n stars in which the line was measured. From this we can already identify two very suspect results, the outlier above 1.0 dex and the one below -1.0 dex. To be able to see more clearly whether a line's residual is systematically large for all, or most, of the stars it was measured in, we plotted 200 Å sections of the spectral range. Figure 14 is a plot of the first 200 Å of the spectral range of the data. Here the filled circles are the mean residual for each line and the crosses are the individual residuals from each star. We can see in Figure 14 that at roughly 3719 Å there is a line where measurements from 11 different stars are all systematically lower than the mean by roughly 0.1 – 0.4 dex. This is a sign that the input data may be incorrect. Errors due to imperfect measurements of equivalent widths and limited S/N along with the use of imperfect model atmospheres and atmospheric parameters cause the spread in star to star measurements.

As a first step towards rejecting unreliable data, all lines with a mean residual above 0.3 dex and below -0.3 dex were inspected. This cut led to seven possible bad lines being identified. For each line several checks were made. These included:

- Checking the measurement log. Here we could see if any notes have been made as to whether the line measured was judged to be suspect, i.e. lie in the wing of a large absorption feature leading to a bad judgement of continuum level.
- Going back to the spectra and looking at the actual line. In some cases with very weak lines, noise can affect the width. Therefore a second look at the line can allow confirmation of whether the line is actually suitable for further calculations.

- Finding the source of the log *gf* value. If the log *gf* used is from a very old source it may be that it is inaccurate, e.g. if the method used to determine the value was inadequate or errors are large. More up to date log *gf*'s may be needed.

- Checking the NIST database to confirm whether any other line may be present in the same region as the Fe I line thus causing a broadening of the line.

After these checks, six of the initial seven lines flagged where removed. A second series of checks was made on those lines that have mean residuals that lie between 0.25 and 0.3 dex and those with a mean residual between -0.25 and -0.3 dex. This cut identified five possibly bad lines. After the checks were completed, three of these five lines where removed. The residuals were then scrutinised one more time by checking lines whose mean lies between 0.2 to 0.25 dex, and -0.2 to -0.25 dex. For this section five of nine lines where removed.

In total 22 lines were flagged as being possibly systematically unsatisfactory. These lines went through the several checks set out above and 14 of them were removed from the
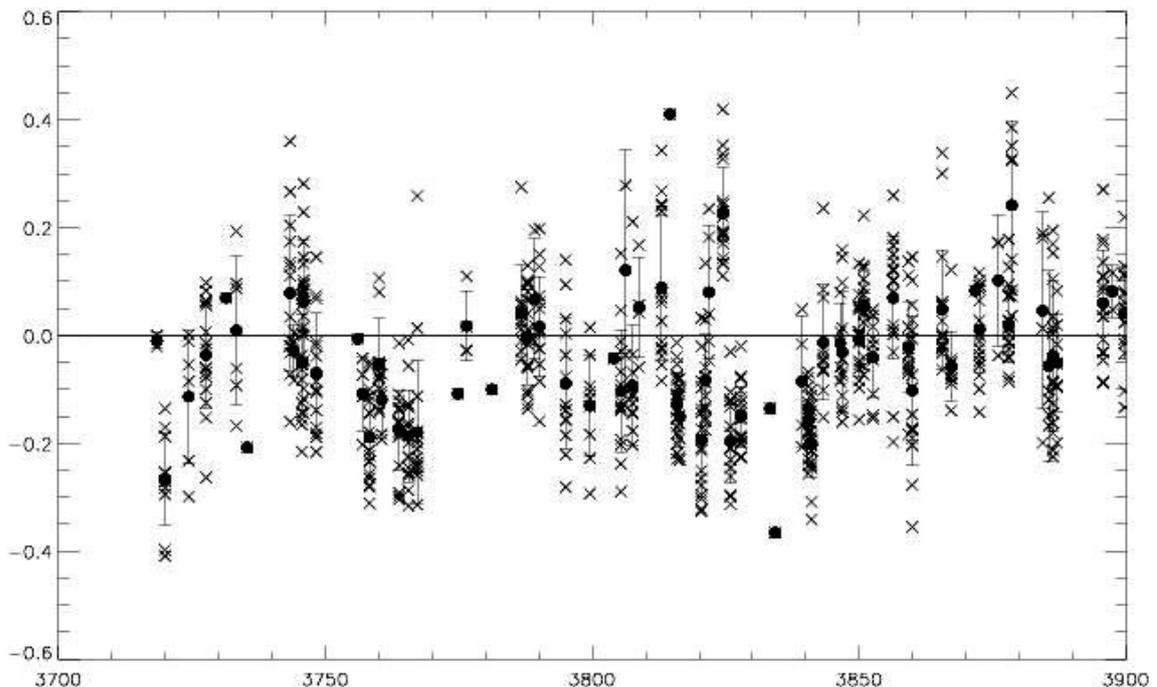
Figure 14 A 200 Å section of the spectral range showing the mean line residual (filled circles) and the individual line residuals (crosses) from each star.

input data for WIDTH6. These lines were also removed from my line list and were not used in the analysis of Paper I.

Figure 15 is a plot of the final mean abundance residuals and standard deviation for each line. It can be seen that there are three lines whose mean residuals are still relatively large, > 0.3 dex. However, there was no obvious reason for discarding them other than the large residuals, and they therefore remain in our analysis. The vast majority of lines that remain have a mean residual between 0.2 dex and -0.2 dex.
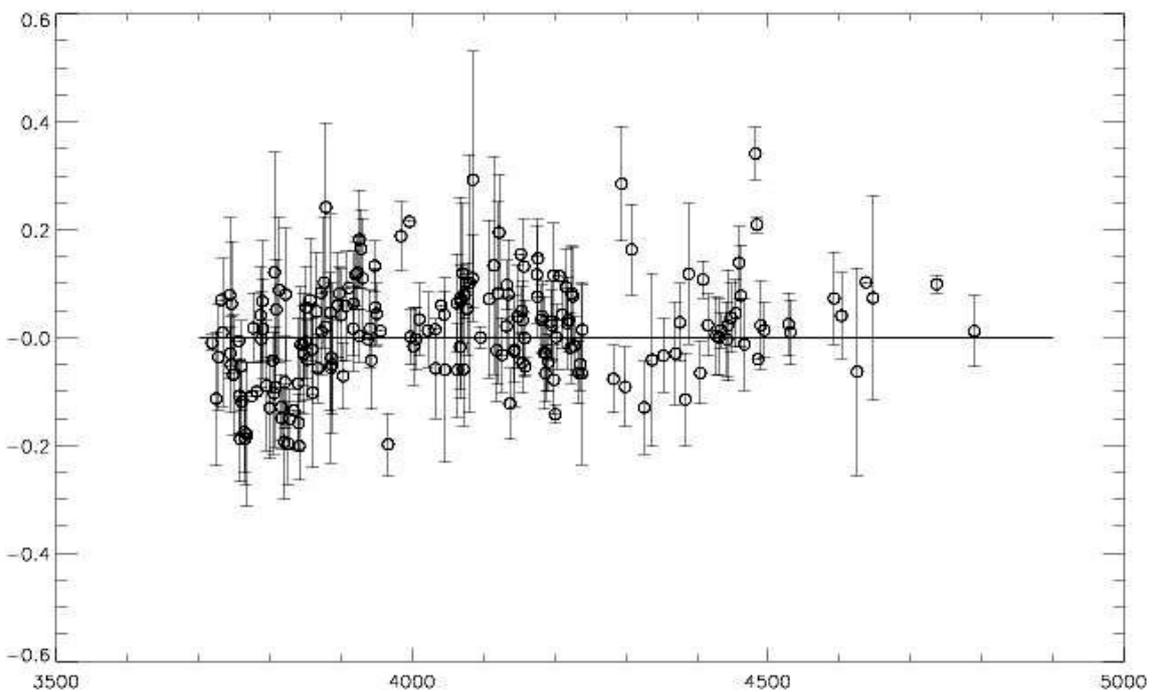
Figure 15 Final plot of mean residuals (open circles) after bad lines have been removed.

5.2. Model atmospheres

In this work two types of model atmospheres are used. In the LTE analysis the Kurucz 06 models are adopted and used with WIDTH6, however, in the NLTE analysis MARCS models are used with MULTI to calculate NLTE corrections to the abundances, whilst

Kurucz models are then used with WIDTH6 to calculate new effective temperatures. It is wise to check that these model atmospheres provide a reliable temperature profile throughout the atmosphere and also that swapping between the atmospheres does not induce large errors in the analysis.

5.2.1. The temperature structure

One way that has been suggested for testing the temperature structure of the atmospheres is through plots of χ of the lower level of a transition versus abundance of each line. If in these plots a group of lines do not give the abundances that the rest of the lines give, then there is a good chance that the model has not produced a reliable temperature profile. An example of such a plot is given in Figure 7 of Chapter 4. Figure 16 gives a sample of these plots for different stars. Table 7 presents the parameters used in the creation of these

Table 7. Parameters used to create χ versus abundance plots from Kurucz model atmospheres.

Star	T_{eff}(K)	log g	[Fe/H]	ξ (Km/s)
HD74000	6070	4.03	-2.20	1.2
HD84937	6168	3.98	-2.35	1.3
HD140283	5769	3.73	-2.54	1.5

plots. It is seen that all the lines are grouped around the mean with only random scatter, as shown by the line of best fit, and there are no trends in the data that may indicate an inaccurate atmosphere that does not represent the star. This *may* lead me to believe that the atmospheres do indeed produce a sensible and reliable temperature gradient that does not have any spurious values for levels within it, and that it is representative of the star. *However*, several parameters are hidden within these plots, i.e. T_{eff}, log g, and microturbulence. These parameters are manipulated in such a way as to reduce trends in the data so that T_{eff} can be deduced. Therefore I would not choose to use these plots as a strong indicator of the realism
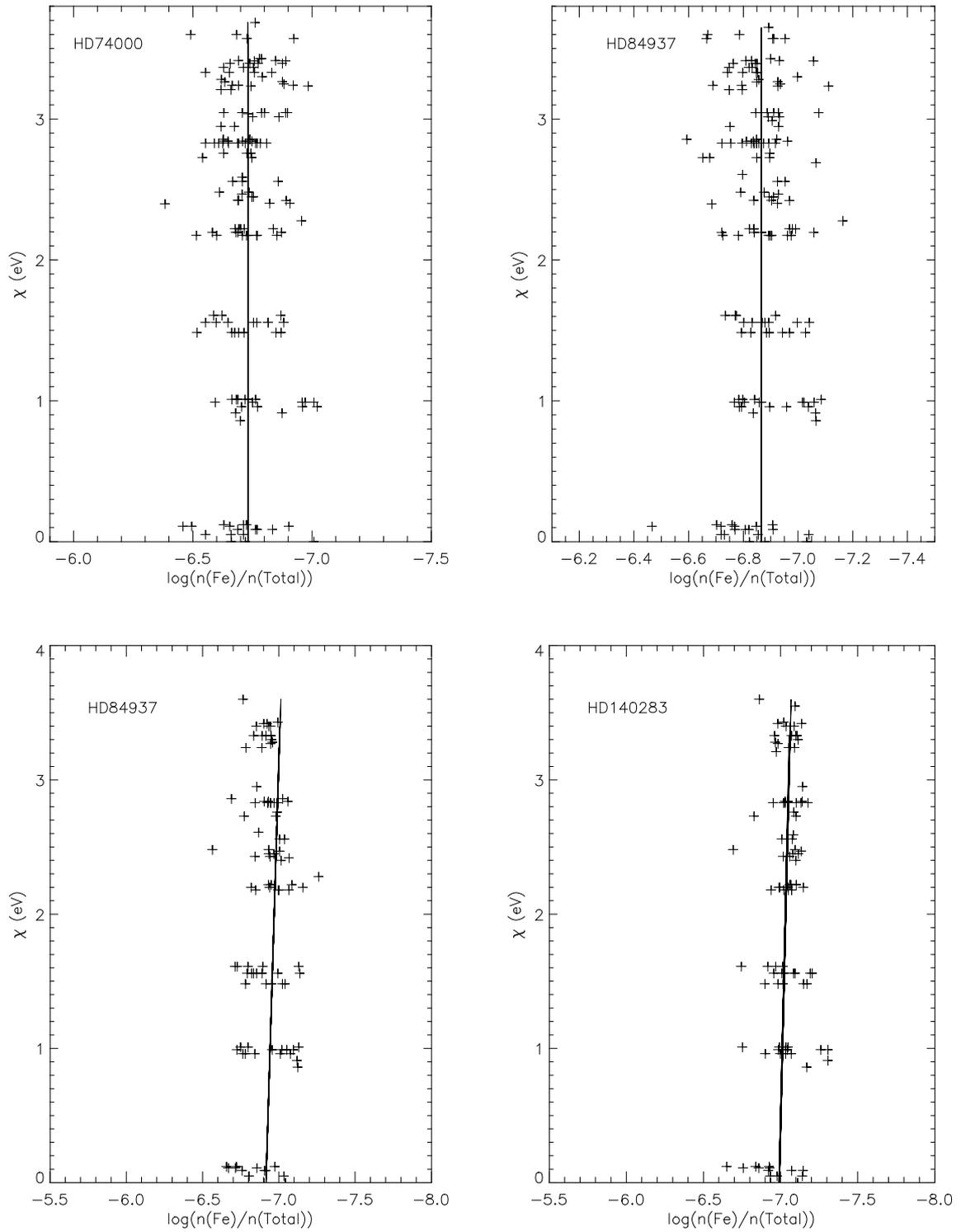
Figure 16. Examples of χ versus abundance plots from adopting Kurucz models (top panels) and MARCS models (bottom panels).

96

of the atmosphere.

A much better indicator of the accuracy of the atmospheres would be to plot A(Fe) versus the log τ_{5000} value at which the line optical depth $\tau_v = 2/3$. This is the characteristic depth of the formation of the line. This plot would give a view of abundance variations through different levels of the atmosphere, and if any trends appeared in this plot it would raise concerns that the atmosphere did not accurately model the star. Figure 17 presents such a plot for HD140283 abundances produced using MARCS models. The slope on the line of best fit has the value 0.012 ± 0.010 (1σ error) indicating there is no trend. It can therefore be concluded that these atmospheres are reliable and it is safe to proceed with their use. As will be shown below, the MARCS and the Kurucz models are very similar, and one can assume that the Kurucz models will exhibit the same behaviour.

5.2.2. Kurucz versus MARCS

In the following chapters of this thesis I study the effects of NLTE on the effective temperature scale, and thus on the Li problem. For this I adopt the code MULTI which uses the MARCS models. Using abundance corrections obtained through this code I then revert back to using WIDTH6 to constrain the temperature. WIDTH6 uses the Kurucz models, as discussed above. Therefore a comparison of the models is carried out to confirm that the switching between models does not introduce unforeseen errors during the process. The two atmospheres must therefore have a comparable T-τ profile. Figure 18 shows this comparison. In these plots the three dashed lines represent the Kurucz models for effective temperatures of 5869 K (top line), 5769 K (middle line) and 5669 K (bottom line). The solid line is the MARCS model for $T_{\mathrm{eff}} = 5769$ K. It is seen that indeed the MARCS and the same T_{eff} Kurucz model are extremely similar. The other parameters are kept the same, i.e. log $g = $ 3.73, [Fe/H] = -2.54 and $\xi = 1.5$ km s^{-1} for each of the atmospheres. The vertical dotted line
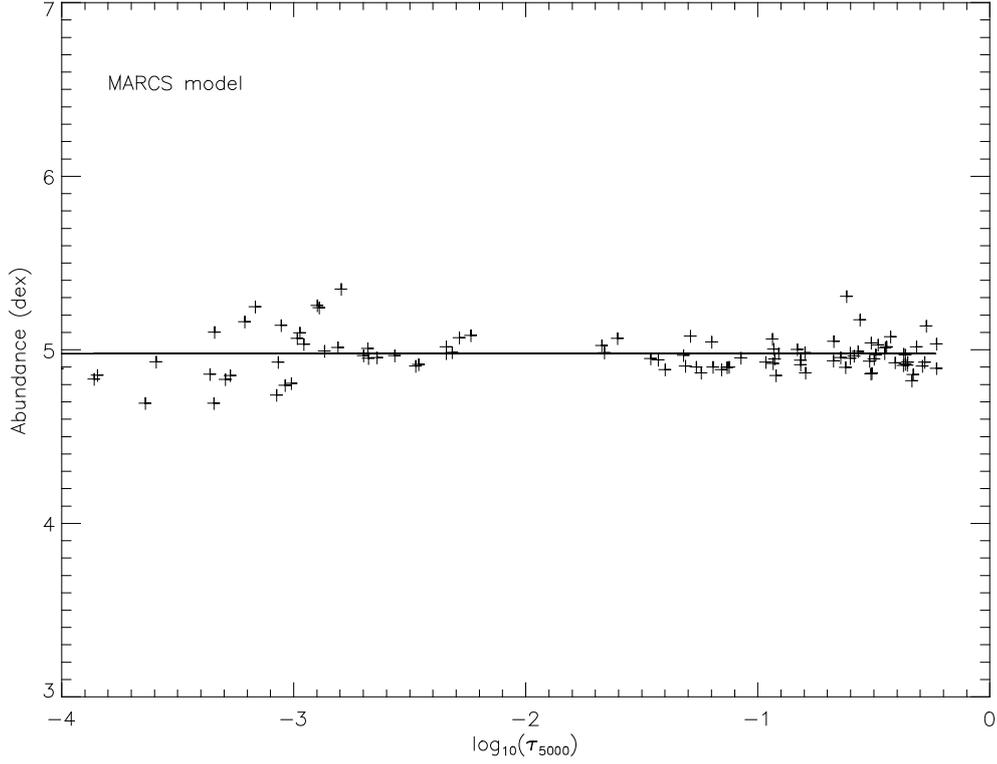
Figure 17. Plot of log τ_{5000} versus abundance for results from HD140283 produced from MULTI using the MARCS models with parameters 5769/3.73/-2.54/1.5 for T_{eff}/log g/[Fe/H]/ξ respectively.

represents the point at which log τ_{5000} = 2/3, the line forming region. In Table 8 I present the temperatures of the Kurucz and MARCS models for several values of log τ_{5000}, including log τ_{5000} = -0.18 (τ_{5000} = 2/3) at which it is expected that $T \approx T_{\text{eff}}$. These depths sample the region of the atmosphere in which much of the line and continuum forming occurs. It can be seen that, over the region -2 < log τ_{5000} < -1, indeed the two atmospheres are very similar in their values, with a mean difference of 12 K. The value $T(\tau_{5000} = 2/3)$ is also roughly that of T_{eff}, which offers a consistency check that the atmospheres are representative of the star. Recall from Chapter 4 that the typical uncertainties in the T_{χ} method are ~ 100 K, I am therefore confident that switching between the two models within my analysis is acceptable and will not induce unforeseen errors into the work

98

As an extra step to check the consistency of switching between the different atmospheres, and also radiative transfer codes, I have checked the LTE abundances produced for the measured lines for both codes. From this I get a standard deviation between the difference (A(MULTI-LTE)-A(WIDTH6)) of 0.065 dex and a mean difference of -0.048 dex for the star HD84937, using the parameters in Table 7. This shows that indeed the two models, and the codes, are comparable in their results. This result is also confirmed by comparing the top right panel and bottom left panel of Figure 16. These are the χ versus abundance plots for HD84937 produced from WIDTH6 and MULTI respectively. It is therefore acceptable to proceed with the NLTE analysis using the methods described in the next few chapters.

Table 8. Temperatures for Kurucz and MARCS models for a T_{eff} = 5769K, log g = 3.73 dex, [Fe/H] = -2.54 and ξ = 1.5 km/s, and the difference between the two temperatures for several log τ_{5000} values across the region in which lines and continuum are formed.

Model	log τ_{5000}				
	-2	-1.5	-1	-0.5	-0.18
Kurucz	4724 K	4807 K	4982 K	5361 K	5831 K
MARCS	4715 K	4793 K	4970 K	5348 K	5796 K
Kurucz - MARCS	9 K	14 K	12 K	13 K	35 K
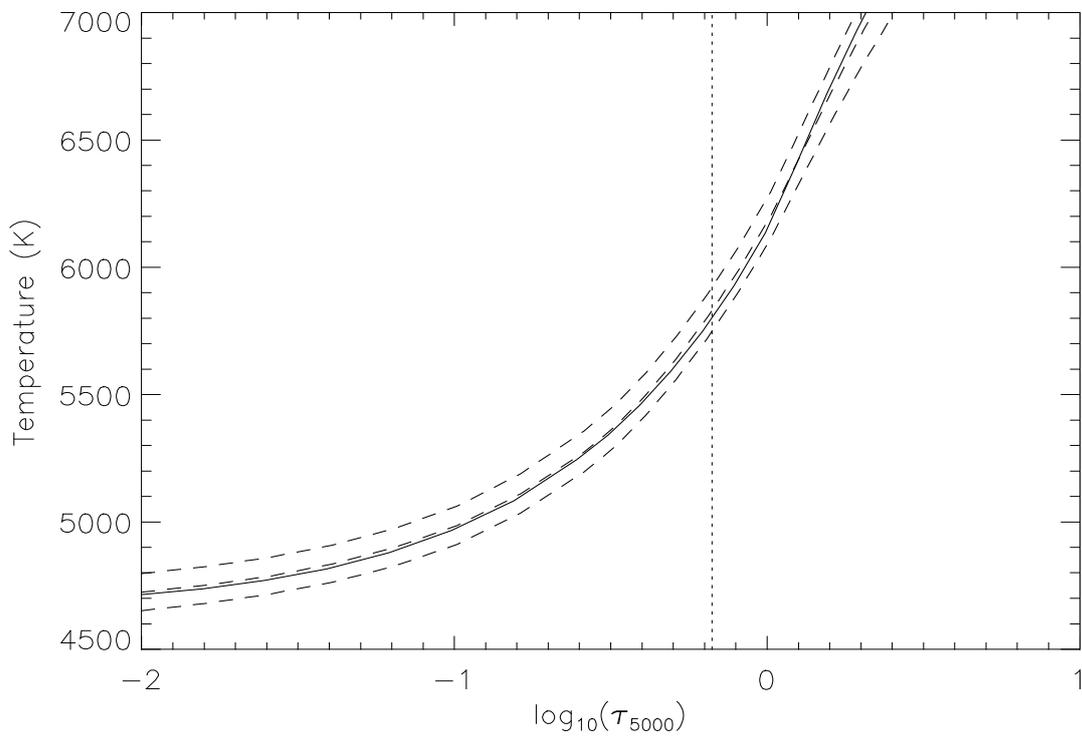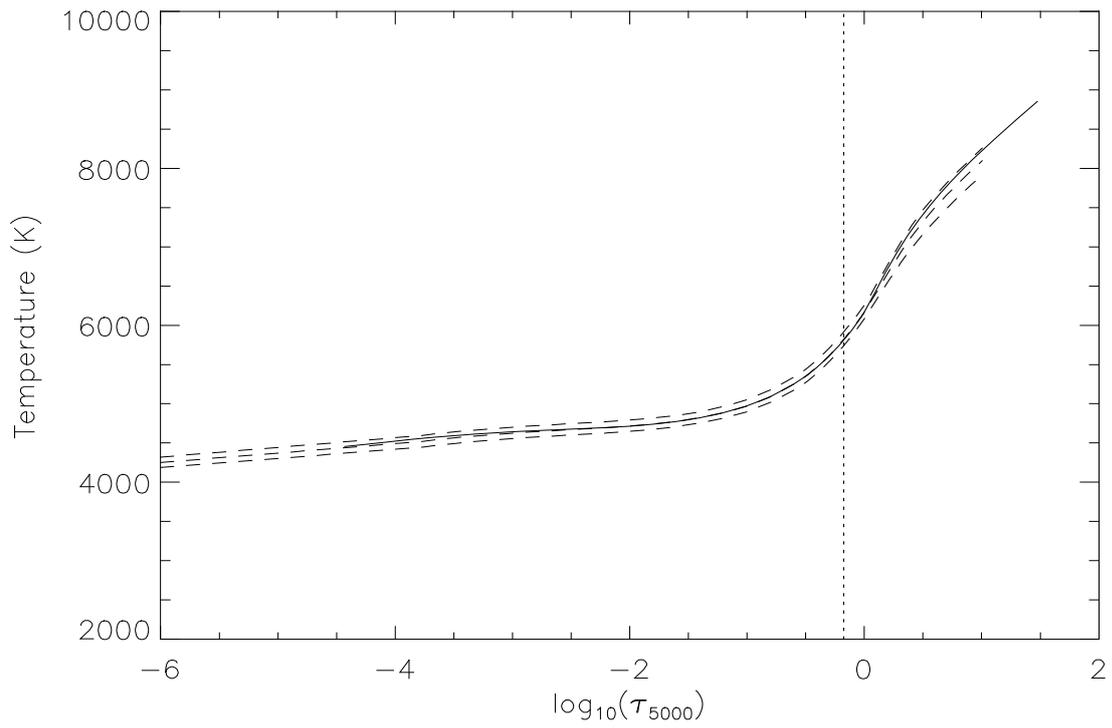
Figure 18 Comparison between Kurucz and MARCS model atmosphere. Dashed lines represent Kurucz models with T_{eff} of 5669 K (bottom line), 5769 K (middle line) and 5869 K (top line). Solid line represents the MARCS model with a T_{eff} of 5769 K. Vertical dotted line shows the point at which $\tau = 2/3$. Bottom panel is a zoomed-in section of the top panel showing the line forming region.

6. Radiative Transfer: LTE vs. NLTE

Many previous studies of the chemical composition of stellar atmospheres have used the simplifying assumption of local thermodynamic equilibrium (LTE) in their calculations (Spite & Spite 1982, Ryan et al. 1996/1999, Arnone et al. 2005, Asplund et al. 2006). However, in many cases this assumption becomes invalid (Thévenin & Idiart 1999, Gratton et al. 1999), and results calculated using it incorrect. A more sophisticated description of the radiative transfer, and line formation, through stellar atmospheres is therefore needed. One improvement in the description of radiation transfer through stellar atmospheres is non-local thermodynamic equilibrium (NLTE) (Rutten 1990, Bruls et al. 1992, Korn 2008). In combination with the improvements in radiative transfer theory there are more sophisticated methods of modelling the stellar atmospheres. 3D hydrodynamic atmospheres are now becoming more widely used (Asplund et al. 1999, Asplund & García Pérez 2001). These allow for a better representation of the temperature and density profiles through an atmosphere. The combination of using NLTE radiative transfer and 3D stellar atmosphere models should in principle allow for a better representation of the physics involved in the formation of spectral lines. In this work however, I look only at the NLTE aspect of line formation since this is highly likely to impact on the temperature calculations using the excitation technique.

A first step is to understand the assumptions of LTE and their limitations. This chapter aims to present the method of LTE line formation, and to show where these assumptions break down, principally due to the presence of an intense radiation field within shallower, line forming layers of stellar atmospheres. This field has a strong effect on the matter through radiative excitations and photoionizations, and their opposite processes. Following this, to determine the population values we must adopt the equations of statistical

equilibrium, i.e. NLTE line formation. Here it will be shown that the radiation field and the state of the gas are intrinsically linked and a method that simultaneously solves the radiative transfer equations and the statistical equilibrium equations is needed.

6.1. LTE

LTE makes assumptions to simplify the modelling of stellar atmospheres. We assume that the matter is in equilibrium with the ambient kinetic temperature, and that the state of this matter can be determined by two thermodynamic variables: the absolute temperature (T) and the total particle density (N). This means that we can use well known equations to determine the properties of both the matter and the radiation field.

The following equations make up the basics of LTE radiative transfer and can be found in many books on the subject, e.g. Milhalas (1978) and Gray (2005) which are both used here. A first step is to calculate the distribution of atoms over different bound levels for which we can use the Boltzmann equation. This states that for a given excitation energy of level i and ionization state j, $\chi_{i,j}$, with statistical weight $g_{i,j}$ and for a temperature T the population of any level, $n_{i,j}$, is

$$\left(\frac{n_{i,j}}{n_{0,j}}\right) = \frac{g_{i,j}}{g_{0,j}} \exp\left(-\chi_{i,j}/kT\right) \tag{6.1}$$

where $i = 0$ is the ground state. It is usual when calculating synthetic profiles that the population distribution relative to the total population, N_j, is wanted. This is given by

$$\left(\frac{n_{i,j}}{N_j}\right) = \frac{g_{i,j}}{U_j} \exp\left(-\chi_{i,j}/kT\right) \tag{6.2}$$

where $N_j = \sum_i n_{i,j}$ and U_j is the partition function, given by $U_j \equiv \sum_i g_{i,j}\exp\left(-\chi_{i,j}/kT\right)$, of the ionization state j.

The determination of the relative numbers of atoms in different ionization stages is done using the Saha equation. There are two version of this equation, one for the ground level

$$\left(\frac{n_{0,j+1}}{n_{0,j}}\right) N_e = \frac{2g_{0,j+1}}{g_{0,j}} \left(\frac{2\pi m_e kT}{h^2}\right)^{\frac{3}{2}} \exp\left(-I_j/kT\right) \qquad (6.3)$$

where N_e is the electron density, m_e is the electron mass and I_j is the energy needed to ionise an electron from ionisation state j, and one comparing the total numbers of atoms in two successive ionization states

$$\left(\frac{N_{j+1}}{N_j}\right) N_e = \frac{2U_{j+1}}{U_j} \left(\frac{2\pi m_e kT}{h^2}\right)^{\frac{3}{2}} \exp\left(-I_j/kT\right) \qquad (6.4)$$

Combined, the Boltzmann and Saha equations provide the distribution of electrons within the different ionization stages of a particular element, known as the Saha-Boltzmann distribution. In order to calculate the particle densities in a specific state, e.g. the number of electrons in a given level for a given temperature etc., for an arbitrary gas in LTE we must also ensure charge and particle conservation. These level populations are then used to calculate the line opacity which in turn dictates the amount of flux absorbed by a particular species and dictates the shape of the emergent profile.

In order to calculate the emergent flux the state of the radiation field needs to be known. This is approximated by the local Planck function:

$$B_\nu(T) = \frac{2h\nu^3}{c^2} \frac{1}{\exp(h\nu/kT) - 1} \qquad (6.5)$$

This is determined by Kirchhoff's laws for radiation which states that "the intensity in a medium in thermodynamic equilibrium is isotropic, and at each frequency depends only on the local temperature".

A quantity used within radiative transfer is the source function. This is the ratio of emission to absorption such that $S_\nu = j_\nu / \alpha_\nu$, where j_ν and α_ν are the emission and absorption coefficients respectively. It represents the change in intensity per unit path along a beam. Kirchhoff also found that S_ν is equal to B_ν everywhere in thermodynamic equilibrium, which simplifies calculations of intensity, or flux, considerably.

With the above equations in hand, knowledge of the continuum opacity is the final aspect that is needed to produce a profile for a given line. The continuum opacity is the sum of several different physical processes; photoionization due to bound-free processes, absorption due to free-free transitions and the effects of absorption from bound-bound transitions, i.e. spectral lines. In most cases the bound-bound transitions are not included in the continuum opacity; however, if there are many lines closely packed together they can act like a continuum opacity. This opacity is dominated by different elements depending on the type of star. In most cases it is due to hydrogen, as this is the most abundant element. In the program stars for this work it is H^- that dominates the continuum opacity.

The spectral line profiles that are formed follow a Voigt function with all the processes of broadening, e.g. thermal and collisional, accounted for within it. With a profile calculated for a given abundance, an equivalent width can be calculated, where the equivalent width is the value for the width of a rectangular line profile that blocks the same amount of spectrum completely, such that

$$W_\lambda \equiv \int \frac{F_c - F(\lambda)}{F_c} \, d\lambda \qquad (6.6)$$

where F_c and $F(\lambda)$ are the continuum and line flux respectively. This allows for a curve of growth for each line to be created. The curve of growth gives a direct relationship between the equivalent width of a spectral line and the abundance of the element. This then allows for the determination of the abundance from the measured equivalent width of the spectral line.

6.2. Beyond LTE

However, if we examine more closely the assumptions of LTE we can see that it lacks the sophistication to deal with the processes that occur in stellar atmospheres. For LTE to hold, the rates of processes within the gas have to be balanced by their opposites. In this case these processes are ones that cause transitions of electrons from one state to another, whether bound or free. There are broadly two groups of process, radiative and collisional. If there is not a balance of the rates within either of these groups then there will be a departure from LTE; in equilibrium all excitations must be balanced by deexcitations, but only overall, not necessarily process by process, e.g. collisional de-excitation and collisional excitation.

For radiative processes to be in equilibrium the radiation field must be in a Planckian form, i.e. $I_\nu = B_\nu(T)$. In the deepest layers of the stellar atmosphere, where densities are high, collisional rates are very large. This leads to high optical depths trapping photons, and creating a blackbody situation. Here the radiation field is therefore Planckian, and LTE does hold as photons become thermalized. This is seen in the calculations presented later (Chapter 7), and in fact LTE holds at $\tau_{5000} \geq 1$. In the outer atmosphere, however, this is not the case. The radiation field is by no means local or isotropic in nature, especially near the boundary of the star were photons freely escape into space. As the distance from the radiation source becomes greater the energy density of the radiation field becomes reduced and conditions for

equilibrium are far from met. Along with this the radiation field has a non-Planckian frequency distribution. At certain frequencies the material can be far more opaque. Therefore, over the frequency range of a line, the radiation field can come from vastly different depths in the atmosphere, opposed to assuming it is represented by S_ν at $\tau_\nu \approx 1$ as in the Eddington-Barbier approximation. This will also mean that the radiation field across a spectral line can be representative of vastly different temperatures. We see therefore that in the case of radiation, conditions of equilibrium are not fulfilled.

For there to be equilibrium in the case of collisions, it is required that the velocity distribution is Maxwellian. If this is the case then the local temperature can be defined as the kinetic temperature of the electrons, as in most cases it is collisions with electrons that are of most importance due to their large abundance. Comparison of the elastic, which move the material towards LTE, and inelastic collisional rates gives the result elastic/inelastic ~ 10^3 (Mihalas 1978). As elastic collisions don't vastly affect equilibrium it can be concluded that a Maxwellian distribution holds for electrons. In some types of stars collisions from atoms and ions can be of importance too. This is the case with metal-poor stars, as will be demonstrated in Chapter 7 & 8. It is acceptable to conclude that the same conditions as for electrons hold for atoms and ions due to the similarity in kinetic temperature of all three (Bhatangar et al. 1955). Therefore, for both electrons and atoms, collisions will tend to drive the system towards LTE. Whether collisional or radiative rates dominate will determine whether the system is in LTE or not.

Through studying the rates of collisional and radiative transitions that affect ionization and excitation equilibrium, i.e. photoionization and collisional ionization against radiative recombination and three-body collisional recombination, it is possible to see through calculations that in the outer atmosphere ($\tau_{5000} < 1$), the radiative rates dominate. It is therefore safe to assume that, due to the non-equilibrium state of the radiation field, that

LTE is not valid in these processes. A more sophisticated process is needed to accurately describe the radiative transfer through many types of stellar atmospheres. That process is non-local thermodynamic equilibrium (NLTE).

6.3. NLTE

6.3.1. Statistical Equilibrium Equations

NLTE gives us a framework with which to describe more accurately the process of radiation transfer in stellar atmospheres. To construct equations for NLTE we invoke statistical equilibrium. This implies that there is a static situation, and that the radiation fields and level populations are independent of time. The assumption of complete redistribution is used in most calculations i.e. photons entering the line are redistributed to other frequencies across the line, e.g. photons entering the line at line centre are redistributed, through scattering etc., to the line wings or visa-versa. This assumption allows for the simplification of calculations, and produces profiles that match observed ones with a good degree of accuracy. However, for a more complete solution partial redistribution should be used, though this leads to a more complicated situation.

The basic equation for calculating level populations is easily derived, and can be found in many textbooks e.g. Mihalas (1978). Consider a volume element moving in a medium. To calculate the number of electrons in a level i, n_i, we look at the net flux passing through that volume element and the net rate at which electrons from other levels, j, are brought into level i due to radiative and collisional transitions. This implies that:

$$\left(\frac{\partial n_i}{\partial t}\right) = -\nabla \cdot (n_i \boldsymbol{v}) + \sum_{j \neq i} \left(n_j P_{j,i} - n_i P_{i,j}\right) \tag{6.7}$$

where $P_{i,j}$ and $P_{j,i}$ denote the total rate from level i to j and j to i respectively. This equation is suitable for both bound-bound and bound-free transitions. The first term on the right hand side can be shown to be the net flux of particles streaming in and out of the volume by use of the divergence theorem. This states that if there is no creation or destruction of matter, the density within a region can only be changed by having a flow into or away from the region through a boundary. This means that a continuity equation, which equates the net flux with a loss or gain of material, can be given for a species. Summing over an entire species gives $N_k = \sum_i n_{i,k}$, where the subscript k is the species, thus the continuity equation is:

$$\left(\frac{\partial N_k}{\partial t}\right) + \nabla \cdot (N_k \boldsymbol{v}) = 0 \qquad (6.8)$$

We see that the first term is indeed the net flux and if no other processes remove or replace particles the density will be due to this flux. The summation in Eq. (6.7) gives the sum of the processes that add or remove electrons in the level i. In a steady state, i.e. $\partial n_i / \partial t = 0$, the equation reduces to:

$$n_i \sum_{j \neq i} P_{i,j} - \sum_{j \neq i} n_j P_{j,i} = -\nabla \cdot (n_i \boldsymbol{v}) \qquad (6.9)$$

For a static atmosphere, i.e. $\nabla \cdot (n_i \boldsymbol{v}) = 0$, this further simplifies to:

$$\left(\frac{\partial n_i}{\partial t}\right) = n_i \sum_{j \neq i} P_{i,j} - \sum_{j \neq i} n_j P_{j,i} = 0 \qquad (6.10)$$

This is the equation of statistical equilibrium which allows us to calculate the level population of a given level i.

In Eq. (6.10) $P_{i,j}$ gives the transition rate from level i to j and is given by:

$$P_{i,j} = A_{i,j} + B_{i,j}\bar{J_v} + C_{i,j} \tag{6.11}$$

where $A_{i,j}$, $B_{i,j}$, and $C_{i,j}$ are the Einstein coefficients for spontaneous, induced and collisional transitions, and $\bar{J_v}$ is the frequency-averaged, angle-averaged radiative field. It is now clearly seen that the level populations depend on the state of the radiation field via $\bar{J_v}$, and thus both n_i and $\bar{J_v}$ have to be solved for simultaneously. As can be seen in Eq. (6.11), $P_{i,j}$ contains both radiative $(A_{i,j}, B_{i,j})$ and collisional $(C_{i,j})$ terms, which can be written in terms of either Einstein transition probabilities or energy-absorption cross-sections. In terms of energy-absorption cross-sections the rates are given by:

for upward radiative rates:

$$R_{i,j} = 4\pi \int_{v_0}^{\infty} \alpha_{i,j}(v)(hv)^{-1}J_v dv \tag{6.12}$$

where $\alpha_{i,j}$ is the absorption cross-section for a given frequency, v, h is the Planck constant, v_0 is the line centre frequency and J_v the mean intensity per unit frequency interval at frequency v;

for downward radiative rates:

$$R_{j,i} = 4\pi \int_{v_0}^{\infty} \alpha_{i,j}(v)(hv)^{-1}\left[\left(\frac{2hv^3}{c^2}\right) + J_v\right] exp(-hv/kT)dv \tag{6.13}$$

To obtain the radiative rates per cm^3 the above are multiplied by the particle density, i.e. n_i for $i \rightarrow j$ transitions and n_j for $j \rightarrow i$ transitions. These general expressions for the radiative rates reduce to:

$$R_{ij} = \begin{cases} A_{ij} + B_{ij}\bar{J}_{ij}, & \text{if } i > j; \\ B_{ij}\bar{J}_{ij}, & \text{if } i < j. \end{cases} \tag{6.14}$$

It is then possible to see how these equations fit into the total transition rate, Eq. (6.11).

For the upward collisional rate:

$$n_i C_{i,j} = n_i n_e \int_{v_0}^{\infty} \sigma_{i,j}(v) v \, dv \equiv n_i n_j q_{ij}(T) \tag{6.15}$$

where v_0 is the velocity corresponding to the threshold energy E_0, such that $E_0 = 1/2 \, m_e v_0^2$ where E_0 is the minimum energy needed to excite an electron, $\sigma_{i,j}(v)$ is the collisional cross-section for transitions from level i to j for a given velocity, v, and $q_{ij}(T)$ is the collision rate for i to j transitions per atom in state i per electron, averaged over Maxwellian velocity distribution at temperature T. The downward rate can be found using the detailed balance arguments, i.e. if there is detailed balance then the upward rate will be equal to the downward rate. This is the case if the velocity distribution of the electrons is in an equilibrium, Maxwellian, form so that:

$$n_i^* C_{i,j} \equiv n_j^* C_{j,i} \tag{6.16}$$

where the asterisk denotes LTE values. This then implies that the downward collision rate is:

$$n_j C_{j,i} = n_j \left(n_i / n_j \right)^* C_{i,j} = n_j \left(n_i / n_j \right)^* n_e q_{i,j}(T) \tag{6.17}$$

In practice we are interested in rates for given cross sections, which are found either experimentally or via quantum-mechanical calculations. This means that the value of $q_{i,j}(T)$ is of importance as it is present in upward and downward rates. Cross sections are usually measured in terms of Bohr radius i.e. $\sigma_{ij} = \pi a_0^2 Q_{ij}$. Then substituting the Maxwellian velocity distribution into Eq. (6.15) we find that:

$$q_{ij}(T) = C_0 T^{1/2} \int_{u_0}^{\infty} Q_{ij}(ukT)\, ue^{-u} du \qquad (6.18)$$

where $u \equiv E/kT$, $C_0 = \pi a_0^2 (8k/m\pi)^{1/2} = 5.5 \times 10^{-11}$ and $u_0 = E_0/kT$. The task is then to find the value of Q_{ij} or equivalently σ_{ij}. Finding reliable values for this can be very difficult and approximations are often used. This is one limitation of radiative transfer calculations; in many cases theoretical approximations for collisional cross sections are used, thus limiting the accuracy of the solutions of the radiative transfer problem. This is the case for heavier elements and transitions arising from excited states.

The above equations are the basic equations for the transition rates. Further manipulation is required depending on whether the transitions are bound-bound or bound-free. This is the case for both radiative and collisional rates. Here my intention is to show the complexities of the NLTE process versus the LTE process, i.e. the link between level populations and the radiation field J_ν.

These rate equations can be combined into a complete rate equation, one of which can be written for each bound state. With this set of rate equations there is still one more variable, the ion density n_K. A further equation is therefore needed to close the system. This can be done by either demanding that the total number of atoms and ions equals the correct fraction of the total number of hydrogen atoms, which is used in the case of trace species. Secondly charge conservation can be invoked. These equations are then used to construct a matrix that contains all the rate data for each level of the atom under study, and allows level populations to be calculated. However, in NLTE we see that the nature of the radiation field plays a part in determining the level populations.

6.3.2. Transfer Equation in NLTE

The transfer equation allows for the calculation of the radiation field through a stellar atmosphere. There are many variations of the equation suited to different problems, e.g. moving or static atmospheres, and for different geometries, e.g. plane-parallel and spherical. In many cases the atmosphere is thin enough compared to the radius of the star that plane-parallel geometry is sufficient. In this case the transfer equation is:

$$\mu \frac{dI_\nu}{d\tau_\nu} = I_\nu - S_\nu \tag{6.19}$$

where I_ν and S_ν are the intensity and source function for a given frequency, ν, respectively, τ_ν the radial optical depth given by $d\tau_\nu = -\kappa_\nu \rho dr$, and $\mu = cos\theta$. The integration of this equation along the line of sight is simple and leads to an equation of the form:

$$I_\nu(\tau_\nu) = \int_0^{\tau_\nu} S_\nu(\tau_\nu) e^{-(t_\nu - \tau_\nu)} dt_\nu + I_\nu(0) e^{-\tau_\nu} \tag{6.20}$$

From Eq. (6.20) it is seen that the intensity at a depth τ_ν is the sum of the averaged source function, which suffers exponential extinction between depths 0 and τ_ν, plus the original intensity from $\tau = 0$ which also suffers extinction. Therefore knowing $S_\nu(\tau_\nu)$ we can solve the radiative transfer problem. In LTE this is a relatively easy process as $S_\nu(T) = B_\nu(T)$ throughout the atmosphere. However, in NLTE this is not the case, the source function now depends on the level populations. Considering the simple two-level atom, the line source function is:

$$S_{\nu_0}^l = (1 - \varepsilon_\nu)J_\nu + \varepsilon_\nu B_\nu \tag{6.21}$$

Here ε_ν is the destruction probability of the photons, which is a function of level population, and ν_0 signifies that this is the form for complete redistribution and is frequency independent.

112

The above equations are from idealised/simplified situations; however, they further illustrate the complexities of NLTE over the simplifying assumptions of LTE.

There are many analytical solutions to the radiative transfer problem, e.g. Schwarzschild-Milne equations, the Eddington-Barbier approximations, for which there is much literature. These serve the purpose of illustrating different aspects to solving various problems, but were also a necessity in an era of pre-computers. For solving the NLTE problem numerically there are various computer codes that now exist.

6.3.3. Solving the NLTE problem

To solve radiative transfer equations using computers, the equations first need to be discretized. This is the process of turning the continuous equations that represent the processes that occur between two intervals, e.g. the stellar surface and the outer atmosphere, into equations that represent a finite number of discrete points between the intervals. In the case of radiative transfer the discretization is in depth, frequency and angle. With this done it is possible to construct a method of solving the transport equation. Two original methods to do this were those derived by Feautrier (Feautrier 1964) and by Rybicki (Rybicki 1971). These two methods are well described in many texts, the explanation that follows is based on that from Mihalas (1978) and lecture notes from a course on "radiative transfer in stellar atmospheres" by R. J. Rutten (http://www.astro.uu.nl/~rutten/Lecture_notes.html).

Feautrier derived a method of developing boundary conditions that made it possible to calculate the mean intensity, J_ν, through different depths at different frequencies and angles. From this he created a robust method for solving the radiative transfer problem; however, his method was for single frequencies i.e. single Feautrier solutions for each frequency are needed. As a spectral line covers a range of frequencies this can be a time consuming problem. Rybicki adapted Feautrier's method. In his method he assumes complete

redistribution. This means that the line source function doesn't vary over the line profile and contains the angle averaged frequency averaged mean intensity, $\bar{J}_{\nu_0}$, instead of the frequency dependent mean intensity, J_ν. By assuming complete redistribution it meant that all frequency information can be grouped together at given depths, which in turn can be solved depth by depth. This allows for quicker computation of the problem.

These two methods work on the assumption that the source function is a known quantity. This is generally not the case. To calculate a new source function for each depth point, a process called lambda iteration is employed. Here a lambda operator, which is a mathematical operator that represents double integration in angle and optical depth, is used to represent J_ν, in the source function, and a step by step procedure is used such that J_ν is calculated, via such methods as Feautrier's (Feautrier 1964), for each transition. This then allows for calculation of level populations over different depths, which in turn allows for the source function to be calculated. This method allows for the solution of the problem to be calculated over many depth points, and for many levels. The classical lambda iteration procedure can suffer from being computationally expensive. This is due to the lambda operator being a large matrix of values, which during the calculations has to be inverted. Due to this, many tricks are utilised so as to speed up convergence to a solution. To do this, an approximate lambda iteration scheme is used so that a simpler matrix has to be inverted. Also preconditioning of the transfer equation and population equations e.g. linearization by cutting all dependences on the radiation field to the first-order term, along with a clever choice of approximate lambda operator, speeds up convergence, giving a faster solution with more accurate values.

In this work I have adopted the MULTI code (Carlsson 1986). The processes of preconditioning, linearization and start-up parameters are well documented in Scharmer and

114

Carlsson (1985). I therefore leave out an in-depth discussion and refer the reader to that paper. MULTI requires input data to perform the calculations. This includes a model atom and a model atmosphere subject to the element and type of star under study. Paper II gives discussion about these inputs and the data that are contained within each one.

6.3.4. NLTE effects

NLTE effects are seen in high temperature, low density environments. This is due to a lack of collisions with electrons/ions, which would act to drive the system towards LTE, and the presence of intense radiation fields in very hot atmospheres. Low density environments include supergiants, whilst metal-poor stars have a lack of electrons leading to a lack of kinetic equilibrium, combined with a lower opacity from metals, giving rise to more intense UV radiation. O stars have a very intense radiation field which clearly dominates over collisions. Here I give a brief description of a range of the basic, sometimes competing, effects NLTE has on line formation. More detailed descriptions can be found in Bruls et al. (1992). These are general effects that, if the transitions are present in your atomic model, affect all atoms suffering from departures from LTE.

Ultraviolet Overionization- This phenomenon occurs because the angle-averaged mean intensity, J_ν, drops less steeply than the (local) Planck function, B_ν, with increasing height in the atmosphere, particularly at the blue end of the spectrum. This leads to a $J_\nu - B_\nu$ excess which has the effect of increasing ionisation from levels around 3-4 eV below the continuum compared to the LTE case. This leads to weaker lines in the NLTE situation compared to LTE due to decreased line opacity.

Bound-Bound Pumping- Like with overionization, electrons get pumped up through energy levels by the ultraviolet radiation which has $J_\nu > B_\nu$. This time, however, the transition occurs within bound states rather than ionising the element.

Resonance line Scattering- In resonance/strong lines the most important factor in the formation process is the line itself. Here photons are lost, either through the surface of the atmosphere or through scattering and thermalization, and therefore no longer play a part in exciting electrons within the relevant levels. This leads to the mean intensity, J_ν, and the line source function, S_ν, dropping well below the local Planck function, B_ν, i.e. $J_\nu < B_\nu$. The consequence of this is overpopulated ground states which leads to LTE calculations giving smaller equivalent widths for the resonance and strong excitation lines, and thus smaller abundances, as they do not take into account of the over population of the ground state. Resonance lines under NLTE conditions are larger than in LTE. This therefore leads to a smaller abundance for a given equivalent width in NLTE. These corrections are appreciable in size.

Photon Suction- Here we have the case that $J_\nu < B_\nu$. This is due to loss of photons through scattering or absorption by strong lines with high probability radiative bound-bound transitions. The loss of photons leads to the overpopulation of the ground state through high collisional coupling to the continuum reservoir of electrons. This also causes a cascade effect of electrons down from higher energy levels through the high probability transitions, which leads to a replenishment siphoned from a population reservoir in the first ionisation stage.

Infrared Overrecombination- In the infrared region of the EM spectrum $J_\nu < B_\nu$ for the deep layers of the photosphere. This is because the continuum processes, photoionization and recombination are characterized by a radiation temperature that can be vastly different from the local electron temperature. This leads to a deficiency of photons in the infrared and thus less chance of ionising the high levels whose transitions lie in this wavelength range, and thus causes a net recombination. This can lead to an overpopulation of the high-levels, i.e. the infrared levels, if no other phenomenon dominates.

116

Fe is one element that is affected by NLTE (Asplund et al. 1999). The most important effect seems to be overionization (Athay & Lites 1972, Thévenin & Idiart 1999); therefore applying Saha's equation would underestimate the degree of ionisation. However, there is also disagreement on the size of the NLTE effect. Whereas Thévenin & Idiart (1999) find that the effects of overionization are significant, Gratton et al. (1999) find the opposite (I return to this point in Chapter 7 – Paper II). Therefore it is necessary that the effects of NLTE on Fe abundance calculations are investigated further. Paper II studies the effect of NLTE on the Fe abundances derived from individual lines and in particular their effect on the temperatures of metal-poor stars derived using the excitation energy technique of Paper I. Following Chapter 7 (Paper II), parts of the NLTE analysis of Fe that were not included in the paper are discussed.

7. Paper II – Lithium abundances of halo dwarfs based on excitation temperatures. II. NLTE

This Chapter is a paper that has been submitted to A&A. The authors are Hosford, A. H., García Pérez, A. E., Collet, R., Ryan S. G., Norris, J. E., and Olive, K. A. The roles of the co-authors were:

- A. E. García Pérez has expertise in NLTE line formation and as my second supervisor was my main guide through the use of the NLTE code and analysis. She provided direction on which tests to undertake and the methods of calculating NLTE abundance corrections.

- R. Collet also has expertise in NLTE line formation. He provided up-to-date versions of the NLTE radiative transfer code MULTI and the model atom that is used as input for this code. He played a role in the NLTE discussion of this paper.

- S. G. Ryan was one of the main developers of this project. He played a part in discussions on the NLTE process and how to apply the NLTE abundance corrections to the effective temperatures. Writing and formulation of the paper were also guided by S. G. Ryan.

- J. E. Norris helped devise the project, and made comments on early versions of the paper

- K. A. Olive helped to devise the project and with his background in cosmology helped shape the discussion of BBN in the Introduction.

Figures and tables are renumbered to continue the sequence of the thesis, rather than the published version of the paper. The font and spacing has been changed from the published Astronomy & Astrophysics styles to the only that most closely, but not perfectly, matches the

remaining parts of the thesis. The pages have been renumbered to continue the sequence of the thesis.

Lithium abundances of halo dwarfs based on excitation temperatures. II. NLTE

A. Hosford[1], A.E. García Pérez[1], R. Collet[2], S.G. Ryan[1], J.E. Norris[3], and K.A. Olive[4]

[1] Centre for Astrophysics Research, University of Hertfordshire, College Lane, Hatfield, AL10 9AB, UK

  e-mail: a.hosford@herts.ac.uk, a.e.garcia-perez@herts.ac.uk, s.g.ryan@herts.ac.uk

[2] Max-Planck-Institut für Astrophysik, Postfach 1317, D-85741 Garching bei München, Germany

  e-mail: remo@mpa-garching.mpg.de

[3] Research School of Astronomy and Astrophysics, The Australian National University, Mount Stromlo Observatory, Cotter Road, Weston, ACT 2611, Australia

  e-mail: jen@mso.anu.edu.au

[4] William I. Fine Theoretical Physics Institute, School of Physics and Astronomy, University of Minnesota, Minneapolis, MN 55455, USA

  e-mail: OLIVE@umn.edu

ABSTRACT

Context.

Aims. The plateau in the abundance of ^{7}Li in metal-poor stars, first discovered by Spite & Spite (1982), was initially interpreted as an observational indicator of the primordial lithium abundance. However, this observational value is in disagreement with that deduced from calculations of Big Bang Nucleosynthesis (BBN), when using the Wilkinson Microwave Anisotropy Probe (WMAP) baryon density measurements. One of the most important factors in determining the stellar lithium abundance is the effective temperature. In a previous study by the authors, new effective temperatures ($T_{\rm eff}$) for sixteen metal-poor halo dwarfs were derived using a local thermodynamic equilibrium (LTE) description of the formation of Fe lines. This new $T_{\rm eff}$ scale reinforced the discrepency.

Methods. For six of the stars from our previous study we calculate revised temperatures using a non-local thermodynamic equilibrium (NLTE) approach. These are then used to derive a new mean primordial lithium abundance in an attempt to solve the lithium discrepancy.

Results. Using the code MULTI we calculate NLTE corrections to the LTE abundances for the Fe I lines measured in the six stars, and determine new $T_{\rm eff}$'s. We keep other physical parameters, i.e. log g, [Fe/H] and ξ, constant at the values calculated in Paper I. With the revised $T_{\rm eff}$ scale we derive new Li abundances.

We compare the NLTE values of $T_{\rm eff}$ with the photometric temperatures of Ryan et al. (1999), the infrared flux method (IRFM) temperatures of Meléndez & Ramírez (2004), and the Balmer line wing temperatures of Asplund et al. (2006).

Conclusions. We find that our temperatures are hotter than both the Ryan et al. (1999) and Asplund et al. (2006) temperatures by typically ~ 110 K - 160 K, but are still cooler than the temperatures of Meléndez & Ramírez (2004) by typically ~ 190 K. The temperatures imply a primordial Li abundance of 2.19 dex or 2.21 dex, depending on the magnitude of collisions with hydrogen in the calculations, still well below the value of 2.72 dex inferred from WMAP + BBN. We discuss the effects of collisions on trends of ^{7}Li abundances with [Fe/H] and $T_{\rm eff}$, as well as the NLTE effects on the determination of log g through ionization equilibrium, which imply a collisional scaling factor $S_{\rm H} > 1$ for collisions between Fe and H atoms.

Key words. Galaxy: halo – Cosmology: early Universe – Stars: abundances – atmospheres – Line: formation – Radiative transfer

1. Introduction

Since its discovery by Spite & Spite (1982), many studies of the plateau in lithium in metal-poor dwarfs have been undertaken, e.g. Spite et al. (1996), Ryan et al. (2000), Meléndez & Ramírez (2004), Bonifacio et al. (2007) and Aoki et al. (2009), confirming its existence. Most studies find a comparable Li abundance (A(Li)[1] $\approx$ 2.0 - 2.1 dex) yet discrepancies still exist, in particular the high value found by Meléndez & Ramírez (2004) (A(Li) = 2.37 dex). However, the biggest discrepancy comes from a comparison of the primordial abundances inferred from observations and that derived from Big Bang Nucleosynthesis (BBN) with the WMAP constraint on the baryon density fraction, $\Omega_{\rm B}h^2$, which leads to A(Li) = 2.72 dex (Cyburt et al. 2008). This is what has become known as the "lithium problem".

Several possibilities have been proposed to explain this discrepancy. Broadly these are: systematic errors in the derived stellar Li abundances; errors in the BBN calculations due to uncertainties in some of the relevant nuclear reaction rates; the destruction of some of the BBN-produced Li prior to the formation of the stars we have observed; or the removal of Li from the photospheres of the stars through their lifetimes (see introduction to Hosford et al. 2009, Paper I, for more details). The possible explanation under study in this work is that of systematic errors in the effective temperature ($T_{\rm eff}$) scale for metal-poor stars. The effective temperature is the most important atmospheric parameter affecting the determination of Li abundances. This is due to the high sensitivity of A(Li) to $T_{\rm eff}$, with $\partial A/\partial T_{\rm eff} \sim 0.065$ dex per 100 K. One reason for the spread in the observed A(Li) is the differences in the $T_{\rm eff}$ scales used by different authors. For instance, Spite et al. (1996) and Asplund et al. (2006) derive a $T_{\rm eff}$ of 5540 K and 5753 K for the star HD140283, respectively. The scale of Meléndez & Ramírez (2004) is on average ~ 200 K hotter than other works. This goes some way to explaining their higher A(Li); other factors, such as the model atmospheres with convective overshooting used in their work, may

---

[1] A(Li)$\equiv log_{10}\left(\frac{N(\rm Li)}{N(\rm H)}\right) + 12.00$

also contribute to the discrepancy. It is important to confirm, or rule out, whether systematic errors in T_{eff} are the cause of the Li problem, and in doing so address the need for other possible explanations.

In previous work (Hosford et al. 2009, - Paper I), we utilised the exponential sensitivity in the Boltzmann distribution to χ/T, where χ is the excitation energy of the lower level of a transition. Using this, we determined T_{eff}'s for eighteen metal-poor stars close to the main-sequence turnoff. This was done by nulling the dependence of A(Fe) on χ for approx 80 – 150 Fe I lines. Two T_{eff} scales were generated due to uncertainty in the evolutionary state of some of the stars under study. It was found that our temperatures were in good agreement with those derived by a Balmer line wing method by Asplund et al. (2006) and those derived by photometric techniques by Ryan et al. (1999). However, our T_{eff} scale was on average ~ 250 K cooler than temperatures from the infrared flux method (IRFM) as implemented by Meléndez & Ramírez (2004). This is not the case for all work done using the IRFM, Alonso et al. (1996) find more comparable effective temperatures for stars we have in common.

The derived mean abundances in Paper I were A(Li) = 2.16 dex assuming main-sequence (MS) membership and A(Li) = 2.10 dex assuming sub-giant branch (SGB) membership. For the five stars that have a known evolutionary state, we calculated a mean A(Li) = 2.18 dex. It is clear that these values are not high enough to solve the lithium problem. However, the analysis of Hosford et al. (2009) assumed that the spectrum was formed in local thermodynamic equilibrium (LTE). This is a standard way of calculating spectra, but oversimplifies the radiative transfer problem, and it was acknowledged in Hosford et al. (2009) that LTE simplification affect those results. Consequently, although it was shown that, within the LTE framework, systematic errors in the T_{eff} scale are not the cause of the disparity between spectroscopic and BBN+WMAP values for the primordial Li, we also need to assess the impact of non-local thermodynamic equilibrium (NLTE) on the determination of stars effective temperatures. That is the aim of the current work.

This work is not intended to be a full dissection of the methods of NLTE, but rather an application of those more complex (and possibly more accurate) methods to derive a new T_{eff} scale and to assess their impact on the lithium problem. However, to do this we need to delve, with some depth, into the processes of NLTE line formation, which we do in Sect. 2. This will give some understanding of the complexities and uncertainties that are involved and give the opportunity to make some generalisations on the important aspects that need to be addressed. In Sect. 3 – 5 we detail our calculations and results, and discuss these further in Sect. 6.

2. NLTE Framework

2.1. The necessity for NLTE

With the availability of high quality spectra, the problem of calculating accurate chemical abundances often comes down to a better understanding of the line formation process. This is of particular importance to this work as the calculation of accurate level populations of the Fe I atom and source functions at the wavelengths of the Fe transitions is crucial to determining T_{eff} from lines of different χ. In LTE calculations, the level populations follow the Boltzmann and Saha

distributions. These assume that the levels are populated, or depopulated, by collisional processes only, and that the temperature characterising this process is the local kinetic temperature. In the deep layers of the atmosphere, at $\tau_{5000} > 1$, where τ_{5000} is the optical depth at 5000Å, LTE is a reasonable assumption. However, it tends to break down at optical depths $\tau_{5000} < 1$, i.e. through most of the line forming region of the photosphere. Therefore neglecting deviations of the level populations from LTE could lead to errors in the T_{eff} derived by excitation dependence. Furthermore, in NLTE calculations, it is not only the level populations that differ from the LTE case. The radiative transitions of the atom must be explicitly considered. The fact that the radiation field is no longer described by a Planck function, and certainly not a Planck function calculated for the local temperature, results in further changes of the spectrum relative to the LTE case. This last effect is very important in metal-poor stars, where the reduced opacity/increased transparency of the atmosphere exposes shallow, cooler layers to the UV-rich spectrum coming from the deeper, hotter layers (Asplund et al. 1999).

For Fe in particular, different studies have come to different conclusions as to the magnitude of the NLTE corrections. Thévenin & Idiart (1999) found that there can be corrections of up to 0.35 dex on Fe I abundances for main-sequence stars at [Fe/H] ≈ -3, and suggest that all work done on metal-poor stars should be carried out using NLTE methods. Gratton et al. (1999), however, find negligible corrections to Fe I abundances and see this as validation that LTE assumptions still hold when studying this type of star. In contrast, work by Shchukina et al. (2005) find higher correction values of ∼0.9 dex and ∼0.6 dex, depending on whether 3D or 1D atmospheres are used. The difference in their conclusions is driven principally by the different relative importance of collisional and radiative transitions in their calculations. Gratton et al. (1999) have relatively stronger collisional transitions, and as a result find smaller deviations from LTE. Shchukina et al. (2005) include no collisions with neutral hydrogen. We return to this important point below, but for now it illustrates that much work still needs to be done in this field before we can be certain of the impact of NLTE.

2.2. The coupling of the radiation field and level populations

Many factors have to be taken into account when computing radiative transfer in NLTE. This leads to a complicated situation where, for example, we have to solve population equations and radiative transfer equations simultaneously. This is due to the level populations and the radiation field being coupled, a fact ignored in LTE calculations. There are large uncertainties in NLTE calculations because of the lack of complete information on the rates of collisional and radiative transitions between energy levels for a given element in all its important ionization states. This is especially true for larger atoms which have a greater number of energy levels, as is the case for Fe.

To solve NLTE problems, a system of rate equations is needed that describes fully the populations of each level within the atom under study. Statistical equilibrium is invoked, i.e. the radiation fields and the level populations are constant with time. The formulation of the problem is well described in Mihalas (1978), from which the following equations are

taken. The population of level i is the sum of all the processes that populate the level minus the processes that depopulate it, such that:

$$\frac{\mathrm{d}n_i}{\mathrm{d}t} = \sum_{j \neq i}^{N} n_j P_{ji} - n_i \sum_{j \neq i}^{N} P_{ij} = 0 \tag{1}$$

where n_i and n_j are the populations of the levels i and j respectively, N is the total number of levels, including continua, and P_{ji} and P_{ij} are the rates of transitions into and out of the level i. The rates are given by:

$$P_{ij} = A_{ij} + B_{ij}\bar{J}_{\nu_0} + C_{ij} \tag{2}$$

where A_{ij}, B_{ij}, and C_{ij} are the Einstein coefficients for spontaneous, radiative and collisional excitation respectively, ν_0 is the frequency of the transition between levels i and j, and $\bar{J}_{\nu_0}$ is the mean intensity averaged over the line profile. It is usually the case that the radiative rates dominate over the collisional ones at optical depths $\tau_{5000} < 1$ implying that LTE assumptions no longer hold in general. The rate equations depend on the mean intensities over the relevant frequencies, $\bar{J}_{\nu_0}$, meaning that the level populations depend on the radiation field. Conversely the radiation field depends on the level populations through the radiative transfer equation. This is seen by examining the simple problem of the two-level atom where the radiative transfer equation is given by:

$$\mu\frac{\mathrm{d}I_\nu}{\mathrm{d}\tau_\nu} = I_\nu - S_\nu^l \tag{3}$$

where I_ν is the intensity at frequency ν, μ is the cosine of the viewing angle, τ_ν is the optical depth and S_ν^l is the line source function, such that:

$$S_\nu^l = \left(\frac{2h\nu^3}{c^2}\right)\left[\left(\frac{n_i g_j}{n_j g_i}\right) - 1\right]^{-1} \tag{4}$$

Here h is Planck's constant, c is the speed of light, g_i and g_j are the statistical weights of the levels i and j respectively, and n_i/n_j gives the ratio of the populations of the levels i and j calculated using the rate equation, Eq. (1). This form of the source function strictly speaking holds under the assumption of complete frequency redistribution but still illustrates the problem of having to solve the two sets of equations simultaneously.

2.3. Transition rates

For the calculation of the level populations, through Eq. 1, radiative and collisional rates are required.

For the radiative rates, the bound-bound transition probabilities and photoionization cross sections are needed for all levels of the atom in all significant ionization states. Two of the larger projects providing values for these are the Opacity Project (Seaton 1987) and the IRON project (Bautista 1997). For Fe, the Opacity Project finds typically a > 10 % uncertainty for their photoionization data (Seaton et al. 1994). The Bautista photoionization values, which are larger than those previously used, lead to increased photoionization rates (Asplund 2005) and hence to lower abundances as overionization becomes more efficient.

For the collisional data, large uncertainties still exist. The two main types of collisions that affect the line profile are those with electrons and neutral hydrogen. Coupling of all levels in the Fe model atom occurs due to these types of collisions, especially in the atmospheres of cool stars where electrons and neutral H are believed to be the dominant perturbers. A simple calculation, like that in Asplund (2005), shows that H I collisions dominate over electron collisions in thermalizing processes in metal-poor stars and are therefore important in calculations of line profiles. For collisions with neutral hydrogen, the approximate formulation of Drawin (1968, 1969) is used as implemented by Steenbock & Holweger (1984). However, through laboratory testing and quantum calculations of collisions with atoms such as Li and Na, it has been shown that Drawin's formula does not produce the correct order of magnitude result for H I collisional cross-sections. In some cases, where comparisons with experimental data or theoretical results can be made, the Drawin recipe overestimates the cross-sections by *one* to *six* orders of magnitude (e.g. Fleck et al. 1991; Barklem et al. 2003). Corrections to the Drawin cross-sections are suggested by Lambert (1993) to compensate for these differences.

Due to the uncertainties in the magnitude of the H collisions, the Drawin cross-sections are scaled with a factor S_H. There are different schools of thought on how to deal with this parameter. Collet et al. (2005) treat it as a free parameter in their work, adopting values of $S_H = 0.001$ and 1 and test the effect this has on their results. Higher values of S_H correspond to more collisions and hence more LTE-like conditions. Their main aim, however, was to test not the efficiency of H collisions but the effects of line-blocking on the NLTE problem. Korn et al. (2003) make it one of their aims to constrain S_H. To do this, they ensure ionization equilibrium between Fe I and Fe II using the log g derived from HIPPARCOS parallax and T_{eff} from H lines. In doing this, they find that a value of $S_H = 3$ holds for a group of local metal-poor stars. This apparently contradicts the statement above that Drawin's formula overestimates the cross-sections. Gratton et al. (1999) use $S_H = 30$. This value was constrained by increasing S_H until spectral features of several elements, i.e. Fe, O, Na and Mg, of RR Lyrae stars all gave the same abundance. With such elevated collisional rates, Gratton et al. (1999) not surprisingly find results very close to LTE, i.e. they find very small NLTE corrections.

Collisions with neutral hydrogen and electrons are important not only in coupling bound states to each other, but also in coupling the whole system to the continuum i.e. to the Fe II ground state (and potentially excited states). This is especially true when considering the high excitation levels. These levels are more readily collisionally ionised than lower levels, and are also coupled to each other by low energy (infrared) transitions, therefore thermalization of the levels occurs which drives the populations more towards LTE values. It is therefore important to have a model atom that includes as many of the higher terms of the atom as possible (Korn 2008), although it is not necessary to include all individual levels. We return to this point in Sect. 4. We describe the model atom and calculations next before moving on to the results.

2.4. The model Fe atom

The Fe model adopted for this work is that of Collet et al. (2005), which is an updated version of the model atom of Thévenin & Idiart (1999). The atom includes 334 levels of Fe I with the highest level at 6.91 eV. For comparison, the first ionization energy is 7.78 eV and the NIST database lists 493 Fe I levels. Many of the highest levels are not included in our model; due in part to computational limitations i.e. the more complicated the model, the greater the computer power and time needed to complete the computations, and because of lack of important information, e.g. photoionization cross sections. We report below on the effects the missing upper levels have on the corrections and try to quantify their importance in the NLTE calculations. The model also includes 189 levels of Fe II with the highest level at 16.5 eV, and the ground level of Fe III. For comparison, the second ionization energy is 16.5 eV, and the NIST database lists 578 Fe II levels. This model configuration leads to the possibility of 3466 bound-bound radiative transitions in the Fe I system, 3440 in the Fe II system, and 523 bound-free transitions. We run the calculations with the whole model, but present results only for the lines that are measured in our program stars.

Oscillator strengths for the Fe I lines are taken from Nave et al. (1994) and Kurucz & Bell (1995), whilst values from Fuhr et al. (1988), Hirata & Horaguchi (1995), and Thévenin (1989, 1990) were used for the Fe II lines. The photoionization cross-sections are taken from the IRON Project (Bautista 1997). Collet et al. (2005) smoothed these cross-sections so as to minimize the number of wavelength points to speed up the computational processes.

Collisional excitations by electrons are incorporated through the van Regemorter formula (van Regemorter 1962) and cross-sections for collisional ionization by electrons are calculated by the methods of Cox (2000). In the case of H collisions, the approximate description of Drawin (1968, 1969), as implemented by Steenbock & Holweger (1984) with the correction of Lambert (1993) and multiplied by S_H, has been used. As we do not intend to constrain S_H, we treat it as a free parameter and adopt values of 0 (maximal NLTE corrections), 0.001 and 1. This allows us to assess the importance of H collisions on the NLTE corrections. For all calculations, the oscillator strength value, f_{ij}, has been set to a minimum of 10^{-3} when there is no reliable data or the f value for a given line is below this minimum. This minimum is set as the scaling between the cross-sections and the f value breaks down for weak and forbidden lines (Lambert 1993).

2.5. The model atmospheres

In this work, we have adopted plane-parrallel MARCS models. These models are used, rather than the Kurucz 1996 models as was done in Hosford et al. (2009), as MULTI needs a specific format for its input, this is provided by the MARCS models as in Asplund et al. (1997). 3D models lead to an even steeper temperature gradient, and hence cooler temperatures in the line forming region (Asplund 2005), but the use of these more sophisticated models is beyond the scope of this work.

2.6. Radiative transfer code

The NLTE code used to produce Fe line profiles and equivalent widths (W_λ) is a modified version of MULTI (Carlsson 1986). This is a multi-level radiative transfer program for solving the statistical equilibrium and radiative transfer equations. The code we adopted is a version modified by R. Collet to include the effects of line-blocking (Collet et al. 2005). To do this, they sampled metal line opacities for 9000 wavelength points between 1000 Å and 20000 Å and added them to the standard background continuous opacities. They found that, for metal-poor stars, the difference between NLTE Fe abundances derived from Fe I lines excluding and including line-blocking by metals in the NLTE calculations is of the order of 0.02 dex or less.

3. NLTE calculations

For this work, we have chosen six of our original program stars (Hosford et al. 2009) that approximately represent the limits of our physical parameters, i.e. one of the more metal-rich, one of the less metal-rich, one of the hotter, one of the cooler etc. Table 9 indicates the stellar parameters for which model atmospheres were created. For the HD stars HIPPARCOS gravities were used. For the other three stars, lower and upper limits on log g are given by theoretical isochrones (see Hosford et al. 2009). In the case of LP815-43, there is uncertainty as to whether it is just above or just below the main-sequence turnoff. The final temperatures are interpolated between these values using a final log g that represents the star at 12.5 Gyr (Table 10). This study is primarily concerned with the formation of Fe I lines.

Table 9. Physical parameters for the atmospheric models used in this work

Star	T_{eff} (K)	[Fe/H] (dex)	log g (dex)	ξ (Kms^{-1})
HD140283	5769	−2.54	3.73	1.5
HD84937	6168	−2.34	3.98	1.3
HD74000	6070	−2.20	4.03	1.2
BD+26° 2621	6225	−2.68	4.47	1.2
BD+26° 2621	6241	−2.67	4.51	1.2
CD−33° 1173	6380	−2.94	4.41	1.5
CD−33° 1173	6391	−2.94	4.47	1.5
LP815−43 (SGB)	6383	−2.71	3.80	1.4
LP815−43 (SGB)	6409	−2.68	3.91	1.4
LP815−43 (MS)	6515	−2.62	4.35	1.4
LP815−43 (MS)	6534	−2.61	4.42	1.4

In Fig. 19, we present the departure coefficients, $b_i = n_i/n_i^{\text{LTE}}$, for the lower (left hand side) and upper (right hand side) levels of all lines we have measured in the star HD140283 in paper I, calculated for three S_H values. The two sets of lines in each plot, coloured. red and blue, represent levels that fall above and below the midpoint of our excitation energy range, i.e. 1.83 eV where our highest lower level of the transition is at 3.65 eV, and 5.61 eV where our highest upper transition level is at 6.87 eV. This is done to better visualise the effects of NLTE on different levels of the atom. We see that in all cases the Fe I levels are under-populated compared to LTE at $\tau_{5000} < 1$. This is primarily due to the effects of

overionization where $J_\nu > B_\nu$ for lines formed from the levels of the atom at around $\chi \sim 4$ eV below the continuum, due to the UV photons having energies $\approx$ 3-4 eV. This causes all levels of the atom to become greatly depopulated, as can be seen from the blue lines. The coupling of the higher levels through collisions and of the lower levels through the large number of strong lines sharing upper levels implies that relative to one another the Fe I level populations approximately follow the Boltzmann distribution. Because of photoionization, the Saha equilibrium between Fe I and Fe II is not fulfilled however and the departure coefficients of Fe I levels are less than unity. In deeper levels of the atmosphere, this leads to both upper and lower levels of a transition being equally affected by the above phenomena (Fig 19 – right hand side). For this reason, the source functions for lines forming at these depths are relatively unaffected in this region, as $S \approx (b_{\text{upper}}/b_{\text{lower}})B_\nu$, and follow a Planckian form (Fig. 20 – right hand panel). The combined effect of the above processes, i.e. depopulation and relatively unaffected source functions, leads to a smaller W_λ and thus weaker lines, and increased abundances compared to the LTE case. For stronger lines, forming further out in the atmosphere, there is a divergence between b_{upper} and b_{lower} and the source function thus diverges from the Planck function (Fig. 20 – left hand panel). In the case where $S_\nu^l < B_\nu$, the source function compensates slightly for the loss of opacity leading to smaller NLTE corrections, the opposite being true for $S_\nu^l > B_\nu$. We see that for the lower level of the weaker line considered in the figure has $\bar{J}_\nu > B_\nu$, whilst $S_\nu^l \approx B_\nu$, which leads to overionization of that level and greater departures than the stronger line and greater NLTE abundance corrections.

Although we see a general decrease in populations compared to LTE, there is a slight recovery in the lower levels (those with χ less than half of our maximum χ value) higher up in the atmosphere, at $\tau_{5000} < 10^{-2}$, Fig. 19. This is most likely due to increased recombination in the upper (infrared) levels followed by a cascade of electrons down to the lower levels.

The effect of H collisions is in general to reduce the spread of departure coefficients and drive populations towards LTE values. This reduction in the spread of departure coefficients comes from the coupling of bound states. The populations are driven towards LTE, as increased collisions with neutral H destroys line photons by themalizing them i.e. their energy is converted into the local kinetic energy of the gas, which is in LTE. More collisions mean that the depth at which the photons are thermalized rises through the atmosphere. This gradually reduces the departures from LTE through the atmosphere as shown in Fig. 19; with an increasing S_{H} the slope in the departure coefficient profile becomes shallower. In Fig. 19 it is interesting to see that the rise in b_i at around $\tau_{5000} \approx -2.5$ for the levels < 1.83 eV becomes smaller with increasing S_{H}. This could in fact mean an increase in NLTE departures for some levels for increasing S_{H}, opposed to increasing S_{H} driving conditions towards LTE which is normally the case. As mentioned above, this rise is most likely caused by increased recombination in the infrared, exactly how this is affected by the increase in S_{H} is not yet known and requires further study.

The decrease in level population at $\tau_{5000} < 1$ causes a drop in opacity for all lines. As a result of this, the lines form deeper in the atmosphere than in LTE. In Fig. 21, we clearly see this effect, where we show the continuum optical depth

τ_{5000} at which the line optical depth $\tau_\nu = 2/3$. We also see that there is an increasingly large logarithmic optical depth difference, $\Delta \log \tau_{5000}(\tau_\nu = 2/3)$, between the formation of weak lines in NLTE and LTE, up to ≈ 50 mÅ, after which the difference becomes constant. With a decrease in opacity compared to LTE, there needs to be an increase of abundance to match the equivalent width of a given line in NLTE. Opacity is not the only variable affected by NLTE, the source function can also be affected. However, it is the dominant force in driving the NLTE departures within the Fe atom. In Fig. 22, we plot the abundance correction versus equivalent width for the star HD140283. We see that there is a positive correction for the different values of S_H. There is a clear trend with equivalent width. It is how this translates to trends with excitation energy χ that will affect T_{eff}: if the abundance corrections only shifted the mean abundance without depending on χ then the derived T_{eff} would not change.
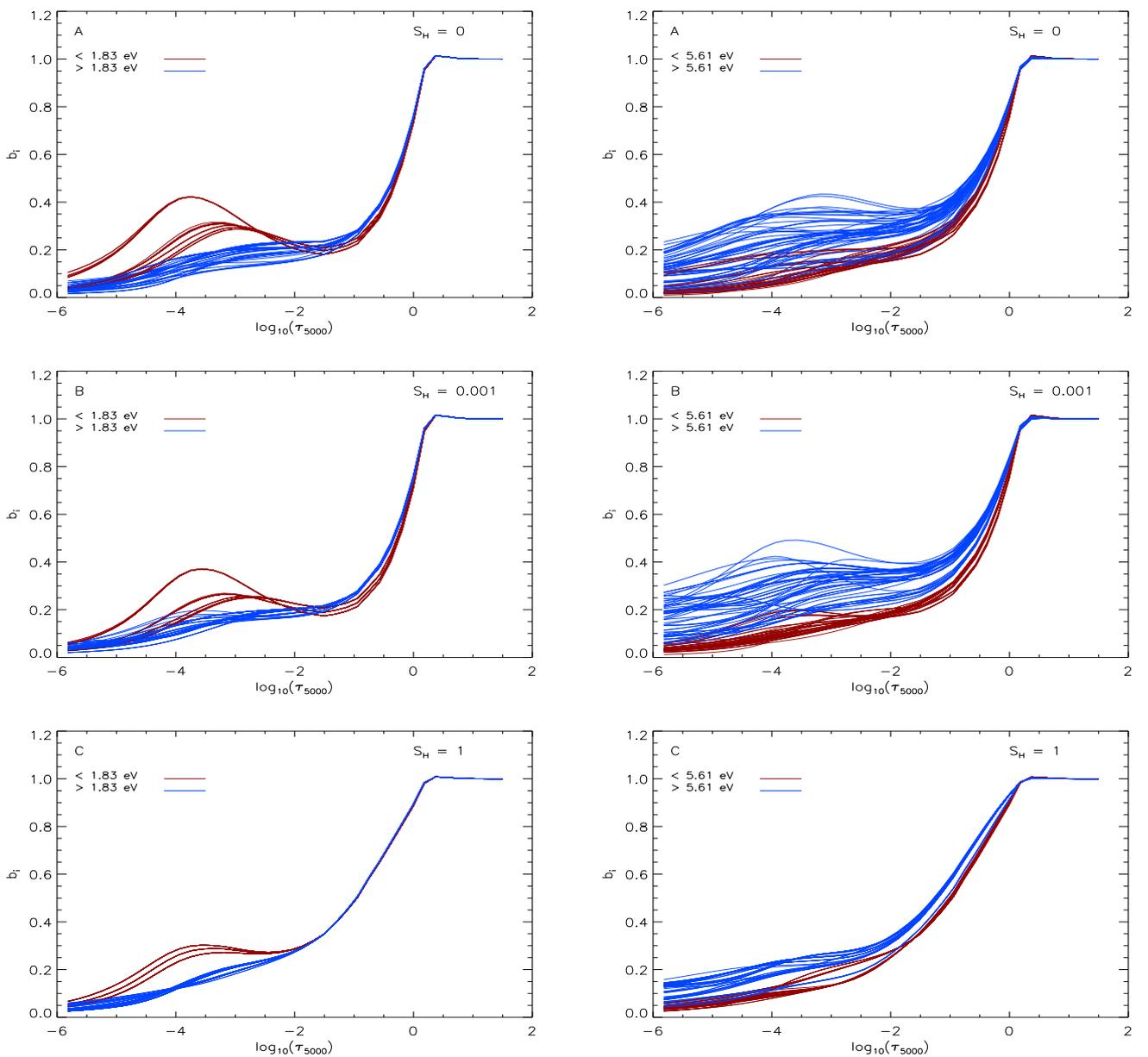
Fig. 19. Departure coefficients for all lower levels (left) and all upper levels (right) of the lines we have studied in the star HD140283. A: $S_H = 0$, B: $S_H = 0.001$, C: $S_H = 1$
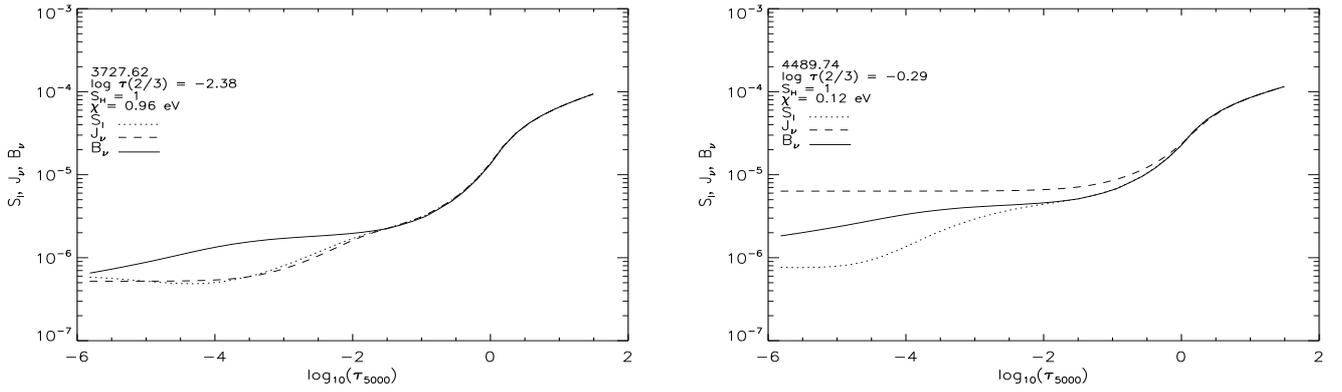
Fig. 20. Source function, S_l, mean intensity, J_ν, and Planck function, B_ν, for two lines whose lower level is close to the ground state - χ = 0.96 eV (left panel) and 0.12 eV (right panel), for S_H = 1, labelled with the lines characteristic formation depth $\log \tau_{5000}$ at which $\tau_\nu = 2/3$.

4. NLTE abundance corrections - deriving, testing, applying

In order to determine a new $T_{\rm eff}$ for a star, we first need to calculate NLTE corrections for the LTE abundances derived in Paper I. Abundance corrections of the form $A_{\rm NLTE,MULTI} - A_{\rm LTE,MULTI}$ are calculated and applied to the LTE abundances from Paper I to generate NLTE abundances on the same scale as that paper, rather than using solely the new NLTE analysis. This procedure is used so as to tie this work to the previous results, thus allowing the limitations of the LTE assumptions in that work to be seen. To do this, a grid of MULTI results for a range of abundances is created with increments of 0.02 dex. The abundance values covered by this grid depend on the spread of abundances from individual lines in each star. MULTI gives an LTE and NLTE equivalent width for each abundance in this grid. A first step is to determine what $W_{\rm LTE}$ from the MULTI grid corresponds to the LTE abundance derived in Paper I (Hosford et al. 2009).
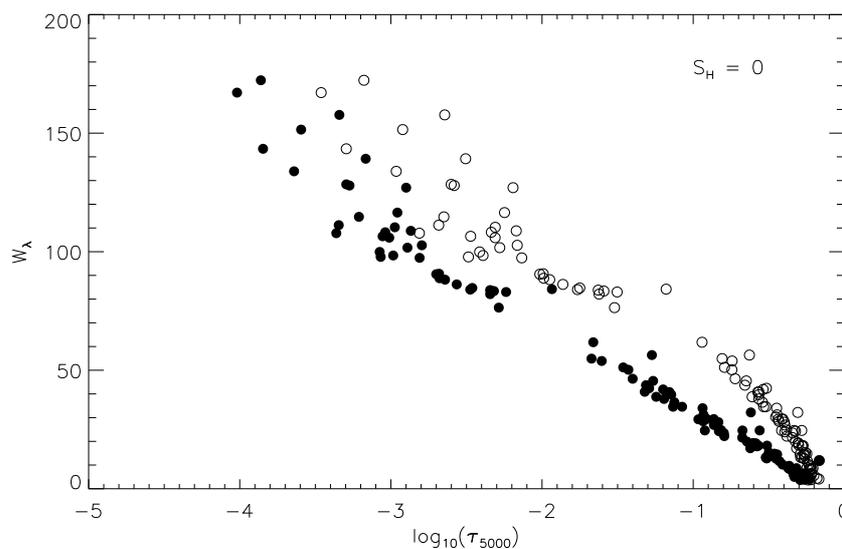
Fig. 21. The depth of formation of Fe I lines, with no H collisions, on the $\log \tau_{5000}$ scale for lines of different equivalent width, in LTE (filled circles) and NLTE (open circles), for HD140283.
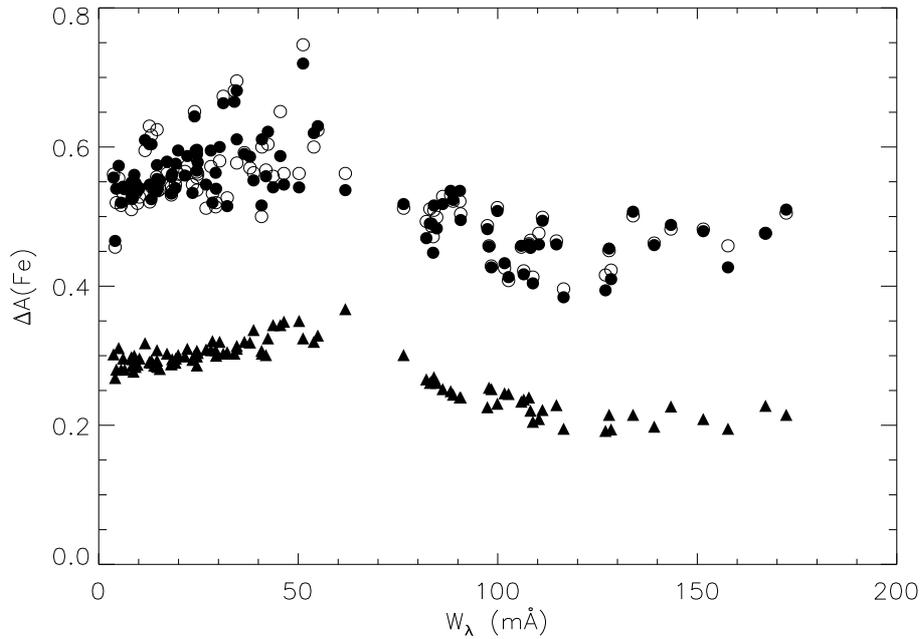
Fig. 22. Abundance correction versus equivalent width for the lines measured in the star HD140283 for $S_H = 1$ (filled triangles), 0.001 (filled circles) and 0 (open circles).

This is done for all Fe lines that are measured in the star. The NLTE abundance inferred for a line is the abundance that corresponds to this W_λ within the grid of MULTI NLTE results. The correction is then calculated as $\Delta A(\text{Fe}) = A(\text{Fe})_{\text{NLTE}} - A(\text{Fe})_{\text{LTE}}$. Fig. 23 shows the corrections for the star HD140283 calculated for the three different S_H values: $S_H = 0$, 0.001 and 1. We see a trend in the abundance correction with χ, where we have values, from least square fits, of:

$$A(\text{Fe}) = 0.490(\pm 0.012) + 0.0216(\pm 0.0055)\chi; \text{ for } S_H = 0 \tag{5}$$

$$A(\text{Fe}) = 0.490(\pm 0.012) + 0.0207(\pm 0.0054)\chi; \text{ for } S_H = 0.001 \tag{6}$$

$$A(\text{Fe}) = 0.244(\pm 0.072) + 0.0178(\pm 0.0032)\chi; \text{ for } S_H = 1 \tag{7}$$

The non-zero coefficient of χ implies that a T_{eff} correction is needed. The values for $S_H = 0$ and $S_H = 0.001$ are very similar and imply that T_{eff} corrections for these two values will be very similar. We therefore decided that corrections for only $S_H = 0$ and 1 would be calculated, $S_H = 0$ representing the maximal NLTE corrections and $S_H = 1$ representing the full Drawinian magnitude of neutral H collisions.

To test the corrections, we compared synthetic profiles from the NLTE abundance with the observed profile, and compared measured W_λ's with NLTE W_λ's from MULTI, obtained from an abundance given by $A_{\text{LTE}} + \Delta A$. The synthetic profiles are convolved with a Gaussian whose width is allowed to vary from line to line. This represents the macroturbulent and instrumental broadening, the latter calculated by fitting Gaussian profiles to ThAr lines in IRAF and found to be ~ 100 mÅ. We found that the profiles match the observed line reasonably well, and that measured and MULTI calculated W_λ's are comparable, with a standard deviation of 2.3 mÅ. This gives us confidence that the corrections are realistic within the framework of the atomic model used. These corrections were then applied to the WIDTH6 LTE abundances
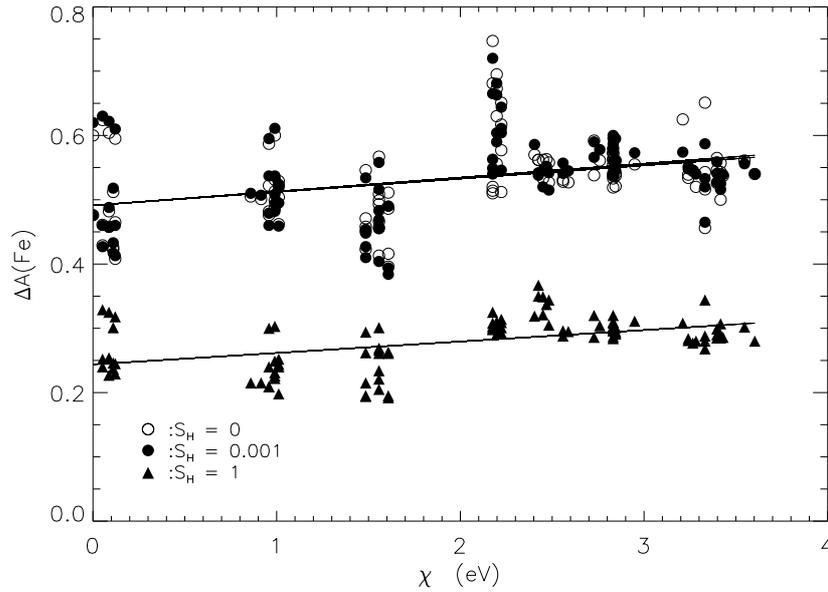
Fig. 23. Abundance correction versus χ for $S_H = 1$ (filled triangles), 0.001 (filled circles) and 0 (open circles) for the measured lines in the star HD140283. Least-squares fits are shown to guide the eye.

used in Paper I and new plots of χ versus A(Fe) were plotted. We then nulled trends in this plot to constrain T_{eff}(NLTE) by recalculating the LTE abundances using the radiative transfer program WIDTH6 (Kurucz & Furenlid 1978) exactly as in Hosford et al. (2009) and reapplying the NLTE corrections, derived here from MULTI for the original LTE parameters.

As noted in Sect. 2.3, it can be important to include the highest levels of the atom in the calculations. It is not necessary to include each individual level however, and it is possible to use superlevels that represent groups of closely spaced levels (Korn 2008). To test the effect of these upper levels, we took the approach of giving the top 0.5 eV of levels in our atomic model an $S_H = 2$ whilst the rest of the levels had $S_H = 1$. We have done this for three situations; A) increasing S_H for just the bound-bound transitions rates, B) increasing S_H for just the bound-free rates and C) increasing S_H for both the bound-bound and bound-free. We discuss here only the case of the bound-free rates as it is only these rates that have an effect, edging the populations towards LTE values. Changing the bound-free rates not only affects the higher levels but translates through all lower ones. In fact it is the lower half of the atomic model that is affected by a greater amount. The result can be seen in Fig. 24 where we plot a level with $\chi = 0.96$ eV and one of the higher levels, $\chi = 3.30$ eV, from our atomic model. Fig. 25 shows the abundance correction against χ for the increased S_H value of the upper levels and for a pure $S_H = 1$ situation. Comparing the differences in abundance correction between $S_H = 1$, and $S_H = 1$ with $S_H = 2$ on the upper levels we see a mean difference $(\Delta A(\text{Fe})_{S_H=1+2} - \Delta A(\text{Fe})_{S_H=1})$ of -0.031 dex for $\chi = 0$ - 2 eV and -0.028 dex for $\chi > 2$ eV, for the star HD140283. These effects equate to a 5 K increase in T_{eff} compared to $S_H = 1$. It is then clear that the upper levels have a slight effect on the final temperatures, and induce a slightly larger NLTE correction. However, in the case of this study, where random errors are of order ~ 80 K, they will not make a significant effect.
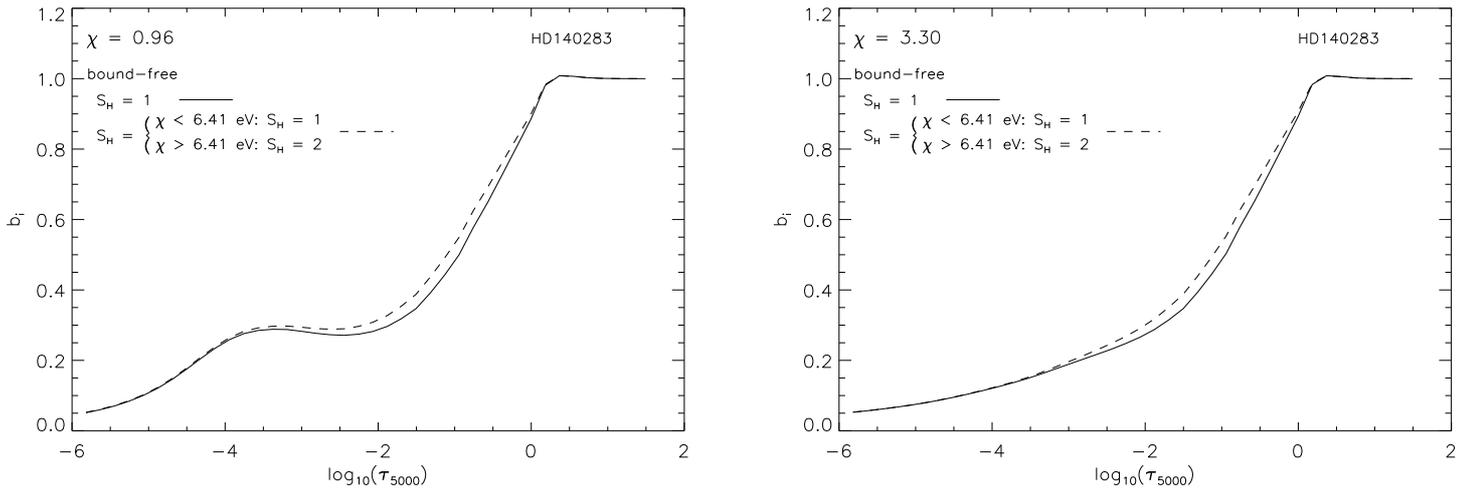
Fig. 24. Dashed line: The effects of increasing the S_H value to 2 for the top 0.5 eV of levels in the atomic model, for bound-free transitions from a low level (left panel) and a higher level (right panel). The remaining levels have $S_H = 1$. Solid line: $S_H = 1$ for all levels.
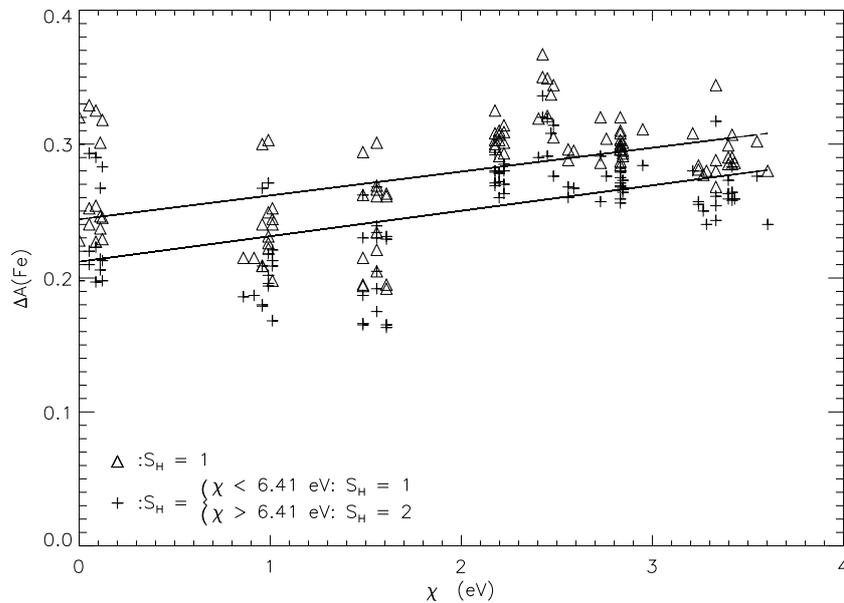
Fig. 25. Comparison between the abundance correction versus excitation energy for the star HD140283 using $S_H = 2$ for the top 0.5 eV of levels of Fe I in the atomic model, and $S_H = 1$ for the remaining levels (crosses) and pure $S_H = 1$ (open triangles).

5. Results

Fe abundance corrections for the stars in Table 9 have been calculated and new temperatures have been derived using the excitation energy technique, as in Paper I but with the NLTE corrections applied as described in Sect. 4. Table 10 lists the new NLTE T_{eff}'s and ΔT_{eff}, such that $\Delta T_{\text{eff}} = T_{\text{eff}}(NLTE) - T_{\text{eff}}(LTE)$, for the selection of stars.

For this work, all the other parameters, viz. log g, [Fe/H] and ξ, were kept at the values found in Hosford et al. (2009). Our aim here, as it was in Hosford et al. (2009), is to narrow down the zero point of the temperature scale by quantifying the systematic errors, albeit at the expense of having larger star to star random errors. Contributions

Table 10. Final T_{eff} and $A(\mathrm{Li})$ for the selection of stars in this study

Star	T_{eff} (LTE) (K)	log g (dex)	(NLTE) $S_H = 0$			(NLTE) $S_H = 1$		
			T_{eff} (K)	ΔT_{eff} (K)	$A(\mathrm{Li})$ (dex)	T_{eff} (K)	ΔT_{eff} (K)	$A(\mathrm{Li})$ (dex)
HD140283	5769	3.73	5850 ± 51	81	2.27 ± 0.03	5838 ± 48	69	2.26 ± 0.03
HD84937	6168	3.98	6318 ± 102	150	2.28 ± 0.07	6261 ± 102	93	2.24 ± 0.07
HD74000	6070	4.03	6211 ± 131	141	2.15 ± 0.09	6145 ± 130	75	2.10 ± 0.09
BD−26°2621	6233	4.49	6298 ± 81	65	2.21 ± 0.05	6292 ± 80	59	2.21 ± 0.05
CD−33°1173	6386	4.44	6293 ± 128	−93	2.09 ± 0.08	6427 ± 113	41	2.18 ± 0.07
LP815-43 (SGB)	6400	3.87	6402 ± 100	2	2.13 ± 0.07	6522 ± 119	122	2.21 ± 0.08
LP815-43 (MS)	6529	4.40	6551 ± 102	22	2.23 ± 0.07	6607 ± 99	78	2.27 ± 0.06

to the errors come from adopted gravity, the nulling procedure in determining the T_{eff}, and smaller contributions from the error in microturbulence, errors in the age, metallicity and initial temperature, T_{phot}, when determining isochronal gravities. In relation to the gravities, the three HD stars had gravities derived using HIPPARCOS parallaxes, and their errors are a reflection of errors propagating through this calculation, whilst for the remaining stars isochrones were used. The isochronal gravities are sensitive to age, with a 1 Gyr difference leading to a change of ∼ 0.03 dex for main sequence (MS) stars and ∼ 0.06 dex for sub-giant (SGB) stars. This equates to a change in T_χ of 12 K and 24 K respectively. These errors are based on LTE sensitivities, as are other errors quoted below. There is also a dependence on the initial temperature, a photometric temperature from Ryan et al (1999), used to determine the isochronal gravity. A +100 K difference leads to +0.06 dex and –0.06 dex for MS and SGB stars respectively. This equates to ± 24 K in T_χ which shows, importantly, that T_χ is only weakly dependent on the initial photometric temperature. Contributions to T_χ is also sensitive to microturbulence, for which an error of ∼ 0.1 km s^{-1} equates to an error of ≈ 60 K.

In the nulling procedure any trends between [Fe/H] and χ are removed. Due to the range in line to line Fe abundances for a particular star, there is a statistical error in the trend which is of order $\sigma = 0.011$ dex per eV, which equates to ≈ 40 K - 100 K depending on the star under study. This error also contains the random line-to-line errors due to equivalent width, gf, and damping values. The final T_{eff} error in Table 10 is then a conflation of this statistical error and the errors from Δage = 1 Gyr, $\Delta\xi = 0.1$ kms^{-1}, Δ[Fe/H] = 0.05 and $\Delta T_{\mathrm{phot}} = 100$ K.

These new T_{eff} values and equivalent widths from Ryan et al. (1999) were then used to calculate new Li by interpolating within a grid of equivalent width versus abundance for different T_{eff}. This grid was taken from Ryan et al. (1996a).

6. Discussion

6.1. The T_{eff} scale

With the addition of the NLTE corrections, we see in Table 10 that there is, for the most part, an increase in T_{eff} from the LTE T_{eff}'s of Hosford et al. (2009), for both cases of S_H. The only exception is CD−33°1173 in the $S_H = 0$ case, for which there is a 93 K decrease. We return to this star below. The T_{eff} corrections we have derived average 59 K for S_H

= 0 and 73 K for $S_H = 1$ (treating LP815−43 as one datum, not two). For $S_H = 0$ the temperature corrections tend to increase at cooler temperatures, whilst the tendency is weaker or opposite for $S_H = 1$, i.e. corrections increase at higher temperatures (obviously the gravity and metallicity of the stars also affects their NLTE corrections, but nevertheless we find it intsructive to consider temperature as one useful discriminating variable). This gives rise to a change in the difference $\Delta T_{\mathrm{eff},S_H=0} - \Delta T_{\mathrm{eff},S_H=1}$ with temperature, with this quantity being negative for the two hottest stars, CD−33°1173 and LP815−43. The switch over from $S_H = 0$ having the larger correction to $S_H = 1$ having the larger correction is at around $T_{\mathrm{eff}} \approx 6200$ K . Further testing has shown that this is not a random error and is clearly something to investigate further in the future. This is further shown by Fig. 26 where the abundance correction versus χ for the stars CD−33°1173 and LP815−43 (SGB) are plotted. It is seen that for LP815−43 (SGB), increasing S_H has a larger effect on the lower excitation lines than for higher ones. This has induced a trend of abundance with χ larger than that of the $S_H = 0$ case. This in turn leads to a larger temperature correction for $S_H = 1$ than for $S_H = 0$. The reason for this effect is still uncertain.

To investigate this behaviour further, the test of increasing the S_H value of the upper levels, as done on HD140283 in Sect 4., has also been performed on LP815−43 for the MS and SGB parameters. This has shown that the effect of collisions with neutral H are indeed larger for the lower levels of the atom, and that this effect is larger for LP815−43 (MS), which is the hottest star. This indicates that there is a temperature dependence, i.e. the difference between the mean difference $(\Delta A(\mathrm{Fe})_{S_H=1+2} - \Delta A(\mathrm{Fe})_{S_H=1})$ (where $S_H = 1 + 2$ indicates the scenario of having $S_H = 2$ for the top 0.5 eV worth of levels) for the levels with $\chi < 2$ eV and those with $\chi > 2$ eV is greater for the hotter star, LP815−43 (MS). However, when performing this test on LP815−43 (SGB), which has a similar log g to HD140283 whilst still being hotter, the effect is not as great as for HD140283. This shows that there is some gravity dependence on the neutral H collisions along with the temperature dependence i.e. the gravity indirectly affects the collisional rates, by impacting on the number density of hydrogen atoms at a given optical depth. Fig. 26, along with Fig. 23, clearly show that NLTE has varying star to star effects, i.e. from the similar effects at different S_H values in HD140283 (Fig. 23), to the differing effects in CD−33°1173 and LP815−43 (SGB) (Fig. 26). The range of ΔT_{eff} values, and the negative value for CD−33°1173, shows the intricacies of the NLTE process, and that generalisations are not easily made when identifying the effects of NLTE on temperatures determined by the excitation energy method. For the purposes of this paper, which is concerned with the effective temperatures in the context of the available NLTE model, it is appropriate to acknowledge these NLTE effects and to move ahead to use them in the study of the Li problem, whilst still recognising that much work remains before we approach a complete description of the Fe atom.

Although we discussed the possibility that the extreme (negative) ΔT_{eff} correction for CD−33°1173 is due to corrrections being temperature-dependent, this unusual case may be in part due to the fact that only a subset of the original lines measured is available through the NLTE atomic model. The atomic model does not contain every level of the Fe atom and therefore some transitions are not present in the calculations. This means that not every line measured for a given star is present in the calculations and leads to a trend being introduced in the χ-abundance plot prior to the trend induced
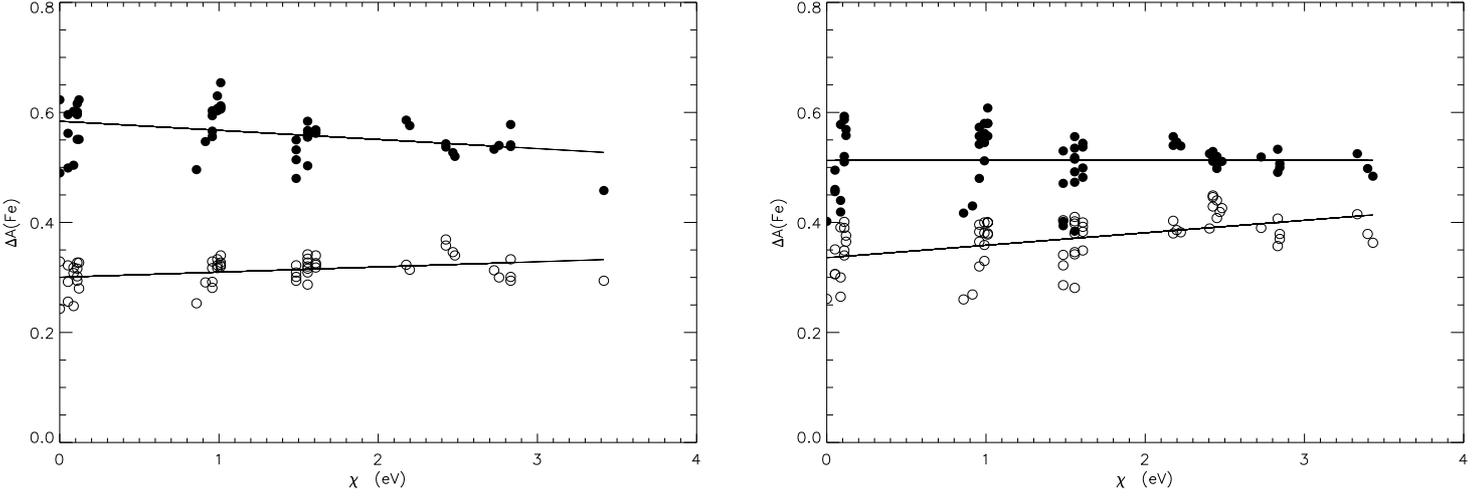
Fig. 26. Abudance correction versus χ for (left panel) CD$-33°1173$ and (right panel) LP815-43 for $S_H = 0$ (filled circles) and $S_H = 1$ (open circles).

by the NLTE corrections. This is because the original nulling of the χ-abundance plot was achieved with a greater number of points. CD$-33°1173$ has the least lines available from the atomic model used with MULTI, however, there is no distinct trend between ΔT_{eff} and the number of lines available for each star, and after testing we found that the effect of the subset, i.e. the measured lines that are available with our atomic model, is to increase the LTE temperature. This implies that the decrease in T_{eff} for this star is most likely due to NLTE effects. Although there is no obvious correlation between the number of lines available and the temperature correction, this emphasises the need for a complete atomic model. This is especially true when considering the abundance of individual lines, as in the excitation technique used in this work.

As in Paper I, we have compared our T_{eff} values with those of Ryan et al. (1999), Meléndez & Ramírez (2004), and Asplund et al. (2006). Fig. 27 presents these comparisons. Comparing against the photometric temperatures of Ryan et al. (1999) for five stars in common, we see that our new T_{eff} scale is hotter by an average of 132 K, with a minimum and maximum of 43 K and 211 K respectively for an $S_H = 0$. Recall that $S_H = 0$ corresponds to the maximal NLTE effect, i.e. no collisions with the hydrogen, for the model atom we have adopted. For $S_H = 1$, our scale is hotter by an average of 162 K, with a minimum and maximum of 101 K and 267 K respectively.

We have three stars in common with Meléndez & Ramírez (2004). Their temperatures are hotter than the ones we derived here by 196 K on average for $S_H = 0$ with a minimum and maximum difference of 27 K and 381 K respectively, and by 193 K on average for $S_H = 1$, with a minimum and maximum difference of 84 K and 247 K respectively. Therefore, even with NLTE corrections we still cannot achieve the high T_{eff} of the Meléndez & Ramírez (2004) study. It has however been noted (Meléndez 2009 - private communication) that the Meléndez & Ramírez (2004) temperatures suffer from systematic errors due a imperfect calibration of the bolometric correction for the choice of photometric bands
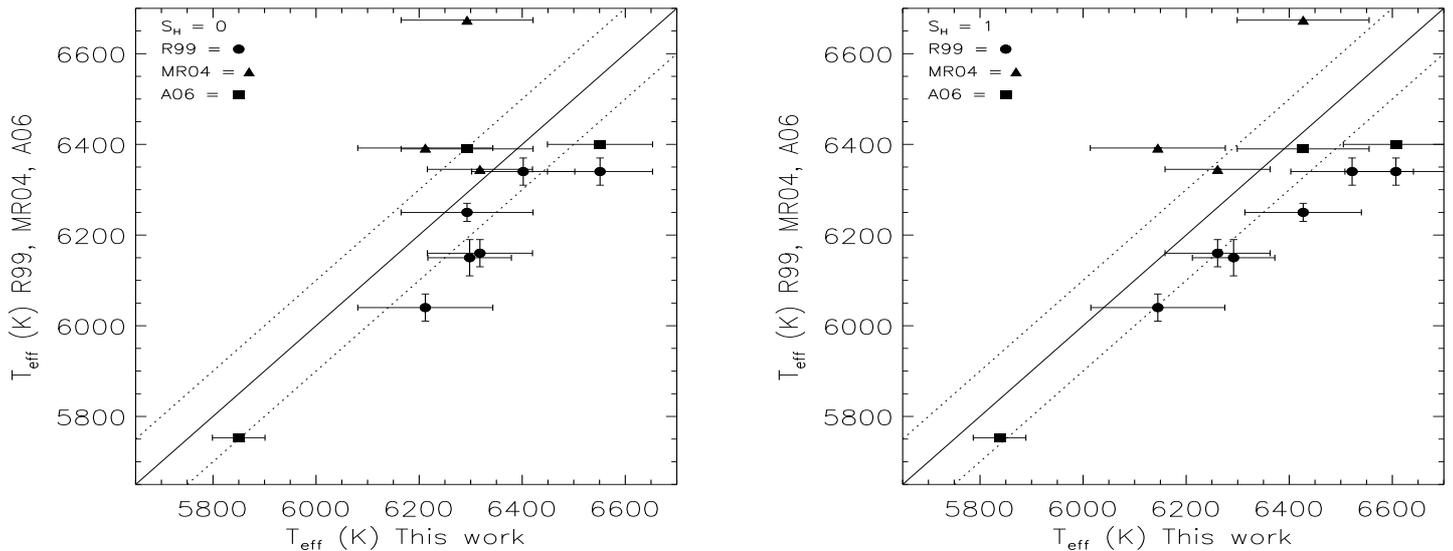
Fig. 27. T_{eff} comparison between this work and Ryan et al. (1999, R99) (filled circles), Meléndez & Ramírez (2004, MR04) (filled triangles) and Asplund et al. (2006, A06) (filled squares), for (left panel) $S_H = 0$ and (right panel) $S_H = 1$. Dashed lines are $\pm$ 100 K limits.

used. This led to an inaccurate zero point and hotter T_{eff}'s than most other studies. The revision of their temperature scale is not yet available and comparisons to their new T_{eff}'s is not possible at this time.

Finally, we have three stars in common with Asplund et al. (2006). Using $S_H = 0$ we obtain temperatures for two of the stars that are hotter than Asplund et al. (2006) by 97 K and 151 K. The third star is CD$-33°1173$, for which we calculated a negative temperature correction, and which is cooler in our study by 97 K. The temperatures for all three stars are hotter in our study than in Asplund et al. (2006) when using $S_H = 1$. Here the average difference is 110 K, values ranging from 37 K to 207 K. If the Asplund et al. (2006) temperatures are affected by NLTE, as stated by Barklem (2007) who expects a 100 K increase in Balmer line temperatures, this would bring the T_{eff} scales back into agreement.

6.2. Lithium abundances

We now address the new Li abundances and their effect on the lithium problem. We see that the introduction of NLTE corrections to the T_{eff} scale has led to temperatures that are of order 100 K hotter than LTE temperature scales, with the obvious exception of the Meléndez & Ramírez (2004) scale. This will then lead to an increase in the mean lithium abundance. Table 10 lists $A(\mathrm{Li})$ for the new temperatures. With these new T_{eff}'s, we calculate a mean Li abundance of $A(\mathrm{Li}) = 2.19$ dex with a scatter of 0.072 dex when using $S_H = 0$, and $A(\mathrm{Li}) = 2.21$ dex with a scatter of 0.058 dex for the $S_H = 1$ case. Consistent with the temperature increase, these values are higher than those found by other studies, in particular Spite et al. (1996), who found a value of $A(\mathrm{Li}) = 2.08$ (± 0.08) dex using a similar iron excitation energy technique but without the NLTE corrections, Bonifacio et al. (2007) with $A(\mathrm{Li}) = 2.10$ (± 0.09) using a Balmer line wing temperature scale, and $A(\mathrm{Li}) = 2.16$ dex or $A(\mathrm{Li}) = 2.10$ depending on the evolutionary state from Hosford et al. (2009). The NLTE corrections have moved the mean Li abundance closer to, but not consistent with, the WMAP value of $A(\mathrm{Li})$
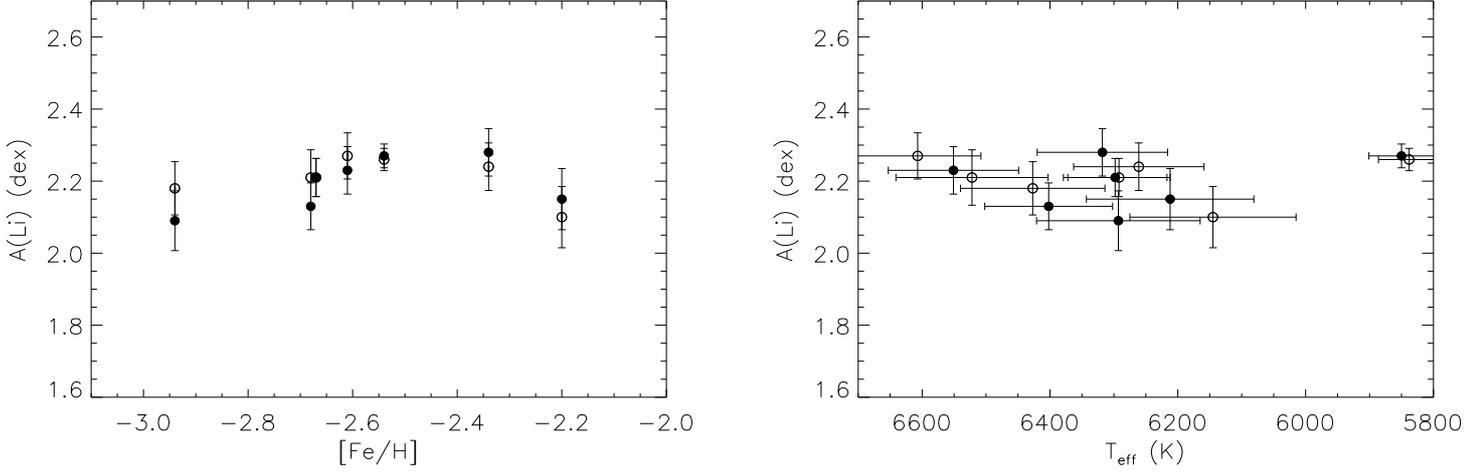
Fig. 28. Lithium abundance versus [Fe/H] (left panel) and T_{eff} (right panel) for $S_H = 0$ (filled circles) and 1 (open circles).

= 2.72 dex, and thus still leaves the lithium problem unsolved. It is noted that even the Meléndez & Ramírez (2004) scale, whilst bringing the observed and theoretical Li abundances closer, still failed to solve the lithium problem.

Fig. 28 shows the lithium abundances versus [Fe/H] and T_{eff}, least squares fits have been performed for both sets of data. In the fit to metallicity we get the values:

$$A(\text{Li}) = 2.55(\pm 0.31) + 0.137(\pm 0.119)[\text{Fe/H}] \tag{8}$$

for $S_H = 0$ and

$$A(\text{Li}) = 2.04(\pm 0.26) - 0.067(\pm 0.102)[\text{Fe/H}] \tag{9}$$

for $S_H = 1$. For $S_H = 0$, we see a similar values to the coefficient of metallicity as Ryan et al. (1999), whilst for $S_H = 1$, we have a value that is about half the size, and has a negative slope. However, our errors are much larger, due to the large random errors and small sample of stars, and therefore no statistically relevant trend can be deduced. For T_{eff}, we get the equations:

$$A(\text{Li}) = 2.77(\pm 0.91) - 0.00009(\pm 0.00015)T_{\text{eff}} \tag{10}$$

for $S_H = 0$ and

$$A(\text{Li}) = 2.09(\pm 0.63) + 0.00002(\pm 0.00010)T_{\text{eff}} \tag{11}$$

for $S_H = 1$. Here we see no statistically relevant trend with T_{eff} for either S_H value.

We also perform the fit as described by Ryan et al. (2000), such that:

$$Li/H = a' + b' Fe/Fe_\odot \tag{12}$$

where a' measures the primordial abundance of Li and b' is a probe of galactic chemical evolution. For this fit, we obtain the primordial values of ^{7}Li/H $= (1.47 \pm 0.27) \times 10^{-10}$ for $S_H = 0$ and ^{7}Li/H $= (1.80 \pm 0.16) \times 10^{-10}$ for $S_H = 1$. Both of these values are far from the high value of ^{7}Li/H $= 5.24^{+0.71}_{-0.62} \times 10^{-10}$ (Cyburt et al. 2008) from WMAP and BBN.

We see then that the addition of NLTE corrections has led to an increase in T_{eff} for most stars. This equates to an increase in A(Li) but it is still not high enough to reconcile the lithium problem. Through the efforts of Hosford et al. (2009) and this study it is safe to conclude that systematic errors in the metal-poor T_{eff} scale are almost certainly not large enough to be the source of the A(Li) discrepancy between observation and WMAP + BBN predictions. This outcome lends strength to other possible explanations, such as processing in the stars, e.g. diffusion, processing in earlier generations of stars, and/or different BBN networks, or more exotic solutions requiring physics beyond the standard model.

It should be noted that while we have computed Fe lines in NLTE to constrain the temperature, our Li abundances are calculated from a grid of abundance versus equivalent width that was constructed under the assumptions of LTE, see Paper I for details. Several studies of the effects of NLTE Li line formation have been conducted. Two of these studies are those of Carlsson et al. (1994) and Lind et al. (2009); they find Li abundance corrections of $\sim +0.013 - +0.020$ dex and $\sim +0.01 - +0.03$ dex respectively for the temperature, log g and [Fe/H] range in this study. Due to the very small size of these corrections we find the use of the LTE grid, combined with our NLTE effective temperatures, to be acceptable in determining Li abundances, and that the introduction of NLTE Li abundances will not significantly aid in solving the lithium problem.

6.3. Implications of NLTE calculations for ionization balance and S_H

Having discussed the effects of NLTE corrections on the T_{eff} scale and the lithium abundances, it is also of interest to note the effect on an aspect of abundance analysis, specifically ionization equilibrium often used in the determination of log g. We can also make a preliminary investigation into constraints we can place on the value of S_H from our results.

It has been noted previously (Gehren et al. 2001) that Fe II lines are relatively unaffected by NLTE. In this work we have also found this to be the case with values for Fe II abundance corrections of order 0.01 dex. Our NLTE calculations induce a mean difference between ΔA(Fe I) and ΔA(Fe II) of 0.39 dex for $S_H = 0$ and 0.27 dex for $S_H = 1$. Knowing that a 0.1 dex change in log g induces a difference of 0.05 dex between Fe I and Fe II abundance, for there to be ionization balance, one would need a correction of $\sim +0.8$ dex and $+0.5$ dex in log g for $S_H = 0$ and 1 respectively. That is, due to overionization, forcing ionization balance for metal-poor dwarfs under LTE calculations would give log g values too low by 0.8 dex ($S_H = 0$) or 0.5 dex ($S_H = 1$). LTE calculations for HD140283 have occasionally yielded gravities lower than the HIPPARCOS gravity by ~ 0.3 (e.g. Ryan et al. 1996b), and for a selection of 13 halo main sequence turnoff stars with HIPPARCOS parallaxes Ryan et al. (2009 - in preperation) determine a mean difference of 0.2 in log g compared to LTE ionization balance. These differences are less than what we compute for $S_H = 1$, and suggest that for the model atom

we are using, the choice of $S_H = 1$ may underestimate the role of collisions with neutral hydrogen in diminishing the departures from LTE for Fe, i.e. that $S_H > 1$. Whilst we have not attempted a detailed derivation of S_H by this method, Korn et al. (2003) has, arriving at a value of $S_H = 3$ based on the analysis of four halo stars and two others. Our results are broadly consistent with their conclusion.

7. Conclusions

We have discussed the processes of NLTE line formation of Fe lines. Here, we have shown the challenges posed by such calculations and the uncertainties that still arise, in particular due to the unknown magnitude of H collisions. One obvious next step would be to tie down the value of S_H for metal-poor stars, for example by forcing the equality of HIPPARCOS gravities and those determined by ionization equilibrium by changing S_H (Korn et al. 2003). For this reason we have discussed the effect of NLTE corrections on the ionization equilibrium and the magnitude of the effect on $\log g$.

Six of the original program stars from Paper I have been analysed to calculate the effects of NLTE on the T_{eff} scale derived from Fe I lines via excitation equilibrium. We have found that the effect of the correction is to cause an increase in T_{eff} ranging from 2 K to 150 K for $S_H = 0$ and 41 K to 122 K for $S_H = 1$. There is one exception; the star CD$-33°1173$ has a negative correction (-93 K) for the $S_H = 0$ case. This may be due to the limited number of Fe lines available for this star, but also emphasises the intricacies of NLTE work which make it difficult to make reliable generalisations.

Our new temperatures have been compared to the photometric temperatures of Ryan et al. (1999), the IRFM of Meléndez & Ramírez (2004), and the Balmer line wing method of Asplund et al. (2006). We find that the NLTE temperatures are hotter than Ryan et al. (1999) by an average of 132 K for $S_H = 0$ and 162 K for $S_H = 1$. Similar results are found when comparing against Asplund et al. (2006) with average differences of 76 K and 110 K for $S_H = 0$ and 1 respectively. The difference between our temperatures and the Asplund et al. (2006) temperatures may be removed if the Balmer line wing method suffers from NLTE effects (Barklem 2007). We find that even with NLTE corrections we are unable to match the high T_{eff}'s of Meléndez & Ramírez (2004). However, it has been acknowledged that their temperatures suffer from systematic errors (Meléndez 2009 - private communication) and a revision of their temperature scale is under way.

With our new T_{eff} scale, new Li abundances have been calculated. This has led to an increase of the mean Li abundance from Hosford et al. (2009) to values of 2.19 dex with a scatter of 0.07 dex and 2.21 dex with a scatter of 0.06 dex for $S_H = 0$ and 1 respectively, both of which lie well below the value of 2.72 dex inferred from WMAP+BBN (Cyburt et al. 2008). This has shown that systematic errors in the T_{eff} scale of metal-poor stars are not the cause for the discrepency.

References

Alonso, A., Arribas, S., & Martinez-Roger, C. 1996, A&AS, 117, 227

Aoki, W., Barklem, P. S., Beers, T. C., et al. 2009, ApJ, 698, 1803

Asplund, M. 2005, ARA&A, 43, 481

Asplund, M., Gustafsson, B., Kiselman, D., & Eriksson, K. 1997, A&A, 318, 521

Asplund, M., Lambert, D. L., Nissen, P. E., Primas, F., & Smith, V. V. 2006, ApJ, 644, 229

Asplund, M., Nordlund, Å., Trampedach, R., & Stein, R. F. 1999, A&A, 346, L17

Barklem, P. S. 2007, A&A, 466, 327

Barklem, P. S., Belyaev, A. K., & Asplund, M. 2003, A&A, 409, L1

Bautista, M. A. 1997, A&AS, 122, 167

Bonifacio, P., Molaro, P., Sivarani, T., et al. 2007, A&A, 462, 851

Carlsson, M. 1986, Uppsala Astronomical Observatory Reports, 33

Carlsson, M., Rutten, R. J., Bruls, J. H. M. J., & Shchukina, N. G. 1994, A&A, 288, 860

Collet, R., Asplund, M., & Thévenin, F. 2005, A&A, 442, 643

Cox, A. N. 2000, S&T, 100, 010000

Cyburt, R. H., Fields, B. D., & Olive, K. A. 2008, Journal of Cosmology and Astro-Particle Physics, 11, 12

Drawin, H. W. 1968, Z. Phys., 211, 404

Drawin, H. W. 1969, Z. Phys., 225, 483

Fleck, I., Grosser, J., Schnecke, A., Steen, W., & Voigt, H. 1991, J.phys. B, 24, 4017

Fuhr, J. R., Martin, G. A., & Wiese, W. L. 1988, Atomic transition probabilities. Iron through Nickel, ed. J. R. Fuhr, G. A. Martin, & W. L. Wiese

Fuhrmann, K., Axer, M., & Gehren, T. 1994, A&A, 285, 585

Gehren, T., Butler, K., Mashonkina, L., Reetz, J., & Shi, J. 2001, A&A, 366, 981

Gratton, R. G., Carretta, E., Eriksson, K., & Gustafsson, B. 1999, A&A, 350, 955

Hirata, R. & Horaguchi, T. 1995, Catalogue of Atomic Spectral Lines

Hosford, A., Ryan, S. G., García Pérez, A. E., Norris, J. E., & Olive, K. A. 2009, A&A, 493, 601

Jedamzik, K. & Pospelov, M. 2009, New J. Phys., 11, 105028

Korn, A. J. 2008, Physica Scripta Volume T, 133, 014009

Korn, A. J., Shi, J., & Gehren, T. 2003, A&A, 407, 691

Kurucz, R. & Bell, B. 1995, Atomic Line Data (R.L. Kurucz and B. Bell) Kurucz CD-ROM No. 23. Cambridge, Mass.: Smithsonian Astrophysical Observatory, 1995., 23

Lambert, D. L. 1993, Physica Scripta Volume T, 47, 186

Lind, K., Asplund, M., & Barklem, P. S. 2009, A&A, 503, 541

Ludwig, H., Behara, N. T., Steffen, M., & Bonifacio, P. 2009, A&A, 502, L1

Meléndez, J. & Ramírez, I. 2004, ApJ, 615, L33

Mihalas, D. 1978, Stellar atmospheres 2nd edition, ed. J. Hevelius

Nave, G., Johansson, S., Learner, R. C. M., Thorne, A. P., & Brault, J. W. 1994, ApJS, 94, 221

Ryan, S. G., Beers, T. C., Deliyannis, C. P., & Thorburn, J. A. 1996a, ApJ, 458, 543

Ryan, S. G., Beers, T. C., Olive, K. A., Fields, B. D., & Norris, J. E. 2000, ApJ, 530, L57

Ryan, S. G., Norris, J. E., & Beers, T. C. 1996b, ApJ, 471, 254

Ryan, S. G., Norris, J. E., & Beers, T. C. 1999, ApJ, 523, 654

Seaton, M. J. 1987, Journal of Physics B Atomic Molecular Physics, 20, 6363

Seaton, M. J., Yan, Y., Mihalas, D., & Pradhan, A. K. 1994, MNRAS, 266, 805

Shchukina, N. G., Trujillo Bueno, J., & Asplund, M. 2005, ApJ, 618, 939

Spite, F. & Spite, M. 1982, A&A, 115, 357

Spite, M., Francois, P., Nissen, P. E., & Spite, F. 1996, A&A, 307, 172

Steenbock, W. & Holweger, H. 1984, A&A, 130, 319

Thévenin, F. 1989, A&AS, 77, 137

Thévenin, F. 1990, A&AS, 82, 179

Thévenin, F. & Idiart, T. P. 1999, ApJ, 521, 753

van Regemorter, H. 1962, ApJ, 136, 906

8. Fe Analysis

In Paper II we discussed some of the aspects of NLTE effects on the formation of Fe lines and on the methods of testing and calculating the NLTE corrections. Here I continue this discussion by presenting the features of NLTE line formation that did not directly influence the temperature scale calculations, but do give further insight into the processes that occur.

8.1. Effect of electron collisional rates on transitions

In Paper II we discussed the effects of collisions with hydrogen in some detail. A further test that was performed was on the effects of the *electron* collisions on the NLTE calculations. I illustrate this through changes in the departure coefficient for two Fe I levels at 0.96 eV and 3.21 eV (Figure 29) and show the effect on the source function and equivalent width of lines arising from these levels (Table 11 and Table 12). The results are not trivial to interpret, since both increases and decreases of some rates produce changes in populations in the same sense, as we demonstrate. Firstly I examine the case for $S_H = 0$, i.e. no collisions with neutral hydrogen are included, as this reveals more clearly the sensitivity of the departure coefficient to electron collisions. Following this I then show the sensitivity to electrons when collisions with neutral hydrogen are included for $S_H = 1$.

From Figure 29 we see that, starting from the parameter set (**A**) adopted in Paper II, in the cases of both increasing and decreasing bound-bound collisional transition rates (for *electron* collisions) by an order of magnitude (**B** and **C**) there is a decrease in b_i for the 0.96 eV level (top panel), whilst they have minimal affect on the 3.21 eV level (lower panel). In the case of a factor of 10 increase, there are more electrons moved into the upper levels from the lower levels, and therefore the populations of these lower levels (e.g. 0.96 eV) decrease and further electrons are lost from the upper levels through overionization. With bound-

bound collisional transition rates decreased to $1/10^{th}$, the radiative rates dominate. A further decrease in collisions will tend to drive the lower populations further from LTE. A slight recovery of the population of the 3.21 eV level (lower panel) due to the increase/decrease in bound-bound collisional transitions can be seen at around $\tau \approx -3$ relative to neighbouring τ values, with the overionization leading to the general departure from LTE.

In the case of bound-free collisional transition rates, an increase or decrease by a factor of 10 (**F** and **G**) leads to a decrease in b_i for the 0.96 eV levels in the same way as for the bound-bound case. The reasons for this are similar to the bound-bound situation. Increasing bound-free collisional rates by a factor of 10 leads to more electrons being collisionally ionised, particularly from the higher levels where less energy is needed, leading to pumping of electrons from the lower levels, which increases the departure from LTE (decreases b_i) for these levels (e.g. 0.96 eV). Decreasing the rates to $1/10^{th}$ means the greater dominance of the radiative rates and therefore greater departures from LTE. For the higher levels, e.g. 3.21 eV, the increase in bound-free rates leads to the same slight increase in b_i as for the bound-bound rates, most probably due to increased thermalization of the levels through increased collisions, leading to electrons being placed into the continuum, and whose energy is redistributed among other free electrons leading to an equilibrium state.

It is seen that the effect of changing the forbidden line collisional transition rates by a factor of 10 (**D** and **E**) has the largest effect on the departure coefficients. For the lower (0.96 eV) level it is the decrease of these rates that leads to the largest affect on b_i, whilst it is increasing these rates that has the largest affect on the higher level (3.21 eV). In the case of the lower level, a decrease in the rate will lead to more electrons remaining in higher levels, and thus aid the decrease in electron numbers for these levels, implying a smaller b_i. An increase will help repopulate the lower levels and reduce the decrease in b_i. The same applies

146

to our 3.21 eV level, which lies midway in the system, i.e. is roughly half way between 0 eV and the highest level in our model atom at 6.91 eV. It should be noted, however, that the oscillator strengths for these collisional transitions are set to a minimum due to the fact that they are not accurately obtainable at present. The values used therefore could be vastly inaccurate and the effects we see on b_i could thus be inaccurate. This is more of a concern when using maximal NLTE effects, i.e. $S_H = 0$, however, as I shall show next, the effects of electron collisions are minimal compared to that of hydrogen collisions. This means the issue of inaccurate oscillator strengths for the forbidden lines is of less importance.

Comparing Figure 29 with Figure 30 we see the effect of the dominance of collisions with neutral H over collisions with electrons. This is seen by the fact that changes in the electron collisional rates no longer have a marked effect on the departure coefficients when H collisions are induced with the full Drawinian magnitude, i.e. $S_H = 1$. I conclude that, if the correct choice for S_H was closer to 0 than to 1, then my calculations would be sensitive to uncertainties in the transition rates associated with electron collisions, e.g. the uncertain oscillator strengths of the forbidden lines. However, as discussed in Paper II Sect. 6.3, our results suggest values for $S_H > 1$, in broad agreement with Korn et al. (2003) who concluded that $S_H = 3$. Under the higher S_H scenario, Figure 30 shows that my results are quite insensitive to order of magnitude changes in the collisional transition rates associated with electrons.

In Table 11 and Table 12 the values of the departure coefficient and the ratio source function/Planck function are presented for the atmospheric depth where the line optical depth is $\tau_{line} = 2/3$. The tables also give the NLTE-to-LTE equivalent width ratio at the surface, for lines at 3727.62 Å ($\chi = 0.96$ eV) and 4736.77 Å ($\chi = 3.21$ eV). These tables make it easier to see the effects of the different changes in the parameters, discussed above, and the

147

effect these have on the equivalent widths of the emerging spectral lines. Also the effects of adding H collisions (Table 12) are clearly seen; the value for the departure coefficients becomes roughly constant across the different parameter sets when H collisions are introduced (with $S_H = 1$) to the different parameters sets. The driving of values towards LTE due to collisions is also evident in the equivalent width values. All equivalent width values are nearer the LTE values when H collisions are added. The effect is larger for the higher (3.21 eV) level. This may be due to the fact that these higher levels have a greater coupling to the continuum, whose velocity distribution is Maxwellian and therefore in LTE, leading to greater thermalization in these levels compared to the lower levels.

Table 11 Collisional effects due to electrons on the departure coefficient (b_i) of the lower level of the transition, the source function (S_l/B_l) and equivalent width ($W_\lambda/W_{\lambda,LTE}$) for $S_H = 0$ at $\tau_{line} = 2/3$. The parameters are as described above.

Parameter set	$\chi = 0.96$ eV, $\lambda = 3727.62$ Å			$\chi = 3.21$ eV, $\lambda = 4736.77$ Å		
	b_l	S_l/B_l	$W_\lambda/W_{\lambda,lte}$	b_l	S_l/B_l	$W_\lambda/W_{\lambda,lte}$
A	0.254	0.606	0.763	0.478	1.192	0.398
B	0.229	0.637	0.786	0.473	1.205	0.306
C	0.225	0.658	0.772	0.472	1.227	0.298
D	0.242	0.645	0.792	0.475	1.248	0.287
E	0.221	0.634	0.776	0.456	1.136	0.317
F	0.229	0.637	0.786	0.473	1.205	0.306
G	0.225	0.657	0.772	0.466	1.224	0.296
H	0.271	0.700	0.887	0.736	1.097	0.542

Table 12 Collisional effects due to electrons on the departure coefficient (b_i) of the lower level of the transition, the source function (S_l/B_l) and equivalent width ($W_\lambda/W_{\lambda,LTE}$) for $S_H = 1$ at $\tau_{line} = 2/3$. The parameters are as described above.

Parameter set	$\chi = 0.96$ eV, $\lambda = 3727.62$ Å			$\chi = 3.21$ eV, $\lambda = 4736.77$ Å		
	b_l	S_l/B_l	$W_\lambda/W_{\lambda,lte}$	b_l	S_l/B_l	$W_\lambda/W_{\lambda,lte}$
A	0.271	0.700	0.887	0.736	1.097	0.542
B	0.272	0.689	0.899	0.735	1.100	0.530
C	0.272	0.689	0.898	0.734	1.103	0.528
D	0.271	0.690	0.899	0.736	1.099	0.531
E	0.272	0.689	0.898	0.734	1.103	0.528
F	0.273	0.688	0.901	0.745	1.102	0.534
G	0.271	0.689	0.898	0.733	1.103	0.528
H	0.254	0.606	0.763	0.478	1.192	0.398
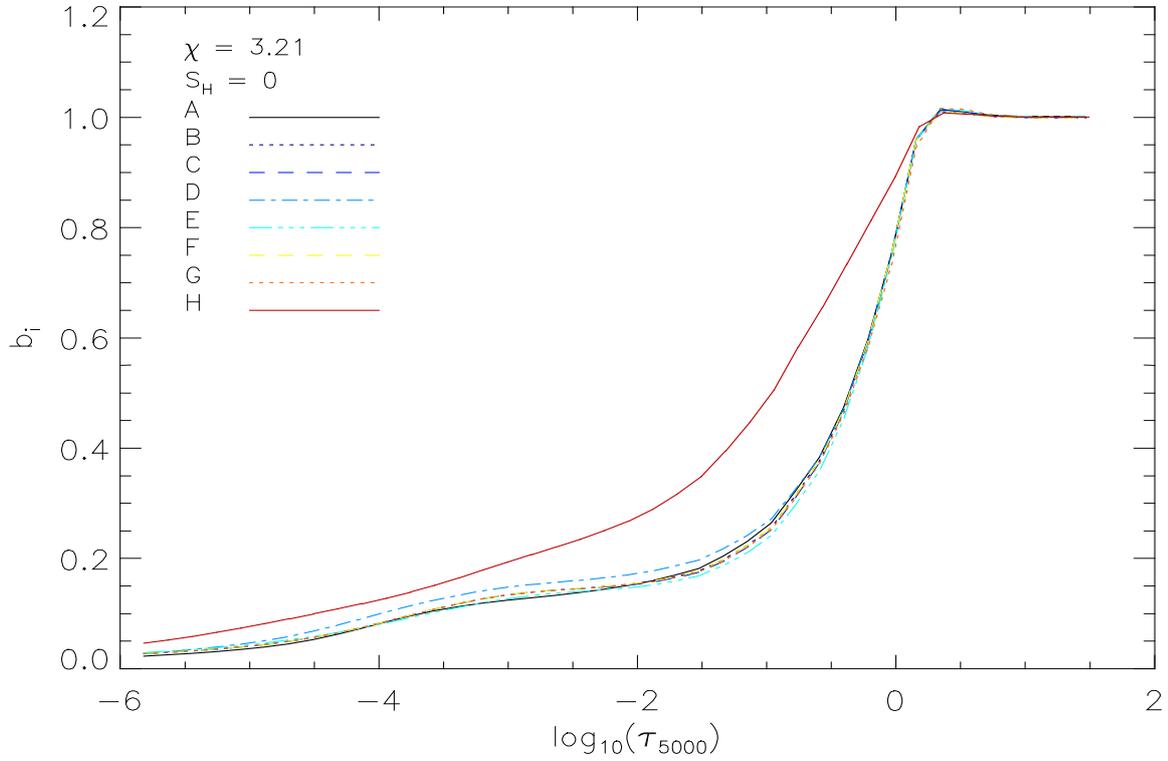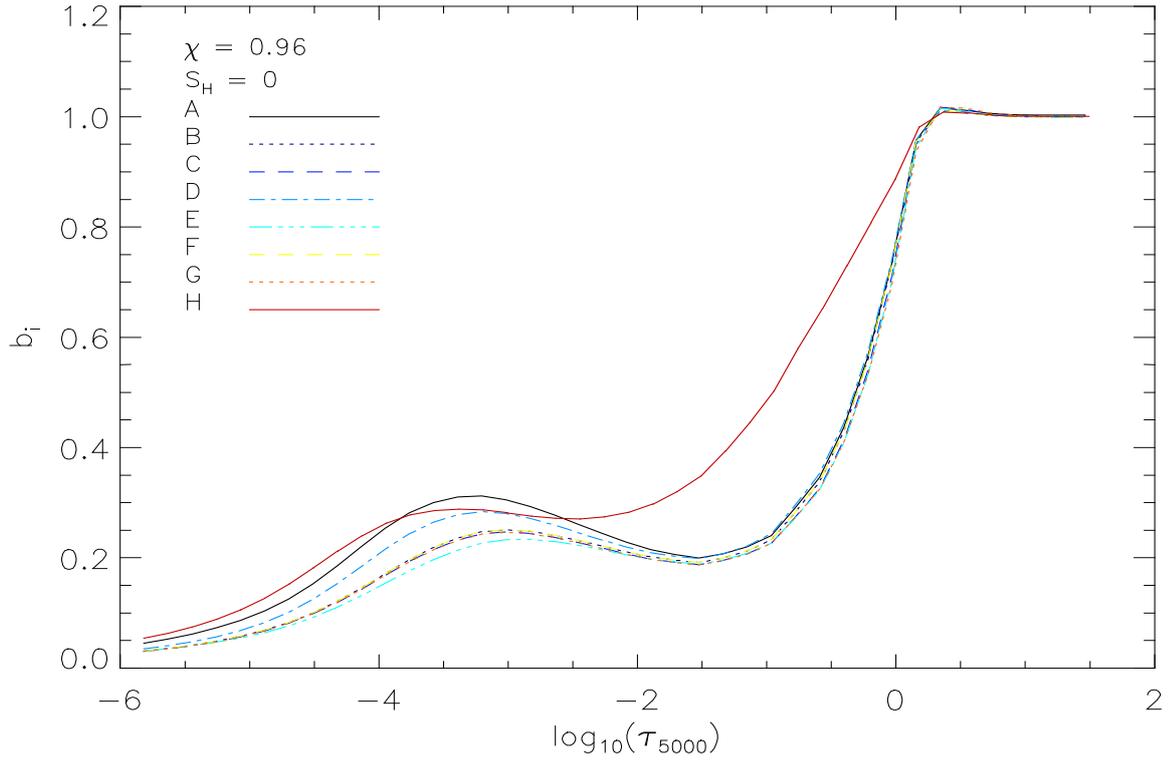
Figure 29 Plots showing the effects of electron collisions on b_i when $S_H = 0$. The different departure coefficients shown are from changing different aspects of electron collisions such that; A: Standard parameters i.e. $S_H = 0$, B: Increasing bound-bound collisional rates with electrons by one order of magnitude, C: Same as B but decreased, D: Collisional excitation rates for forbidden lines increased by one order of magnitude, E: Same as D but decreased, F: Bound-free collisional rates by electrons increased by one order of magnitude, G: Same as F but decreased, and H: With $S_H = 1$.

149
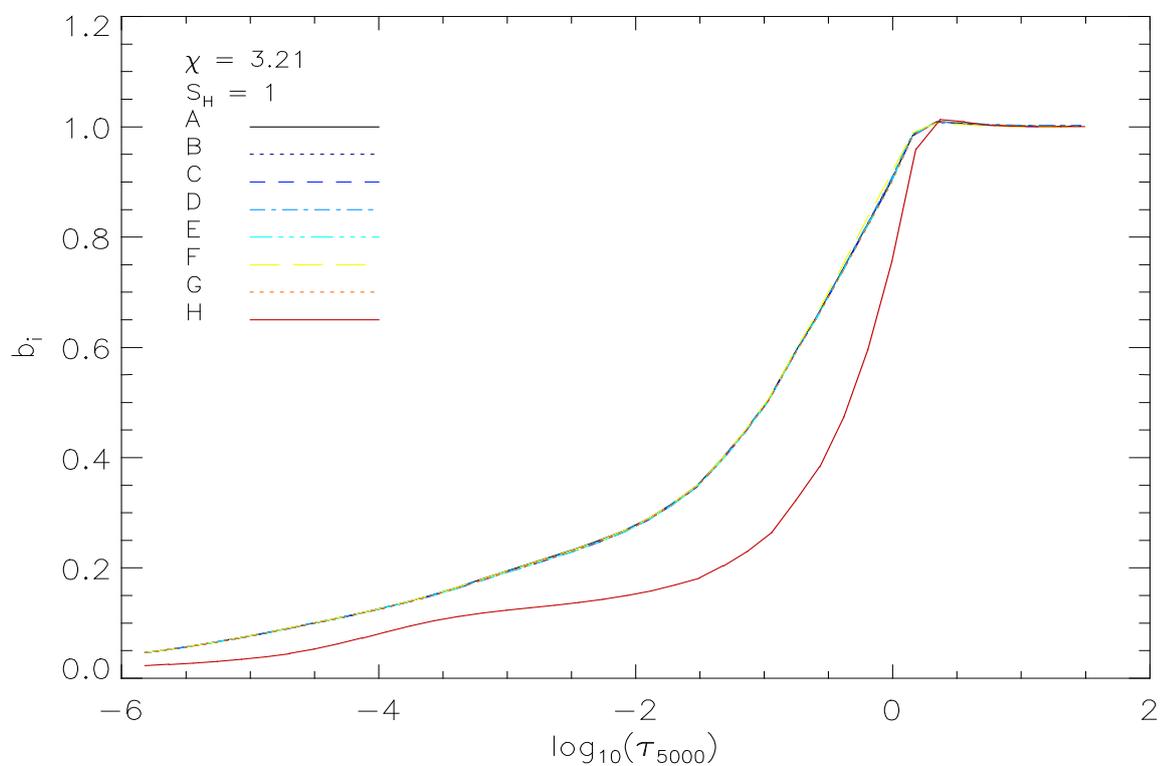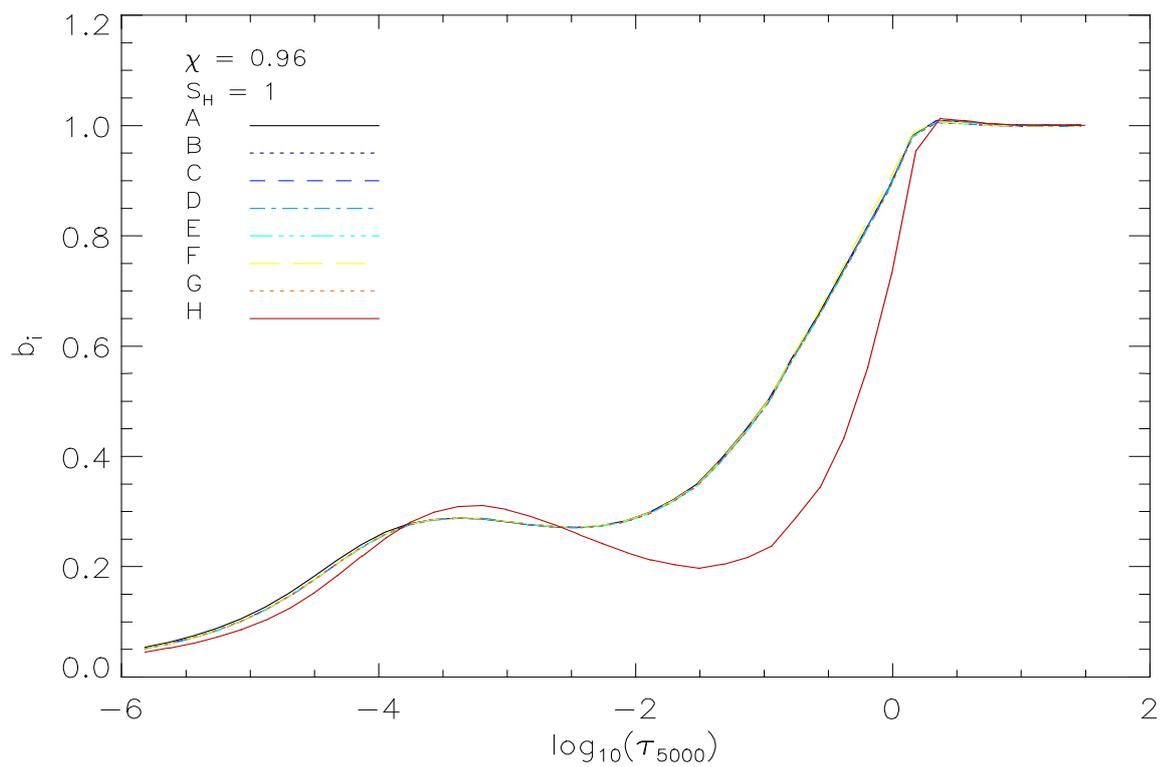
Figure 30 Plots showing the effects of electron collisions on b_i when $S_H = 1$. The different departure coefficients shown are from changing different aspects of electron collisions such that; A: Standard parameters, i.e. $S_H = 1$. B: Increasing bound-bound collisional rates with electrons by one order of magnitude, C: Same as B but decreased, D: Collisional rates for forbidden lines increased by one order of magnitude, E: Same as D but decreased, F: Bound-free collisional rates by electrons increased by one order of magnitude, G: Same as F but decreased, and H: With $S_H = 0$.

150

8.2. Testing NLTE Corrections

Here I continue the discussion of testing the NLTE corrections. To do this, either the measured equivalent width and the equivalent width calculated from the NLTE abundance can be compared, or synthetic and observed line spectra can be compared. I do both. In the case of equivalent widths, the values calculated should be comparable to those measured. The calculated equivalent width is the MULTI width for an abundance such that $A = A_{\mathrm{LTE,WIDTH6}} + \Delta A$ where ΔA is the abundance correction given by $\Delta A = A_{\mathrm{LTE,MULTI}} - A_{\mathrm{NLTE,MULTI}}$. This abundance is then used to interpolate within a grid of equivalent widths from results produced for different abundances from MULTI. It can be seen from Figure 31 that there is a good concordance between the measured and NLTE equivalent widths, particularly at $W_\lambda < 100$ mÅ, with a standard deviation of 3.02 mÅ. The systematic difference at $W_\lambda > 100$ mÅ may be due to the use of Gaussian profiles to measure the equivalent widths were a Voight profile might have been preferable. This then supports the view that the NLTE code is calculating the radiative transfer problem correctly.

Further to this we compare the observed and synthetic spectra. To do this we interpolate within a grid of results from MULTI for different abundances using the NLTE abundance for each measured line in the spectra. Figure 32 presents a section of this comparison for a subset of the measured lines. The good comparison between the two, which is indicative also of the rest of the lines in the sample, shows that MULTI is producing reliable results. There are the exceptions of the couple of lines whose continuum appears not to be fit well, i.e. the lines at 3767.19 Å and 3795.00 Å. These lines are on the wings of a broad absorption feature, and for this reason their continuum appears lower.

Once the NLTE corrections ΔA have been calculated, we plot them versus χ for each line. Figure 33 presents the plots for the remaining HD stars that were not presented in

Figures 23, 25 and 26 of Paper II. Gravities are known well for the HD stars, but less well for the remainder of our sample. Figure 34 and Figure 35 present the plots for the upper and lower gravity limits of the remaining stars. The varying slopes of the trend lines in these plots illustrate the star to star differences of the abundance corrections, and reemphasise the point made in paper II, that it is difficult to makes generalisations about the NLTE correction even for a group of stars which are similar to one another in many respects, i.e. they are all metal-poor main-sequence turnoff stars. It is therefore necessary to carefully evaluate the NLTE effects on each individual star for an accurate study. Figures 33, 34 and 35 present visually the results of the calculations which led to the results presented in tabular form in Paper II, Table 7.
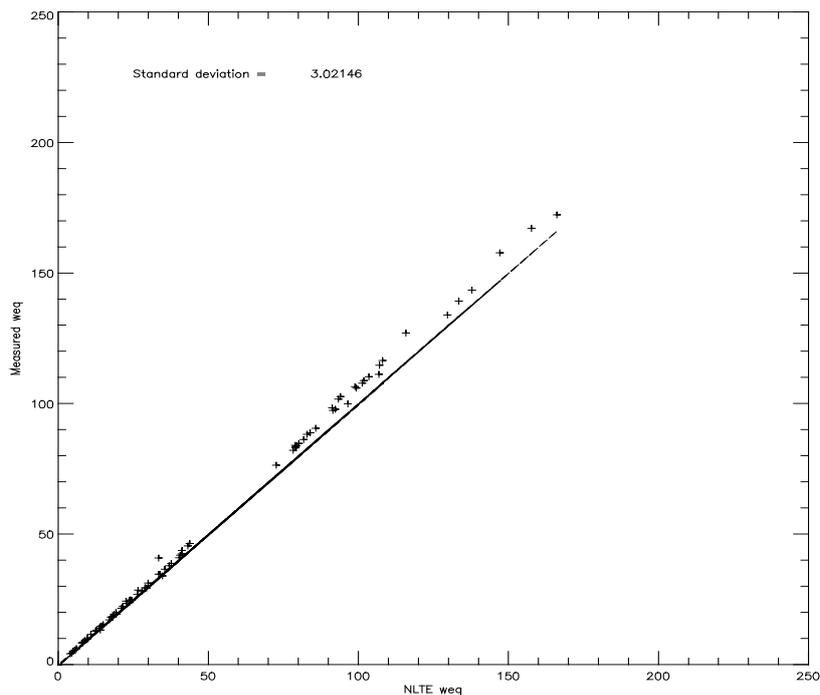
Figure 31 Comparison between measured equivalent width and the equivalent width calculated using the abundance corrections for the star HD140283 with $S_H = 1$.

This point marks the conclusion of the work on the LTE and NLTE effective temperature scales, and their effects on the Li problem. I now go on to discuss the abundances of other elements present in the spectrum of my program stars.
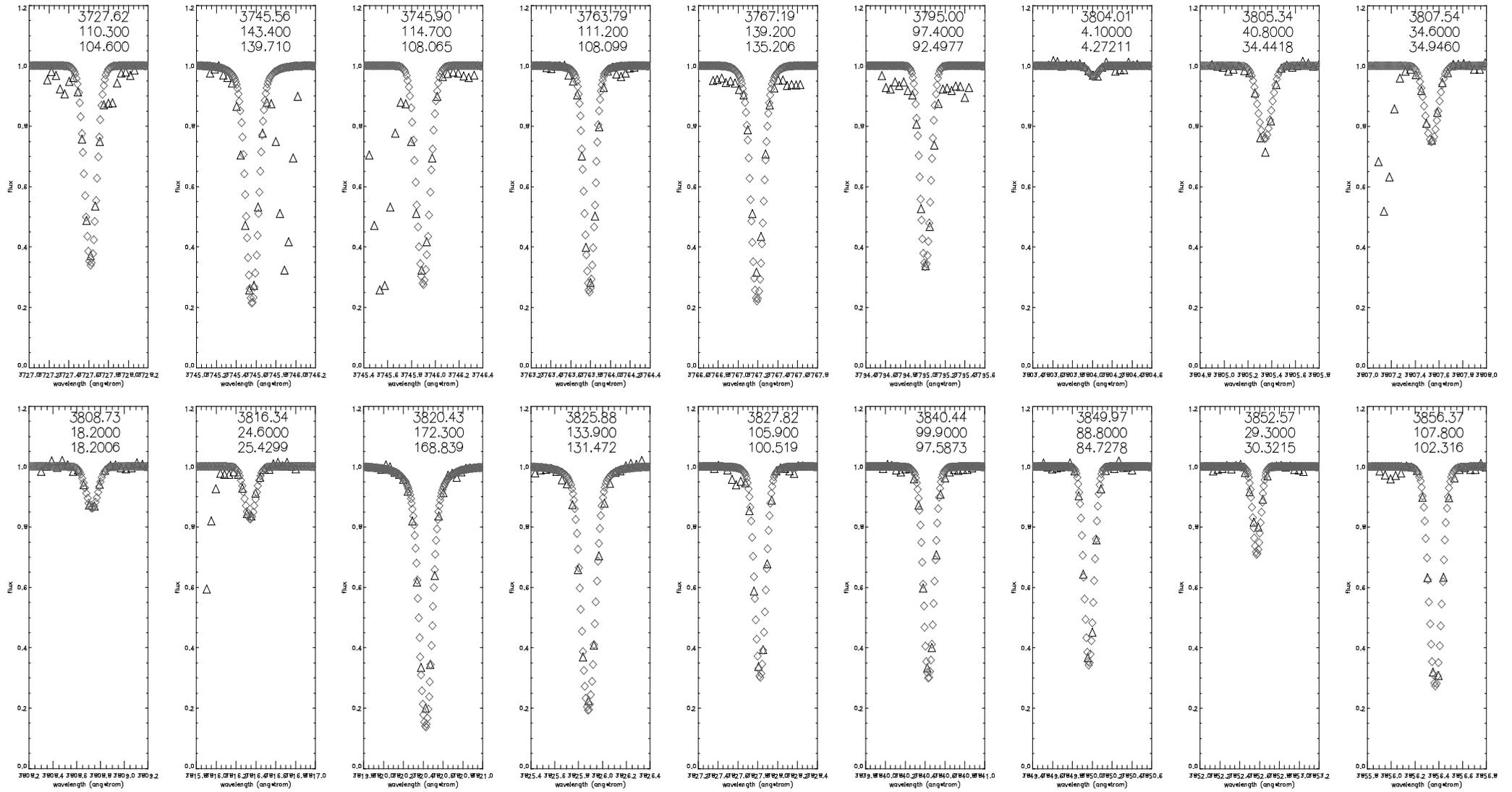
Figure 32 Comparisons between observed spectral lines (triangles) and synthetic spectra produce by MULTI (diamonds) for the star HD140283 with SH = 1. The legend in each box is the wavelength, measured equivalent width (**m**Å) and the MULTI equivalent width (**m**Å).

153
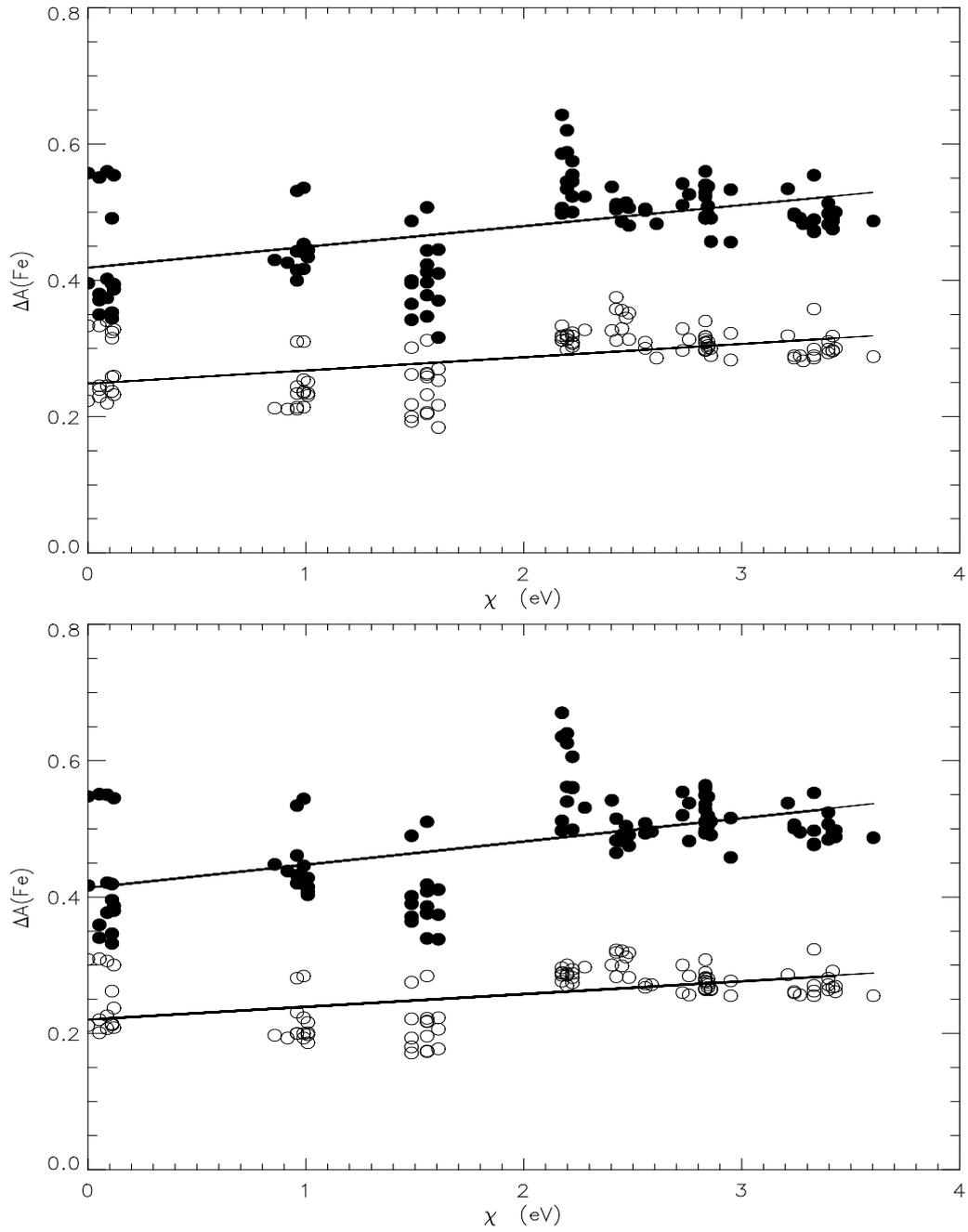
Figure 33 Abundance correction versus χ for the stars (Top panel) HD84937 and (Bottom panel) HD74000 for $S_H = 0$ (filled circles) and 1 (open circles).

154
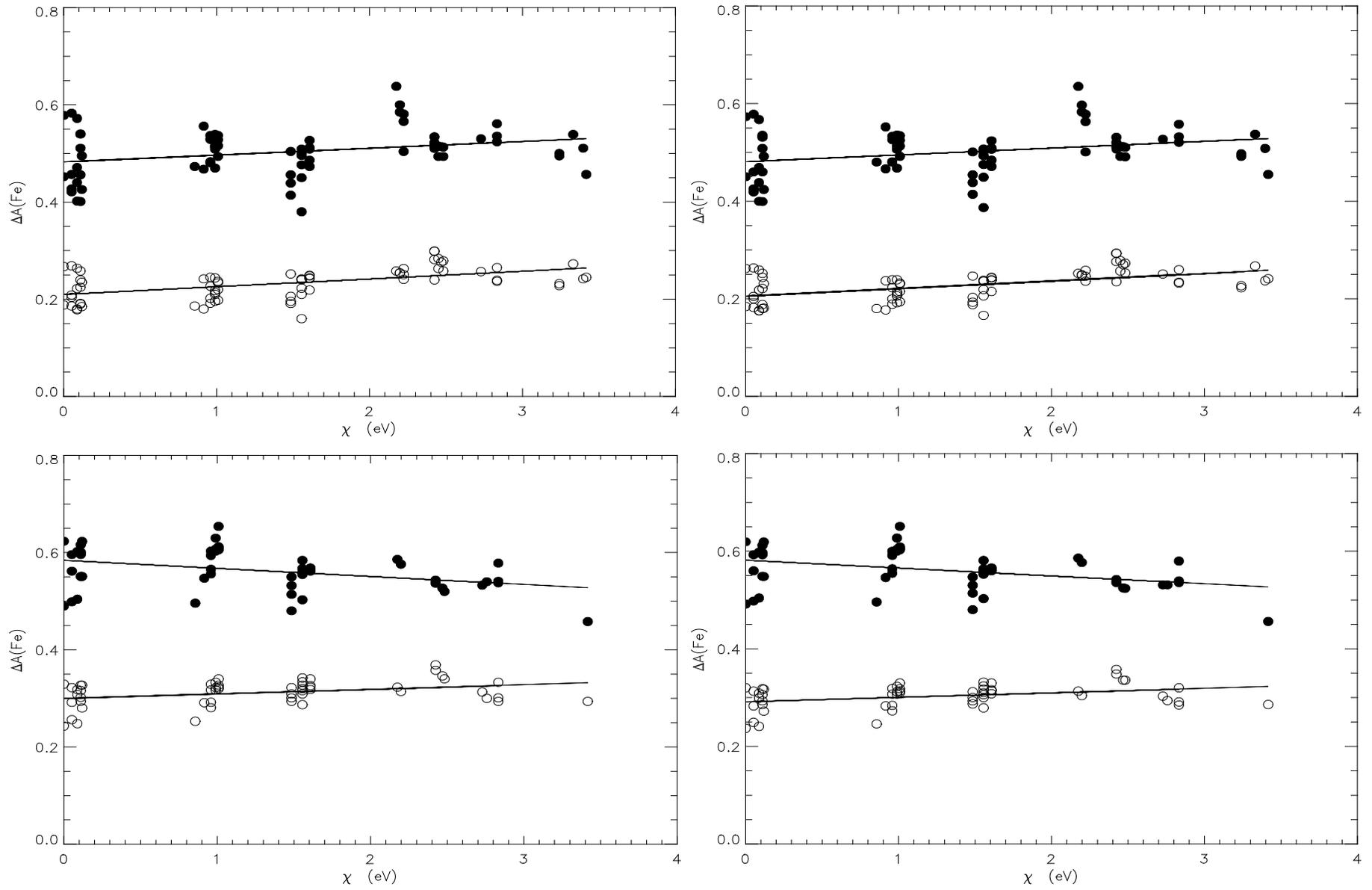
Figure 34 Abundance correction versus χ for the upper (left panels) and lower (right panels) limits of the stars (top panels) BD+26 2621 and (bottom panels) CD-33 1172 for $S_H = 0$ (filled circles) and 1 (open circles).

155
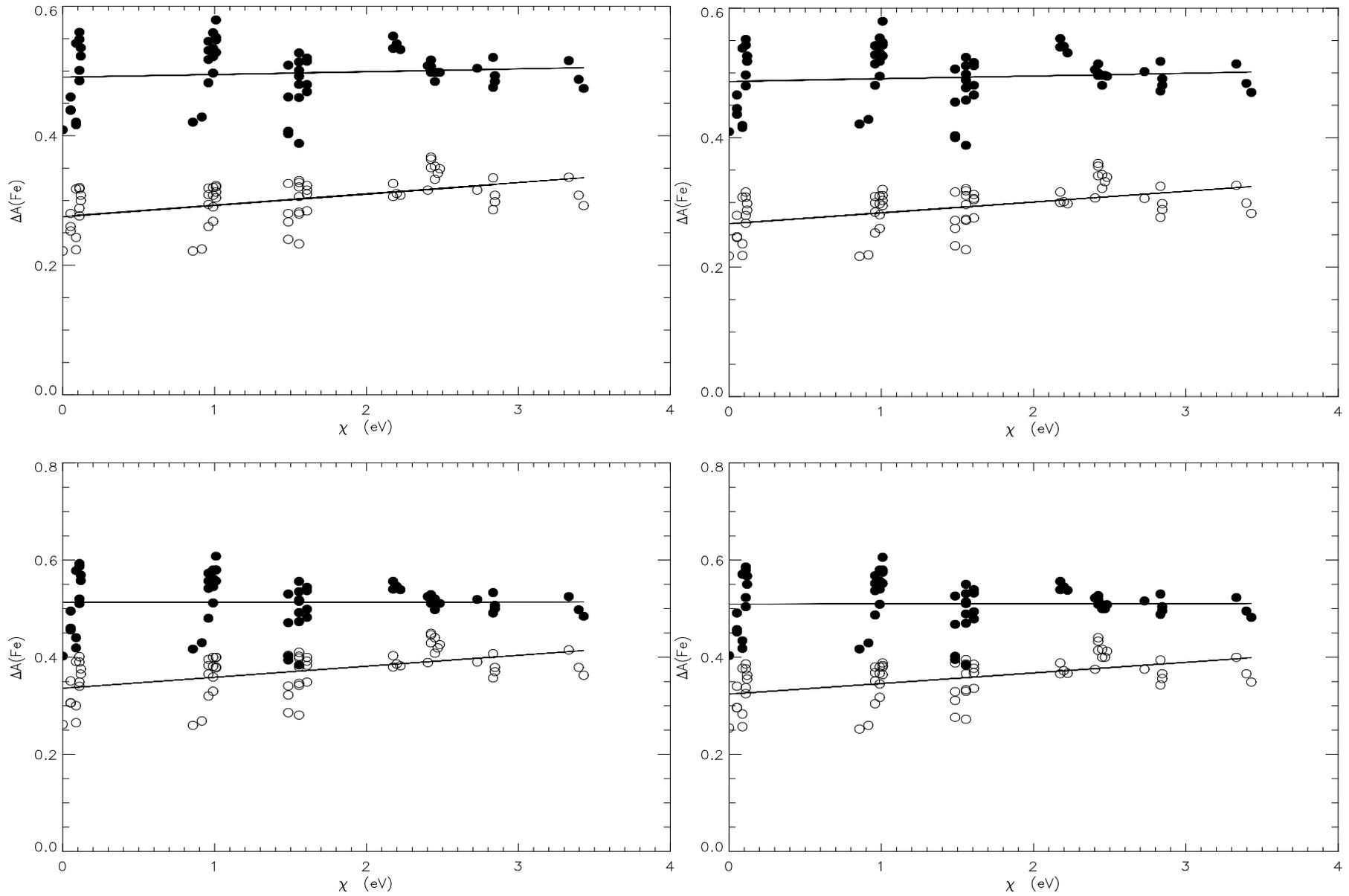
Figure 35 Abundance correction versus χ for the upper (left panels) and lower (right panels) limits of the star LP815-43 SGB (lower panels) and MS (top panels) for $S_H = 0$ (filled circles) and 1 (open circles).

156

9. Titanium, the lithium problem and Galactic chemical evolution

At this point in the thesis I have presented the new T_{eff} calculations in LTE (Paper I – Chapter 4) and NLTE (Paper II – Chapter 7). Supporting these studies I have presented a more detailed discussion on the data analysis (Chapters 2, 3 & 5) along with detailed explanations of the radiative transfer calculations (Chapters 6 & 8). While the principal aim of this thesis was to address the Li problem and in particular effective temperature scales using the abundance of Fe I lines, it is, however, possible to follow the same procedure using spectral lines of other elements. The element that has the most available lines after Fe is Ti. It is therefore possible to attempt to use Ti II to derive the effective temperatures of the program stars. As Ti I and Ti II lines are present in the spectra of the stars it is also possible to use ionisation equilibrium for the determination of log g. In this chapter I present an analysis of the Ti lines and discuss any constraints to the lithium problem they may present.

The lithium problem is also part of the larger problem of Galactic chemical evolution. Due to that large spectral range of the program data there are many lines from several different chemical elements. Having derived new effective temperature scales in the previous parts of this thesis, I can use these to test chemical evolution models by calculating new abundances for the available elements. In the second part of this chapter I present the abundance calculated for the other available elements and compare the results with theories of Galactic chemical evolution.

9.1. Ti I and Ti II as temperature and gravity indicators

The same procedure for constraining the effective temperature using Fe lines is adopted here for Ti II. Equivalent widths are measured and used as input for WIDTH6. Any trends in plots of χ versus Ti abundance are nulled, as discussed in Chapter 4. For this all other parameters

have been kept at the values derived in the Fe analysis, i.e. log g from HIPPARCOS parallax for the HD stars or from isochrones for the remaining stars, [Fe/H] from Fe abundances and ξ from nulling trends in plots of equivalent width versus abundance of individual Fe lines. When calculating log g through ionisation balance I adopt the T_{eff} derived as T_χ from the LTE Fe work.

As the HD stars have well defined parameter sets and evolutionary states, it is sensible to complete the Ti analysis on these stars before considering the rest of the program stars. This is due to the ability to calculate log g value from HIPPARCOS parallax as for these stars, and the many other studies of these stars. Table 13 present the results of the Ti analysis and those from the Fe for comparison. Errors in T_{eff} (Ti) are purely from the nulling procedure and those in log g (Ti) are from the standard error on the mean abundance of Ti I and Ti II.

It can be seen that using the Ti lines results in much higher effective temperatures; the difference between T_{eff} (Ti) and T_{eff} (Fe) is 487 K, 659 K and 378 K for HD140283, HD74000 and HD84937 respectively. The 1σ errors induced by the nulling procedure above ($\pm$230 K to $\pm$ 283 K) are greater than twice the total errors of the Fe analysis, which includes contributions from log g, microturbulence, age, and metallicity. These contributions will lead the T_{eff} (Ti) errors to become even larger; in particular the errors in T_{eff} from microturbulence will be of the same order as those from the nulling procedure. It is therefore clear that using Ti II as a constraint on T_{eff} is counterproductive as the statistical errors are very substantial, and values appear contradictory to those of my Fe analysis and results of previous studies (Asplund et al. 2006 and Meléndez & Ramírez 2004).

The values of log g derived through Ti ionisation balance also are unrealistic results, since when compared to the HIPPARCOS parallax values, differences of -0.19 dex, -0.30 dex

and -0.28 dex are obtained for HD140283, HD74000, and HD84937 respectively. As the HIPPARCOS values are known to be the most reliable, it is obvious that the Ti derived values are low by an average -0.26 dex, and offer no useful constraint.

Table 13. Stellar parameters derived using Fe lines and Ti lines. $\Delta T_{eff} = T_{eff}$ (Ti) - T_{eff} (Fe) and $\Delta \log g = \log g$ (Ti) - $\log g$ (Hipp).

Star	T_{eff}(Fe) (K)	$\log g$ (Hipp) (dex)	[Fe/H]	number of lines (Ti II)	T_{eff}(Ti) (K)	ΔT_{eff} (K)	$\log g$ (Ti) (dex)	$\Delta \log g$ (dex)
HD140283	5769 ± 39	3.73 ± 0.12	-2.54	35	6256 ± 241	487	3.54 ± 0.08	-0.19
HD74000	6070 ± 127	4.03 ± 0.18	-2.20	36	6729 ± 283	659	3.73 ± 0.12	-0.30
HD84937	6168 ± 102	3.98 ± 0.12	-2.34	36	6546 ± 230	378	3.70 ± 0.06	-0.28

The reasons for these differences could be due to the smaller number of measureable lines for Ti and the restricted range of excitation energies they sample. The effect of this is shown in Figure 36. It can clearly be seen that the Ti II lines do not cover the range of χ values that the Fe lines do. The Ti II lines cover the range only from 0.6 eV to 2.6 eV, whereas Fe I range from 0.0 eV to 3.6 eV. This leads will greatly affect the ability to accurately null the χ trends and derive a reliable temperature that is representative of the star. It is for this reason also that the errors are much larger as they stem from the statistical errors from the slope, which will decrease with an increase in the number of lines. Also Ti probably suffers significantly from NLTE effects, like Fe, due again predominantly to overionization. Evidence for this can be seen in the similarity of the atomic structure of the two elements, which also have similar ionisation energies; 7.87 eV and 16.18 eV for Fe I and Fe II respectively compared to 6.82 eV and 13.58 eV for Ti and Ti II respectively. This will particularly effect the ionisation balance determination of $\log g$ using Ti, and like iron, will mean that gravities determined in this way are not suitable for use. It is particularly striking that the average difference in $\log g$ for Ti compared to the HIPPARCOS values (-0.26 dex) is very similar to that reported in Chapter 7 for Fe – 0.3 dex (Ryan et al 1996b), and is

comparable to that inferred from the NLTE analysis of Fe with $S_H = 1$, i.e. 0.5 dex (Chapter 7, Sect. 6.3 – paper II). This is a clear indicator that the NLTE effects that Fe suffers may also be at play in the Ti analysis. It should be noted that overionization is not the only NLTE effect that these elements suffer, therefore NLTE corrections to Ti will be χ dependent as they were for Fe (Chapter 7 – paper II, Figure 23).
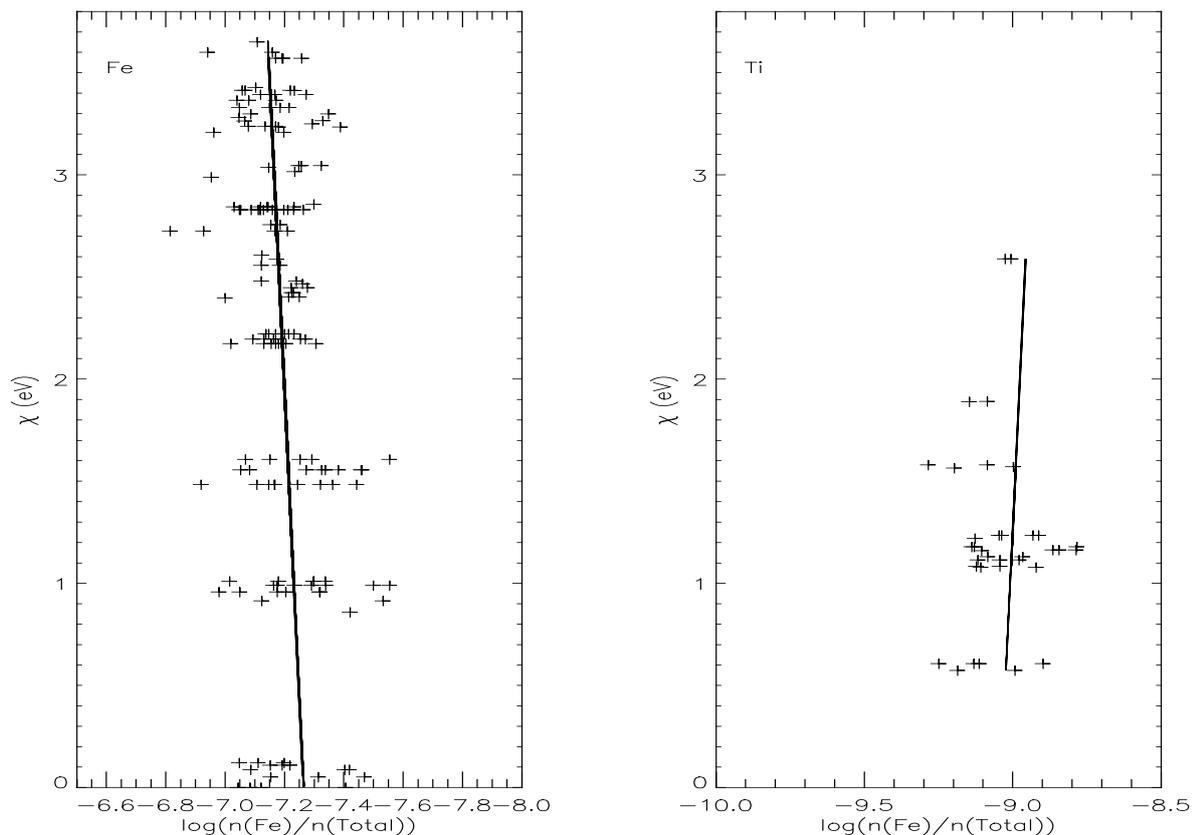
Figure 36. Comparison of plots of χ versus log abundance produced from Fe I abundances (left panel) and Ti II abundances (right panel) for the star HD140283.

These factors combined show that Ti is not a very useful constraint in determining T_{eff} and log g. For this reason, further analysis using Ti will have no useful effect on solving the lithium problem, especially when the need is to narrow down systematic errors.

160

However, the lithium problem is part of the larger issue of Galactic chemical evolution (GCE), i.e. how do the elements of the Galaxy evolve over time. As there are many different elements with lines present in the spectrum of these stars, and with a new effective temperature scale in hand, it would seem logical to perform a full abundance analysis of the remaining elements. This will allow me to see how effective temperatures derived using the methods in this thesis affect the theories of GCE. This is what follows in the remainder of this chapter.

9.2. The evolution of the elements in the Milky Way

Over the course of its history, the Milky Way has undergone a vast amount of star formation. This has lead to a continuous exchange of material between the interstellar medium (ISM), from which the stars are formed, and the stars themselves. Examining the chemical compositions of different classes of stars allows the chemical evolution history of the Galaxy to be discerned. In particular, the low-mass, low-metallicity of stars within the halo of our Galaxy indicate that they are extremely old. The chemical composition of these stars therefore represents the composition of the early Galaxy.

Through numerous theoretical calculations of nucleosynthesis, e.g. Nomoto et al. (1984), Thielemann et al. (1990), and observational studies, e.g. Ryan et al. (1996), Argast et al. (2000, 2002), Cayrel et al. (2004), Arnone et al. (2005), it is now inferred that the enrichment of the early Galaxy was due to supernovae Type II (SNII), whilst chemical evolution was aided by supernovae Type Ia (SNIa). It is, however, still uncertain as to the exact yields and mixing volume of the SNII. If SNII were numerous, and the enriched material produced by them was spread over a large distance, then the distribution of chemical abundances of the early Galaxy would be homogenous even at the lowest metallicity. However, if the mixing volume of the SNII is more local then inhomogeneties will appear at

lower metallicities, which will be reflected in the abundance patterns of metal-poor stars. In a large study of the chemical abundances of extremely metal-poor stars, Ryan et al. (1996) found evidence, i.e. a real star-to-star scatter in abundances with lower metallicities, for a more chaotic scenario for halo formation which involves independently evolving clouds. This evidence supports the more inhomogeneous interpretation of chemical evolution. Argast et al. (2000, 2002) further support this scenario with their implementation of an inhomogeneous Galactic chemical evolution (iGCE) code. However, Arnone et al. (2005) calculated the abundances for Mg, Ti, Ca, and Cr across a metallicity range of $-3.45 < [\text{Fe/H}] < -2.17$, with the aim of tracing early galactic mixing. They found that Mg shows a flat trend with very little scatter, i.e. a standard deviation about the mean of ~ 0.06 dex. This would seem to imply a homogenous scenario in which the ISM was well mixed. With obvious contradictions in results, it is necessary to investigate further into the abundances of metal-poor stars to narrow down the precise scenario for early GCE. Here I hope to aid in this by examining the abundance of several chemical elements within my program stars. This will not be a full, in depth, investigation but an initial examination to identify any evidence for supporting either scenario for GCE.

9.3. Observational data and abundance calculations

Using the spectra from Paper I, I have measured equivalent widths (Appendix to this chapter, Table 24 and Table 25), and calculated the elemental abundance ratios [X/Fe], for the elements: Mg I, Al I, Si I, Ca I, Sc II, Ti I, Ti II, V II, Cr I, Cr II, Mn I, Co I, Ni I, Zn I, Sr II, Y II, and Ba II. **Error! Reference source not found.** presents the line list used for this analysis. The line list contains a broad sample of spectral lines that are available within the spectral range of my data and have been measured in other studies of metal-poor stars. The equivalent width of each line was measured in IRAF by fitting Gaussian profiles. These equivalent widths did not undergo the

Table 14. Line list for additional elements.

Element	λ (Å)	log gf	χ (eV)	Element	λ (Å)	log gf	χ (eV)
Mg I	3829.36	-0.48	2.71	Ti II	4417.72	-1.43	1.17
	3832.30	-0.13	2.71		4418.34	-1.99	1.24
	3838.29	-0.10	2.72		4443.80	-0.70	1.08
	4057.51	-0.89	4.35		4444.55	-2.21	1.12
	4167.27	-0.71	4.35		4450.48	-1.51	1.09
	4571.10	-5.61	0.00		4468.49	-0.60	1.13
	4702.99	-0.38	4.35		4470.87	-2.28	1.17
Al I	3944.01	-0.64	0.00		4501.26	-0.76	1.12
	3961.52	-0.34	0.01		4533.96	-0.77	1.24
Si I	3905.52	-1.04	1.91		4563.76	-0.96	1.22
Ca I	4226.73	0.24	0.00		4571.95	-0.53	1.57
	4283.01	-0.22	1.89		4589.96	-1.79	1.24
	4289.36	-0.30	1.88		4708.66	-2.37	1.24
	4318.65	-0.21	1.90		4779.98	-1.37	2.05
	4434.96	-0.01	1.89	Cr I	3991.12	0.25	2.55
	4454.78	0.26	1.90		4254.33	-0.11	0.00
	4455.89	-0.53	1.90		4274.80	-0.23	0.00
Sc II	4246.83	0.24	0.32		4289.72	-0.36	0.00
	4314.08	-0.10	0.62		4616.12	-1.19	0.98
	4320.72	-0.25	0.61		4646.15	-0.70	1.03
	4324.99	-0.44	0.60	Cr II	4558.65	-0.66	4.08
	4400.39	-0.54	0.61		4588.20	-0.64	4.08
	4415.55	-0.67	0.60		4824.08	-1.22	3.88
Ti I	3729.81	-0.30	0.00		4848.21	-1.14	3.87
	3924.53	-0.88	0.02	Mn I	4030.75	-0.47	0.00
	3958.21	-0.12	0.05		4033.06	-0.62	0.00
	3989.76	-0.14	0.02		4034.48	-0.81	0.00
	3998.64	0.00	0.05		4055.54	-0.07	2.15
	4533.24	0.53	0.85		4823.52	0.14	2.32
	4534.78	0.34	0.84	Co I	3842.05	-0.77	0.92
	4681.91	-1.02	0.05		3845.46	0.01	0.92
	4840.87	-0.45	0.90		3873.11	-0.66	0.43
Ti II	3741.63	-0.11	1.58		3873.96	-0.87	0.51
	3757.67	-0.46	1.57		3894.07	0.10	1.05
	3759.29	0.27	0.61		3995.30	-0.22	0.92
	3761.32	0.17	0.57		4121.31	-0.32	0.92
	3761.88	-0.61	2.59	Ni I	3775.57	-1.41	0.42
	3776.03	-1.34	1.58		3783.52	-1.31	0.42
	3813.38	-2.02	0.61		3807.14	-1.22	0.42
	3900.52	-0.45	1.13		3831.69	-2.27	0.42
	3913.45	-0.53	1.12		3858.29	-0.95	0.42
	3987.63	-2.73	0.61		4231.03	0.29	3.55
	4012.37	-1.75	0.57		4470.49	-0.40	3.40
	4025.14	-1.98	0.61		4648.65	-0.10	3.42
	4028.33	-1.00	1.89		4714.42	0.23	3.38
	4053.80	-1.21	1.89		4715.76	-0.32	3.55
	4163.66	-0.40	2.59		4829.02	-0.33	3.55
	4287.87	-2.02	1.08	Zn I	4722.15	-0.34	4.03
	4290.24	-1.12	1.17		4810.53	-0.14	4.08
	4300.06	-0.49	1.18	Sr II	4077.71	0.15	0.00
	4301.94	-1.20	1.16		4215.52	-0.17	0.00
	4312.87	-1.16	1.18	Y II	3774.33	0.21	0.12
	4330.70	-2.06	1.18		3788.70	-0.07	0.10
	4394.06	-1.77	1.22		3950.36	-0.49	0.10
	4395.04	-0.51	1.09	Ba II	4554.03	0.16	0.00
	4399.78	-1.27	1.24				

more stringent test that the Fe equivalent widths went through, i.e. plotting of equivalent width versus FWHM in velocity space and testing of residuals as in Chapters 4 (Paper I) and 5, due to the smaller number of lines available for each element. This means that where a bad line was measured, it may have continued through the analysis, however in some cases these lines showed up in the abundances by inducing large errors and could be eliminated or flagged.

Having obtained the atmospheric parameters for each star through the Fe analysis (Chapters 4 and 7), it was possible to run WIDTH6 with these values and the equivalent widths for the additional elements. This is a simple LTE analysis of each element. Moreover hyperfine splitting effects are not taken into account for the elements Mn, Co, Sr, Y, and Ba, for which the splitting may be important. WIDTH6 gives abundances as $\log(X/n_{\mathrm{TOT}})$, while the final $[X/\mathrm{Fe}]$ values are given by:

$$[X/\mathrm{Fe}] = \log(X/n_{\mathrm{TOT}})_{\mathrm{star}} - \log(\mathrm{Fe}/n_{\mathrm{TOT}})_{\mathrm{star}} - \log(X/\mathrm{Fe})_{\odot}$$

The solar values are taken from Grevesse & Sauval (1998) and are given in Table 15. Table 16 and Table 17 list the results of $[X/\mathrm{Fe}]$ calculated using my effective temperatures from the LTE analysis discussed in previous chapters. The abundances in Table 16 where calculated using the main-sequence (MS) temperatures, whilst Table 17 uses the sub-giant branch (SGB) temperatures. Errors in the final abundances are the quadrature sum of the errors in the $\log(X/n_{\mathrm{TOT}})$, $\log(\mathrm{Fe}/n_{\mathrm{TOT}})$ and $\log(X/\mathrm{Fe})_{\odot}$ and the effective temperature sensitivity. Errors in $\log(X/n_{\mathrm{TOT}})$ and $\log(\mathrm{Fe}/n_{\mathrm{TOT}})$ come from the statistical error in abundance calculated in WIDTH6, i.e. the standard error due to line-to-line scatter, and errors in $[X/\mathrm{Fe}]_{\odot}$ come from Grevesse & Sauval (1998) (Table 15). Temperature sensitivity errors are calculated by increasing the effective temperature of the model used with WIDTH6 by 100 K. The difference in abundance that this T_{eff} change induces is then the sensitivity to a

164

change in temperature of 100 K. Errors due to changes in log g and ξ are not included, however, from Table 3 Ryan et al. 1996 it can be seen that they are very small and would not adversely affect the results presented here. The errors for abundances calculated using my effective temperatures are given in Table 18 and Table 19. In the cases where only one measureable line is present, WIDTH6 does not calculate an error on the abundance. In these cases I take the error on a single Fe line inferred from the Fe abundance calculations as it is this element which has the greatest number of measureable lines. These therefore approximate the error for other elements. Table 20 presents the number of lines that were measured in each star. Table 21 lists the abundances calculated using the photometric temperatures from the work of Arnone et al. (2005). My sample is a subset of the stars used in their study, and allows for a comparison between different methods of determining effective temperature. Errors in the abundances based in the photometric temperatures of Arnone et al. (2005) are given in Table 22.

Table 15 Solar [X/Fe] values**.**

Element	log(X/Fe) (dex)	Error (dex)
[Fe/H]	-4.53	0.05
[Mg/Fe]	0.11	0.05
[Al/Fe]	-1.00	0.07
[Si/Fe]	0.08	0.05
[Ca/Fe]	-1.11	0.02
[ScII/Fe]	-4.30	0.10
[TiI/Fe]	-2.45	0.06
[TiII/Fe]	-2.45	0.06
[VII/Fe]	-3.47	0.02
[CrI/Fe]	-1.80	0.03
[CrII/Fe]	-1.80	0.03
[MnI/Fe]	-2.08	0.03
[CoI/Fe]	-2.55	0.04
[NiI/Fe]	-1.22	0.04
[ZnI/Fe]	-2.87	0.08
[SrII/Fe]	-4.50	0.07
[YII/Fe]	-5.23	0.03
[BaII/Fe]	-5.34	0.05

Table 16 Abundance ratios for the elements available in the spectrum of the program stars using the MS LTE effective temperatures.

Starname	[Fe/H]	[Mg I/Fe]	[Al I/Fe]	[Si I/Fe]	[Ca I/Fe]	[Sc II/Fe]	[Ti I/Fe]	[Ti II/Fe]	[Cr I/Fe]	[Cr II/Fe]	[Mn I/Fe]	[Co I/Fe]	[Ni I/Fe]	[Sr II/Fe]	[Y II/Fe]	[Ba II/Fe]
BD-13 3442	-2.66	0.21	-0.81	-0.10	0.27	0.44	0.52	0.63	-0.13	0.61	0.18	...	-0.15	0.02	...	-0.70
BD+20 2030	-2.63	0.14	-0.83	0.03	0.25	0.39	0.41	0.54	-0.18	...	0.20	0.21	-0.14	-0.11	-1.06	-0.24
BD+24 1676	-2.53	0.15	-0.93	0.02	0.29	0.41	0.48	0.62	-0.16	0.37	0.37	0.25	-0.08	0.09	...	...
BD+26 2621	-2.67	0.05	-0.92	-0.02	0.19	0.21	0.46	0.42	-0.32	...	0.16	0.26	-0.07	-0.49	...	...
BD+26 3578	...	...	...	...	...	...	...	...	...	...	...	...	...	...	...	...
BD+3 740	-2.72	0.05	-0.83	-0.02	0.34	0.38	0.58	0.61	-0.20	0.00	0.22	0.28	-0.12	-0.20	...	-0.53
BD+9 2190	-2.68	0.08	-0.89	-0.11	0.16	0.35	0.45	0.45	-0.12	0.00	0.32	0.38	-0.20	-0.37	...	-0.21
CD-33 1173	-2.94	0.15	-0.84	-0.07	0.25	0.24	...	0.45	-0.24	0.00	0.21	0.45	-0.13	0.54	...	...
CD-35 14849	-2.36	0.08	-0.91	...	0.19	0.15	0.21	0.43	-0.25	0.42	0.19	0.21	-0.05	-0.36	0.21	-0.73
CD-71 1234	-2.52	0.01	-0.92	-0.02	0.23	0.24	0.31	0.47	-0.20	0.48	0.21	0.34	0.04	-0.65	...	...
G64-12	-3.32	0.30	-0.67	0.02	0.34	0.10	0.87	0.52	-0.17	...	...	0.75	-0.09	0.09	...	-0.06
G64-37	-3.29	0.17	-0.71	-0.03	0.33	...	0.63	0.53	-0.26	...	0.04	...	-0.03	-0.01	...	-0.24
LP635-14	-2.48	0.13	-0.83	-0.09	0.25	0.22	0.39	0.48	-0.23	0.23	0.21	0.28	-0.13	-0.01	0.32	0.31
LP815-43	-2.61	-0.13	-0.98	-0.19	0.15	0.75	0.36	...	-0.24	...	0.11	...	-0.20	-0.13	...	-0.53
HD84937	...	...	...	...	...	...	...	...	...	...	...	...	...	...	...	...
HD140283	...	...	...	...	...	...	...	...	...	...	...	...	...	...	...	...
HD74000	-2.20	0.24	-0.54	0.16	0.26	0.12	0.31	0.39	0.34	0.34	-0.35	0.16	-0.04	-0.15	0.11	0.43

Table 17 Abundance ratios for the elements available in the spectrum of the program stars using the SGB LTE effective temperatures.

starname	[Fe/H]	[Mg I/Fe]	[Al I/Fe]	[Si I/Fe]	[Ca I/Fe]	[Sc II/Fe]	[Ti I/Fe]	[Ti II/Fe]	[Cr I/Fe]	[Cr II/Fe]	[Mn I/Fe]	[Co I/Fe]	[Ni I/Fe]	[Sr II/Fe]	[Y II/Fe]	[Ba II/Fe]
BD-133442	-2.74	0.32	-0.84	-0.06	...	...	0.43	...	-0.18	0.44	0.12	...	-0.22	-0.11	...	-0.93
BD+202030	-2.69	0.24	-0.86	0.15	0.29	0.15	0.34	0.34	-0.23	...	0.13	0.13	-0.21	-0.22	-1.31	-0.48
BD+24 1676	-2.57	0.26	-0.96	0.13	0.31	0.15	0.42	0.39	-0.20	0.12	0.31	0.17	-0.14	...	...	...
BD+26 2621	...	...	...	...	...	...	...	...	...	...	...	...	...	...	...	...
BD+26 3578	-2.42	0.27	-0.81	0.11	0.40	0.14	0.31	0.39	-0.11	-0.40	0.70	0.58	0.34	-0.24	-0.24	-0.63
BD+3 740	-2.82	0.17	-0.84	0.03	0.38	0.20	0.55	0.45	-0.24	...	0.17	0.23	-0.17	-0.35	...	-0.72
BD+9 2190	-2.75	0.18	-0.90	-0.09	0.20	0.16	0.43	0.28	-0.15	...	0.28	0.34	0.02	-0.54	...	-0.40
CD-33 1173	...	...	...	...	...	...	...	...	...	...	...	...	...	...	...	...
CD-35 14849	...	...	...	...	...	...	...	...	...	...	...	...	...	...	...	...
CD-71 1234	-2.54	0.10	-0.95	0.10	0.23	-0.05	0.24	0.21	-0.23	0.19	0.15	0.26	0.01	-0.89	...	...
G64-12	-3.31	0.41	-0.68	0.01	0.39	-0.19	0.86	0.24	-0.19	...	...	0.71	-0.12	-0.16	...	-0.32
G64-37	-3.30	0.37	-0.74	-0.04	0.36	0.01	0.60	0.23	-0.29	...	0.01	...	-0.07	-0.26	...	-0.52
LP635-14	-2.61	0.26	-0.83	-0.02	0.30	0.05	0.35	0.33	-0.25	0.13	0.15	0.22	-0.18	-0.10	0.13	0.15
LP815-43	-2.68	-0.04	-0.99	-0.18	...	...	0.46	0.22	-0.27	...	0.07	...	-0.24	-0.26	...	-0.70
HD84937	-2.34	0.24	-0.79	0.10	0.30	0.25	0.38	0.46	...	-0.29	-0.41	0.22	-0.09	-0.03	-0.01	0.02
HD140283	-2.54	0.16	-0.78	0.11	0.13	0.11	0.21	0.27	-0.20	0.29	0.44	0.31	0.13	-2.39	-0.36	-0.79
HD74000	...	...	...	...	...	...	...	...	...	...	...	...	...	...	...	...

Table 18 Errors in the abundances calculated using the MS LTE effective temperatures.

Starname	[Fe/H]	[Mg I/Fe]	[Al I/Fe]	[Si I/Fe]	[Ca I/Fe]	[Sc II/Fe]	[Ti I/Fe]	[Ti II/Fe]	[Cr I/Fe]	[Cr II/Fe]	[Mn I/Fe]	[Co I/Fe]	[Ni I/Fe]	[Sr II/Fe]	[Y II/Fe]	[Ba II/Fe]
BD-13 3442	0.09	0.13	0.16	0.14	0.10	0.13	0.14	0.09	0.11	0.06	0.16	...	0.11	0.12	...	0.11
BD+20 2030	0.11	0.12	0.20	0.15	0.14	0.13	0.13	0.09	0.11	...	0.11	0.13	0.14	0.15	0.08	0.12
BD+24 1676	0.07	0.10	0.11	0.10	0.09	0.12	0.10	0.09	0.08	0.09	0.10	0.10	0.09	0.12	...	0.09
BD+26 2621	0.11	0.13	0.17	0.16	0.11	0.13	0.13	0.10	0.12	...	0.11	0.14	0.14	0.14	...	0.12
BD+26 3578	...	...	...	...	...	...	...	...	...	...	...	...	...	...	...	...
BD+3 740	0.11	0.13	0.17	0.16	0.12	0.14	0.15	0.10	0.12	...	0.12	0.15	0.13	0.15	...	0.13
BD+9 2190	0.13	0.14	0.21	0.18	0.11	0.13	0.17	0.10	0.13	...	0.13	0.15	0.15	0.16	...	0.14
CD-33 1173	0.07	0.09	0.13	0.10	0.09	0.12	...	0.09	0.08	...	0.13	0.09	0.09	0.11	...	0.09
CD-35 14849	0.06	0.10	0.16	0.09	0.08	0.12	0.09	0.09	0.07	0.06	0.07	0.10	0.08	0.12	0.06	0.08
CD-71 1234	0.07	0.09	0.21	0.10	0.09	0.12	0.10	0.09	0.08	0.06	0.08	0.13	0.13	0.10	...	0.09
G64-12	0.10	0.11	0.14	0.14	0.10	0.12	0.20	0.09	0.11	...	...	0.11	0.13	0.13	...	0.11
G64-37	0.11	0.12	0.17	0.16	0.12	0.14	0.12	0.09	0.13	...	0.11	...	0.13	0.14	...	0.12
LP635-14	0.12	0.17	0.19	0.18	0.12	0.14	0.14	0.10	0.13	0.17	0.13	0.15	0.14	0.15	0.10	0.14
LP815-43	0.11	0.12	0.19	0.16	0.10	0.80	0.23	0.10	0.11	...	0.12	...	0.14	0.15	...	0.12
HD84937	...	...	...	...	...	...	...	...	...	...	...	...	...	...	...	...
HD140283	...	...	...	...	...	...	...	...	...	...	...	...	...	...	...	...
HD74000	0.13	0.13	0.27	0.18	0.12	0.13	0.15	0.10	0.17	0.11	0.15	0.15	0.15	0.16	0.09	0.14

Table 19 Errors to the abundances calculated using the SGB LTE effective temperatures.

Starname	[Fe/H]	[Mg I/Fe]	[Al I/Fe]	[Si I/Fe]	[Ca I/Fe]	[Sc II/Fe]	[Ti I/Fe]	[Ti II/Fe]	[Cr I/Fe]	[Cr II/Fe]	[Mn I/Fe]	[Co I/Fe]	[Ni I/Fe]	[Sr II/Fe]	[Y II/Fe]	[Ba II/Fe]
BD-13 3442	0.09	0.12	0.16	0.14	0.10	0.13	0.13	0.09	0.11	0.06	0.16	...	0.11	0.13	...	0.11
BD+20 2030	0.11	0.11	0.20	0.15	0.10	0.13	0.13	0.09	0.11	...	0.11	0.13	0.14	0.14	0.08	0.12
BD+24 1676	0.09	0.09	0.12	0.10	0.07	0.12	0.10	0.09	0.08	0.09	0.10	0.10	0.09	0.11	...	...
BD+26 2621	...	...	...	...	...	...	...	...	...	...	...	...	...	...	...	...
BD+26 3578	0.08	0.10	0.19	0.13	0.08	0.12	0.12	0.09	0.17	0.40	0.10	0.12	0.11	0.12	0.08	0.10
BD+3 740	0.14	0.13	0.17	0.16	0.11	0.14	0.15	0.09	0.12	...	0.12	0.15	0.13	0.15	...	0.13
BD+9 2190	0.13	0.13	0.22	0.18	0.11	0.13	0.17	0.10	0.13	...	0.13	0.15	0.15	0.16	...	0.14
CD-33 1173	...	...	...	...	...	...	...	...	...	...	...	...	...	...	...	...
CD-35 14849	...	...	...	...	...	...	...	...	...	...	...	...	...	...	...	...
CD-71 1234	0.06	0.09	0.21	0.10	0.07	0.12	0.10	0.09	0.08	0.06	0.08	0.13	0.16	0.11	...	...
G64-12	0.09	0.13	0.14	0.14	0.09	0.12	0.20	0.09	0.11	...	...	0.11	0.13	0.13	...	0.11
G64-37	0.10	0.12	0.17	0.16	0.09	0.14	0.12	0.09	0.13	...	0.11	...	0.13	0.15	...	0.12
LP635-14	0.11	0.12	0.18	0.16	0.10	0.13	0.13	0.09	0.12	0.17	0.12	0.14	0.14	0.14	0.09	0.13
LP815-43	0.11	0.12	0.19	0.16	0.10	0.79	0.22	0.10	0.12	...	0.12	...	0.14	0.16	...	0.12
HD84937	0.12	0.11	0.23	0.15	0.10	0.12	0.12	0.09	0.16	0.61	0.13	0.12	0.15	0.15	0.14	0.12
HD140283	0.08	0.08	0.29	0.09	0.08	0.12	0.09	0.08	0.10	0.06	0.08	0.09	0.09	0.10	0.07	0.08
HD74000	...	...	...	...	...	...	...	...	...	...	...	...	...	...	...	...

Table 20 The number of lines measured for each element in the spectrum of each star.

Star name	[Fe/H]	[Mg I/Fe]	[Al I/Fe]	[Si I/Fe]	[Ca I/Fe]	[Sc II/Fe]	[Ti I/Fe]	[Ti II/Fe]	[Cr I/Fe]	[Cr II/Fe]	[Mn I/Fe]	[Co I/Fe]	[Ni I/Fe]	[Sr II/Fe]	[Y II/Fe]	[Ba II/Fe]
BD-13 3442	86	6	2	1	7	6	4	28	3	1	3	...	4	2	...	1
BD+20 2030	98	6	2	1	4	5	6	26	3	...	3	2	3	2	1	1
BD+24 1676	96	6	2	1	7	6	5	32	...	2	4	2	4	2	...	...
BD+26 2621	107	5	2	1	6	2	5	24	3	...	3	3	3	2	...	...
BD+26 3578	126	6	2	1	4	5	6	32	4	2	5	6	10	2	3	1
BD+3 740	94	5	2	1	6	4	4	25	3	...	3	4	4	2	...	1
BD+9 2190	146	5	2	1	6	5	3	24	3	3	...	4	5	2	...	1
CD-33 1173	126	5	2	1	4	2	...	22	3	...	2	1	4	2	...	...
CD-35 14849	69	6	2	1	7	6	4	31	3	1	...	6	6	2	1	1
CD-71 1234	127	6	2	1	7	6	4	29	3	1	3	5	4	2	...	...
G63-12	59	4	2	1	4	1	2	16	3	...	...	1	3	2	...	1
G64-37	71	4	2	1	4	2	1	20	3	...	2	...	4	2	...	1
LP635-14	163	6	2	1	7	6	4	32	3	2	3	5	4	2	2	1
LP815-43	157	4	2	1	6	2	2	22	3	...	...	...	2	2	...	1
HD84937	164	6	2	1	7	5	7	36	5	2	3	5	7	2	2	1
HD140283	124	...	...	...	...	...	...	...	...	...	...	...	...	...	...	...
HD74000	84	7	2	1	7	5	5	36	5	3	5	5	7	2	3	1

Table 21 Abundance ratios calculated using the atmospheric parameters of Arnone et al. (2005).

Star name	[Fe/H]	[Mg I/Fe]	[Al I/Fe]	[Si I/Fe]	[Ca I/Fe]	[Sc II/Fe]	[Ti I/Fe]	[Ti II/Fe]	[Cr I/Fe]	[Cr II/Fe]	[Mn I/Fe]	[Co I/Fe]	[Ni I/Fe]	[Sr II/Fe]	[Y II/Fe]	[Ba II/Fe]
BD-13 3442	-2.78	0.39	-0.78	-0.06	0.36	0.21	0.54	0.40	-0.14	0.42	-0.61	...	-0.17	-0.24	...	-0.91
BD+20 2030	-2.63	0.28	-0.81	0.12	0.34	0.18	0.45	0.31	-0.17	...	-0.56	0.24	-0.13	-0.40	-1.24	-0.43
BD+24 1676	-2.79	0.43	-0.78	0.16	0.50	0.33	0.63	0.52	...	0.36	-0.30	0.37	-0.01	-0.13	...	...
BD+26 2621	-2.80	0.19	-0.87	0.03	0.28	0.11	0.51	0.31	-0.30	...	-0.61	0.29	-0.08	-0.64	...	...
BD+26 3578	-2.44	0.29	-0.81	0.11	0.43	0.13	0.34	0.37	-0.11	-0.39	-0.10	0.59	0.34	-2.28	-0.24	-0.64
BD+3 740	-2.84	0.19	-0.80	0.00	0.42	0.20	0.61	0.41	-0.19	...	-0.57	0.29	-0.12	-0.43	...	-0.70
BD+9 2190	-2.78	0.20	-0.95	-0.06	0.19	0.07	0.36	0.22	-0.20	-0.87	...	0.27	-0.04	-0.59	...	-0.50
CD-33 1173	-3.11	0.29	-0.78	-0.04	0.36	0.09	...	0.30	-0.20	...	-0.56	0.48	-0.11	-0.49	...	...
CD-35 14849	-2.49	0.19	-0.90	0.09	0.25	0.05	0.21	0.32	-0.29	0.37	...	0.19	-0.09	-0.28	0.04	-0.84
CD-71 1234	-2.55	0.09	-0.91	0.03	0.27	0.13	0.33	0.36	-0.21	0.38	-0.58	0.34	0.02	-0.79	...	...
G63-12	-3.46	0.43	-0.59	0.05	0.44	0.01	0.94	0.42	-0.11	...	...	0.80	-0.04	-0.06	...	-0.15
G64-37	-3.15	0.27	-0.79	-0.06	0.30	0.01	0.55	0.24	-0.32	...	-0.82	...	-0.10	-0.20	...	-0.52
LP635-14	-2.53	0.28	-0.82	-0.03	0.31	-0.01	0.40	0.25	-0.22	0.02	-0.59	0.28	-0.15	-0.21	0.09	0.09
LP815-43	-2.61	-0.04	-1.09	-0.16	0.12	-0.39	0.34	0.08	-0.37	...	-0.85	...	-0.34	-0.23	...	-0.88
HD84937	-2.42	0.34	-0.62	0.10	0.35	0.18	0.44	0.37	-0.01	-0.31	-0.38	0.26	-0.09	-0.26	-0.05	-0.11
HD140283	...	...	...	...	...	...	...	...	...	...	...	...	...	...	...	...
HD74000	-2.25	0.24	-0.56	0.12	0.27	0.17	0.33	0.44	-0.01	0.41	-0.34	0.17	-0.05	-0.17	0.16	0.41

Table 22 Errors on the abundance ratios calculated using the Arnone et al (2005) photometric parameters.

Star name	[Fe/H]	[Mg I/Fe]	[Al I/Fe]	[Si I/Fe]	[Ca I/Fe]	[Sc II/Fe]	[Ti I/Fe]	[Ti II/Fe]	[Cr I/Fe]	[Cr II/Fe]	[Mn I/Fe]	[Co I/Fe]	[Ni I/Fe]	[Sr II/Fe]	[Y II/Fe]	[Ba II/Fe]
BD-13 3442	0.06	0.10	0.14	0.08	0.08	0.12	0.11	0.09	0.08	0.06	0.14	...	0.17	0.09	...	0.08
BD+20 2030	0.06	0.08	0.18	0.09	0.08	0.13	0.09	0.09	0.07	...	0.07	0.09	0.10	0.11	0.06	0.08
BD+24 1676	0.06	0.08	0.10	0.08	0.07	0.12	0.09	0.08	...	0.09	0.11	0.08	0.08	0.10	...	...
BD+26 2621	0.06	0.10	0.14	0.09	0.08	0.12	0.10	0.09	0.08	...	0.07	0.09	0.10	0.10	...	...
BD+26 3578	0.06	0.09	0.17	0.09	0.07	0.12	0.10	0.08	0.16	0.40	0.32	0.09	0.08	0.10	0.07	0.08
BD+3 740	0.06	0.10	0.13	0.09	0.09	0.13	0.11	0.09	0.07	...	0.07	0.10	0.08	0.11	...	0.08
BD+9 2190	0.06	0.08	0.18	0.08	0.06	0.12	0.13	0.08	0.07	0.06	...	0.09	0.08	0.11	...	0.08
CD-33 1173	0.06	0.08	0.12	0.08	0.07	0.11	...	0.09	0.07	...	0.12	0.07	0.08	0.10	...	...
CD-35 14849	0.05	0.09	0.16	0.08	0.07	0.12	0.09	0.08	0.06	0.06	...	0.09	0.08	0.11	0.06	0.07
CD-71 1234	0.06	0.08	0.21	0.08	0.08	0.12	0.09	0.09	0.07	0.06	0.07	0.12	0.12	0.09	...	...
G63-12	0.06	0.09	0.11	0.08	0.08	0.11	0.17	0.09	0.08	...	...	0.07	0.09	0.10	...	0.08
G64-37	0.06	0.09	0.13	0.08	0.06	0.13	0.08	0.09	0.09	...	0.07	...	0.09	0.11	...	0.08
LP635-14	0.06	0.08	0.15	0.08	0.06	0.12	0.09	0.08	0.07	0.17	0.07	0.09	0.08	0.09	0.07	0.08
LP815-43	0.06	0.09	0.16	0.09	0.08	0.12	0.20	0.09	0.07	...	0.08	...	0.09	0.17	...	0.08
HD84937	0.06	0.08	0.20	0.08	0.07	0.12	0.09	0.08	0.15	0.61	0.11	0.08	0.11	0.10	0.13	0.08
HD140283	0.05	...	...	...	...	...	...	...	...	...	...	...	...	...	...	...
HD74000	0.06	0.09	0.24	0.08	0.08	0.12	0.10	0.08	0.14	0.11	0.12	0.08	0.08	0.10	0.07	0.08

9.4. Results and Discussion

The most remarkable aspect of the Arnone et al. (2005) investigation was the result giving a small intrinsic star-to-star dispersion in [Mg/Fe] , viz. $\sigma \lesssim 0.06$ dex. This result was inferred from their analysis of four Mg lines (i.e. at 5172.70 Å, 5183.62 Å, 5528.40 Å and 5711.10 Å) in their sample of stars. Although my sample of stars is smaller, my spectra are at shorter wavelengths, which gives me access to a larger, and different, set of spectral lines, with a similar S/N ratio (~ 100) and resolution (R ~ 40,000). To see whether or not I find a similarly small scatter for [Mg/Fe], and for additional elements, I concentrate on elements that have many spectral lines (Table 20) and no hyperfine structure, namely Mg, Ca, Ti, and Ni. I also include the alpha element Si, though it has only one spectral line and Al, which has two lines.

In Figure 37 to Figure 41 I present the plots for the alpha elements: Mg I, Si I, Ca I, and for Ti I and Ti II. It is these elements that are useful for the examination of mixing in the Galaxy, through the presence of trends and scattering. Three panels are shown for each element: the top two use $T_{\chi,\text{LTE}}$ values for the MS and SGB assumptions of gravity where the evolution state is uncertain (see Chapter 4), while the lower plot uses the photometric temperatures of Arnone et al. (2005). The fits in each plot are least squares fits, either weighted by the errors (dotted line) or unweighted (solid line). The equations of the unweighted cases are shown in Table 23. I remind the reader that T_{χ} scales should have better systematic errors but worse star-to-star scatter, whilst the converse is true for T_{PHOT}.

Concerning Mg I, Figure 37, based on 4 – 7 spectral lines there is a slight trend with [Fe/H], [Mg/Fe] showing an increase at [Fe/H] < -3 for both the weighted and unweighted fits. From the values of the slope coefficients for the MS (-0.19 ± 0.09) and SGB (-0.19 ± 0.11) results, it is seen that they are only marginally significant. However, these trends seem to be at odds with the observations of Arnone et al. (2005), who find no trend whatsoever for

the [Fe/H] range of ~ -2 to -3.5, the equation of their fit being [Mg/Fe] = $(0.00 \pm 0.04) \times$ [Fe/H] + (0.31 ± 0.12). I also find an intrinsic scatter that is greater than theirs, with values of 0.10 dex and 0.12 dex for the MS and SGB temperatures respectively, as opposed to 0.06 dex found by Arnone et al. (2005). This is to be expected though, as observational errors (Table 18 and Table 19) for my work are of order 0.12 dex, thus not allowing for values smaller than this to be obtained. I also see a similar slight trend (-0.07 ± 0.13) and high scatter (0.13 dex) when adopting the atmospheric values of Arnone et al. (2005), where again my observational errors (of order 0.09 dex) restrict the level to which the intrinsic scatter can be deduced. These values are smaller than the models of inhomogeneous Galactic chemical evolution (iGCE), e.g. Argast et al. (2000, 2002), where at [Fe/H] < -3 more scatter is implied, i.e. $\sigma > 0.2$ dex, as the ISM is only enriched locally. In this scenario the ISM becomes more homogeneous in the metallicity range -2 < [Fe/H] < -1, where there is an overlap of well mixed and partially mixed areas of the ISM, leading to some scatter. Comparing the scatter found in this work with that of Argast et al. (2000, 2002), for the metallicity range covered in this work (-3.4 < [Fe/H] < -2.2), they find values of $\sigma \sim 0.4$ dex and $\sigma \sim 0.16$ dex, depending on whether SNII yields from Thielemann et al. (1996) or yields from a H1 empirical model were used. The latter a model that corresponds to iron yields that relate to the mass of the progenitors of two SN, 1997D and 1998bw, and assumes higher mass models for the progenitor of both of them compared to their other models. In particular they take the progenitors to have masses of 26 $M_\odot$ and 40 $M_\odot$ respectively. This model leads to a roughly constant Fe yield up until 25 $M_\odot$ with a sudden drop at this point followed by a steady increase to 0.79 $M_\odot$ of synthesised Fe for the 50 $M_\odot$ progenitor. My results therefore lie between those of Arnone et al (2005) and Argast et al. (2000, 2002), however there is a close agreement with the latter if the H1 model yields are used. It is not until [Fe/H] > -1 that

174

there is complete homogeneity in the models. I do not cover this range of [Fe/H] and therefore am unable to see if this is the case observationally.

Although I find contrasts between the Arnone et al. (2005) results for Mg, I do find similar results for Ca, Figure 39, and Ti, Figure 40 and Figure 41. With Ca, I find a slight increase in abundance with decreasing [Fe/H], with a value for the slope of -0.13 ± 0.05 and -0.06 ± 0.07 for the MS and SGB respectively. Here only the MS case is statistically

Table 23 A list of least squares fits equations and scatter values.

Element	Parameter set	OLS equation	$\sigma_{scatter}$ (dex)
Mg I	MS	[Mg/Fe]=(-0.42 ± 0.25) + (-0.19 ± 0.09) · [Fe/H]	0.10
	SGB	[Mg/Fe]=(-0.28 ± 0.30) + (-0.19 ± 0.11) · [Fe/H]	0.12
	Photometric	[Mg/Fe]=(0.07 ± 0.35) + (-0.07 ± 0.13) · [Fe/H]	0.13
Si I	MS	[Si/Fe]=(-0.21 ± 0.20) + (-0.06 ± 0.07) · [Fe/H]	0.07
	SGB	[Si/Fe]=(-0.26 ± 0.28) + (-0.09 ± 0.10) · [Fe/H]	0.10
	Photometric	[Si/Fe]=(0.41 ± 0.22) + (0.14 ± 0.08) · [Fe/H]	0.09
Ca I	MS	[Ca/Fe]=(-0.12 ± 0.15) + (-0.13 ± 0.05) · [Fe/H]	0.07
	SGB	[Ca/Fe]=(0.14 ± 0.18) + (-0.06 ± 0.07) · [Fe/H]	0.07
	Photometric	[Ca/Fe]=(0.28 ± 0.28) + (-0.02 ± 0.10) · [Fe/H]	0.10
Ti I	MS	[Ti/Fe]=(-0.89 ± 0.23) + (-0.50 ± 0.08) · [Fe/H]	0.17
	SGB	[Ti/Fe]=(-0.70 ± 0.29) + (-0.42 ± 0.10) · [Fe/H]	0.16
	Photometric	[Ti/Fe]=(-0.82 ± 0.38) + (-0.47 ± 0.14) · [Fe/H]	0.18
Ti II	MS	[Ti/Fe]=(0.45 ± 0.21) + (-0.02 ± 0.08) · [Fe/H]	0.08
	SGB	[Ti/Fe]=(0.71 ± 0.23) + (0.14 ± 0.08) · [Fe/H]	0.09
	Photometric	[Ti/Fe]=(0.44 ± 0.29) + (0.04 ± 0.10) · [Fe/H]	0.10
Al I	MS	[Al/Fe]=(-1.52 ± 0.15) + (-0.25 ± 0.05) · [Fe/H]	0.09
	SGB	[Al/Fe]=(-1.28 ± 0.22) + (-0.16 ± 0.08) · [Fe/H]	0.09
	Photometric	[Al/Fe]=(-1.04 ± 0.34) + (-0.08 ± 0.12) · [Fe/H]	0.12
Ni I	MS	[Ni/Fe]=(-0.15 ± 0.19) + (-0.02 ± 0.07) · [Fe/H]	0.07
	SGB	[Ni/Fe]=(0.35 ± 0.43) + (0.15 ± 0.16) · [Fe/H]	0.16
	Photometric	[Ni/Fe]=(-1.04 ± 0.33) + (-0.08 ± 0.12) · [Fe/H]	0.14

significant. Similar scatter is also found to that of Arnone et al. (2005), with values of 0.07 dex for both MS and SGB effective temperatures, compared to their value of 0.09 dex. My observational errors for Ca are 0.11 dex and 0.09 dex for the MS and SGB temperatures respectively. Using the photometric parameters of Arnone et al. (2005) I find slightly larger scatter (0.10 dex) and a smaller slope, i.e. -0.02 ± 0.10. The larger scatter is restricted by the observational error, which has a mean of 0.07 dex; these results suggest a more homogenous situation. Unlike the other alpha elements, the Ca yield is not strongly dependent on the progenitor mass, but on the energy of the SN explosion (Argast et al. 2000). This then acts as another means of testing the iGCE results qualitatively. If scatter is low, this would imply a small range of [Ca/Fe] in the stars, and either a small range in SN II energies, or a high degree of mixing. Inspecting Argast et al. (2000) printed figures suggests a much larger degree of scatter in the iGCE models. Ideally we would quantify this from tables of yields. Unfortunately Argast et al. (2000) does not tabulate or otherwise quantify the scatter which results from their calculations, and hence we cannot make as detailed a comparison with his results as Arnone et al. (2005) could do with Argast as a co-author. These values would suggest a more homogeneous situation than the Argast et al. (2000) calculations suggest.

The notable trend seen in Ti in Arnone et al. (2005) is reproduced here in my Ti I results, with a slope of -0.50 ± 0.08 and -0.42 ± 0.10 for the MS and SGB temperatures respectfully. However, as in their work, only one or two Ti I lines are measurable in many of the stars. This limits my ability to say anything certain about these results. In the case of Ti II, I measure ~20 - 35 lines in each star. Here I do not reproduce the trend seen in Ti I, finding values of the slope of -0.02 ± 0.07 and 0.14 ± 0.08 for the MS and SGB. I find a low scatter for both the MS and SGB cases, 0.08 dex and 0.09 dex respectively, which would point to a more homogeneous situation. Similar values to the MS case are found when using the Arnone parameters, with a slope of 0.04 ± 0.10 and intrinsic scatter of 0.10 dex. There is lack of

knowledge about the formation sites and processes of this element, i.e. observationally determined abundances show that the element exhibits similar hallmarks to the alpha elements, whilst theoretical calculations point towards it scaling with iron, and therefore predict lower abundances (Timmes, Woosley & Weaver 1995); this implies that very little can be deduced from this result. Nevertheless, the shallow slopes for Ti II are less than 2σ effects, i.e. consistent with no real change.

Si, Figure 38, is similar to the other alpha elements. Slope values of -0.06 ± 0.07 and 0.08 ± 0.10 for the MS and SGB respectively, are found. This suggests there is no statistically relevant slope. The scatter in the two cases is 0.07 dex and 0.10 dex. The Arnone et al. (2005) parameters give a larger result for the slope of 0.14 ± 0.08, and but a similar scatter of 0.09 dex. This would imply a more homogeneous scenario, as from, inspecting their figures, the Argast et al. (2000) results suggest a higher degree of scatter in this element. However, only one line is present in any of the stars and these results are far from conclusive.

The well known underabundance is seen in the Al LTE plots, Figure 42, although with a slight trend to increasing abundance with decreasing [Fe/H], i.e. with values of -0.25 ± 0.05 and -0.16 ±0.08 for the MS and SGB cases respectively. The slope when using the photometric parameters is -0.08 ± 0.12, here there is no statistical significance. The scatter is 0.09 dex for both the MS, and SGB cases, whilst it is slightly more for the photometric temperature case, 0.12 dex. However, these abundances are derived using only two lines in this case and Al is known to suffer from strong NLTE effects (Baumueller & Gehren 1997). The usefulness of this result is then questionable.

Ni is the final element I present, Figure 43. We see that there is essentially no trend in either parameter set with slope values of 0.02 ± 0.07, 0.15 ± 0.16 and -0.08 ± 0.12 for the MS, SGB and photometric temperature cases. The intrinsic scatter in each case is 0.07 dex,

0.16 dex and 0.14 dex. These values are all restricted by the mean observational errors, which are 0.13 dex for both MS and SGB temperatures and 0.09 dex for the photometric temperatures. It is this element (atomic number $Z = 28$) that most closely follows the formation of Fe ($Z = 26$), and can act as a test on the reliability of the measured abundance data. If the data are reliable you would not expect a variation in [Ni/Fe], as is the case with this work, within the limits of the observational errors.

Other elements that are in Table 16, Table 17, and Table 21 are not presented in the plots as they are unsuitable for this analysis, either due to the limited number of lines or the existence of HFS effects which we have not attempted to model here.

Although I have concentrated on comparing this work with the studies of Argast et al. (2000) and Arnone et al. (2005), it is worthwhile making a note of the outcomes of other important studies, in particular Cayrel et al. (2004). In their work they have calculated the abundances of the elements from C to Zn for a large group of extremely metal-poor stars, including both dwarfs and giants. For most cases they find no significant trend with [Fe/H], which is in contrast to a couple of my elements. The intrinsic scatters found in their work are of similar magnitude for the majority of the elements in this study; however, we achieve a lower scatter for Al. This may then suggest that the iGCE theory predicts a scatter that is too large, and the early Galaxy was not as inhomogeneous as Argast et al. (2000) suggests.

9.5. Conclusion

I have calculated the abundance ratios of a selection of elements that have spectral lines within the spectra of my program stars. For each element I have computed a least squares fit to the data and calculated the intrinsic scatter of each, Table 23 lists the equations to these fits and the scatter values. I have found that several of the elements show trends and some degree of scatter, however, many of these trends are not statistically significant and the scatter is

comparable to the observational error. It has been shown that there may be some evidence for a more inhomogeneous situation than claimed by Arnone et al. (2005), as there seems to be a degree of scatter in the abundances. However the scatter predicted by Argast et al (2000, 2002) for the lightest elements, is a lot larger than I have found here. The large scatter found by Argast et al (2000) may be due to the mass dependence of the SN II yields that they have used. The calculation of these yields is ever evolving. Use of yields from more recent calculations, e.g. Fröhlich et al. (2008), may reduce the intrinsic scatter in these models and could be examined in further work on this topic.
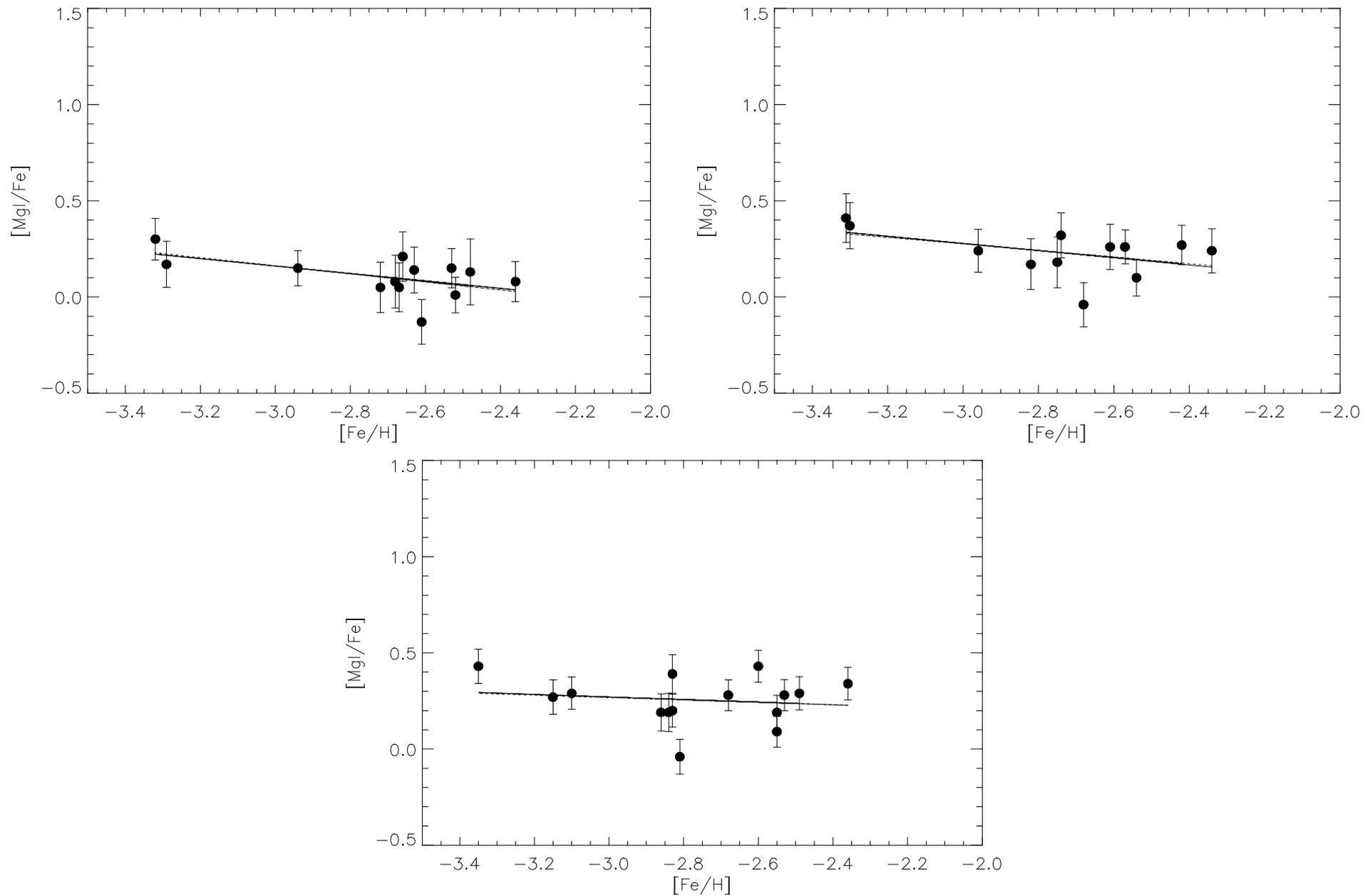
Figure 37 Isotopic ratio versus metallicity for the alpha element Mg calculated from the MS effective temperatures and (top left panel), the SGB effective temperatures (top right panel), and from photometric temperatures (bottom panel). The solid line is a simple least squares fit and the dotted line is a weighted fit.
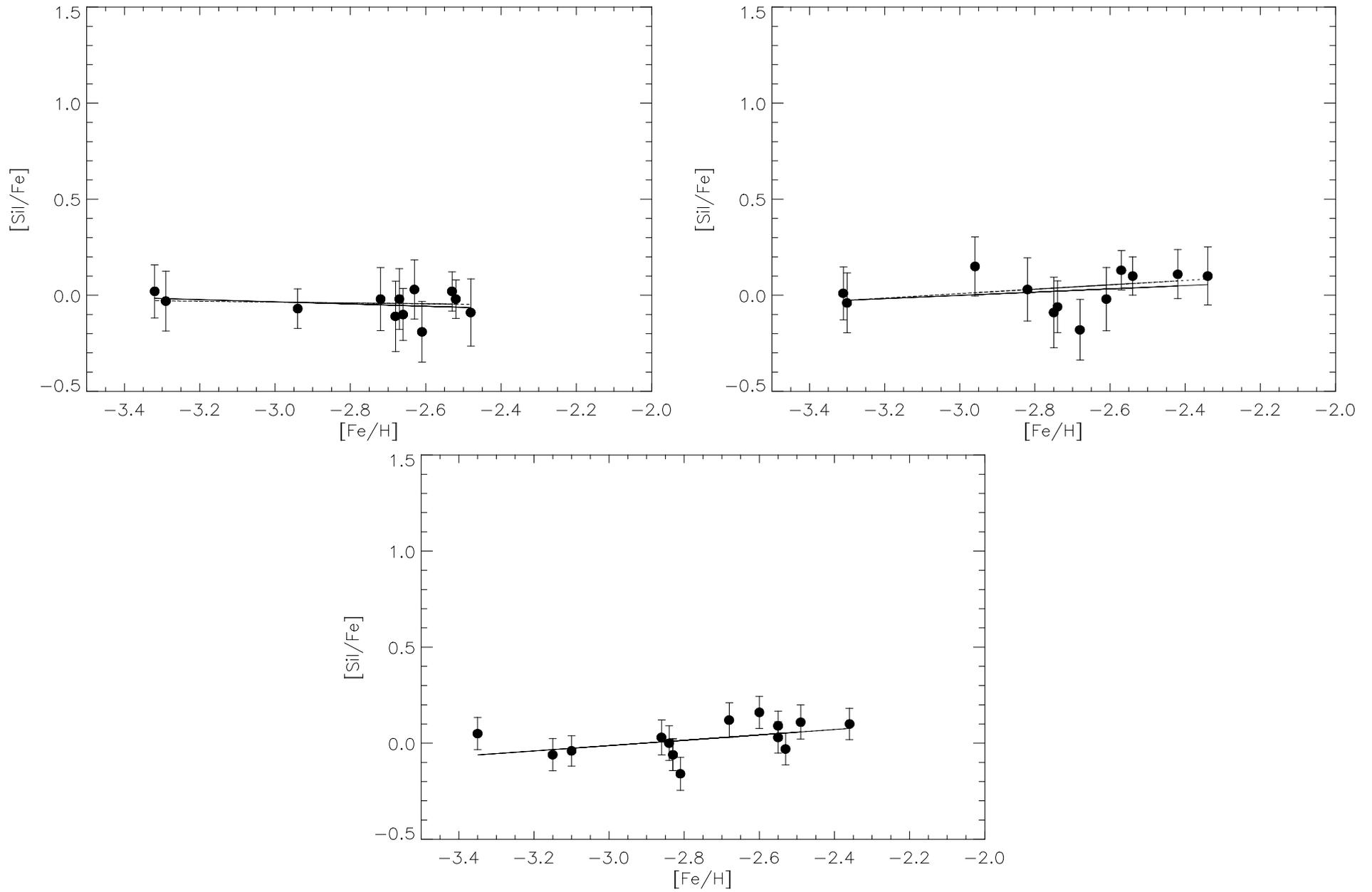
Figure 38 Isotopic ratio versus metallicity for the alpha element Si calculated from the MS effective temperatures and (top left panel), the SGB effective temperatures (top right panel), and from photometric temperatures (bottom panel). The solid line is a simple least squares fit and the dotted line is a weighted fit.
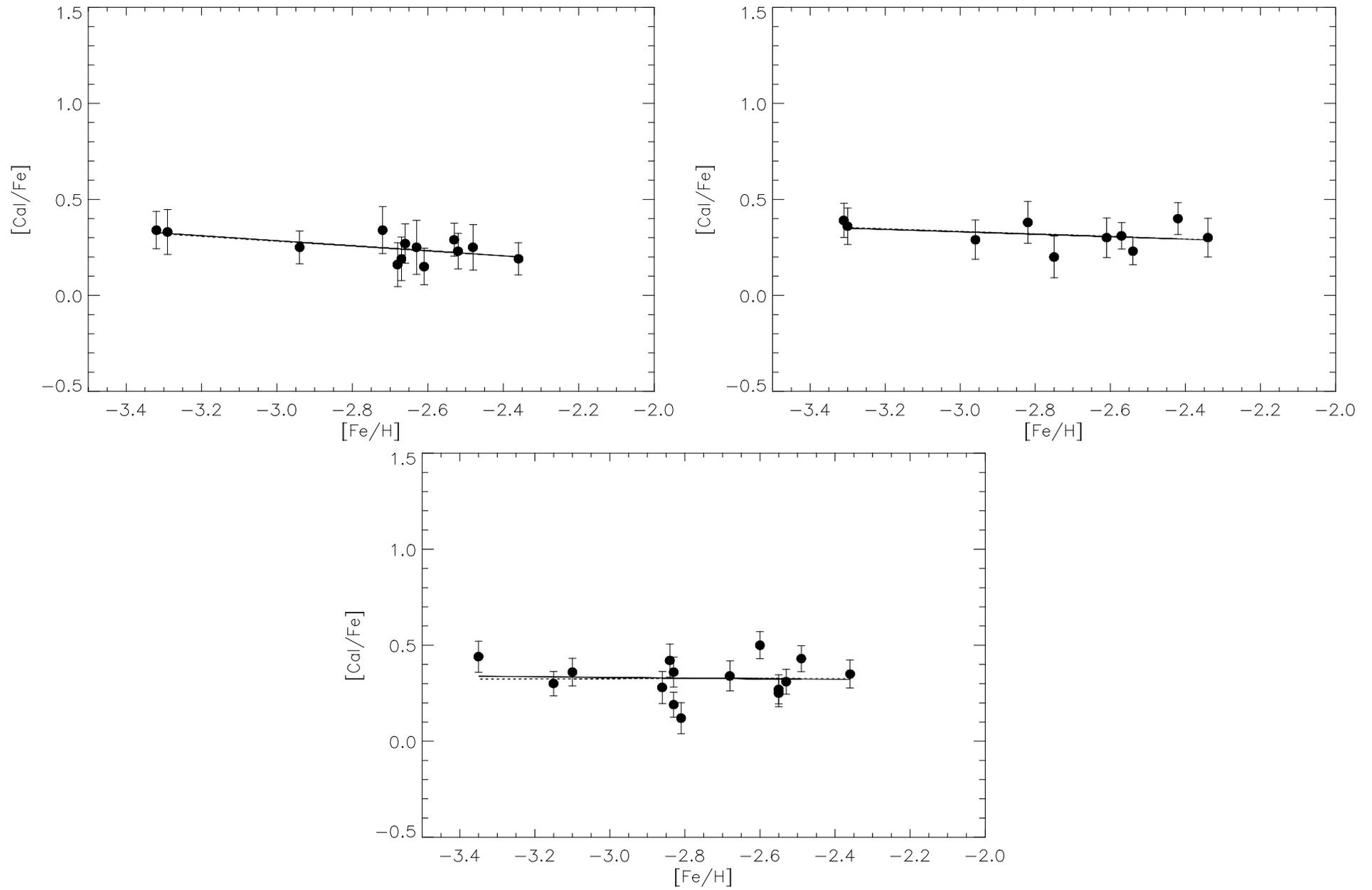
Figure 39 Isotopic ratio versus metallicity for the alpha element Ca calculated from the MS effective temperatures and (top left panel), the SGB effective temperatures (top right panel), and from photometric temperatures (bottom panel). The solid line is a simple least squares fit and the dotted line is a weighted fit.
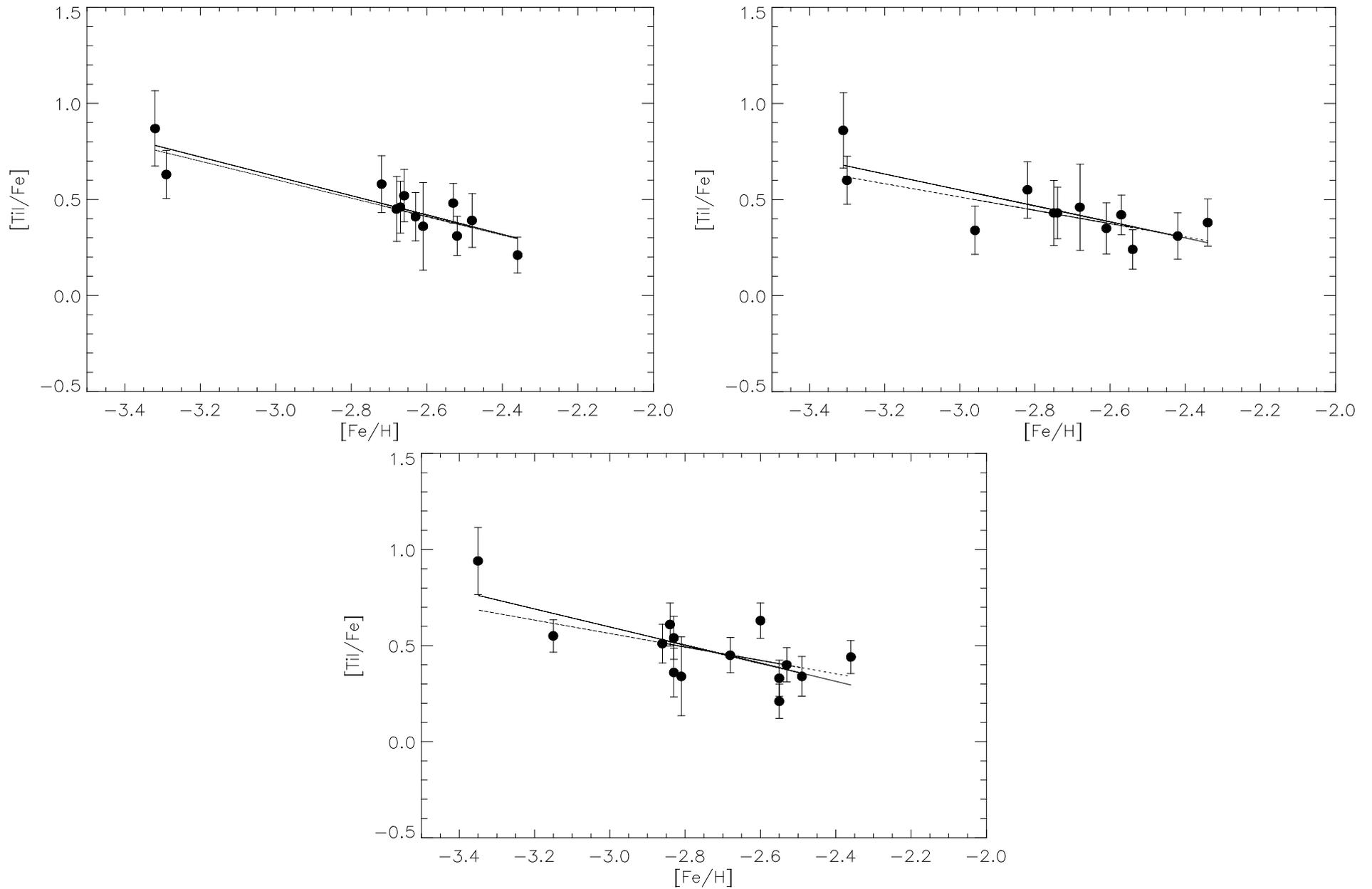
Figure 40 Isotopic ratio versus metallicity for the alpha element Ti I calculated from the MS effective temperatures and (top left panel), the SGB effective temperatures (top right panel), and from photometric temperatures (bottom panel). The solid line is a simple least squares fit and the dotted line is a weighted fit.
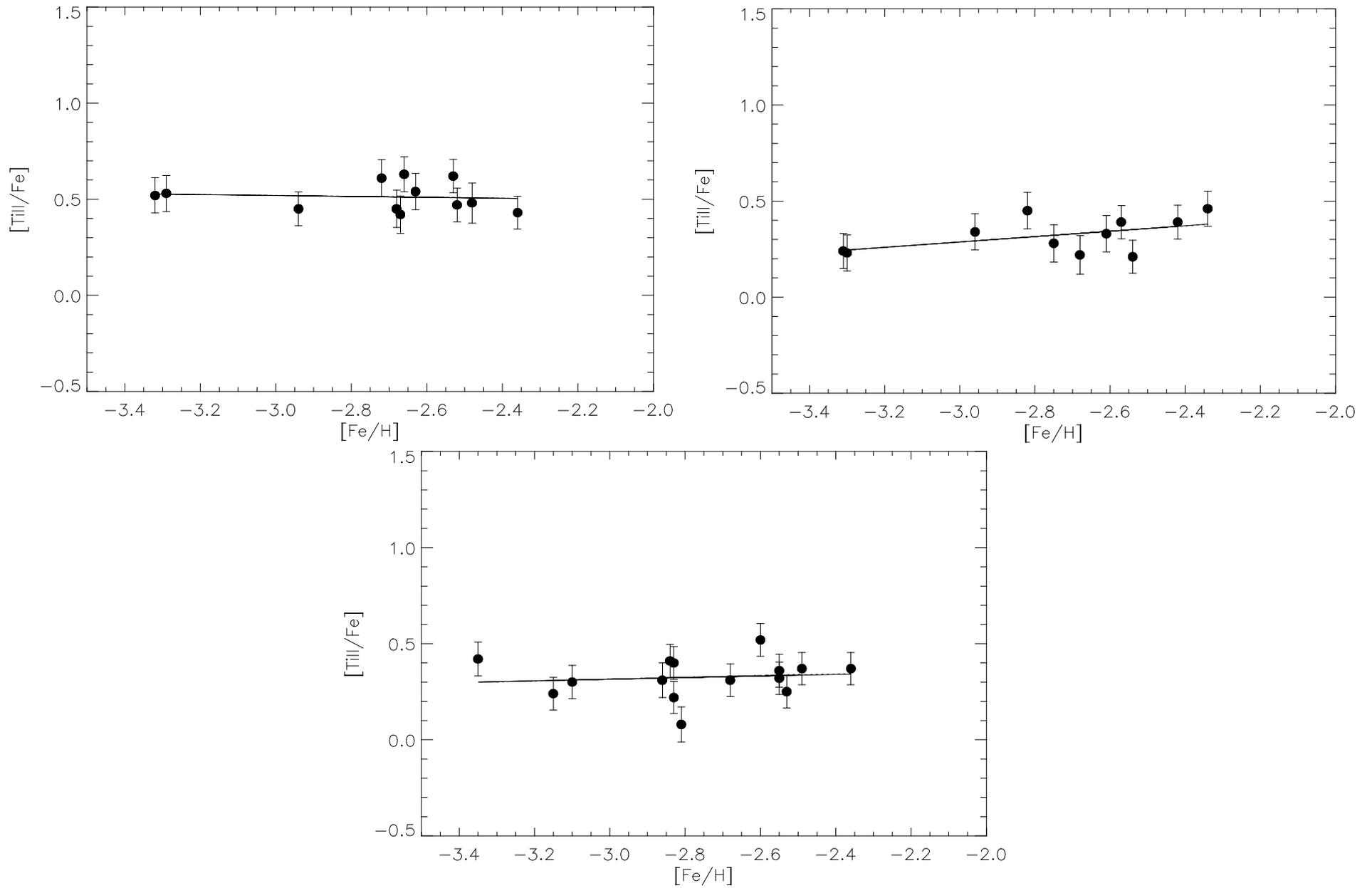
Figure 41 Isotopic ratio versus metallicity for the alpha element Ti II calculated from the MS effective temperatures and (top left panel), the SGB effective temperatures (top right panel), and from photometric temperatures (bottom panel). The solid line is a simple least squares fit and the dotted line is a weighted fit.
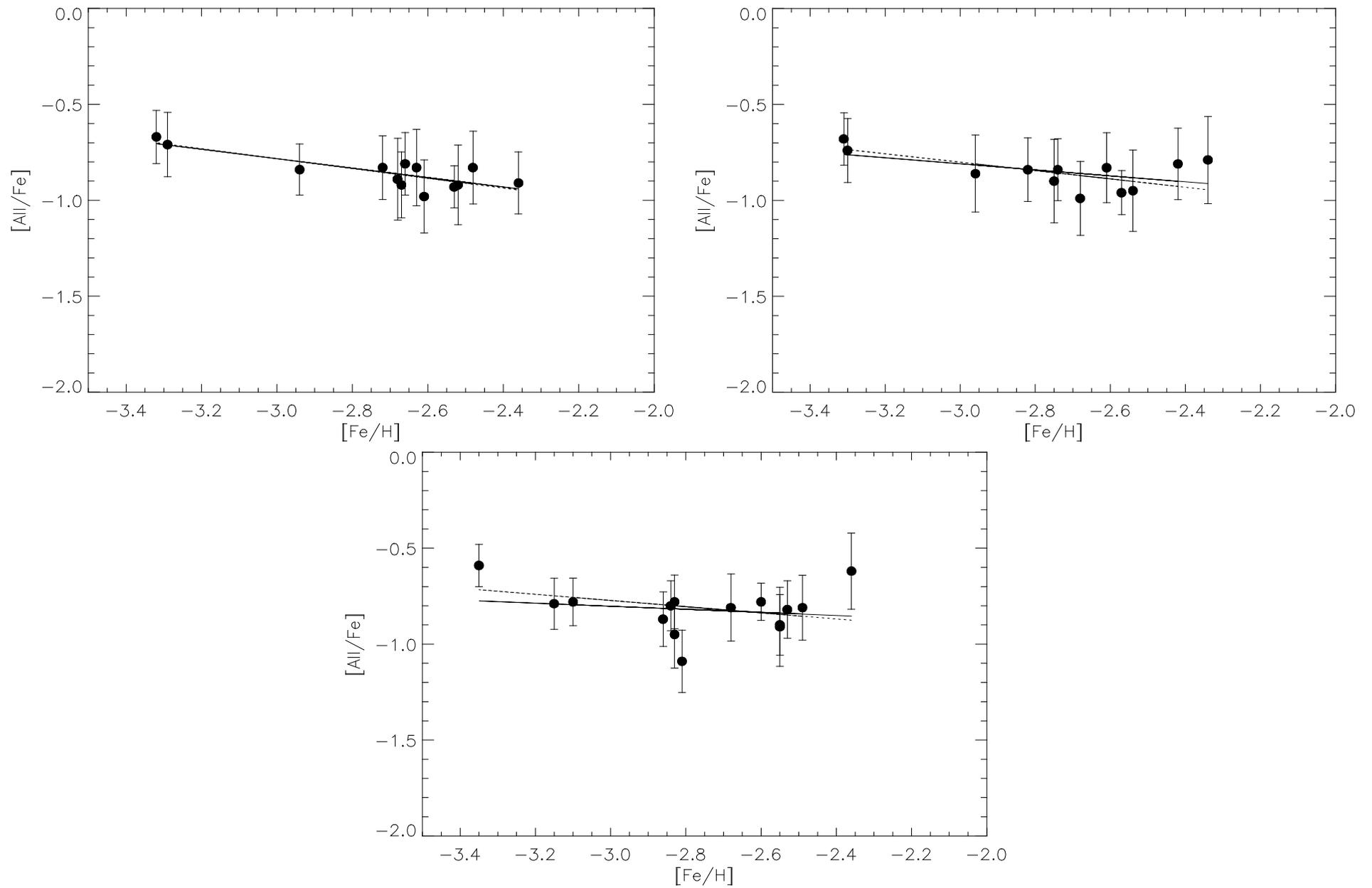
Figure 42 Isotopic ratio versus metallicity for the alpha element Al calculated from the MS effective temperatures and (top left panel), the SGB effective temperatures (top right panel), and from photometric temperatures (bottom panel). The solid line is a simple least squares fit and the dotted line is a weighted fit.
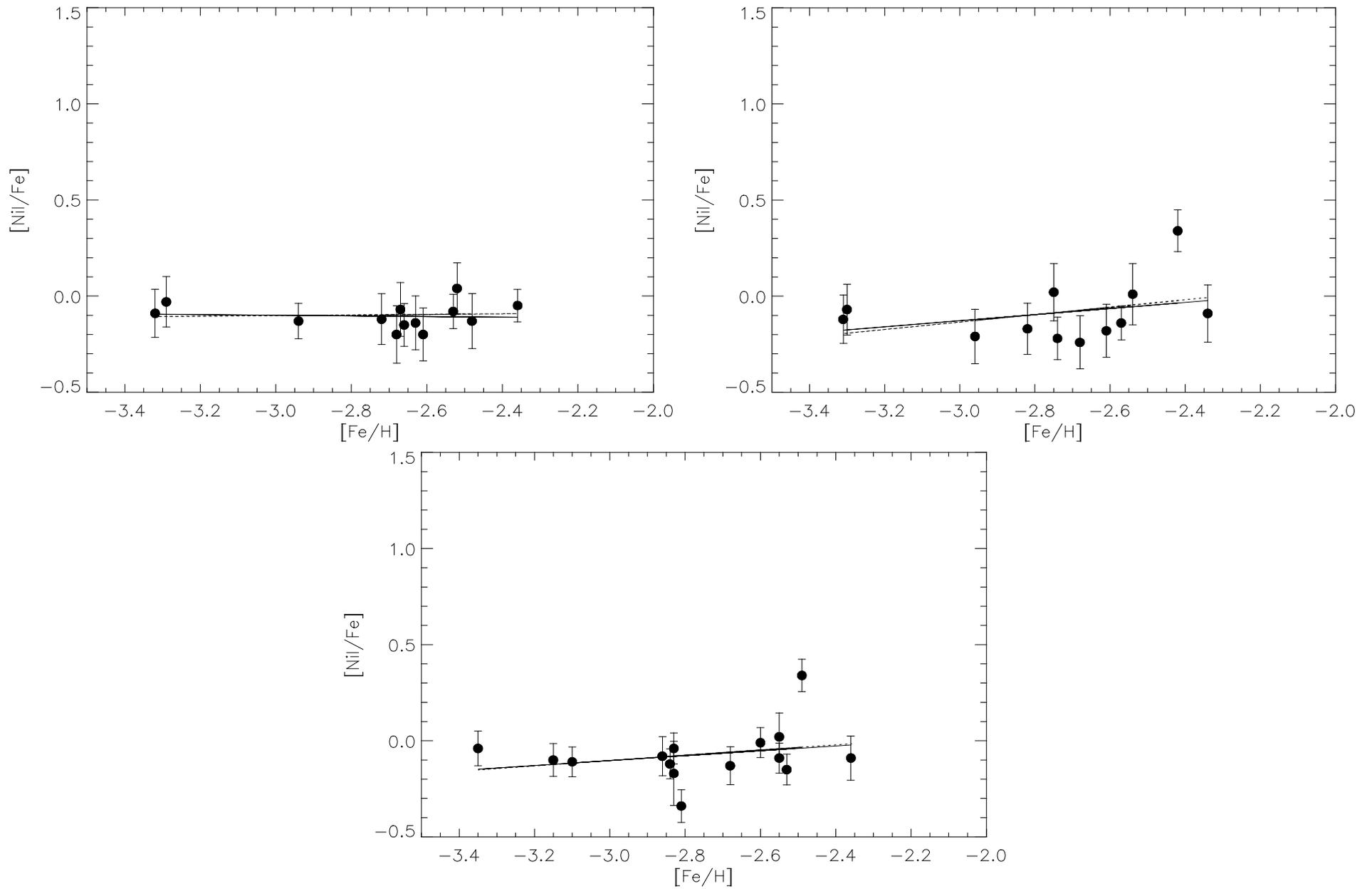
Figure 43 Isotopic ratio versus metallicity for the alpha element Ni calculated from the MS effective temperatures and (top left panel), the SGB effective temperatures (top right panel), and from photometric temperatures (bottom panel). The solid line is a simple least squares fit and the dotted line is a weighted fit.

Tables that follow are an appendix to this chapter.

Table 24 Table of equivalent widths for the elements under study. Units for all measurements are in pm.

| Element	λ (Å)	BD-13 3442	BD+20 2030	BD+24 1676	BD+26 2621	BD+26 3578	BD+3 740	BD+9 2190	CD-33 1173	CD-35 14849
Mg I	3829.36	9.23	10.59	11.38	9.34	11.91	9.73	9.11	8.20	12.63
	3832.30	12.96	13.49	13.13	11.75	14.58	11.49	10.54	10.05	14.81
	3838.29	13.27	13.61	14.36	13.81	16.84	12.04	11.32	11.36	17.57
	4057.51	1.92	1.29	1.74	...	2.42	...	...	...	2.34
	4167.27	1.74	1.68	1.96	1.47	2.95	1.29	1.32	0.78	2.65
	4571.10	...	...	...	...	...	...	...	...	...
	4702.99	2.51	3.08	3.42	2.46	4.70	1.25	1.73	1.25	4.09
Al I	3944.01	4.35	5.10	3.79	4.06	6.59	3.81	3.45	2.47	6.15
	3961.52	4.79	5.06	5.92	4.53	6.67	4.49	3.40	3.06	6.33
Si I	3905.52	8.26	9.75	10.01	9.25	11.14	8.65	7.77	6.94	11.77
Ca I	4226.73	12.19	12.27	12.84	12.00	17.90	11.10	10.51	10.27	14.91
	4283.01	1.80	2.17	2.41	1.37	3.37	1.76	1.35	0.96	3.18
	4289.36	0.82	1.74	2.03	1.63	3.08	1.53	0.88	...	2.41
	4318.65	2.16	2.29	2.45	1.99	3.11	1.85	...	...	2.73
	4434.96	2.44	...	3.19	1.97	...	2.41	1.63	1.32	3.78
	4454.78	3.44	...	4.57	3.11	...	...	2.56	2.08	5.19
	4455.89	1.05	...	1.38	...	...	1.02	0.47	...	1.67
Sc II	4246.83	5.27	4.61	5.69	3.96	6.81	4.01	4.08	2.76	4.97
	4314.08	1.91	2.23	2.91	1.61	3.20	1.63	1.47	0.85	2.41
	4320.72	1.67	...	2.00	...	2.42	...	1.18	...	1.74
	4324.99	1.71	1.56	1.41	...	2.08	1.02	0.88	...	1.62
	4400.39	0.97	0.91	1.14	...	...	...	0.91	...	0.95
	4415.55	0.65	1.13	1.19	...	1.33	0.86	...	...	0.81
Ti I	3729.81	...	0.95	...	...	...	...	...	...	...
	3924.53	...	...	...	...	...	...	...	...	...
	3958.21	1.28	1.22	1.61	1.32	...	...	...	...	...
	3989.76	1.56	1.19	2.00	1.04	1.84	1.76	1.05	...	1.24
	3998.64	1.67	1.98	1.76	1.17	1.64	1.19	0.68	...	1.76
	4533.24	0.71	1.04	1.28	1.31	1.83	0.92	0.75	...	1.55
	4534.78	...	0.68	0.80	0.99	1.08	0.73	...	...	0.90
	4681.91	...	...	...	...	0.47	...	...	...	...
	4840.87	...	...	...	...	...	...	...	...	...
Ti II	3741.63	4.62	3.72	5.07	3.75	5.70	4.68	3.51	2.33	4.53
	3757.67	3.56	2.70	3.39	2.44	4.09	3.15	2.33	1.51	3.69
	3759.29	9.84	10.23	10.72	8.69	11.76	9.64	9.37	8.48	10.64
	3761.32	10.03	9.46	10.14	8.67	11.05	9.84	9.25	7.89	9.92
	3761.88	1.03	...	0.53	1.21	1.38	...	...	...	...
	3776.03	...	0.79	0.59	...	1.13	...	...	...	...
	3813.38	2.25	1.10	1.76	1.09	2.67	1.78	0.74	...	1.67
	3900.52	6.06	6.47	6.82	5.45	7.23	6.03	5.38	4.19	6.68
	3913.45	5.64	6.01	6.76	5.02	7.69	5.62	5.00	3.67	6.47
	3987.63	...	...	...	...	...	...	...	...	...
	4012.37	1.90	2.24	2.74	1.50	3.56	2.15	1.61	0.94	2.51
	4025.14	1.13	...	1.18	0.84	2.08	...	...	...	1.27
	4028.33	1.05	0.65	1.33	...	1.56	...	0.61	...	0.93
	4053.80	...	...	1.28	...	1.19	0.50	...	...	1.04
	4163.66	1.45	1.14	1.49	0.78	...	...	0.88	...	1.28
	4287.87	0.63	0.85	1.12	...	1.58	...	...	...	1.12
	4290.24	3.51	3.45	4.27	2.45	5.26	3.08	2.29	1.67	3.92
	4300.06	4.88	5.03	6.17	4.27	6.79	4.87	4.28	3.41	5.73
	4301.94	2.01	2.09	2.64	1.36	3.07	1.52	1.42	0.74	2.16
	4312.87	2.01	2.30	3.18	1.68	3.68	2.14	1.84	0.92	2.80
	4330.70	...	...	...	...	0.73	0.54	...	...	...
	4394.06	0.85	...	0.91	...	...	...	...	...	...
	4395.04	5.57	5.67	6.60	4.74	7.55	5.27	4.56	3.51	6.08
	4399.78	2.02	2.04	2.40	1.50	3.28	1.85	1.21	0.59	2.21
	4417.72	2.44	2.22	2.99	1.32	3.42	2.34	1.20	0.88	2.52
	4418.34	...	...	0.74	...	0.69	...	...	...	0.46

Table 24 Cntd.

Element	λ (Å)	BD-13 3442	BD+20 2030	BD+24 1676	BD+26 2621	BD+26 3578	BD+3 740	BD+9 2190	CD-33 1173	CD-35 14849
Ti II	4443.80	4.62	5.02	5.49	4.06	6.63	4.67	3.62	2.71	5.42
	4444.55	...	0.36	0.40	...	...	...	...	...	...
	4450.48	1.53	1.53	2.15	...	2.43	1.26	0.84	0.69	1.84
	4468.49	4.81	5.34	6.40	4.22	6.53	5.32	4.06	3.41	5.49
	4470.87	...	...	...	...	0.83	...	...	...	0.48
	4501.26	4.69	...	...	3.28	6.11	4.31	3.25	2.59	4.84
	4533.96	4.68	4.90	5.85	3.35	6.42	4.38	3.81	2.76	5.39
	4563.76	3.45	3.70	4.47	2.80	5.52	3.25	2.93	1.84	4.45
	4571.95	4.04	4.43	5.44	3.28	6.29	4.42	3.60	2.48	4.85
	4589.96	...	...	1.22	...	1.75	0.87	...	0.55	1.04
	4708.66	...	...	...	...	...	...	...	...	...
	4779.98	...	...	...	...	...	...	...	...	0.82
V II	3951.96	...	0.37	...	0.61	...	...	...	...	...
	4023.39	0.60	...	...	0.49	...	...	...	...	...
Cr I	3991.12	...	...	...	...	...	...	...	...	...
	4254.33	4.38	4.67	5.09	3.90	5.57	3.98	4.03	2.52	5.79
	4274.80	3.65	4.46	4.53	3.61	5.45	3.56	3.35	2.21	5.15
	4289.72	3.63	3.51	3.94	2.59	4.72	2.52	2.56	1.52	4.54
	4616.12	...	...	...	...	...	...	...	...	...
	4646.15	...	...	...	...	...	...	...	...	...
Cr II	4558.65	0.74	...	0.50	...	0.10	...	...	...	0.83
	4588.20	...	...	0.71	...	0.60	...	...	...	...
	4824.08	...	...	...	...	...	...	...	...	...
	4848.21	...	...	...	...	...	...	...	...	...
Mn I	4030.75	2.17	2.93	3.38	2.35	6.68	2.17	2.08	1.00	3.93
	4033.06	2.42	2.07	2.56	1.78	5.48	1.62	1.45	1.11	2.97
	4034.48	0.72	1.51	1.96	1.33	4.76	0.95	1.16	...	2.54
	4055.54	...	...	0.28	...	0.61	...	...	...	...
	4823.52	...	...	...	...	0.57	...	...	...	...
Co I	3842.05	...	...	...	...	1.34	...	...	...	...
	3845.46	...	1.65	2.17	1.66	3.96	1.69	1.36	1.19	2.09
	3873.11	...	...	...	1.45	...	...	1.20	...	2.39
	3873.96	...	...	...	...	3.36	...	...	...	...
	3894.07	...	1.89	...	1.52	4.47	0.96	...	...	2.50
	3995.30	...	...	1.26	...	3.28	0.89	1.01	...	2.34
	4121.31	...	...	...	...	3.02	0.95	0.62	...	1.28
Ni I	3775.57	2.03	2.43	2.82	3.12	5.75	1.76	1.98	1.00	4.10
	3783.52	2.42	3.52	3.54	...	6.21	2.28	2.40	1.62	4.48
	3807.14	2.61	2.97	3.99	3.16	6.71	2.75	3.09	1.59	4.41
	3831.69	...	...	...	...	2.78	...	0.54	...	1.44
	3858.29	4.19	...	4.80	4.43	7.33	4.22	4.56	2.95	6.03
	4231.03	...	...	...	...	1.55	...	...	...	...
	4470.49	...	...	...	...	0.56	...	...	...	...
	4648.65	...	...	...	...	0.51	...	...	...	...
	4714.42	...	...	...	...	...	...	...	...	0.68
	4715.76	...	...	...	...	0.48	...	...	...	...
	4829.02	...	...	...	...	0.37	...	...	...	...
Zn I	4722.15	...	...	...	...	0.53	...	...	...	...
	4810.53	...	...	...	...	0.47	...	...	...	...
Sr II	4077.71	7.06	6.46	7.94	5.07	0.76	6.21	5.48	4.54	7.52
	4215.52	5.87	5.76	7.14	3.85	0.41	5.21	3.84	3.49	6.73
Y II	3774.33	...	0.10	...	...	1.53	...	...	...	...
	3788.70	...	...	...	...	1.04	...	...	...	...
	3950.36	...	...	...	...	0.38	...	...	...	...
Ba II	4554.03	0.65	1.87	...	...	2.17	0.81	1.39	...	1.20

Table 25 Table of equivalent widths for the elements under study. Units for all measurements are in pm.

Element	λ (Å)	CD-71 1234	G64-12	G64-37	LP635-14	LP815-43	HD84937	HD140283	HD74000
Mg I	3829.36	10.85	7.34	7.52	11.19	7.99	12.84	12.97	15.09
	3832.30	12.99	8.90	9.07	13.81	9.45	15.65	17.88	19.36
	3838.29	15.10	10.35	10.20	15.32	10.31	18.07	...	21.04
	4057.51	0.94	...	...	1.47	...	2.74	1.81	3.56
	4167.27	1.55	...	...	2.14	...	3.27	2.90	4.58
	4571.10	...	...	...	...	...	...	0.68	0.86
	4702.99	3.31	0.86	...	3.52	1.44	4.97	...	6.63
Al I	3944.01	5.56	1.83	2.25	5.50	3.08	7.24	8.81	10.02
	3961.52	5.09	2.53	2.68	5.86	3.19	6.89	7.32	9.19
Si I	3905.52	10.40	5.52	5.92	9.76	7.34	11.75	13.50	14.17
Ca I	4226.73	13.03	8.90	9.19	13.17	11.24	14.60	15.76	16.99
	4283.01	2.67	...	...	2.57	...	3.79	2.97	4.13
	4289.36	2.13	0.51	...	1.79	0.94	2.82	2.39	3.64
	4318.65	2.51	...	0.67	2.32	1.12	3.28	2.76	4.27
	4434.96	3.08	0.83	0.92	3.22	1.68	4.50	3.84	5.65
	4454.78	4.27	1.25	1.83	4.40	2.74	5.87	...	6.89
	4455.89	1.31	...	...	1.48	0.47	2.34	1.82	3.00
Sc II	4246.83	4.84	1.12	1.74	4.50	2.70	6.67	6.70	6.88
	4314.08	2.36	...	...	2.27	...	3.66	3.91	3.94
	4320.72	1.86	...	0.47	1.74	...	...	2.87	...
	4324.99	1.25	...	...	1.26	...	2.26	2.55	2.76
	4400.39	1.08	...	...	0.88	...	1.99	1.73	1.93
	4415.55	0.65	...	...	0.82	4.72	1.84	1.48	1.76
Ti I	3729.81	...	...	...	...	...	1.58	1.59	1.83
	3924.53	...	...	...	...	...	...	0.63	...
	3958.21	...	...	...	...	...	2.42	2.03	3.72
	3989.76	1.64	0.96	...	1.55	1.26	2.15	2.49	2.53
	3998.64	1.61	...	0.70	1.61	...	2.28	2.81	3.02
	4533.24	1.00	0.45	...	1.32	0.55	1.82	1.70	...
	4534.78	0.75	...	...	0.74	...	1.32	1.24	1.62
	4681.91	...	...	...	...	...	0.43	0.40	...
	4840.87	...	...	...	...	...	...	...	...
Ti II	3741.63	4.39	...	1.49	4.75	3.37	6.10	5.49	6.46
	3757.67	3.74	0.87	0.98	3.13	1.91	4.28	4.31	5.12
	3759.29	10.19	6.82	7.08	10.53	8.61	11.49	11.02	12.04
	3761.32	9.88	6.94	7.18	10.03	8.99	11.47	10.98	...
	3761.88	1.72	...	...	...	...	1.19	0.98	2.00
	3776.03	...	...	...	1.03	...	1.49	1.22	2.23
	3813.38	1.25	...	...	1.74	0.96	3.03	2.58	2.92
	3900.52	6.18	2.74	2.75	6.63	4.93	...	7.31	7.76
	3913.45	6.14	2.18	2.95	6.42	4.19	7.93	7.00	8.32
	3987.63	...	...	...	...	...	0.65	0.43	...
	4012.37	2.42	0.68	0.75	2.63	1.82	3.90	3.67	4.30
	4025.14	1.29	...	...	1.36	...	2.12	1.92	2.43
	4028.33	0.81	...	...	1.35	...	1.85	1.27	2.13
	4053.80	...	...	...	1.01	...	1.49	0.95	1.45
	4163.66	1.37	...	...	1.43	1.01	2.47	1.54	2.57
	4287.87	1.07	...	...	1.05	1.00	1.49	1.22	1.79
	4290.24	3.72	0.74	0.91	3.54	2.11	5.27	4.90	5.92
	4300.06	5.20	1.83	1.81	5.40	3.19	7.02	6.58	7.64
	4301.94	2.06	...	...	1.90	1.00	3.75	3.27	4.22
	4312.87	2.58	...	0.81	3.08	1.42	4.30	5.04	4.81
	4330.70	0.63	...	...	0.37	...	0.73	0.60	0.80
	4394.06	...	...	...	...	...	1.38	1.04	1.43
	4395.04	5.62	2.35	2.67	6.17	4.23	7.70	6.97	7.74
	4399.78	2.08	...	0.42	2.15	0.87	3.50	2.98	3.80
	4417.72	...	...	0.50	2.57	1.37	3.86	3.48	4.10
	4418.34	...	...	...	0.39	...	0.84	0.76	1.21

Table 25 Cntd.

Element	λ (Å)	CD-71 1234	G64-12	G64-37	LP635-14	LP815-43	HD84937	HD140283	HD74000
Ti II	4443.80	4.88	1.62	1.75	5.14	...	6.88	6.22	5.68
	4444.55	0.38	...	...	0.48	...	0.67	0.61	0.93
	4450.48	1.58	0.37	0.57	1.69	...	2.80	2.54	3.18
	4468.49	5.40	1.92	2.13	5.35	3.46	6.95	6.63	7.18
	4470.87	...	...	...	...	...	0.88	0.83	0.79
	4501.26	4.76	1.31	1.84	4.71	3.06	6.39	5.81	6.57
	4533.96	4.84	1.83	1.77	5.23	3.16	7.31	6.14	7.29
	4563.76	3.73	1.12	1.32	4.30	2.69	5.76	...	6.08
	4571.95	4.61	1.51	1.91	4.83	3.25	6.44	5.48	6.58
	4589.96	0.85	...	...	1.09	...	1.78	1.54	1.87
	4708.66	...	...	...	...	...	...	...	0.58
	4779.98	...	...	...	...	...	0.91	...	1.07
V II	3951.96	...	...	...	...	...	0.52	0.61	0.56
	4023.39	...	...	...	...	...	0.50	0.49	0.53
Cr I	3991.12	...	...	...	...	...	0.95	0.43	1.31
	4254.33	5.14	1.82	2.06	5.12	3.43	6.59	6.59	7.19
	4274.80	4.83	1.51	1.66	4.66	2.87	6.06	6.45	6.98
	4289.72	4.48	0.84	0.90	3.94	2.18	5.24	5.76	6.13
	4616.12	...	...	...	...	...	...	0.52	0.59
	4646.15	...	...	...	...	...	0.81	0.95	...
Cr II	4558.65	0.75	...	...	0.69	...	1.10	0.80	1.56
	4588.20	...	...	...	0.36	...	0.08	...	1.06
	4824.08	...	...	...	...	...	...	0.41	0.94
	4848.21	...	...	...	...	...	...	...	...
Mn I	4030.75	3.46	...	0.65	3.14	1.53	...	6.68	5.13
	4033.06	2.74	...	0.48	2.48	1.01	4.23	5.48	5.51
	4034.48	1.85	...	...	1.63	...	3.02	4.76	4.47
	4055.54	...	...	...	...	...	...	0.61	0.82
	4823.52	...	...	...	...	...	0.57	0.57	1.17
Co I	3842.05	...	...	...	...	...	0.76	1.34	...
	3845.46	2.05	...	...	1.77	...	2.67	3.96	3.50
	3873.11	1.91	...	...	2.10	...	2.45	...	2.74
	3873.96	2.23	...	...	...	...	...	3.36	...
	3894.07	...	...	...	2.03	...	2.84	4.47	4.41
	3995.30	1.70	...	...	1.88	...	2.54	3.28	2.57
	4121.31	1.32	0.65	...	1.10	...	...	3.02	2.54
Ni I	3775.57	3.46	0.54	0.83	2.50	1.64	3.47	5.75	5.07
	3783.52	3.92	...	1.30	3.68	...	4.82	6.21	5.68
	3807.14	4.23	1.14	1.79	3.71	...	5.14	6.71	5.66
	3831.69	...	...	...	...	...	1.78	2.78	2.34
	3858.29	7.33	1.97	2.52	5.49	2.98	6.21	7.33	6.88
	4231.03	...	...	...	...	...	...	1.55	...
	4470.49	...	...	...	...	...	0.35	0.56	...
	4648.65	...	...	...	...	...	...	0.51	0.69
	4714.42	...	...	...	...	...	0.35	...	1.35
	4715.76	...	...	...	...	...	...	0.48	...
	4829.02	...	...	...	...	...	...	0.37	...
Zn I	4722.15	...	...	...	...	...	0.42	0.53	...
	4810.53	...	...	...	...	...	0.41	0.47	0.90
Sr II	4077.71	5.31	4.66	4.86	8.35	6.62	9.03	0.76	10.04
	4215.52	3.81	3.64	3.31	7.20	4.93	8.19	0.41	7.97
Y II	3774.33	...	...	...	2.08	...	1.88	1.53	3.21
	3788.70	...	...	...	1.42	...	1.78	1.04	2.49
	3950.36	...	...	...	...	...	...	0.38	1.15
Ba II	4554.03	...	0.65	0.54	4.81	0.80	4.80	2.17	7.11

10. Conclusions and Future Work

10.1. Conclusion

A detailed solution to the "lithium problem" has yet to be given. This thesis investigated one of the fundamentals in deriving the observational Li abundance, the stellar effective temperature. The study has consisted of two parts; derivation of the Li abundance using effective temperatures calculated using the simple assumptions of LTE, and the more sophisticated method of NLTE, the aim being to determine whether systematic errors in the effective temperature scale of metal-poor turn-off stars is the cause of the discrepancy. This has been done by utilising the exponential sensitivity of level populations, approximated by the Boltzmann equation, to χ/T, allowing the effective temperature to be constrained via plots of χ versus abundance.

The single line radiative transfer program WIDTH6 has been adopted for calculating the abundances in LTE, and constraining the effective temperature. With this program it has also been possible to constrain microturbulence, through plots of equivalent width versus abundance, and [Fe/H] with the calculated Fe abundance. It was, however, not possible to constrain log g with WIDTH6. Instead HIPPARCOS gravities were used where available or failing this isochronal gravities were adopted. The use of isochrones leads to two separate temperature scales, one for the main-sequence (MS) and one for the sub-giant branch (SGB). Tables of all the physical parameters calculated in LTE analysis can be found in Chapter 4. In Chapter 2 and 3, I give details of the data reduction processes and line broadening mechanisms, while unpublished parts of the LTE analysis are discussed in Chapter 4.

New effective temperatures have been calculated and all errors have been accounted for (Chapter 4 – Paper I: Hosford et al. 2009). The T_{eff} scales have been compared to temperature scales from other works derived using different methods. It was found that the

excitation energy temperature scales from this work are comparable to the photometric scale of Ryan et al. (1999), and the Balmer line wing scale of Asplund et al. (2006). However the temperatures from this work are still cooler than those from the IRFM adopted by Melendez & Ramirez (2004), by on average ~ 250 K. It has since been noted (Melendez – private communication) that their temperature scale suffers from systematic errors in the calibration procedure, and their scale is being revised.

Concerning the lithium abundances, mean values using the excitation temperatures were found to be $A(\text{Li}) = 2.16$ dex for the MS scale and $A(\text{Li}) = 2.10$ dex for the SGB scale. The scatter around the means was found to be 0.074 dex and 0.068 dex for the MS and SGB respectively. For five of the stars, it was possible to constrain the evolutionary state. The mean Li abundance calculated for these stars is $A(\text{Li}) = 2.18$ dex with a scatter of 0.038 dex. The small values of the scatter measurements indicates that we have reproduced the Li plateau, however, the mean values derived here are not high enough to solve the lithium problem, the WMAP value being $A(\text{Li}) = 2.72$ dex (Cyburt et al. 2008). Although the values derived in this work do not eliminate the discrepancy, they are similar to other works utilising LTE assumptions to derive effective temperatures, in particular to that of Spite et al. (1996) who found a value of $A(\text{Li}) = 2.08$ (± 0.08) dex and who also use an excitation method to determine their temperatures, and Bonifacio et al. (2007) who find a value of $A(\text{Li}) = 2.10$ (± 0.09) dex using a Balmer line wing method to derive their temperatures.

An investigation into whether there is evidence of a dependence of $A(\text{Li})$ on [Fe/H] or T_{eff} has also been performed. Firstly a multiple regression fit was calculated, linear in T_{eff} and [Fe/H]. This showed no statistically significant trend in either [Fe/H] or T_{eff} for the SGB case. There was evidence of a trend in [Fe/H] for the MS case with the coefficient being just statistically significant (~ 3σ), however, it is not certain whether all the stars belong to the MS evolutionary state. Following this, linear regression fits were performed separately for

[Fe/H] and T_{eff}. Similar results are found in regards to T_{eff}, i.e. there are no significant trends. For [Fe/H] a similarity is found in the coefficient to the values of Ryan et al. (1999) and Asplund et al. (2006). However, large errors in the SGB coefficient means there is no useful constraint for that set of values, and the lack of knowledge of the evolutionary state of the stars mean that the MS coefficient, although being $> 3\sigma$, is not a certain constraint. A final fit was performed following the description of Ryan et al. (2000), with the form:

$$\text{Li/H} = a' + b' \, \text{Fe/Fe}_{\odot} \qquad (10.1)$$

Here a' directly measures the primordial abundance of lithium. Values of $^{7}\text{Li/H} = (1.18 \pm 0.10) \times 10^{-10}$ and $^{7}\text{Li/H} = (1.10 \pm 0.10) \times 10^{-10}$ were found for the MS and SGB cases respectively.

Following the study of effective temperatures using the assumptions of LTE, a more sophisticated method has been used, that of NLTE. This is done for six of the original program stars, representing approximately one of the hottest stars, one of the coolest stars, one of the most metal rich stars etc. Considerable effort has gone into understanding the intricacies of Fe line formation under the conditions of NLTE. The NLTE code that has been used for this work on is MULTI (Carlsson 1986), with some updates implemented by Collet et al. (2005) regarding the inclusion of line-blocking. Two issues have been identified in regards to NLTE calculations: the need for a complete model atom in calculations and the uncertainty in the collisional scaling factor S_{H}, which affects the efficiency of collisions with neutral hydrogen. It is important to include as many of the higher levels in the model atom as possible (Korn 2008) as these levels are more readily collisionally ionised and are also

coupled to each other through low energy (infrared) transitions. It has been shown (Chapter 7 – Paper II) that the effect of inducing more collisions on the upper levels is to change the inferred effective temperatures by + 5 K. This small value does not substantially affect my work as random errors are of order ~ 80 K. The importance comes in demonstrating that the effects of the upper levels translate down to lower levels, and that for elements with many strong lines, such as Fe, a small change in the atom has effects that are felt through the whole atom, from the highest to the lowest levels.

In Chapter 7 the S_H value has also been discussed. Within this work two values for S_H have been used, $S_H = 0$, i.e. maximal NLTE effects, and $S_H = 1$, the full Drawinian magnitude for collisions. This is a very important factor and as to date its value is still very uncertain. This difference in S_H, equates to differences in effective temperature ranging from +6 K to +66 K for four of the six cases we have investigated, and -134 K to -56 K for the remaining two cases. Values of S_H, inferred or adopted in previous works, range from 30 (Gratton et al 1999) to 0.01 (Collet et al. 2005) to zero, with other values in between. These can lead to much larger, or smaller, temperature changes relative to LTE depending on the value used. My results also demonstrates that NLTE effects can be very different from star to star and that it is difficult to make generalizations, even about a small group of six stars which at first sight seem quite similar to one another, such as is used here. A preliminary investigation has been performed into identifying the value of S_H. The ionisation balance has been used for this purpose. It has been found that $S_H = 1$ may exaggerate the NLTE effect on the ionisation balance and hence may underestimate the role of collisions with neutral hydrogen, implying possibly that $S_H > 1$. This would put the value more in line with that of works such as Korn et al. (2003) who find a value $S_H = 3$.

The effective temperatures calculated here using the NLTE methods have again been compared to the scales of Ryan et al. (1999), Melendez & Ramirez (2004), and Asplund et al.

(2006). The new scale is hotter than the Ryan et al. (1999) scale by an average of 132 K and 162 K for $S_H = 0$ and 1 respectively, with a range from 43 K to 211 K. Temperatures found are still cooler than the Melendez & Ramirez (2004) temperatures by an average of 196 K and 193 K, with ranges of 27 K to 381 K and 84 K to 247 K for $S_H = 0$ and 1 respectively. Finally the effective temperatures for two of the stars that are in common with Asplund et al. (2006) are hotter by 97 K and 151 K for $S_H = 0$, whilst the third is cooler by 97 K. For $S_H = 1$ all three stars are hotter in this work by an average of 110 K, with a range of 37 K to 207 K. It has been noted (Barklem 2007) that the Balmer line temperatures may also suffer from NLTE effects, with possible increases of ~ 100 K. This would bring the two sets of temperatures back into agreement.

Lithium abundances have been calculated with the new NLTE effective temperatures. Mean values of $A(Li) = 2.19$ dex with a scatter of 0.072 dex and $A(Li) = 2.21$ dex with a scatter of 0.058 dex have been derived for $S_H = 0$ and 1 respectively. An increase from the LTE values is clearly evident; however, it is far from being a big enough increase to solve the lithium problem. Fits to [Fe/H] and T_{eff} have been performed. They show no statistically relevant trend for either value of S_H. The same fit represented by Eq. (9.1) was also carried out giving values of $^7Li/H = (1.47 \pm 0.27) \times 10^{-10}$ for $S_H = 0$ and $^7Li/H = (1.80 \pm 0.16) \times 10^{-10}$ for $S_H = 1$.

It is therefore clear that the introduction of NLTE corrections has not had a big enough effect on the effective temperatures to solve the lithium problem. The NLTE study (Chapter 7) combined with the LTE study (Chapter 4) have shown that systematic errors in the metal-poor T_{eff} scale are not large enough to cause the $A(Li)$ discrepancy between observation and WMAP+BBN calculations. This therefore adds strength to other possible

explanations for the discrepancy, i.e. diffusion, processing by an earlier generation of stars, and/or different BBN networks (Korn et al. 2006, Coc & Vangioni 2005).

The final part of this thesis is the examination of Ti as a constraint of the effective temperature and log g, followed by a study of the abundances of other elements in the spectrum of the program stars. The abundance study is completed using the parameters derived in the LTE analysis, and their impact on our picture of galactic chemical evolution (GCE) is assessed.

The Ti analysis of the three HD stars proved that this element was not suitable for the use of constraining temperature or gravity. The calculated temperatures are 6256 ± 241 K, 6729 ± 283 K and 6546 ± 230 K for HD140283, HD74000 and HD84937 respectively, where I quote 1σ errors. These errors are in fact an underestimate of the total errors, based only on the nulling procedure. The difference between these and the Fe T_{eff} values, 5769 ± 39 K, 6070 ± 127 K and 6168 ± 102 K for HD140283, HD74000 and HD84937 respectively, is 487 K, 659 K and 378 K which shows the Ti T_{eff} values are unhelpfully large. The Ti analysis yields log g values of 3.54 ± 0.08 dex, 3.73 ± 0.12 dex and 3.70 ± 0.06 dex for HD140283, HD74000, and HD84937 respectively, with differences from the HIPPARCOS values (3.73 dex, 4.03 dex and 3.98 dex) of -0.19 dex, -0.30 dex and -0.28 dex. These values are unrealistic compared to the well known parameters derived for these stars. The average difference is -0.26 dex, suggesting the presence of NLTE effects, specifically overionization of the neutral state. It was therefore decided it would not be fruitful to continue this analysis with the remaining program stars. Following this I have presented the abundances and errors for several elements. Abundance ratios have been plotted, and implications of trends and scatter discussed. For Mg these trends and scatters point to a slightly more inhomogeneous scenario for the early galaxy than that shown by Arnone et al. (2005), however, I do not find the degree of scatter that Argast et al. (2000) have found in their calculations, suggesting the

196

early Galaxy was not as inhomogeneous as they predicted. This is only a very brief look at the other elemental abundances. For a full understanding of where these stars fit into GCE more quantitative comparisons with models will need to be made, thus allowing for constraints on GCE theories.

10.2. Future Work

In the work on LTE, particular attention was made in quantifying the main sources of errors, both random and systematic. One issue identified was the uncertainties in $\log g$. The lack of sufficiently accurate HIPPARCOS data led to the use of theoretical isochrones to calculate $\log g$; which in turn gave two possible evolutionary states for many of the program stars. It is obvious then that an attempt to precisely determine $\log g$ for each star is needed. This can be done through the use of sufficiently precise Strömgren photometry. Therefore a next step would to be to write a proposal for the acquisition of this data allowing for the determination of $\log g$. This will also be possible to do with the parallaxes that will be determined by GAIA when it is launched.

One of the largest sources of random error comes from the statistical error in the determination of effective temperature. This may be reduced through the use of higher S/N and higher resolution data, which would allow for greater accuracy in measuring equivalent widths, and through more accurate gf and damping values. The combination of reducing errors and defining evolutionary states would also allow for better fits of A(Li) to [Fe/H], with smaller errors on the coefficients. The trends that are seen for the MS case may then prove useful.

From the NLTE study some obvious aspects need to be investigated further. As stated the Fe model atom adopted in this work was not a full atom, i.e. many of the upper levels of the atom were not present. It would seem worthwhile to construct a complete atom to fully

investigate the effect of the missing upper levels. Whilst I believe on the basis of my calculations this would not greatly affect the outcome of the result found here, i.e. it introduces an error of order 5 K, it would be necessary for further work into the NLTE formation of Fe lines, especially as Fe is very important as a diagnostic of the metallicities of stars.

Following this the next obvious task should be a dedicated study of the value of S_H. As calculations predicting the relative abundances of neutral hydrogen and electrons within these stars, i.e. hydrogen is more abundant; suggest that hydrogen collisions play an important role in metal-poor stars (e.g. Asplund 2005) the precise value of S_H is very important. I have touched on this in Chapter 7, giving a brief look at the use of ionisation equilibrium to present a rough estimate to the value of S_H. This limit suggests that an $S_H > 1$, perhaps $S_H \approx 3$ as Korn (2003) concluded, would be a more suitable value with my combination of atom, atmosphere etc. A recalculation of the effective temperatures using S_H = 3 should be carried out so as to determine the effects of this increased value.

Further use of the abundances of the other elements besides Fe in the spectrum of the stars will be desirable. Here I have only presented a brief look at trends and scatter in some of the elements, and what these suggest in respect to galactic chemical evolution (GCE). For a more detailed investigation, quantitative comparisons with GCE models will need to be carried out, which in turn requires access to the detailed numerical results of iGCE modelling. This will allow for constraints to be made on GCE theory.

11. References

Ahmed, S. N., et al. 2004, Physical Review Letters, 92, 181301

Alonso, A., Arribas, S., & Martínez-Roger, C. 1996, A&AS, 117, 227

Alonso, A., Arribas, S., & Martínez-Roger, C. 1999, A&A, 139, 335

Andersen, J., Gustafsson, B., & Lambert, D. L. 1984, A&A, 136, 65

Angulo, C., et al. 2005, ApJ, 630, L105

Anstee, S. D., & O'Mara, B. J. 1995, MNRAS, 276, 859

Aoki, W., Barklem, P. S., Beers, T. C., et al. 2009, ApJ, 698, 1803

Arnone, E., Ryan, S. G., Argast, D., Norris, J. E., & Beers, T. C. 2005, A&A, 430, 507

Argast, D., Samland, M., Gerhard, O. E., & Thielemann, F.-K. 2000, A&A, 356, 873

Argast, D., Samland, M., Thielmann, F. –K., & Gerhard, O. E. 2002, 388, 842

Asplund, M., Gustafsson, B., Kiselman, D., & Eriksson, K. 1997, A&A, 318, 521

Asplund, M., Nordlund, E., Trampedach, R., & Stein, R. F. 1999, A&A, 346, L17

Asplund, M. & García Pérez, A. E. 2001, A&A, 372, 601

Asplund, M. 2005, ARA&A, 43, 481

Asplund, M., Nissen, P. E., Lambert, D. L., Primas, F. & Smith, V. V. 2005, IAU Symp, 228, 53

Asplund, M., Lambert, D. L., Nissen, P. E., Primas, F., & Smith, V. V. 2006, ApJ, 644, 229

Athay, R. G., & Lites, B. W. 1972, ApJ, 176, 809

Bahcall, J. N., Pinsonneault, M. H., & Basu, S. 2001, ApJ, 555, 990

Bard, A., Kock, A., & Kock, M. 1991, A&A, 248, 315

Bard, A. & Kock, M, 1994, A&A, 282, 1014

Barklem, P. S., & O'Mara, B. J. 1997, MNRAS, 290, 102

Barklem, P. S., O'Mara, B. J., & Ross, J. E. 1998. MNRAS, 296, 1057

Barklem, P. S., Piskunov, N., & O'Mara, B. J. 2000, A&A, 363, 1091

Barklem, P. S., Stempels, H. C., Allende Prieto, C., Kochukhov, O. P., Piskunov, N., & O'Mara, B, J. 2002, A&A, 385, 951

Barklem, P. S., Belyaev, A. K., & Asplund, M. 2003, A&A, 409, L1

Barklem, P. S. 2007, A&A, 466, 327

Bell, R. A. 1981 private communication

Baumueller, D. & Gehren, T. 1997, A&A, 325, 1088

Bautista, M. A. 1997, A&AS, 122, 167

Bhatangar, P., Krook, M., Menzel, D., & Thomas, R. 1955, Vistas in Astronomy, 1, 296

Blackwell, D. E., Ibbetson, P. A., Petford, A. D., & Shallis, M. J. 1979, MNRAS, 186, 633

Blackwell, D. E., Petford, A. D., & Shallis, M. J., 1979, MNRAS, 186, 657

Blackwell, D. E., Shallis, M. J., & Selby, M. J. 1979, MNRAS. 188, 847

Blackwell, D. E., Petford, A. D., Shallis, M. J., & Simmons, G. J. 1980, MNRAS, 191, 445

Blackwell, D. E., Petford, A. D., Shallis, M. J., & Simmons, G. J. 1982, MNRAS, 199, 43

Blackwell, D. E., Petford, A. D., & Simmons, G. J., 1982, MNRAS, 210, 595

Bonifacio, P., Molaro, P., Silvarani, T., et al. 2007, A&A, 462, 851

Bruls, J. H. M. J., Rutten, R. J., Shchukina, N. G. 1992, A&A, 265, 237

Carlsson, M. 1986, Uppsala Astronomical Observatory Reports, 33

Carlsson, M., Rutten, R. J., Bruls, J. H. M. J., & Shchukina, N. G. 1994, A&A, 288, 860

Castelli, F., Gratton, R. G., & Kurucz, R L. 1997, A&A, 318, 841

Cayrel, R., Steffen, M., Chand, H., Bonifacio, P., Spite, M., Spite, F., Petitjean, P., Ludwig, H. G., & Caffau, E., 2007, A&A, 473, 37

Coc, A., Vangioni-Flam, E., Cassé, M. & Rabiet, M. 2002, Phys. Rev. D65, 043510

Coc, A., Vangioni-Flam, E., Descouvemont, P., Adahchour, A. & Angulo, C., 2004, ApJ, 600, 544

Coc, A., & Vangioni, E. 2005, IAU Symp, 228, 13Collet, R., Asplund, M., & Thévenin, F. 2005, A&A, 442, 643

Coc, A., Olive, K. A., Uzan, J.-P., & Vangioni, E. 2006, Phys. Rev. D, 73, 083525

Coc, A., Nunes, N. J., Olive, K. A., Uzan, J.-P., & Vangioni, E. 2007, Phys. Rev. D, 76, 023511

Collet, R., Asplund, M., & Th´evenin, F. 2005, A&A, 442, 643

Cottrell, P. L., & Norris, J. E. 1978, ApJ, 221, 893

Cox, A. N. 2000, S&T, 100, 010000

Cyburt, R. H., Fields, B. D., & Olive, K. A. 2001, New Astronomy, 6, 215

Cyburt, R. H., Fields, B. D., & Olive, K. A. 2003, Phys. Lett. B567, 227

Cyburt, R. H. 2004, Phys. Rev. D, 70, 023505

Cyburt, R. H., Fields, B. D., & Olive, K. A. 2004, Phys. Rev. D, 69, 123519

Cyburt, R. H., Ellis, J., Fields, B. D., Olive, K. A., & Spanos, V. C. 2006, Journal of Cosmology and Astro Particle Physics, 11, 14

Cyburt, R. H., Fields, B. D., & Olive, K. A. 2008,Journal of Cosmology and Astro-Particle Physics, 11, 12

Damour, T., & Nordtvedt, K. 1993, Physical Review Letters, 70, 2217

Damour, T., & Nordtvedt, K. 1993, Phys. Rev. D, 48, 3436

Damour, T., & Pichon, B. 1999, Phys. Rev. D, 59, 123502

Dmitriev, V. F., Flambaum, V. V., & Webb, J. K. 2004, Phys. Rev. D, 69, 063506

Drawin, H. W. 1968, Z. Phys., 211, 404

Drawin, H. W. 1969, Z. Phys., 225, 483

Dunkley, J., et al. 2008, ArXiv e-prints, 803, arXiv:0803.0586

Ellis, J., Olive, K. A., & Vangioni, E. 2005, Physics Letters B, 619, 30

Feautrier, P. 1964, Comptes Rendus Acad. Sci. Paris, 258, 3189

Feng, J. L., Su, S., & Takayama, F. 2004, Phys. Rev. D, 70, 075019

Fields, B.F., & Sarkar, S., 2006 in Yao, W.-M., & et al. 2006, Journal of Physics G Nuclear Physics, 33, 1

Fleck, I., Grosser, J., Schnecke, A., Steen, W., & Voigt, H. 1991, J.phys. B, 24, 4017

Fröhlich, C., Fischer, T., Liebendörfer, M., Thielemann, F. –K., Truran, J. W. 2008 IAUS, 250, 401

Fuhr, J. R., Martin, G. A., & Wiese, W. L. 1988, Journal of Physical and Chemical Reference Data, 17, 4

Fuhrmann, K., Axer, M., & Gehren, T. 1992, A&A, 271, 451

Fuhrmann, K., Axer, M., & Gehren, T. 1994, A&A, 285, 585

García Peréz, A. E., Inoue, S., Aoki, W., & Ryan, S. G. 2008, Precision Spectroscopy in Astrophysics, Proceedings of the ESO/Lisbon/Aveiro Conference, 9

Gehren, T., Butler, K., Mashonkina, L., Reetz, J., & Shi, J. 2001, A&A, 366, 981

Gratton, R. G., Carretta, E., Eriksson, K., & Gustafsson, B. 1999, A&A, 350, 955

Gray, D. F. 2005, The Observation and Analysis of Stellar Photospheres, 3rd Edition, Cambridge University Press

Grevesse, N., & Sauval, A. J. 1998, SSRv, 85, 161

Hamaguchi, K., Hatsuda, T., Kamimura, M., Kino, Y., & Yanagida, T. T. 2007, Phys. Lett. B, 650, 268

Hannaford, P., Lowe, R. M., Grevesse, N. & Noels, A. 1992, A&A, 259, 301

Heise, C. & Kock, M. 1990, A&A, 230, 244

Hirata, R. & Horaguchi, T. 1995, Catalogue of Atomic Spectral Lines

Hosford, A., Ryan, S. G., García Pérez, A. E., Norris, J. E., & Olive, K. A. 2009, A&A, 493, 601

Jedamzik, K. 2004, Phys. Rev. D, 70, 063524

Jedamzik, K., Choi, K.-Y., Roszkowski, L., & Ruiz de Austri, R. 2006, Journal of Cosmology and Astro-Particle Physics, 7, 7

Jedamzik, K. & Pospelov, M. 2009, New J. Phys., 11, 105028

Kirchhoff, G. and Bunsen, R. 1860, Poggendorff's Ann, 110, 160

Korn, A. J., Grundahl, F., Richard, O., Barklem, P. S., Mashonkina, L., Collet, R., Piskunov, N., & Gustafsson, B. 2006, Nature, 442, 657

Korn, A. J. 2008, Physica Scripta Volume T, 133, 014009

Korn, A. J., Shi, J., & Gehren, T. 2003, A&A, 407, 691

Kroll, S. & Kock, M, 1987, A&AS, 67, 225

Kurucz, R. L. 1993, IAU Colloq. 138: Peculiar versus Normal Phenomena in A-type and Related Stars, Astronomical Society of the Pacific Conference Series, 44, 87

Kurucz, R. & Bell, B. 1995, Atomic Line Data (R.L. Kurucz and B. Bell) Kurucz CD-ROM No. 23. Cambridge, Mass.: Smithsonian Astrophysical Observatory, 1995., 23

Lambert, D. L. 1993, Physica Scripta Volume T, 47, 186

Lind, K., Asplund, M., & Barklem, P. S. 2009, A&A, 503, 541

Ludwig, H., Behara, N. T., Steffen, M., & Bonifacio, P. 2009, A&A, 502, L1

Magain, P. 1987, A&A, 181, 323

Meléndez, J., & Ramírez, I. 2004, ApJ, 615, L33

Menzel, D. H., & Milne, E. A., 1966, "Selected papers on the transfer of radiation", Dover Publications

Milhalas, D., 1978, Stellar atmospheres 2nd edition, ed, J. Hevelius

Milne, E. A. 1930, Handbuch der Astrophysik 3, Part 1, Chap. 2, 65

Moity, J. 1983, A&AS, 52, 37

Nave, G., Johansson, S., Learner, R. C. M., Thorne, A. P., & Brault, J. W. 1994, ApJS, 94, 221

Nomoto, K., Thielemann, F. K., & Yokoi, I. 1984, ApJ, 286, 644

Norris, J. E., Ryan, S. G., & Stringfellow, G. S. 1994, ApJ, 423, 386

Norris, J. E., Ryan, S. G., & Beers, T. C. 2001, ApJ, 561, 1034

O'Brian, T. R., Wickliffe, M. E., Lawler, J. E., Whaling, W., & Brault, J. W. 1991, JOptSocAmB, 8, 1185

Olive, K. A., Steigman, G., & Walker, T. P. 2000, Phys. Rep., 333, 389

Peterson, R., Carney, B. W. 1979, ApJ, 231, 762

Piau, L., Beers, T. C., Balsara, D. S., Sivarani, T., Truran, J. W., & Ferguson, J. W. 2006, ApJ, 653, 300

Ramírez, I., & Meléndez, J. 2005, ApJ, 626, 446

Richard, O., Michaud, G., & Richer, J. 2005, ApJ, 619, 538

Rutten, R. J. 1990, ASPC, 9, 91

Ryan, S. G. Beers, T. C., Deliyannis, C. P., Thorburn, J. A. 1996, ApJ, 458, 543

Ryan, S. G., Norris, J. E., Beers, T. C. 1996, ApJ, 471, 254

Ryan, S. G., Beers, T. C., Deliyannis, C. P., & Thorburn, J. A. 1996a, ApJ, 458, 543

Ryan, S. G. 1998, A&A, 331, 1051

Ryan, S. G., Norris, J. E., Beers, T. C. 1999, ApJ, 523, 654

Ryan, S. G., Beers, T. C., Olive, K. A., Fields, B. D., & Norris, J. E. 2000, ApJ, 530, L57

Ryan, S. G., Kajino, T., Beers, T. C., et al. 2001, ApJ, 549, 55

Ryan, S. G., Kajino, T., Beers, T. C., Suzuki, T. K., Romano, D., Matteucci, F., & Rosolankova, K. 2001, ApJ, 549, 55

Rybicki, G. B. 1971, J.Q. S. R. T., 11, 589

Salati, P. 2003, Phys. Lett. B,571. 121

Scharmer, G. B., & Carlsson, M. 1985, J. Comp. Phys. 59, 56

Seaton, M. J. 1987, Journal of Physics B Atomic Molecular Physics, 20, 6363

Seaton, M. J., Yan, Y., Mihalas, D., & Pradhan, A. K. 1994, MNRAS, 266, 805

Shchukina, N. G., Trujillo Bueno, J., & Asplund, M. 2005, ApJ, 618, 939

Schnabel, R., Kock, M. & Holweger, H. 1999, A&A, 342, 610

Spite, F. & Spite, M. 1982, A&A, 115, 357

Spite, M., Francois, P., Nissen, P. E., & Spite, F. 1996, A&A, 307, 172

Steenbock, W. & Holweger, H. 1984, A&A, 130, 319

Thévenin, F. 1989, A&AS, 77, 137

Thévenin, F. 1990, A&AS, 82, 179

Thévenin, F. & Idiart, T. P. 1999, ApJ, 521, 753

Thielemann, F. K., Hashimoto, M., & Nomoto, K. 1990, ApJ, 349, 222

Timmes, F. X., Woosley, S. E. & Weaver, T. A. 1995, ApJS, 98, 617

Vangioni-Flam, E., Olive, K A., Fields, B. D. & Cass´e, M. 2003 ApJ. 585, 611

van Regemorter, H. 1962, ApJ, 136, 906